

WA School of Mines: Minerals, Energy and Chemical Engineering

**Synthesis and Photocatalytic Application of Novel Heterojunction
Nanocomposites as Photocatalysts**

Yazi Liu

**This thesis is presented for the Degree of
Doctor of Philosophy
of
Curtin University**

December 2018

Declaration

To the best of my knowledge and belief this thesis contains no material previously published by any other person except where due acknowledgement has been made.

This thesis contains no material which has been accepted for the award of any other degree or diploma in any university.

Signature: Yazi Liu (Yazi Liu)

Date: 10/12/2018

Acknowledgement

I would like to express my most enthusiastic gratitude to my principal supervisor, Prof. Shaobin Wang. Prof. Wang is the most rigorous and resourceful professor I have ever met. He is so modest and considerate, always ready to stop his work in hand for discussions with me, which always motivates me to spark many new ideas. His support and tolerance has infused me with strong endeavour and determination to adventure in the fantastic world full of academic and scientific unknowns. Prof. Wang's great guidance and passion for research have been and will be profoundly influencing my whole life.

Equally, I owe my sincere gratitude to my co-supervisor, Prof. Hongqi Sun, for the inspiration and warm encouragement. Whenever I got stuck with challenges and confusions, he is always willing to guide me through the tough journey, help revise the manuscript, and address the reviewers' critical comments during my PhD study without reservation. I would not have these great publications without his continuous inputs to my manuscripts. I am lucky and proud to be his student.

I am grateful to my postgraduate supervisor, Prof. Cheng Sun at Nanjing University, for his encouragement and support to me in pursuing my PhD degree overseas and chasing my dream. My sincere gratitude also goes to Prof. Xinyong Li at Dalian University of Technology for all kinds of suggestions for the benefits of my research and career.

I would like to express my great appreciation to Dr. Huayang Zhang and Dr. Xiaoguang Duan for providing coach and support to my ideas and experiments during my PhD journey. I am thankful to Prof. Zhenyu Chu and Dr. Xiaochen Guo who taught me a lot about electrochemistry which has opened up a new gate for my future research. I also thank Profs. Jun Ke, Jie Liu and Wei Wang for their fruitful discussions each time I feel blank.

I want to appreciate Jian Xu, Shanshan Ding, Ying Liu and Prof. Shaogui Yang for helping with the related characterizations and contributions to my paper from Nanjing, China. Also, I show thankfulness to Prof. Shaomin Liu and Dr. Lihong Liu for generous praise and encouragement for my research and career during the past three years.

I am also thankful to my friends and colleagues, Li Zhou, Xiaojie Li, Jinqiang Zhang, Xinyuan Xu, Lei Shi, Hong Wu, Jian Kang, Wenjie Tian, Chen Wang, Panda Yao, Jiaquan Li, Wenran

Gao, Chi Zhang, Ping Liang, Yu Yin, Qi Yang, Muhammad, Dr. Caili Wang, Dr. Linfeng Zhai and Dr. Liang Zhao. Thank you, pals, I cannot imagine the life without you! I also want to thank Tuhua Li, my trusted friend, who is always there to help me go through my hard time overseas.

I want to give my gratitude to the technician team, Roshanak, Yu, Jimmy, Andrew, Guanliang, Ann, Anja, Jason, Araya, and Karen. Thank you all for helping prepare the chemicals and training me how to use the equipment and software. Specifically, I would send my greatest appreciation to Roshanak, who is always there caring about my instruments and so helpful and considerate.

And last, but not least, I would like to express my deepest love to my family: my husband Pengcheng Tang, my mum Yun Li and my son Yiliu Tang. Without your firm support and unconditional love, I would never be able to go through such a tough journey both academically and mentally. I truly thank you for your warm accompany and tremendous sacrifice. Especially, to my aged mum who trudged in between China and Australia numerous times to support my study. I owe my deep gratitude to my husband and my son for your tolerance and understanding, who are always there when I turn to for help and console. I can never go so far without your constant and eternal encouragement. The faith to make you feel proud of me has inspired me to survive such changeling and depressing time. I love you all dearly.

Abstract

Visible-light-responsive photocatalysts, bismuth-based and g-C₃N₄-based heterojunction composites, have attracted numerous attention in photocatalytic degradation of pollutants and solar energy conversion. Designing various novel heterojunction nanocomposites has demonstrated enhanced photocatalytic activity by inhibiting the recombination rate of photo-generated charge carriers and reducing the over-potential for photoreduction or photooxidation reactions. Convincingly, p-n heterojunction of BiFeO₃@TiO₂ with a core-shell structure exhibited much higher photocatalytic oxidation towards different dyes under visible light irradiation. Bismuth-based hybrids such as BiOI/BiOCl have displayed superb photocatalytic activity for the degradation of various industrial dyes under natural sunlight irradiations, demonstrating high significance for the remediation of industrial wastewater. Additionally, it also exhibited an excellent photo-oxidation ability with enhanced O₂ evolution from water. *In-situ* electron paramagnetic resonance (EPR) testing shows that the photodegradation was ascribed to the superoxide radicals, oxidative holes, and minor amount of hydroxyl radicals. Apart from the bismuth-based heterogeneous coupling compounds, Metal sulfides (phosphides)/g-C₃N₄ composite heterostructures such as MoS₂/g-C₃N₄ and CoP/g-C₃N₄ have demonstrated enhanced photocatalytic and electrocatalytic hydrogen evolution performances for water splitting. MoS₂ or CoP can serve as an electron acceptor as well as the active sites on the surface of g-C₃N₄, leading to the formation of an intimate contact interface with a decreased onset potential, lower charge-transfer resistance and higher reductive potential. Different morphologies of 0D/2D/3D MoS₂ were systematically studied for depositing on g-C₃N₄ nanosheets, showing variance in photocatalytic H₂ activity. The 3D/2D hybrid of MoS₂/g-C₃N₄ presents better photocatalytic performance than its 0D/2D and 2D/2D analogues, owing to its unique flower-like nanostructure of MoS₂ with exposure of more active edge planes and shortened diffusion channels for charge transfer and separation. Finally, the unique heterojunction of CoP/g-C₃N₄ exhibits superior photocatalytic, electrocatalytic H₂ evolution performances, photoelectrochemical response as well as excellent overall water splitting activity. For the first time, CoP-based photocatalysts as effective photo, electro and photochemical HER catalysts with evident enhancement have been investigated simultaneously. The findings would significantly contribute to photocatalytic applications of bismuth-based and g-C₃N₄-based nanocomposites for artificial photosynthesis and environmental remediation.

Publications by the Author

Published and Accepted Papers:

1. **Yazi Liu**, Xinyuan Xu, Jinqiang Zhang, Huayang Zhang, Wenjie Tian, Xiaojie Li, Moses O Tade, Hongqi Sun, Shaobin Wang. Flower-like MoS₂ on graphitic carbon nitride for enhanced photocatalytic and electrochemical hydrogen evolutions. *Applied Catalysis B: Environmental*. 2018, 239, 334-344.
2. **Yazi Liu**, Huayang Zhang, Jun Ke, Jinqiang Zhang, Wenjie Tian, Xinyuan Xu, Xiaoguang Duan, Hongqi Sun, Moses O Tade, Shaobin Wang. 0D(MoS₂)/2D(g-C₃N₄) heterojunctions in Z-scheme for enhanced photocatalytic and electrochemical hydrogen evolution. *Applied Catalysis B: Environmental*. 2018, 228, 64-74.
3. **Y Liu**, S Ding, J Xu, H Zhang, S Yang, X Duan, H Sun, S Wang. Preparation of p-n heterojunction photocatalyst BiFeO₃@TiO₂ with core-shell structure for visible photocatalytic degradation. *Chinese Journal of Catalysis*. 2017, 38, 1052-1062.
4. **Y Liu**, J Xu, L Wang, H Zhang, P Xu, X Duan, H Sun, S Wang. Three-dimensional BiOI/BiOX (X= Cl or Br) nanohybrids for enhanced visible-light photocatalytic activity. *Nanomaterials*. 2017, 7(3) 64.
5. **Yazi Liu**, Dan Sun, Sadegh Askari, Jenish Patel, Manuel Macias Montero, Somak Mitra, Richao Zhang, Davide Mariotti, Paul Maguire. Enhanced dispersion of TiO₂ nanoparticles in polymer through plasma-liquid interaction. *Scientific Reports*. 2015, 5, 15765.
6. Fanpeng Meng, **Yazi Liu**, Jun Wang, Xiaoyao Tan, Hongqi Sun, Shaomin Liu, Shaobin Wang. Temperature dependent photocatalysis of g-C₃N₄, TiO₂ and ZnO: differences in photoactive mechanism. *Journal of Colloid and Interface Science*. 2018, 532, 321-330.
7. Danjun Mao, Anqing Yu, Shanshan Ding, Fei Wang, Shaogui Yang, Cheng Sun, Huan He, **Yazi Liu**, Kai Yu. One-pot synthesis of BiOCl half-shells using microemulsion droplets as templates with highly photocatalytic performance for the degradation of ciprofloxacin. *Applied Surface Science*. 2016, 389, 742-750.

Manuscripts Submitted or in Preparation:

1. **Yazi Liu**, Jinqiang Zhang, Xiaoguang Duan, Hongqi Sun, Shaobin Wang. Graphitic carbon nitride decorated with CoP nanocrystals for enhanced photo, electro and photoelectrochemical H₂ evolution. (**to be submitted**)

2. Zhenyu Chu; **Yazi Liu**; Huayang Zhang; Jinqiang Zhang; Hongqi Sun; Moses O Tade; Shaobin Wang. Dual-functional Prussian blue core-shell nanocubes for high performance of electrochemical and photoelectrochemical biosensing. (**submitted to Environmental Science: Nano**)

Referred Conference

Yazi Liu, Huayang Zhang, Shaobin Wang. Photocatalytic and electrochemical hydrogen evolution over MoS₂ quantum dots loaded on g-C₃N₄ catalysts. The International Symposium on the relations between Homogeneous and Heterogeneous Catalysis, ISHHC 18: Catalysis – Enabling the Future. July 22-25, 2018, Sydney, NSW Australia. (Abstract 86580)

Content

Declaration	i
Acknowledgement	ii
Abstract	iv
Publications by the Author	v
Content	vii
Chapter 1. Introduction	- 1 -
1.1 Background	- 1 -
1.2 Research objectives	- 3 -
1.3 Thesis outline	- 3 -
References	- 5 -
Chapter 2. Literature Review	- 7 -
2.1 Environmental remediation and energy crisis	- 7 -
2.2 Solar energy conversion process	- 7 -
2.2.1 Solar cell	- 7 -
2.2.2 Photocatalytic reduction of CO ₂	- 8 -
2.2.3 Photocatalytic degradation of pollutants	- 9 -
2.2.4 Photocatalytic water splitting	- 10 -
2.3 Hydrogen evolution process	- 12 -
2.3.1 Electrocatalytic hydrogen evolution reaction	- 12 -
2.3.2 Photocatalytic hydrogen evolution reaction	- 14 -
2.3.3 Photoelectrochemical hydrogen evolution reaction	- 16 -
2.4 g-C ₃ N ₄ -based heterojunction photocatalysts	- 17 -
2.4.1 Pristine g-C ₃ N ₄	- 17 -
2.4.2. Design and construction of inorganic semiconductor-g-C ₃ N ₄ heterostructures	- 20 -
2.4.2.1. Metal oxides/g-C ₃ N ₄ composite heterostructures	- 21 -
2.4.2.2. Metal sulfides/g-C ₃ N ₄ composite heterostructures	- 24 -
2.4.2.3. Metal phosphides/g-C ₃ N ₄ composite heterostructures	- 29 -
2.5 Bismuth-based complex oxides as visible light photocatalysts	- 32 -
2.5.1 Synthesis and photocatalytic application of bismuth oxyhalides	- 32 -
2.5.1.1 Crystal and electronic structure	- 32 -
2.5.2.1 Crystal and electronic structure	- 36 -
2.5.2.2 Photoactivity enhancement via modification	- 38 -
2.5.2.3 Summary and outlook	- 41 -

2.5.3 Synthesis and photocatalytic application of bismuth tungstates.....	- 41 -
2.5.3.1 Crystal and electronic structure.....	- 41 -
2.5.3.2 Photoactivity enhancement via modification.....	- 42 -
2.5.3.3 Summary and outlook.....	- 44 -
2.6 Conclusions and perspectives	- 44 -
References	- 45 -
Chapter 3. Preparation of p-n Heterojunction of BiFeO₃@TiO₂ with a Core-Shell Structure for Visible Light Photocatalytic Degradation.....	- 54 -
Abstract.....	- 55 -
3.1 Introduction	- 55 -
3.2 Experimental section	- 57 -
3.2.1 Materials.....	- 57 -
3.2.2 Sample Preparation	- 57 -
3.2.3 Characterization Techniques	- 58 -
3.2.4 Evaluation of Photocatalytic Activity	- 58 -
3.2.5 Photoelectrochemical Measurements.....	- 59 -
3.3 Results and Discussion.....	- 59 -
3.3.1 Morphology and Structure	- 59 -
3.3.2. Optical Properties	- 61 -
3.3.3 Photocatalytic Degradation of Methyl Violet	- 64 -
3.3.4 Photocatalytic Degradation of Other Dyes with BiFeO ₃ @TiO ₂ (mass ratio 1:1).....	- 73 -
3.4 Conclusions	- 74 -
References.....	- 102 -
Chapter 4. Three-Dimensional BiOI/BiOX (X = Cl or Br) Nanohybrids for Enhanced Visible-Light Photocatalytic Activity.....	- 80 -
Abstract.....	- 81 -
4.1 Introduction	- 81 -
4.2 Experimental Section.....	- 83 -
4.2.1 Materials	- 83 -
4.2.2 Synthesis of BiOX (X = Cl, Br, I)	- 83 -
4.2.3 Synthesis of BiOI/BiOX (X = Cl, Br)	- 83 -
4.2.4 Characterization Techniques.....	- 84 -
4.2.5 Evaluation of the Photocatalysts.....	- 85 -
4.3 Results and Discussion.....	- 85 -
4.3.1 Morphology and Structure.....	- 85 -

4.3.2 Optical Properties.....	- 89 -
4.3.3 XPS Analysis	- 89 -
4.3.4 Specific Surface Areas and Pore Structure	- 91 -
4.3.5 Photocatalytic Degradation of MO	- 92 -
4.4 Conclusions	- 102 -
References.....	- 102 -
Chapter 5. 0D (MoS₂)/2D (g-C₃N₄) Heterojunctions in Z-Scheme for Enhanced Photocatalytic and Electrochemical Hydrogen Evolution	- 105 -
Abstract.....	- 106 -
5.1 Introduction	- 106 -
5.2 Experimental Section.....	- 108 -
5.2.1 Synthesis of Photocatalysts.....	- 108 -
5.2.2 Characterization Techniques.....	- 109 -
5.2.3 Photocatalytic Activity Evaluation.....	- 110 -
5.2.4 Photoelectrochemical Measurements	- 110 -
5.2.5 Electrocatalytic Hydrogen Evolution.....	- 111 -
5.3 Results and Discussion.....	- 111 -
5.3.1 Phase Structure, Morphology and Composition of Catalysts	- 111 -
5.3.2 Optical Properties.....	- 116 -
5.3.3 Photocatalytic H ₂ -Production Activity and Stability.....	- 119 -
5.3.4 Photocatalytic Mechanism	- 123 -
5.4 Conclusions	- 129 -
References	- 130 -
Chapter 6. Flower-Like MoS₂ on Graphitic Carbon Nitride for Enhanced Photocatalytic and Electrochemical Hydrogen Evolutions	- 134 -
Abstract.....	- 135 -
6.1 Introduction	- 135 -
6.2 Experimental Section.....	- 137 -
6.2.1 Materials	- 137 -
6.2.2 Synthesis of the Catalysts	- 137 -
6.2.3 Characterization Techniques.....	- 138 -
6.2.4 Evaluation of Photocatalytic Activity.....	- 139 -
6.2.5 Photoelectrochemical Measurements	- 139 -
6.2.6 Electrocatalytic Hydrogen Evolution.....	- 139 -
6.3 Results and Discussion.....	- 139 -
6.3.1 Crystal Structure, Morphology and Composition	- 139 -

6.3.2 Optical Properties.....	- 148 -
6.3.3 Photocatalytic HER Activity and Stability.....	- 149 -
6.3.4 Photocatalytic Mechanism	- 153 -
6.4 Conclusions	- 159 -
References	- 161 -
Chapter 7. Graphitic Carbon Nitride Decorated with CoP Nanocrystals for Enhanced Photo, Electro and Photoelectrochemical H₂ evolution	- 165 -
Abstract.....	- 166 -
7.1 Introduction	- 166 -
7.2 Experimental section	- 168 -
7.2.1 Materials	- 168 -
7.2.2 Synthesis of the catalysts.....	- 168 -
7.2.2.1 Synthesis of g-C ₃ N ₄	- 168 -
7.2.2.2 Synthesis of Co(OH) ₂	- 168 -
7.2.2.3 Synthesis of CoP	- 168 -
7.2.2.4 Synthesis of CoP-C ₃ N ₄ composite	- 168 -
7.2.2.5 Synthesis of Pt-CoP/C ₃ N ₄ composite	- 169 -
7.2.3 Characterization techniques	- 169 -
7.2.4 Evaluation of photocatalytic activity.....	- 169 -
7.2.5 Photoelectrochemical measurements	- 170 -
7.3 Results and discussion	- 170 -
7.3.1 Crystal structure, morphology and composition	- 170 -
7.3.2 Optical properties.....	- 175 -
7.3.3 Photocatalytic HER and water splitting activity	- 176 -
7.3.4 Photocatalytic mechanism.....	- 178 -
7.4 Conclusions	- 184 -
References	- 185 -
Chapter 8. Conclusions and Perspectives.....	- 187 -
8.1 Conclusions	- 187 -
8.1.1 Preparation of p-n Heterojunction of BiFeO ₃ @TiO ₂ with a Core-Shell Structure for Visible Light Photocatalytic Degradation.....	- 187 -
8.1.2 Three-Dimensional BiOI/BiOX (X = Cl or Br) Nanohybrids for Enhanced Visible-Light Photocatalytic Activity	- 188 -
8.1.3 0D (MoS ₂)/2D (g-C ₃ N ₄) Heterojunctions in Z-Scheme for Enhanced Photocatalytic and Electrochemical Hydrogen Evolution.....	- 189 -
8.1.4 Flower-Like MoS ₂ on Graphitic Carbon Nitride for Enhanced Photocatalytic and Electrochemical Hydrogen Evolutions	- 190 -

8.1.5 Graphitic Carbon Nitride Decorated with CoP Nanocrystals for Enhanced Photo, Electro and Photoelectrochemical H ₂ Evolution.....	- 190 -
8.2 Perspectives and suggestions for future research.....	- 191 -
Appendix.....	- 193 -

Chapter 1. Introduction

1.1 Background

Recently, with the deterioration of the whole environment, most countries in the world are facing a series of environmental problems, especially the water resources that human beings depend on. High-concentrated refractory toxic organic pollutants discharged from a large number of industrial and mining processes, for example, in power generation, paper making, printing and dyeing, and metallurgical industries, have become an important part of wastewater, which has already posed a major threat on human health. Traditional treatment technologies towards these refractory toxic waste water include adsorption, flocculation, sedimentation, filtration, gas stripping, etc, all of which simply separate or concentrate the contaminants, or just transfer the contaminants from one phase to another, leading to a secondary pollution inevitably. In the past decades, research on pollutant control has gradually been shifted to advanced oxidation processes (AOPs) by chemical degradation. AOPs can be divided into wet air (catalytic) oxidation, supercritical water (catalytic) oxidation, photocatalytic oxidation, and general (catalytic) oxidation based on the difference of the generation approach for radicals as well as the reaction conditions. Among them, photocatalytic oxidation stands out to be an attractive technology for utilization of sunlight as an energy source, which solves the critical problems for both environmental purification and energy crisis simultaneously. Since the semiconductor photocatalytic oxidation reaction system can convert the absorbed solar energy into chemical energy, many reactions that are difficult to be realized under normal conditions can be carried out smoothly under relatively mild conditions. In the presence of a photocatalyst, sunlight and air can directly decompose many organic pollutants into some small inorganic molecules (CO_2 and H_2O), removing hazardous materials without causing secondary pollution.

In 1972, Fujishima and Honda discovered that H_2 and O_2 can be released via a TiO_2 -based photoelectrochemical water splitting cell [1]. Since then, TiO_2 has become one of the most popular green photocatalysts. In addition to its application in water and air purification, recent research on TiO_2 has also made some progress in sterilization, water splitting, nitrogen fixation and CO_2 reduction. Various organic pollutants could achieve mineralization unselectively by virtue of TiO_2 [1-5].

However, distinct defects have been found on traditional TiO_2 -based photocatalysts. The quantum efficiency is relatively low due to fast recombination of photo-generated electrons

and holes, unfavorable visible light utilization, and rapid deactivation. The solar energy utilization efficiency is particularly low due to the wide energy band structure of the titanium dioxide semiconductor ($E_g=3.2$ eV), denoting its limitation to absorb ultraviolet light only or ultraviolet light in sunlight (the ultraviolet radiation in sunlight only accounts for 5%). All these seriously restrict the large-scale application of TiO_2 -based photocatalysts in aspects of environmental purification and solar energy conversion. Therefore, development of novel photocatalysts with higher quantum efficiency and broader photo-response range has become challenging topics in the environmental photocatalytic field.

Recently, much attention have been focused on the study of bismuth-based visible light photocatalysts such as BiFeO_3 [6], BiVO_4 [7], Bi_2O_3 [8], Bi_2MoO_6 [9], BiOX [10] and Bi_2WO_6 [11] etc., with high activity for environmental pollutants degradation as well as water splitting. Bismuth-based complex oxides, BiOX ($X = \text{Cl}, \text{Br}, \text{I}$) and BiFeO_3 have exhibited remarkable photocatalytic performances owing to their specific crystal and electronic structures as well as unique physicochemical attributes [6, 10]. In addition, numerous efforts have been attached to the 2D (two-dimensional) materials with a layered structure, such as graphene and graphitic-like carbon nitride, due to their optimal chemical and physical properties. Specifically, metal-free semiconductor as graphitic carbon nitride ($g\text{-C}_3\text{N}_4$) has been extensively studied owing to its layered structure, reasonable electronic structure, feasible synthesis with earth-abundant precursors, thermal stability and bio-compatibility, and has shown paramount application potentials in photocatalysis [12-14]. Therefore, two typical types of visible-light-responsive bismuth-based and $g\text{-C}_3\text{N}_4$ -based photocatalysts were chosen for a systematic study in both artificial photosynthesis and environmental remediation. In the typical process, the photo-generated electrons/holes will migrate to the surface of the photocatalysts to participate in desired electrochemical (redox) processes. Pure $g\text{-C}_3\text{N}_4$, for example, can absorb visible light with a narrow band gap and suitable electronic band levels but is of a low quantum efficiency because of the high recombination rate of photo-excited charge carriers. To promote a higher photocatalytic efficiency for practical application, various modification strategies have been developed to optimize the photoelectrical structures of $g\text{-C}_3\text{N}_4$, including selection of various synthesis precursors [15,16], preparation of porous $g\text{-C}_3\text{N}_4$ [17,18], metal or non-metal doping as well as heterojunction nanocomposites designing [19-20]. Among these, heterogeneous coupling and surface engineering with co-catalysts has been proven to be a prominent and practical route for enhancement of photocatalytic activity.

1.2 Research objectives

This study focuses on the development of novel and robust heterojunction nanocomposites as photocatalysts to remove pollutants from wastewater, and to generate clean and renewable solar fuels from water splitting. Meanwhile, this study also aims at providing insights into the intrinsic mechanisms of enhanced photocatalytic performance integrating deliberate materials design and comprehensive analytic techniques concerning photochemical, electrochemical and photoelectrochemical properties. The detailed research objectives of this study are listed as follows.

1. Designing novel g-C₃N₄-based and bismuth-based heterostructures with simple and facile physical/chemical strategies.
2. Employing the fabricated nanocomposites for photocatalytic degradation of organic contaminants such as dyes under visible light irradiations.
3. Unveiling the intrinsic active sites and charge transfer scheme of the photocatalytic reaction processes for dyes degradation and water reduction.
4. Carrying out photocatalytic and electrocatalytic water splitting for evolution of H₂ /O₂ with featured semiconductor heterostructures.
5. Elucidating the mechanism for the photo-reactivity enhancement as well as the photo-stability of the heterojunction composites.

1.3 Thesis outline

This thesis includes eight chapters: introduction (this chapter), literature review (Chapter 2), results and discussions (Chapter3-7), conclusions and perspectives (Chapter 8).

Chapter 1 — Introduction — briefly introduces the research background related to environmental issues and energy crisis. The research objectives and structural organization of this dissertation are illustrated.

Chapter 2 — Literature review — focuses on the recent literature survey of water splitting for hydrogen generation and water treatment techniques with semiconductor-based heterojunctions as the photocatalysts.

Chapter 3 — *Preparation of p-n Heterojunction of BiFeO₃@TiO₂ with a Core-Shell Structure for Visible Light Photocatalytic Degradation* (Adapted from *Chinese Journal of Catalysis*. 2017, 38: 1052–1062 and reuse permission has been obtained) — highlights the design of p-n heterojunction BiFeO₃@TiO₂ with a core-shell structure showing extremely high photocatalytic degradation performance of various dyes in wastewater treatment under visible light irradiations.

Chapter 4 — *Three-Dimensional BiOI/BiOX (X = Cl or Br) Nanohybrids for Enhanced Visible-Light Photocatalytic Activity* (Adapted from *Nanomaterials*. 2017, 7: 64 and reuse permission has been obtained) — unravels the synthesis and characterization of flower-like BiOI/BiOX (X = Br or I) hybrids with a unique three dimensional (3D) architecture. After evaluation under visible light illumination, BiOI/BiOCl was demonstrated to be with superior photocatalytic activity for both water oxidation and dyes degradation.

Chapter 5 — *0D (MoS₂)/2D (g-C₃N₄) Heterojunctions in Z-Scheme for Enhanced Photocatalytic and Electrochemical Hydrogen Evolution* (Adapted from *Applied Catalysis B: Environmental*. 2018, 228: 64-74 and reuse permission has been obtained) — reports the preparation of MoS₂ quantum dots (MSQDs) with high water dispersity. The MSQDs were employed to decorate graphitic carbon nitride (g-C₃N₄, CN) nanosheets to obtain 0D (MoS₂)/2D (g-C₃N₄) heterojunctions, exhibiting enhanced photocatalytic and electrocatalytic hydrogen evolution performance. Also, a direct Z-scheme charge transfer mechanism of the MSQD-CN hybrid was proposed for the enhancement.

Chapter 6 — *Flower-Like MoS₂ on Graphitic Carbon Nitride for Enhanced Photocatalytic and Electrochemical Hydrogen Evolutions* (Adapted from *Applied Catalysis B: Environmental*. 2018, 239: 334-344 and reuse permission has been obtained) — introduces a facile strategy to construct three-dimensional (3D)/two-dimensional (2D) nanojunctions for a drastically enhanced activity in both photocatalytic and electrochemical hydrogen generation for water reduction.

Chapter 7 — *Graphitic Carbon Nitride Decorated with CoP Nanocrystals for Enhanced Photo, Electro and Photoelectrochemical H₂ Evolution* — investigates the effect of CoP as an effective cocatalyst both in photocatalytic and electrocatalytic hydrogen evolution with high

photoelectrochemical activity. The mechanism responsible for the enhancement was further elaborated.

Chapter 8 — *Conclusions and perspectives* — summarizes the main research outputs in this thesis and proposes perspectives for further study in photocatalytic aspects.

References

- [1] Fujishima A, Honda K. Electrochemical study of spectral sensitization [J]. *Nature*, 1972, **37**, 238.
- [2] X. Wu, G. Q. Lu, L. Wang, *Energy Environ. Sci.*, 2011, **4**, 3565-3572.
- [3] S.N.H. Jaafar, L.J. Minggu, K. Arifin, M.B. Kassim, W.R.D. Wan, *Renew. Sust. Energ. Rev.*, 2017, **78**, 698-709.
- [4] Y. Liu, S. Yang, J. Hong, C. Sun, *J Hazard Mater*, 2007, **142**, 208-215.
- [5] W. Ho, J.C. Yu, J. Lin, J. Yu, P. Li, *Langmuir*, 2004, **20**, 5865-5869.
- [6] Y. Zhang, A.M. Schultz, L. Li, H. Chien, P.A. Salvador, G.S. Rohrer, *Acta Mater.*, 2012, **60**, 6486–6493.
- [7] W. Zhao, Y. Liu, Z. Wei, S. Yang, H. He, C. Sun, *Appl. Catal. B: Environ.*, 2016, **185**, 242–252.
- [8] J. Ke, J. Liu, H. Sun, H. Zhang, X. Duan, P. Liang, X. Li, M.O. Tade, S. Liu, S. Wang, *Appl. Catal. B: Environ.*, 2017, **200**, 47-55.
- [9] J. Ke, X.G. Duan, S. Luo, H.Y. Zhang, H.Q. Sun, J. Liu, M. Tade, S.B. Wang, *Chem. Eng. J.*, 2017, **313**, 1447–1453.
- [10] L. Ye, L. Zan, L. Tian, T. Peng, J. Zhang, *Chem. Commun.*, 2011, **47**, 6951–6953.
- [11] C. Zhang, G. Chen, C. Li, J. Sun, C. Lv, S. Fan, W. Xing, *ACS Sustain. Chem. & Eng.*, 2016, **4**, 5936-5942.
- [12] J. Duan, S. Chen, M. Jaroniec, S.Z. Qiao, *ACS nano*, 2015, **9**, 931-940.
- [13] P. Niu, L. Zhang, G. Liu, H.-M. Cheng, *Adv. Func. Mat.*, 2012, **22**, 4763-4770.
- [14] T. Sano, S. Tsutsui, K. Koike, T. Hirakawa, Y. Teramoto, N. Negishi, K. Takeuchi, *J. Mater. Chem. A*, 2013, **1**, 6489-6496.
- [15] Y. Zhang, J. Liu, G. Wu, W. Chen, *Nanoscale*, 2012, **4**, 5300-5303.
- [16] G. Zhang, J. Zhang, M. Zhang, X. Wang, *J. Mater. Chem.*, 2012, **22**, 8083-8091.
- [17] J. Xu, H. Wu, X. Wang, B. Xue, Y. Li, Y. Cao, *Phys. Chem. Chem. Phys.*, 2013, **15**, 4510-4517.
- [18] J. Xu, Y. Wang, Y. Zhu, *Langmuir*, 2013, **29**, 10566-10572.
- [19] L. Gu, J. Wang, Z. Zou, X. Han, *J. Hazard. Mater.*, 2014, **268C**, 216-223.
- [20] S. Kumar, T. Surendar, A. Baruah, V. Shanker, *J. Mater. Chem. A*, 2013, **1**, 5333-5340.

Every reasonable effort has been made to acknowledge the owners of copyright material. I would be pleased to hear from any copyright owner who has been omitted or incorrectly acknowledged.

Chapter 2. Literature Review

2.1 Environmental remediation and energy crisis

In the past decades, human society has had an unrelenting and greedy appetite towards fossil fuels due to the rapid growth of human population and economic development. Increasing consumption of fossil fuels has led to series of global challenges including deteriorating environmental situation as well as energy crisis, constituting two most critical problems facing humanity today. In particular, incessant depletion of fossil fuels will definitely contribute to the accumulation of CO₂ concentration in the atmosphere, causing urgent greenhouse effects globally [1]. Fortunately, we have the potential to reduce the CO₂ emission from fossil fuels combustion by either using clean energy, for instance, hydrogen, or converting them into renewable, carbon-neutral energy sources. As a hot research topic, photocatalysis provides a feasible route to help solve these two critical issues.

2.2 Solar energy conversion process

Among various renewable energy sources, solar energy stands out to be the largest sustainable natural resource which could serve our future energy demands and replace fossil fuels potentially. Photocatalytic technology turns out to be one promising strategy, which takes advantage of the abundant and sustainable solar energy with efficient utilization and conversion [2]. This strategy involves so-called artificial photosynthesis and can be implemented via photocatalytic processes. Solar energy, as an inexhaustible and environmentally friendly energy source, could solve aforementioned problems [3-5]. So far, it has been widely used for conversion into electric energy via solar cells [6], water splitting into hydrogen and oxygen [7-9], reducing CO₂ into organic fuels and water reduction into hydrogen [10-13], as well as organic pollutants removal [14-17].

2.2.1 Solar cell

As an inexhaustible energy resource, solar energy can be harnessed and converted into electric energy via utilization of photovoltaic cells. Currently, most of the available commercial solar cells are well-known silicon solar cells and thin film solar cells, which use high-cost and energy-consuming materials [18-19]. Over the last decade, dye sensitized solar cells (DSSC) have been demonstrated as the more effective solar cells which exhibit greater potentials with higher conversion efficiencies and lower costs, compared to previous generations [20]. The

schematic mechanism for DSSC is well illustrated in Figure 2.1. When photoexcited, many dyes have the ability to inject electrons into the conduction band of a semiconductor such as TiO_2 , which is deposited onto a FTO glass substrate. The electrons will diffuse to the conductive substrate and then flow into the external circuit. Thus the dye in the oxidized state is reductively regenerated by the reduced electrolyte (I^-); while the oxidized electrolyte (I_3^-) is reduced after receiving the electrons at the counter electrode (usually FTO glass coated with Pt), thereby a cycle is completed. The electricity is produced during the combination between the electrons and holes through an external circuit.

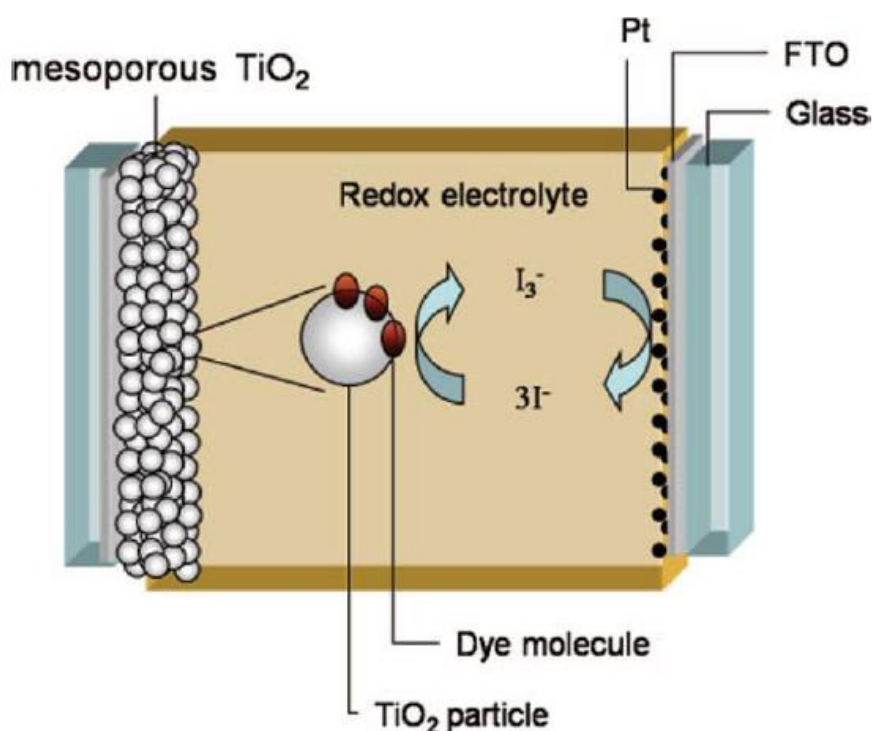


Figure 2.1. Schematic representation of the dye-sensitized solar cell [21]. Reproduced with permission of the American Chemical Society.

2.2.2 Photocatalytic reduction of CO_2

Early in 1979, Inoue et al. [22] discovered that CO_2 could be converted to hydrocarbon fuels such as methane, methanol etc. by virtue of photocatalytic reduction process in the semiconductor aqueous suspension. Ever since that, the mechanism and efficiency of photocatalytic CO_2 reduction based on various semiconductors have been explored broadly. Very recently, research focus has been centred around development of novel, high-efficient and photo-stable catalysts with widespread visible light response. For instance, Liu et al. [23] found that in the presence of water vapor, Zn_2GeO_4 of ultrathin and ultra-long nanoribbons could drastically promote the photocatalytic CO_2 reduction efficiency to produce methanol.

Graphitic carbon nitride (g-C₃N₄), showing up as a recent shining star of organic and metal-free photocatalysts, was proven to exhibit high potential application in versatile solar energy conversion processes, including photocatalytic H₂ evolution from water splitting, photocatalytic degradation of organic pollutants as well as photocatalytic CO₂ reduction [24]. Figure 2.2 presents a possible mechanism for photocatalytic CO₂ reduction process. The photo-excited charge carriers upon visible light illumination will be transferred and separated on the surfaces of g-C₃N₄. Specifically, OH⁻/H₂O will combine with scavenging holes to release O₂, while the generated H[•] from H₂O could react with those carbon species to form HCO₃⁻ (or CO₃²⁻), which will further capture the electrons to produce CO₂^{-•}, and finally generate CH₃OH after a series of reactions [25]. The in-depth mechanism concerning selective reaction and products still needs further study.

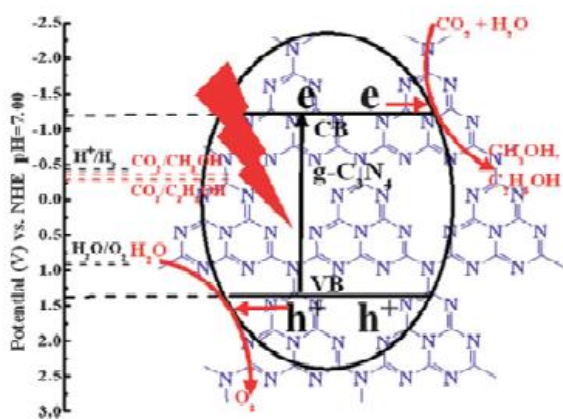


Figure 2.2. Possible photocatalytic mechanism for CO₂ reduction with g-C₃N₄ [25]. Acknowledgement to Royal Society of Chemistry.

2.2.3 Photocatalytic degradation of pollutants

Photocatalysis over semiconductors has always maintained as one of the most attractive research topics worldwide in recent years. The research on the basis and application of photocatalytic oxidation technology to solve the increasingly deteriorated environmental pollution is being advanced rapidly [26]. A large number of research reports indicate that various organic pollutants including aliphatic hydrocarbons, esters, nitrogen-containing organic compounds, surfactants, insecticides and herbicides, etc. in water can be decomposed via photocatalytic oxidation, achieving complete mineralization. Some organic substances such as chloroform, carbon tetrachloride, hexachlorocyclohexane and pentachlorophenol, which could not be oxidized by ozone, can still be effectively photolyzed and removed by photocatalysis [27]. As a metal-free and stable visible-light responsive photocatalyst, g-C₃N₄ has gathered incessant attention with prominent applications in both gas and liquid phase

degradation of environmental pollutants. Recent researches convince that g-C₃N₄ exhibits high visible light photocatalytic activity in removing of nitric oxide or acetaldehyde, which are typical air pollutants and often detected in automobile exhausts [28, 29]. Application of g-C₃N₄-based photocatalysts in liquid phase is a major focus with numerous studies targeting the removal of organic contaminants from water environment such as various dye molecules [30, 31]. As such, the schematic illustration of pollutants degradation mechanism over g-C₃N₄ is depicted in Figure 2.3. Under light illumination with energy higher than its band-gap, photo-generated holes and electrons will get involved in several redox reactions on the surface of the catalyst and produce various highly reactive free radicals, which could play a key role in promoting the mineralization of organic compounds. As a reactive species, $\cdot\text{OH}$ can lead to the oxidation of substances and serve as the main oxidant in heterogeneous photocatalysis except for the holes. Served as the photoelectron trapping agent, O₂ is mainly adsorbed on the surface of the photocatalyst and inhibits the recombination of electron-holes. Meanwhile, it could contribute to the production of superoxide anion radical $\cdot\text{O}_2^-$, which becomes another source of $\cdot\text{OH}$ via protonation reactions.

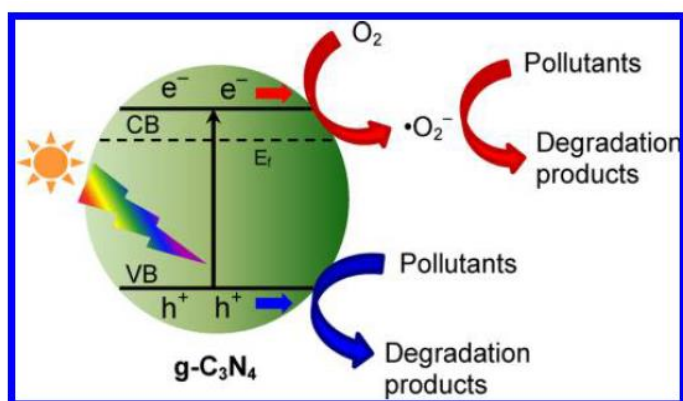


Figure 2.3. Photocatalytic degradation mechanism of pollutants over pristine g-C₃N₄ [26]. Reproduced with permission of the American Chemical Society.

2.2.4 Photocatalytic water splitting

As a promising and ideal alternative energy to fossil fuels, H₂ presents the highest energy density as 140 MJ. kg⁻¹ as a chemical fuel [32]. Hydrogen evolution from water via photocatalytic or electrocatalytic process has been widely studied during recent years. Achieving overall water splitting process for generation of H₂ and O₂ simultaneously is always challenging, although numerous efforts have been put in related research focusing on the development of highly functional photocatalysts and co-catalysts [33-35]. In general, photocatalysts should have a band structure with a suitable band gap energy to be excited by

sunlight. As shown in Figure 2.3, when the energy of incident light is larger than that of the band gap, electrons and holes are generated in the conduction and valence bands, respectively. The photogenerated electrons and holes cause redox reactions similar to electrolysis. Water molecules are reduced by the electrons to form H_2 and also oxidized by the holes to form O_2 for overall water splitting. The basic theoretic requirements for efficient photocatalysts are that they should have both suitable band gap energy and levels of the conduction and valence bands. In detail, the band gap of the semiconductor should be narrow enough to absorb more photons from sunlight to generate electron and hole pairs. The bottom level of the conduction band has to be more negative than the redox potential of H^+/H_2 (0 V vs. NHE), while the top level of the valence band should be more positive than the redox potential of O_2/H_2O (1.23 V). As shown in Figure 2.4 [36], it is harsh for common semiconductors like TiO_2 and $g-C_3N_4$ to meet all those requirements. In addition, effective charge separation and fast charge transportation are also needed to migrate the photo-generated carriers to corresponding surface reactive sites. Practically, most of the well reported photocatalysts with high activity for water splitting include the functional design of the co-catalysts to engineer and promote the evolution of O_2 and H_2 from water. Sometimes, dual cooperative co-catalysts can not only promote surface catalytic kinetics for evolution of H_2 and O_2 separately, but also accelerate charge separation and migration more efficiently. The detailed mechanism was well illustrated in Figure.2.5 [37].

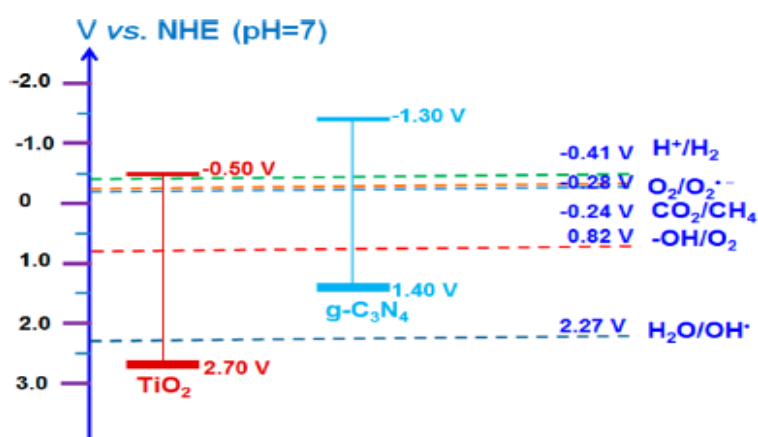


Figure 2.4. Schematic band structure for typical photocatalyst of TiO_2 and $g-C_3N_4$ with redox potentials for photoreduction and photooxidation [36]. Reproduced with permission of the American Chemical Society

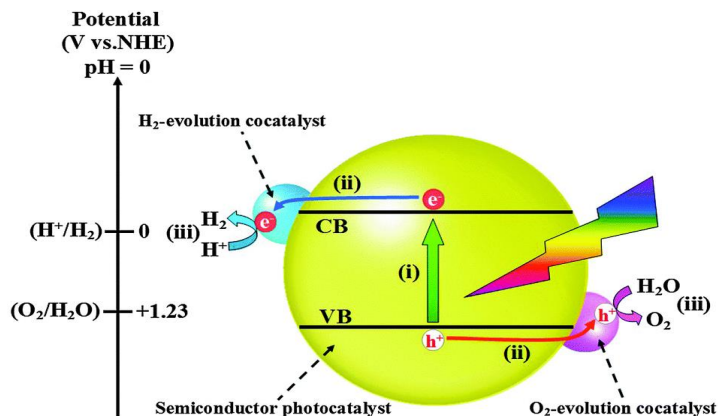


Figure 2.5. Schematic mechanism of photocatalytic water splitting over a semiconductor photocatalyst loaded with both O₂- and H₂-evolution co-catalysts [37]. Acknowledgement to Royal Society of Chemistry.

2.3 Hydrogen evolution process

2.3.1 Electrocatalytic hydrogen evolution reaction

With the advancing on the development and utilization of hydrogen energy, electrolyzed water technology has also been rapidly and widely explored. Compared with novel techniques, such as hydrogen production from fossil fuels via catalytic thermal decomposition or from biomass and solar energy, hydrogen production from electrolyzed water is relatively mature with a long history and applied up to date (Figure 2.6). In addition, the consumed electrical energy can be generated from renewable energy resources such as wind, hydraulic and nuclear energy, and will definitely take the lead in the near future, which will definitely help alleviate the increasingly serious energy crisis [38-39]. However, the widespread application in practice is

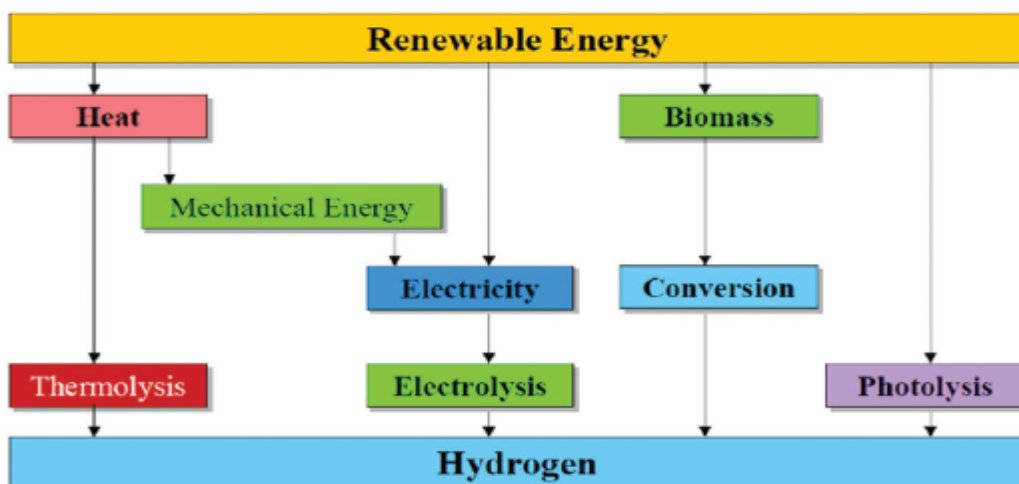


Figure 2.6. Feasible pathways for hydrogen evolution from renewable energy [44]. Reproduced with permission of the science publishing group.

drastically constrained due to the relatively high cost. Continuous efforts on construction and improvement of low-cost and high efficient noble metal-free electrocatalysts with earth-abundant elements to replace Pt-based materials have been made and achieved appealing cost-competitive hydrogen over the past decades [40-43].

Therefore, reducing the consumption of electrical energy, lowering the over-potential of the cathode materials and enhancing the overall efficiency of hydrogen evolution have become the research trends and always pose challenges continuously. Development of novel cathode materials and catalysts with high catalytic activity has also become the hot research topics on hydrogen production from electrolyzed water.

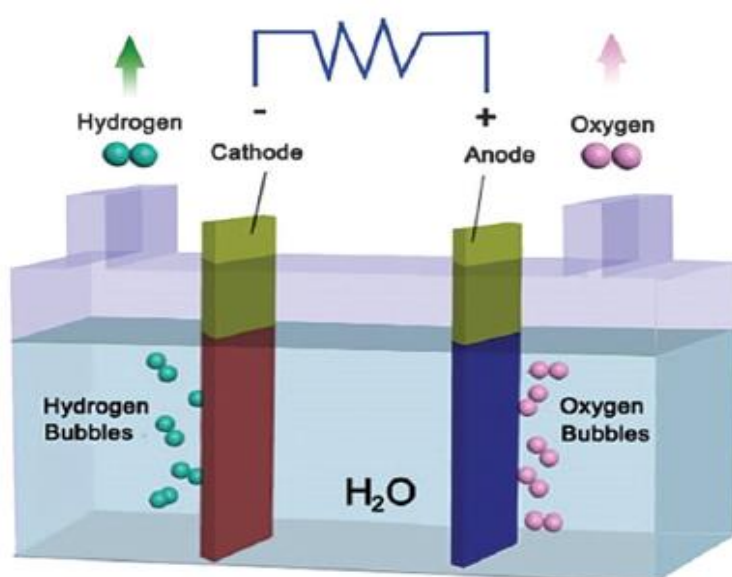
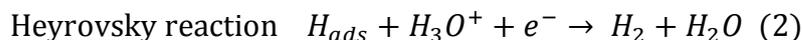
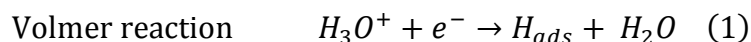


Figure 2.7. Schematic diagram of electrocatalytic water splitting process [45]. Acknowledgement to Royal Society of Chemistry.

Figure 2.7 illustrates a basic process of electrocatalytic water splitting for release of H_2 and O_2 . The anode is loaded with a material with excellent oxygen evolution activity, while a hydrogen evolution catalyst will be coated on the surface of the cathode. Once external voltage was employed to both the electrodes, decomposition of H_2O will proceed to produce H_2 and O_2 with lots of bubbles observed on the surface of the electrodes. The released hydrogen will be stored for fuel cells. Thus, the electrocatalytic water splitting process is composed of two half reactions: oxygen evolution reaction (OER) and hydrogen evolution reaction (HER). In the hydrogen evolution reaction, it is generally believed that hydrogen atoms on the surface of the electrode are formed initially, followed by desorption from the electrode and convert into hydrogen molecules. The adsorption force between hydrogen atoms and the electrode is the main force existed between the particles and the electrode. Three possible steps are proposed

for the HER process in acidic media, known as the Volmer, the Heyrovsky and the Tafel steps, respectively [46].



To evaluate the catalytic performance of a HER catalyst, several parameters are put forward for comprehensive measurement and comparison, including Tafel plots, onset potential, total electrode activity and stability, etc. So far, noble metal-free HER catalysts such as metal sulfides [47- 48], phosphides [49-50], carbides [51], nitrides [52-53], selenides [45] and metal-free catalysts [54-55] have attracted enormous attention for their low-cost and remarkable performance. The strategies for HER activity improvement, the design and structure engineering of the materials as well as the relationship construction between them have been systematically studied. Among them, nanoscaled MoS₂ has been demonstrated to be a potentially applicable HER catalyst by numerous studies in a long term. Liu's group has reported monolayer MoS₂ quantum dots with an average size about 3.6 nm, which exhibits a high HER performance with a low over-potential at 160 mV as well as a small Tafel slope of 59 mV.dec⁻¹ [56].

2.3.2 Photocatalytic hydrogen evolution reaction

Except for the hydrogen evolution via electrocatalytic water splitting, another route utilizing solar energy conversion to produce hydrogen is also a promising technique, which draws enormous attention recently. The approach of photocatalytic overall water splitting with semiconductor photocatalysts is potentially economical and scalable to directly convert abundant solar energy to hydrogen fuels for storage. However, this process is a non-spontaneous uphill reaction which requires a large amount of extra energy to drive (237 kJ/mol under standard conditions) [57]. Looking into the water reduction half reaction with sacrificial hydrogen evolution, specific electron donors are adopted as sacrificial agents to speed up the oxidation process with photo-generated holes in the system. As illustrated in Figure 2.8, most of the electron donors (TEOA or methanol) will be easily oxidized by holes since their oxidation potential is lower than that of water, leaving abundant electrons for water reduction reaction. Thus, the photocatalytic H₂ evolution efficiency would be enhanced drastically. The semiconductor itself usually acts as a photon absorber to be excited to generate hole-electron

pairs. Under most circumstances, a cocatalyst is preferred to lower the overpotential for H₂ evolution reactions and often acts as the surface active sites over the semiconductor. Meanwhile, cocatalysts could form certain heterojunction interface with the semiconductor photocatalyst and facilitate the faster separation and transportation of electron-hole pairs. Finally, electrons will be trapped by protons adsorbed at the interface for reduction into H₂. To be a reasonable semiconductor photocatalyst, it should meet the following two criteria: a suitable band gap to harvest photons from solar energy as well as a much more negative conduction band bottom compared to the reduction potentials of water.

Graphitic carbon nitride is considered to be an ideal photocatalyst for hydrogen evolution with a narrow band gap responsive to visible light [58-60]. Recently, Wang's group indicated that a crystalline tri-s-triazine-based graphitic carbon nitride showed an extremely high photocatalytic H₂ evolution performance with the apparent quantum yield (AQY) reaching 50.7% at irradiation light wavelength of 405 nm [61]. As for cocatalysts, Pt has always been proven to be the most effective cocatalysts for photocatalytic H₂ evolution among all the noble metals. However, recent research has been focused on the development of numerous non-noble metal or non-metal based cocatalysts due to the high-cost and scarcity of the noble metals. The pioneering work was firstly reported by Li's group in 2008 [62]. As a non-noble metal cocatalyst, 0.2 wt% MoS₂ was loaded on CdS semiconductor, leading to the enhancement of photocatalytic activity by up to 36 times. For the same amount of cocatalyst loading at 0.2 wt%, the rate of H₂ evolution on MoS₂/CdS is even higher than that on Pt/CdS, as shown in Figure 2.9.

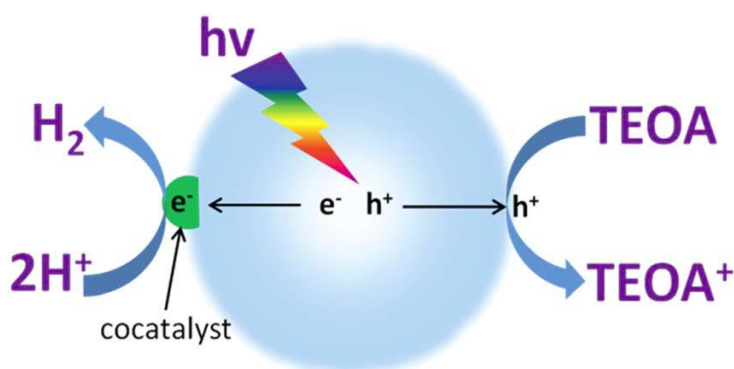


Figure 2.8. Schematic diagram of photocatalytic hydrogen evolution with TEOA as a sacrificial agent driven by a semiconductor photocatalyst modified by a cocatalyst [57]. Acknowledgement to Royal Society of Chemistry.

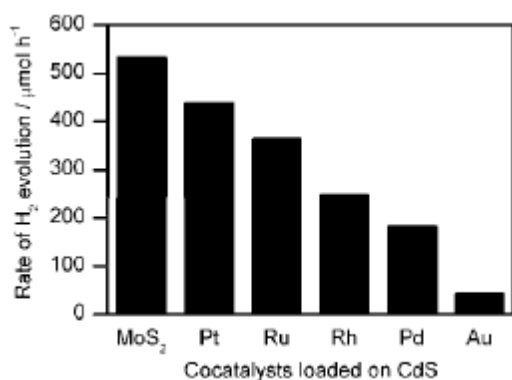


Figure 2.9. The rate of photocatalytic H₂ evolution over CdS loaded with different cocatalysts at 0.2 wt% [62]. Reproduced with permission of the American Chemical Society.

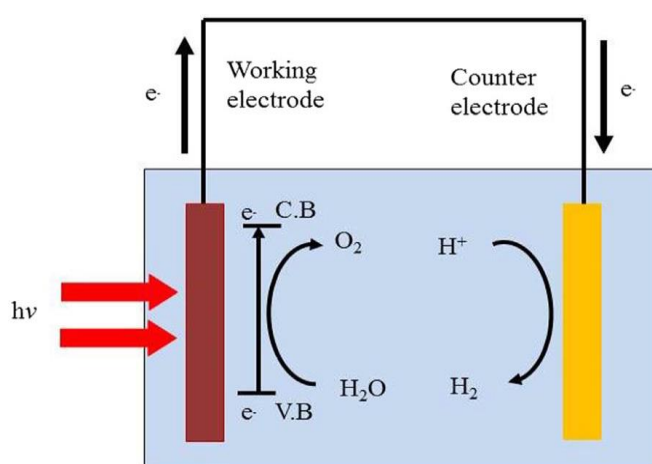
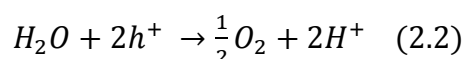
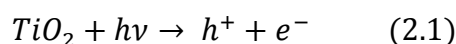


Figure 2.10. Schematic diagram of a PEC cell [63]. Reproduced with permission from Elsevier.

2.3.3 Photoelectrochemical hydrogen evolution reaction

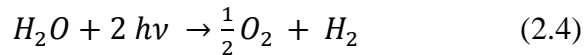
Photoelectrochemical (PEC) water splitting can be regarded as an integration process of photons harvesting and electrocatalytic water splitting, which is quite appealing but also very challenging. Dating back to 1972, Fujishima and Honda first discovered that H₂O can be decomposed into H₂ and O₂ with photon-induced water splitting process on TiO₂ electrode with no external voltage provided [64]. A basic PEC cell is illustrated in Figure 2.10. Usually an n-type semiconductor like TiO₂ is adopted as a photoanode to absorb light energy. The photo-induced holes and electrons will then be separated towards different directions. The holes will remain on the surface of the photoanode and then get involved in oxidation of H₂O to O₂, while the electrons will be transferred through the external circuit to the counter electrode (usually Pt) for water reduction to H₂.

The detailed reaction process includes the following three steps:





Thus, the overall PEC water splitting reaction could be summarized as follows:



As for the PEC water splitting process to produce hydrogen, the key component is also the structure/composition and electronic properties of the photoelectrodes (photoanode and photocathode). Specifically for a working electrode, it is supposed to be a light harvesting material with high HER activity to gain excellent PEC hydrogen evolution performance. Recently, Chen's group [65] reported a novel MoS₂/S-doped g-C₃N₄ heterojunction film showing enhanced visible-light PEC activity for H₂ evolution. In detail, S-doped g-C₃N₄ film was coated on indium–tin oxide (ITO) glass substrates by a CVD approach, then a visible-light response MoS₂ layer was further deposited via a hydrothermal process. The as-synthesized heterojunction film stably reached a high anodic photocurrent as $\sim 1.2 \times 10^{-4}$ A/cm² under visible light illumination (XE4030 Xe lamp, 150 W, UV cut-filter with $\lambda > 420$ nm, light intensity at ~ 100 mW/cm²) at the bias potential of +0.5 V versus Ag/AgCl, which is an ideal candidate as photoanodes for PEC cells. The enhancement of the PEC performance could be attributed to the increased light absorption capability as well as the facilitated separation of charge carriers due to the formation of the p-n heterojunction between MoS₂ and S-doped g-C₃N₄. Lianos's group adopted nanocrystalline BiVO₄ obtained via a simple wet chemistry approach as the photoanode for PEC hydrogen generation from water splitting. The maximum rate of hydrogen generation reaches 0.15 mmol/h with electric bias at 1.4 V vs Ag/AgCl and chemical bias of 0.37 V with 0.5 M aqueous NaHCO₃ [66]. Additionally, Incident Photon-to-Current Efficiency (IPCE) and applied bias photon-to-current efficiency (ABPE) are two important parameters to characterize the efficiency of a PEC cell [67-68].

2.4 g-C₃N₄-based heterojunction photocatalysts

2.4.1 Pristine g-C₃N₄

The discovery of C₃N₄ could be dated back to very early days in 1834 [69], when Liebig and Berzelius synthesized some polymer derivative materials of carbon nitride and named as “melon”. Until recently in the 1990s, the research interest on melon-based β -C₃N₄ has been raised up because of its extremely high bulk hardness and thermal stability. Among the five types of C₃N₄, graphitic carbon nitride (g-C₃N₄) owns the most stable graphite-like sheet

structure. The unique semiconductor structure with loose layers makes it a potential catalyst in photocatalysis field.

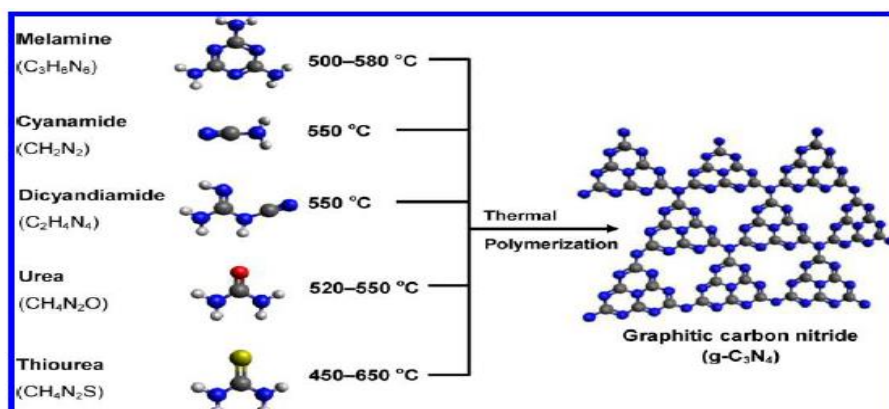


Figure 2.11. Illustration of synthesis routes to graphitic carbon nitride from various precursors. The blue, black, red, yellow and white balls represent N, C, O, S and H atoms, accordingly [26]. Reproduced with permission of the American Chemical Society.

As a popular organic and metal-free photocatalysts, graphitic carbon nitride ($g\text{-C}_3\text{N}_4$) has been proven to exhibit high potential application in versatile solar energy conversion processes. Wang et al. [24] pioneeringly discovered that, polymeric graphitic carbon nitride ($g\text{-C}_3\text{N}_4$) synthesized from cyanamide manifested outstanding photocatalytic activity for H_2 evolution under visible-light irradiation. Afterwards, numerous researchers shift interests to fabrication of $g\text{-C}_3\text{N}_4$ via adopting various nitrogen-rich organic precursors. Among all those common precursors such as cyanamide, urea stands out to be the most economic approach to achieve visible-light-driven photocatalysts with excellent performance. Perseverant efforts have been made to fabricate $g\text{-C}_3\text{N}_4$ via thermal treatment of different nitrogen-rich precursors, which is summarized in Figure 2.11. The photo-activity of graphitic carbon nitride is closely related to its physicochemical stability as well as electronic band structure, which is intrinsically dependent on the condensation degree and unique structure of its heptazine ring. As is shown in Figure 2.4, $g\text{-C}_3\text{N}_4$ possesses a theoretical band gap energy of 2.7 eV, with N elements contributing to its valance band at +1.4 eV and C elements mainly support the conduction band at -1.3 eV. Accordingly, the nitrogen atoms would serve as the preferred oxidation sites for H_2O to release O_2 , while the carbon atoms would be the reduction sites for H_2 evolution within the Melem matrix [70]. Therefore, by selecting appropriate precursor types and reaction conditions for thermal polymerization, an ideal nanostructure of $g\text{-C}_3\text{N}_4$ could be achieved with a perfect C/N ratio, high porosity, large specific surface area, thin nanosheets and reasonable band structure [71]. To the best of our knowledge, the relatively low crystalline $g\text{-C}_3\text{N}_4$ with

structural defects due to incomplete condensation by evidence of a lower molar ratio of C/N than ideal value of 0.75 indicates a higher photocatalytic activity with defects as more active sites than bulk materials [72]. The comparison for the morphology difference of g-C₃N₄ using urea and melamine was manifested clearly in Figure 2.12. Relative to adopting melamine as a precursor, g-C₃N₄ derived from urea exhibits thinner and smaller flat sheets with wrinkles showing a high porosity, which contributes to higher photoactivity for both CO₂ reduction and photocatalytic H₂ evolution [26, 73-74]. Accordingly, the BET surface area of the sample derived from urea is also ten times higher than that from melamine [26]. Similar results could also be observed from Figure 2-13. All these results further prove the outstanding performance of urea-derived-g-C₃N₄ owing to its unique porous nanostructure and higher degree of polymerization.

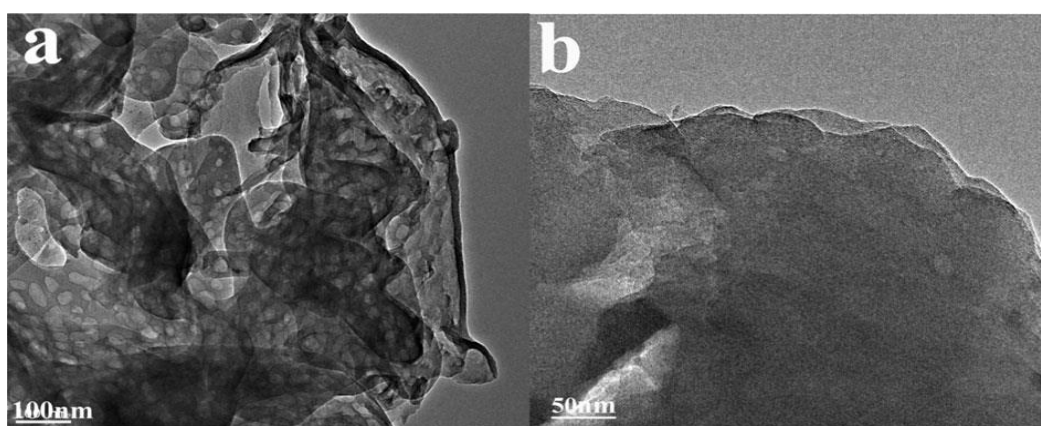


Figure 2.12. TEM images of the obtained g-C₃N₄ from (a) urea; (b) melamine under the same thermal polymerization conditions [25]. Acknowledgement to Royal Society of Chemistry.

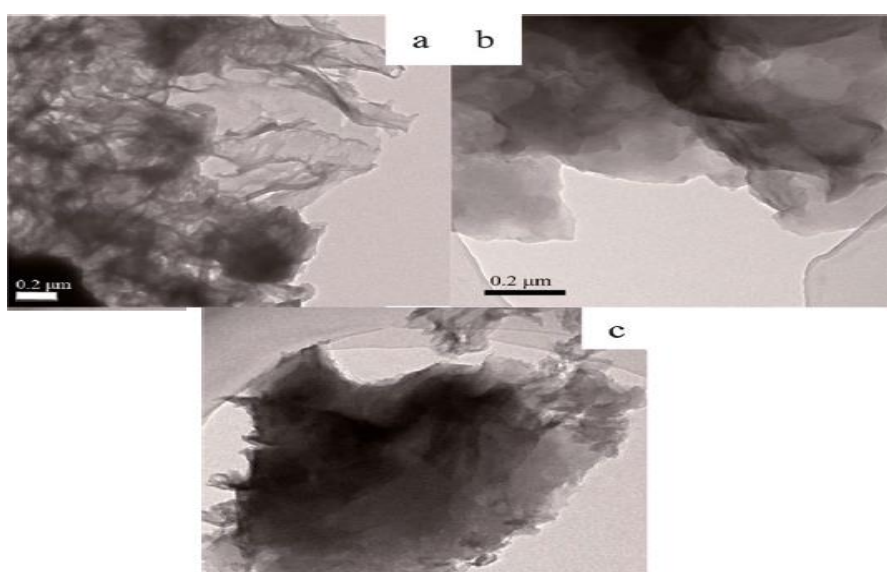


Figure 2.13. TEM images of the obtained g-C₃N₄ from (a) urea; (b) thiourea and (c) dicyandiamide under the same thermal polymerization conditions [74]. Acknowledgement to Royal Society of Chemistry.

The calcination temperature and pyrolysis time are two key factors in determining the physicochemical properties of a urea-derived-g-C₃N₄. Based on previous studies [75-77], increased calcination temperature could drastically result in the enhancement in crystallinity and specific surface area of the product. The prolonged thermal annealing process could lead to the distinct exfoliation of the stacking layers of g-C₃N₄ with reduced size and increased porosity. These two elements should be taken into consideration for design and nanoarchitecture engineering of g-C₃N₄ for improved performance.

2.4.2. Design and construction of inorganic semiconductor-g-C₃N₄ heterostructures

Because of its ideal semi-conductivity with superior optical features together with its high stability, graphitic carbon nitride (g-C₃N₄) has attracted worldwide attention [78], emerging as a promising and excellent visible-light-responsive photocatalyst for photocatalytic water splitting [79-81], photocatalytic CO₂ reduction [82–84] as well as pollutants degradation [85]. However, when pure g-C₃N₄ gets excited upon visible light, it showed relatively low quantum efficiency with high recombination rate of photo-generated charge carriers. Moreover, it suffers from the low electrical conductivity and also self-decomposition by photo-excited holes throughout the photocatalytic processes, which will hamper the practical application of solar energy utilization over g-C₃N₄. To promote a higher photocatalytic efficiency for practical application, various modification strategies have been developed to optimize the photoelectrical structures of g-C₃N₄, including selection of various synthesis precursors [86-87], preparation of porous g-C₃N₄ [88-89], metal or non-metal doping as well as heterojunction nanocomposites designing [90-92]. Among these, heterogeneous coupling and surface engineering with co-catalysts has been proven to be a prominent and practical route for enhancement of photocatalytic activity in the following aspects: (1) the visible light absorption capability is able to be improved; (2) the existence of cocatalysts can provide more active sites and reduce over-potentials for redox reactions; (3) the construction of heterojunction systems (such as a p-n heterojunction) is beneficial for faster separation and transfer of charge carriers; and (4) the stability of the photocatalysts can be enhanced due to the depositing of proper functional groups via surface passivation.

2.4.2.1. Metal oxides/g-C₃N₄ composite heterostructures

Among various inorganic semiconductor coupled g-C₃N₄ heterostructures, metal oxides such as TiO₂ [93-95], Co₃O₄ [96-98], ZnO [99], and WO₃ [100] have become a new research focus for modification of g-C₃N₄. Outstandingly, TiO₂ and Co₃O₄ have been most intensively studied as suitable candidates for the successful formation of hybrid heterostructures with g-C₃N₄. Li's group developed porous N-TiO₂/g-C₃N₄ heterojunctions via an in-situ microwave assisted approach, showing enhanced visible light photocatalytic performances for degradation of dyes [101]. The optimal photocatalytic activity could be found at 40 wt% loading of N-TiO₂. The main reason for the enhancement of photocatalytic activity could be attributed to the construction of the type-II heterojunction [102], which promotes the more efficient separation of electrons and holes than pure N-TiO₂ or g-C₃N₄. As illustrated in Figure 2.14, the electrons on LUMO level of g-C₃N₄, which is more negative relative to the conduction band (CB) level of N-TiO₂, would be transferred to the lower laying CB level of N-TiO₂ to form an electron centre, while the holes will be injected from the valence band (VB) level to that of g-C₃N₄ in the opposite direction. Meanwhile, superoxide anion radical $\cdot\text{O}_2^-$ was confirmed to be the predominant oxidative radicals for degradation of RhB.

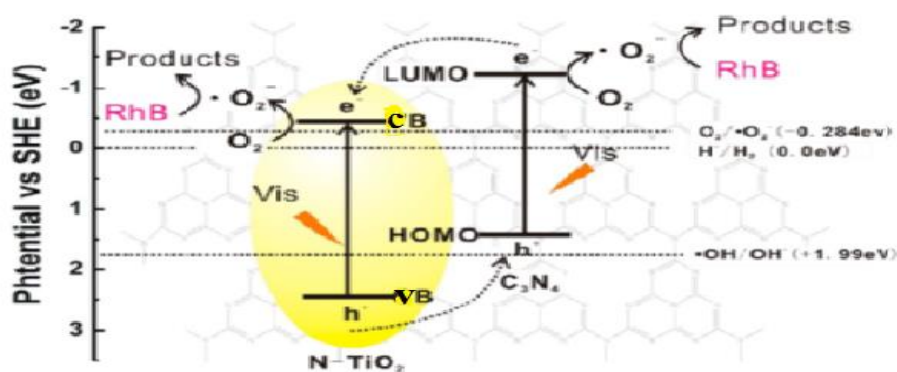


Figure 2.14. Schematic diagram of energy band structure and possible reaction mechanism for N-TiO₂/g-C₃N₄ heterojunctions [101]. Reproduced with permission of the American Chemical Society.

Another report from Yu's group [103] revealed that a direct g-C₃N₄-TiO₂ Z-scheme photocatalyst prepared via simple calcination of commercial P25 and urea has exhibited higher photocatalytic activity than pure P25 for oxidative decomposition of HCHO in air. At the optimal loading amount of g-C₃N₄, the apparent reaction rate constant of the composite could reach as high as 2.1 times of that on pure P25. The construction of direct Z-scheme nanocomposites gives unprecedented insights into efficient separation of photo-induced charge

carriers for improvement of photocatalytic activity. Different from traditional type-II heterojunction, the photo-excited electrons by UV irradiation from TiO₂ would be transferred from CB of TiO₂ to VB of g-C₃N₄ directly without any mediator, and then further excited to CB of g-C₃N₄ later on. Thus, the electrons will be efficiently separated from the holes which are stored in the VB of TiO₂. Both of them will then be involved in respective redox reactions for production of highly reactive radicals such as $\cdot\text{OH}$ and $\cdot\text{O}_2^-$, facilitating the faster decomposition of HCHO. (Figure 2.15)

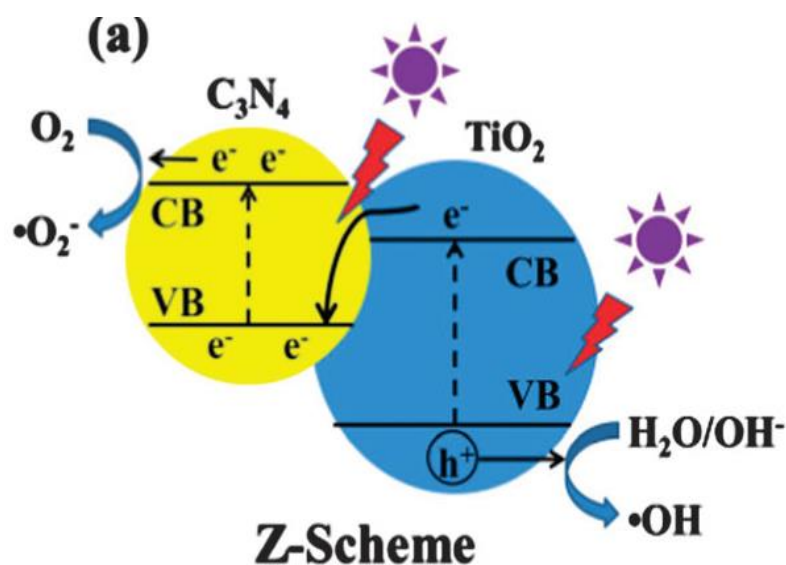


Figure 2.15. Schematic diagram of charge transfer mechanism for direct g-C₃N₄-TiO₂ Z-scheme photocatalysts under UV irradiation. [103]. Acknowledgement to Royal Society of Chemistry.

Apart from the different heterojunction system constructed between TiO₂ and g-C₃N₄ semiconductors, various nanostructured TiO₂ including 0D nanoparticles ~ 3D nanospheres can be tuned and synthesized via a simple seed-induced solvothermal approach [104]. Among its analogues, well-dispersed 3D mesoporous-TiO₂ /2D g-C₃N₄ showed the highest photocatalytic activity for dyes degradation under visible light. Most recently, enhanced photocatalytic activity focusing on controlling of specific exposed {001} facets for anatase TiO₂ with high energy or incorporating other phases of TiO₂ (such as brookite) other than traditional anatase has become a research hotspot [105-107]. Construction of a novel and green synthesis approach still remains a challenging task for fabrication of a stable and effective TiO₂/g-C₃N₄ heterostructure.

Except for the well-studied TiO₂/g-C₃N₄ heterostructure, Co₃O₄ is another metal oxide, which attracts continuous attention due to its supreme oxidation ability and a relatively narrow band gap of 2.1 eV for water splitting and photocatalytic degradation of pollutants [108-109].

In 2013, Ge's group obtained a Co_3O_4 -g- C_3N_4 heterojunction photocatalyst via a facile mixing and calcination method [96], which exhibited enhanced photocatalytic activity for degradation of MO. The optimal loading of 0.2 wt% Co_3O_4 contributes the highest photocatalytic efficiency, which is 7.5 folds higher than that of pure g- C_3N_4 . As manifested in Figure 2.16 (a), the introduction of Co_3O_4 formed intimate contact interfaces with g- C_3N_4 , promoting the transfer of photo-induced holes from g- C_3N_4 to Co_3O_4 , while leaving the electrons in Conduction band of g- C_3N_4 . Thus, the recombination of electron-holes charge carriers has been suppressed effectively. The superoxide anion radical $\cdot\text{O}_2^-$ and the holes facilitate the photo-oxidation of methyl orange molecules. This result is further confirmed by photoluminescence (PL) spectra listed in Figure 2.16 (b).

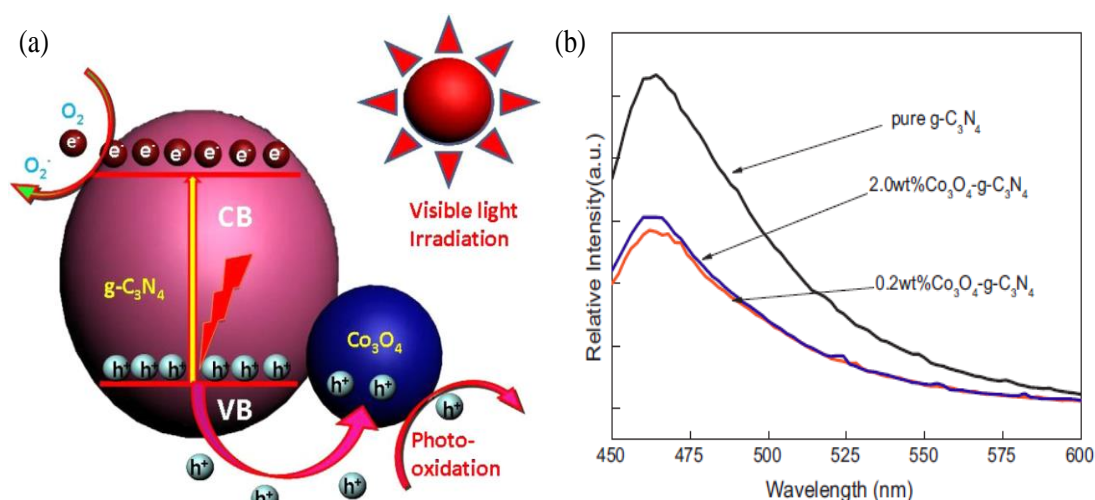


Figure 2.16. (a) Schematic diagram of degradation mechanism for MO over Co_3O_4 -g- C_3N_4 heterojunction photocatalyst under visible light irradiations; and (b) PL spectra of Co_3O_4 -g- C_3N_4 heterojunction photocatalyst [96]. Reproduced with permission from Elsevier.

Wang's group [97] reported the decoration of 3D flower-like $\text{Co}(\text{OH})_2/\text{Co}_3\text{O}_4$ on 2D g- C_3N_4 via a simple coating approach. The introduction of cobalt hydroxide/oxide apparently enhanced the photoelectric effect for a promoted photocatalytic OER activity, owing to the improved separation and transfer of charge carriers as well as electronic conductivity. The unique hydrocalcite structure of α - $\text{Co}(\text{OH})_2$ contributes to the superior properties for electronic transfer, which might explain the higher OER performance of $\text{Co}(\text{OH})_2/\text{g-}\text{C}_3\text{N}_4$ than $\text{Co}_3\text{O}_4/\text{g-}\text{C}_3\text{N}_4$. Specifically, at a loading content of 7 wt% of $\text{Co}(\text{OH})_2$, the constructed $\text{Co}(\text{OH})_2/\text{g-}\text{C}_3\text{N}_4$ possessed optimal photocatalytic OER activity, which is 5 times higher than that of pure g- C_3N_4 . Later on, monodispersed quantum dots of Co_3O_4 were fabricated and further deposited on porous g- C_3N_4 nanosheets via an annealing process [98]. It was discovered that the annealing temperature in-situ induced numerous pores around Co_3O_4 quantum dots on the

surface of g-C₃N₄ and built a heterojunction with strong interfacial interaction. The higher annealing temperature led to a higher BET surface area, stronger absorption ability within visible-light range, better oxidation ability and superior photoelectrochemical performance, contributing to an optimal photocatalytic OER activity at 0.8% Co₃O₄-g-C₃N₄-300, which is nearly 5 times as high as that of pure g-C₃N₄ for O₂ production under visible light.

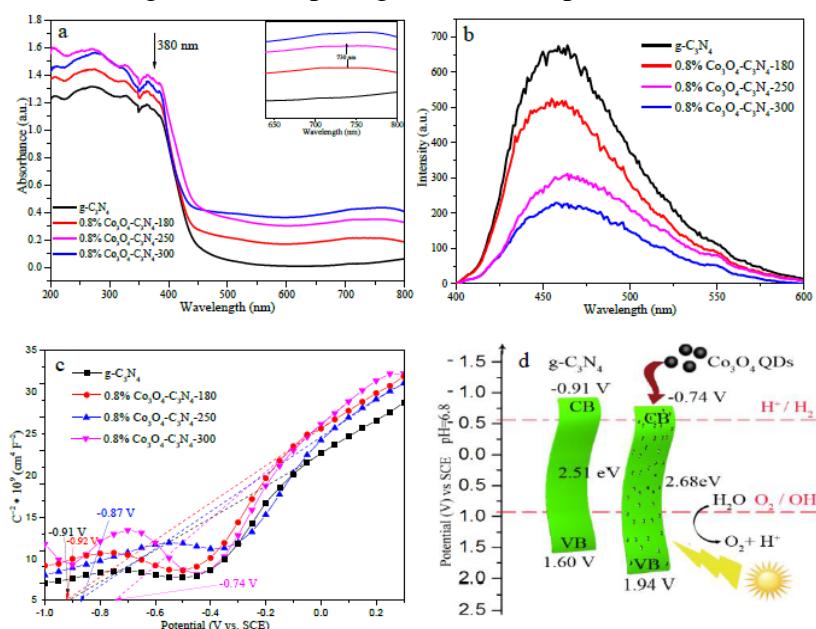


Figure 2.17. (a) UV-vis DRS; (b) PL spectra; (c) Mott-Schottky curves for pure g-C₃N₄ and 0.8% Co₃O₄-C₃N₄ at various annealing temperature; and (d) band structure diagram for g-C₃N₄ before and after decoration of Co₃O₄ [98]. Reproduced with permission from Elsevier.

Additionally, incorporating g-C₃N₄ with other metal oxides have also been systematically used to form heterojunction photocatalysts, such as WO₃/g-C₃N₄ [110], Fe₃O₄/g-C₃N₄ [111], Cu₂O/g-C₃N₄ [112], MoO₃/g-C₃N₄ [113], and NiO/g-C₃N₄ [114], etc. All these composite nanostructures pose new insights for designing hybrid catalysts for various photoredox applications in solar energy conversion and removal of environmental contaminants.

2.4.2.2. Metal sulfides/g-C₃N₄ composite heterostructures

Among various noble metal-free cocatalysts for modification of g-C₃N₄ for enhanced photocatalytic activity, transition metal dichalcogenide (TMD) such as MoS₂ and WS₂ based cocatalysts have become the most popular research targets recently. Owing to their layered nanostructure and electronic properties similar to graphene, earth-abundant and easily fabricated MoS₂ stands out to be one of the most ideal candidates as cocatalysts in photocatalytic applications [115-116].

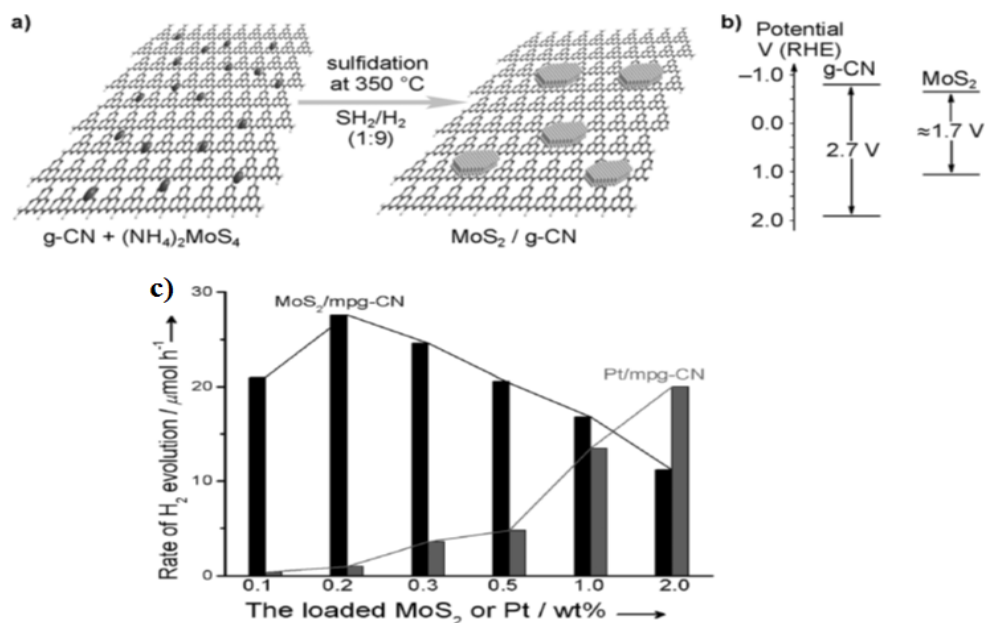


Figure 2.18. (a) Fabrication procedure of gas-phase sulfidation and the obtained ideal structure model of layered nanojunction; (b) Band structure diagram for g-C₃N₄ and MoS₂; and (c) Rate of photocatalytic H₂ evolution on mpg-CN loaded with different cocatalysts [12], reproduced with permission from Wiley-VCH Verlag GmbH & Co. KGaA.

The pioneering work from Hou et al. reported the construction of a thin layered heterojunction with MoS₂ slabs grown over the surface of mesoporous g-C₃N₄ [12]. Looking into Figure 2.18(a), the analogous structures of MoS₂ and g-C₃N₄ could enlarge the contact area around their interface layers and shorten the pathway for electrons transport over the surface of MoS₂. Meanwhile, the band structure diagram in Figure 2.18(b) shows that, upon visible light irradiation, the photo-generated electrons from g-C₃N₄ could be transferred to conduction band of MoS₂ to facilitate the faster separation and migration of charge carriers. As an excellent HER cocatalyst, thin layers of MoS₂ could boost H₂ evolution owing to the high exposure of sulfur edges of the crystal layers. Thus, the presence of MoS₂ as cocatalysts could serve as electron collectors for efficient H₂ release once the unsaturated sulfur atoms trap enough protons from the solution. Apparently, the maximum photocatalytic H₂ evolution could be achieved when the loading amount of MoS₂ reached 0.2 wt%, which performs much better than the 0.2 wt% Pt/mpg-CN analogue under the exactly same conditions. When the loading content keeps increasing to 2.0 wt%, the Pt/mpg-CN surprisingly outperformed the as-synthesized MoS₂/mpg-CN. The thin junction constituted by thin planar of MoS₂ is beneficial for efficient light absorption as well as lower barriers for electrons transport. This optimal system reached an apparent quantum yield of 2.1% at wavelength of 420 nm. One shortcoming

falls into the instability due to the photo-oxidation/corrosion of MoS₂ during the cycling runs. Since that, MoS₂ has attracted numerous research attention as cocatalysts for electrocatalytic and photocatalytic H₂ evolution as well as in other photocatalytic applications [117-118]. Li et al. [119] synthesized 2D g-C₃N₄/2D MoS₂ heterojunction photocatalysts adopting a simple impregnation and calcination process. 2D g-C₃N₄ and MoS₂ nanosheets were obtained via ultrasonication of bulk materials with acid exfoliation. Under visible light irradiation, this composite heterojunction photocatalyst displayed significantly enhanced activity with considerable stability towards degradation of MO and RhB. Figure 2.19 illustrates the fabrication scheme of 2D g-C₃N₄/2D MoS₂ heterojunction and also presents the proposed mechanism for charge transfer over the interface of the 2D MoS₂/g-C₃N₄ composites with remarkably enhanced photocatalytic performance. The typical type-II charge transfer scheme contributed to the reduction of recombination probability of photogenerated charge carriers. Consequently, abundant holes accumulated in the valence band (VB) of g-C₃N₄ for faster oxidation of dye molecules.

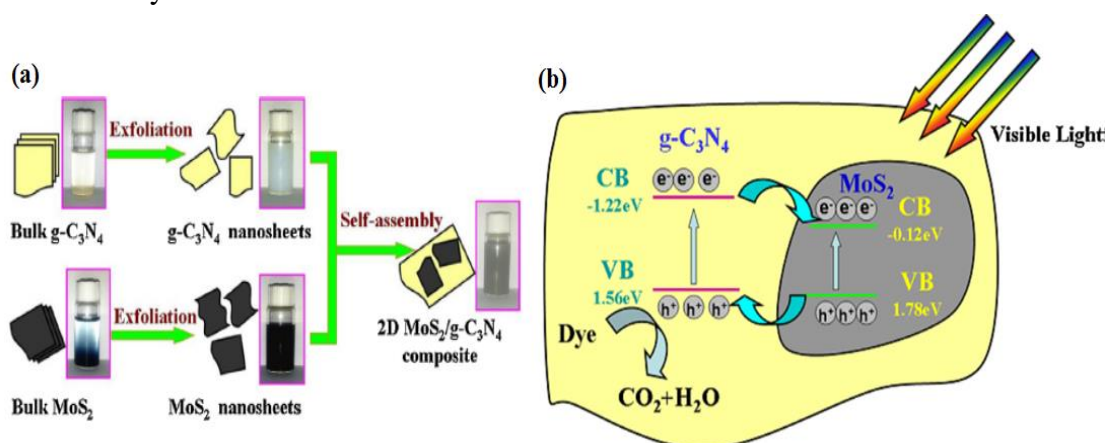


Figure 2.19. (a) Fabrication procedure illustration of 2D MoS₂/g-C₃N₄ heterojunction; (b) Proposed photocatalytic mechanism diagram of 2D MoS₂/g-C₃N₄ heterojunction composites [119]. Reproduced with permission from Elsevier.

Wang's group [120] has fabricated water soluble and stably dispersed MoS₂ quantum dots (MSQD) and further deposited on g-C₃N₄ nanosheets to obtain a 0D MoS₂/2D g-C₃N₄ heterojunction nanocomposites with improved photocatalytic and electrocatalytic H₂ evolution performance. MSQD was prepared via a facile one-pot hydrothermal process with high stability and dispersion in water with a uniform particle size around 2~5 nm. Compared to MoS₂ nanosheets, MoS₂ quantum dots could contribute more exposed edges for unsaturated sulfur atoms as active sites with higher electrocatalytic H₂ evolution performance accordingly. The quantum confinement effect could also shift the optical properties and realignment of energy

band structures. Compared to 0.2 wt% Pt-CN and pure CN (without any cocatalyst), the average rate of H₂ evolution for 0.2 wt% MSQD-CN has increased by 1.3 and 8.1 times, respectively. The optimal 5 wt% MSQD-CN achieved the highest photocatalytic H₂ evolution activity with an average H₂ evolution rate reaching as high as 577 μmol. h⁻¹. g⁻¹. The introduction of MSQD as a cocatalyst effectively lowered the overpotential barrier for HER process and enhanced electrical conductivity for transport of charge carriers. Additionally, the construction of MSQD-CN hybrid with an intimate contact interface of p-n heterojunction formed matches well with a direct Z-scheme charge transfer system. The detailed synergetic mechanism among Pt, MSQD and CN can be discovered in Figure 2.20, which clearly illustrates the process of facilitated electron transfer and separation. The electrons stored in conduction band of MSQD will trap H⁺ for H₂ released with higher reductive potential. Afterwards, a 3D flower-like MoS₂ composed of nanosheets with thin layers were fabricated by a simple green approach and attached to the surface of 2D g-C₃N₄ nanosheets via {002} phase of MoS₂ to form an intimate contact. Other than the chemically inert phase of {002}, more active phase of {103} has been confirmed for exposure, leading to possible exposure of more active sites for enhanced HER performance. This unique 3D porous architecture constituted by ultrathin nanoplates via self-assembling exhibits significantly enhanced photocatalytic and electrocatalytic H₂ evolution performance, especially under visible light irradiations. In addition, this 3D MoS₂/2D g-C₃N₄ nanostructure was proven to surpass its 0D and 2D MoS₂ analogues with a better photocatalytic H₂ evolution performance and extremely high catalytic stability [121].

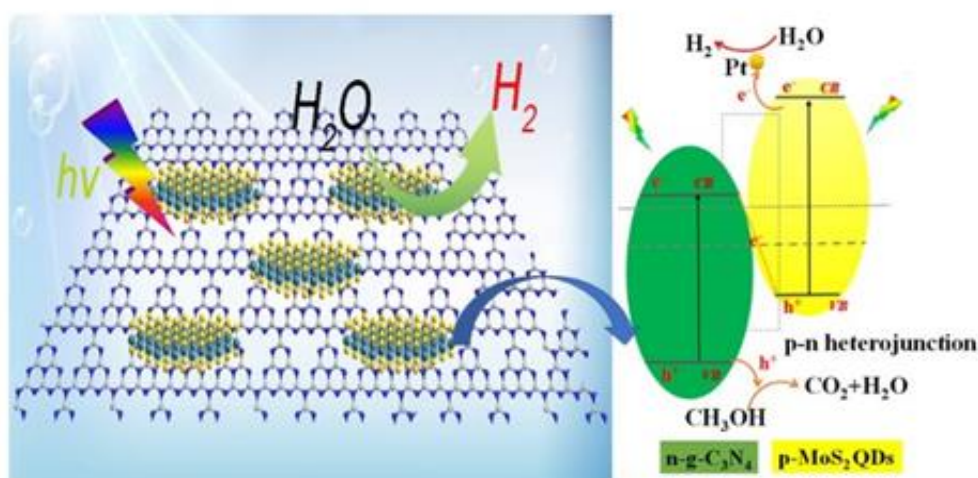


Figure 2.20. Schematic illustration of photocatalytic H₂ evolution performance for MoS₂ QDs loaded on g-C₃N₄ and proposed mechanism for the enhanced charge transfer process [120]. Reproduced with permission from Elsevier.

Another widely studied metal sulfide cocatalyst, CdS has also drawn much attention due to its narrow band gap of 2.4 eV in the past few years [122-124]. CdS quantum dots have been successfully fabricated and then further dispersed over the surface of g-C₃N₄ to achieve a drastically increased photocatalytic activity for pollutants degradation and water reduction. The coupling of CdS quantum dots could extend the absorption edges to a longer wavelength range with enhanced visible light absorption ability, which could be tuned by adjusting the content of CdS. The perfect match of energy levels of CdS and g-C₃N₄ constitutes a typical Type-II heterojunction system, in which photo-excited holes will be shifted from CdS to g-C₃N₄ while CdS acts as an electron collector. Thus, the challenge of photocorrosion issue with CdS will be remarkably overcome, showing a prominent increase in photostability. As shown in Figure 2.21c, no obvious decrease of H₂ evolution performance was observed after 28 h irradiation on 30 wt% CdS QDs/g-C₃N₄ composites. Due to the much more efficient separation of charge carriers at the interface of the heterojunction as illustrated in Figure 2.21, the visible light photocatalytic H₂ evolution activity and stability can be drastically enhanced relative to pure g-C₃N₄ [125].

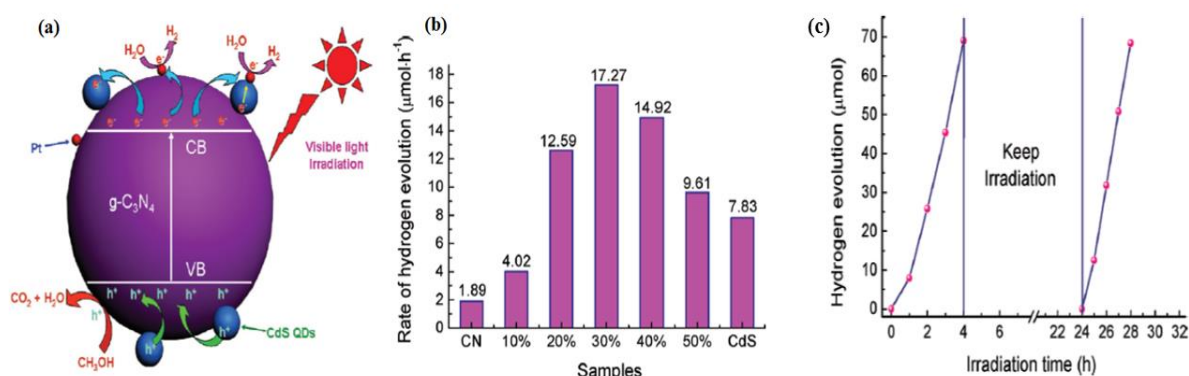


Figure 2.21. (a) Schematic diagram of photo-induced charge transfer process over CdS QDs/g-C₃N₄ heterojunction system; (b) Photocatalytic H₂ evolution performance for g-C₃N₄ loaded with different content of CdS QDs and (c) Cyclic runs for the photocatalytic H₂ evolution with 30 wt% CdS QDs/g-C₃N₄ composites under visible light [125]. Reproduced with permission of the American Chemical Society.

Other metal sulfides based photocatalysts such as WS₂ [126], NiS [127], ZnS [128], Cd_{1-x}Zn_xS [129-130] can also serve as cocatalysts to promote g-C₃N₄-based photocatalytic H₂ evolution from water. These investigations provide more insights in designing scalable, sustainable and effective H₂ evolution photocatalysts with a high stability.

2.4.2.3. Metal phosphides/g-C₃N₄ composite heterostructures

Recently, transition metal phosphides (TMPs) such as CoP, Co₂P and Ni₂P have attracted intensive attention as cocatalysts in electrocatalytic and photocatalytic H₂ evolution process due to their excellent performance as HER catalysts. For the first time, Fu's group found that cobalt phosphide (Co₂P) could be a potential cocatalyst for CdS nanorods as the photocatalyst for efficient photocatalytic H₂ evolution, demonstrating the highest H₂ evolution rate up to 19373 $\mu\text{mol} \cdot \text{h}^{-1} \cdot \text{g}^{-1}$ with the apparent quantum yield reaching 6.8% after 10 h irradiation of LED light ($30 \times 3 \text{ W}$, $\lambda \geq 420 \text{ nm}$) [131]. Later on, cobalt phosphide has been confirmed to serve as effective co-catalysts to boost the photocatalytic hydrogen evolution activity on g-C₃N₄ and TiO₂. Zhang's group fabricated a hybrid heterostructure of CoP/TiO₂ with significant enhancement of photocatalytic H₂ evolution rate (8350 $\mu\text{mol} \cdot \text{h}^{-1} \cdot \text{g}^{-1}$) by 11 times relative to pristine TiO₂ under irradiation of a 300 W Xe lamp [132]. Zeng et.al constructed a heterostructure of 1D Co₂P nanorod/2D g-C₃N₄ nanosheet by a solution-phase process with enhanced visible light photocatalytic H₂ evolution performance. The maximum average hydrogen evolution rate of 53.3 $\mu\text{mol} \cdot \text{h}^{-1} \cdot \text{g}^{-1}$ could be obtained at the optimal loading content of Co₂P at 3 wt% under illumination of simulated solar light provided by a 300 W Xe lamp (UV cut-off filter with $\lambda > 420 \text{ nm}$) [133]. This solution-phase approach for hybridizing 1D/2D heterostructure could be extended to engineering other novel nanomaterials for boosting of photocatalytic H₂ evolution from water splitting. Very recently, Yan's group [134] reported the as-synthesized CoP/g-C₃N₄ composite heterojunction for remarkably enhanced visible light photocatalytic H₂ production rate. At the optimal loading amount of 0.25 wt% CoP, the photocatalytic H₂ evolution rate reached 474.4 $\mu\text{mol} \cdot \text{h}^{-1} \cdot \text{g}^{-1}$, which is 113 times higher than that of pristine g-C₃N₄ and even higher than that of Pt/g-C₃N₄ under irradiation of simulated solar light provided by a 300 W Xe lamp (UV cut-off filter with $\lambda > 420 \text{ nm}$). Moreover, it also boasts at a sound photo-stability without any decrease after cycling runs. The well-matched band energy structures constitutes a type-II heterojunction for efficient charge transfer and separation system, as illustrated in Figure 2.22. Except for application in photocatalytic H₂ evolution reaction, cobalt phosphide has also been adopted as a co-catalyst to modify graphitic carbon nitride in overall water splitting without any sacrificial agent. Wang's group demonstrated that CoP and Pt can act as dual cocatalyst on the surface of g-C₃N₄ to promote the release of O₂ and H₂ respectively in a molar ratio of 1:2 [135]. The introduction of CoP boosts the charge separation and reduce the over-potential for OER process as it can also act as a prominent OER electrocatalyst [136]. As depicted in Figure 2.23, g-C₃N₄ loaded with dual

co-catalysts of Pt and CoP showed the best photocatalytic performance for overall water splitting into H₂ and O₂ compared to g-C₃N₄ loaded with Pt or Pt-Co₃O₄ as co-catalysts. Furthermore, g-C₃N₄ only or g-C₃N₄ loaded with CoP cannot show any photocatalytic activity for overall water splitting. After several repeated runs, the photocatalytic water splitting performance dropped a little, probably because the interface binding between the photocatalyst and co-catalysts became loose. The design of dual co-catalysts for overall water splitting without any sacrificial agent provides a novel strategy to facilitate the kinetics for both OER and HER process.

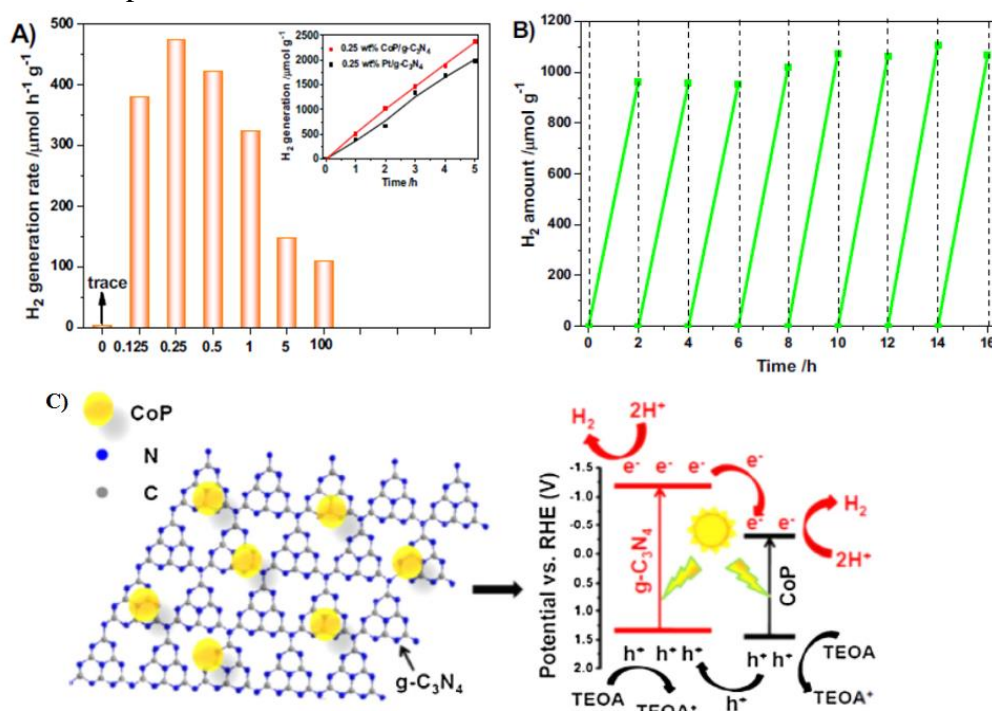


Figure 2.22. A) Photocatalytic hydrogen evolution performance for g-C₃N₄ loaded with different content of CoP. Inset: comparison of photocatalytic H₂ evolution amount vs. time over 0.25 wt% CoP/g-C₃N₄ and 0.25 wt% Pt/g-C₃N₄. B) Cyclic runs for photocatalytic H₂ evolution on 0.25 wt% CoP/ g-C₃N₄. And C) Mechanism diagram of charge transfer process over CoP/g-C₃N₄ heterojunction system [134]. Reproduced with permission from Elsevier.

Other metal phosphide cocatalysts such as Ni_xP and NiCoP have also been brought to the research forefront of photocatalytic hydrogen evolution [137-139]. NiCoP/g-C₃N₄ was synthesized via a simple one-pot technique and displayed extremely high photocatalytic hydrogen evolution performances with an average H₂ evolution rate of 1643 μmol. h⁻¹. g⁻¹, which was elevated by 21 times relative to g-C₃N₄ [138]. Colloidally fabricated Ni₁₂P₅ nanoparticles were firmly anchored on nanoporous g-C₃N₄ by a simple ultrasonic approach for enhanced visible light photocatalytic H₂ evolution performance by Zeng et al. [140]. This heterostructure achieved high AQY of 4.67% at the wavelength of 420 nm.

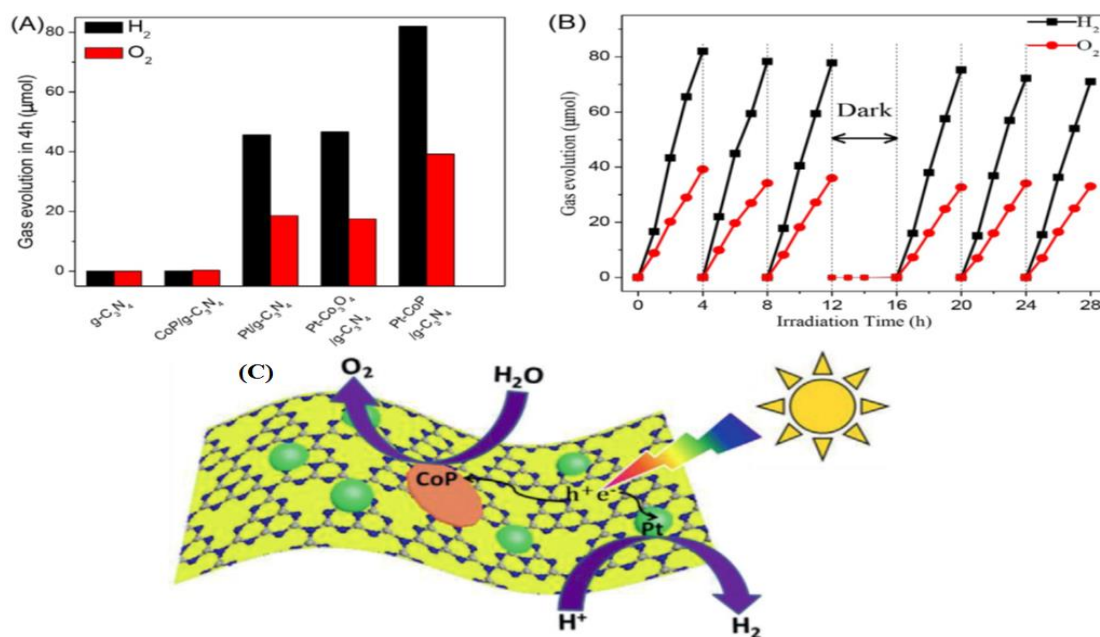


Figure 2.23. (A) Photocatalytic overall water splitting performance for g-C₃N₄ loaded with different cocatalysts. (B) Continuous runs of overall water splitting by 3 wt% Pt-3 wt% CoP-g-C₃N₄. (C) Schematic diagram of the cooperation of dual cocatalysts of Pt and CoP over surface of g-C₃N₄ for photocatalytic water splitting process [135], reproduced with permission from Wiley-VCH Verlag GmbH & Co. KGaA.

Apart from the results shown above, other construction of g-C₃N₄-based heterojunctions have also been mentioned in previous reports. Carbon-g-C₃N₄ heterojunctions, metal-g-C₃N₄ heterostructures, metal organic framework (MOF)-g-C₃N₄ heterostructures, conducting polymer-g-C₃N₄ together with other forms of complex-g-C₃N₄ as sensitizers also turn out to be promising photocatalysts for various applications. Looking into the future, more efforts should be devoted to : (1) developing new strategies for exploiting efficient visible light absorption to longer wavelength (above 500 nm) to mimic the natural photosynthesis process; (2) reinforcing the heterostructure between cocatalyst and the photocatalyst to achieve a high stability, especially for metal sulfides; (3) employing scalable exfoliation techniques for single or few-layered g-C₃N₄ for potential industrial applications; (4) combining theoretical calculation with innovative approach for the design of site-selective loading of cocatalysts and crystal facet tailoring of photocatalysts; and (5) developing green and simple synthesis technique without any secondary hazards. In summary, g-C₃N₄-based photocatalysts will definitely keep booming as a research hotspot with challenges and opportunities in the following years.

2.5 Bismuth-based complex oxides as visible light photocatalysts

Embarking on the journey searching for visible-light responsive photocatalysts, researchers discovered that bismuth-based complex oxides can serve as one type of potential candidates because of their unique electronic structures. Compared to valance band of TiO_2 which contains only O 2p orbitals, the valence band of bismuth-based complex oxides is composed of hybrid orbitals of both Bi 6s and O 2p. The distortion of well-dispersed Bi 6s orbital could benefit the mobility of photoinduced charge carriers and reduce the band gap [141-143]. Within the past few decades, many efforts have been made for the development of bismuth-based visible light photocatalysts with high performances for environmental pollutants degradation as well as water splitting, such as BiVO_4 [141], BiFeO_3 [142], Bi_2O_3 [143], Bi_2MoO_6 [144], BiOX [145] and Bi_2WO_6 [146] etc. Among them, bismuth oxyhalides, bismuth ferrite perovskites and bismuth tungstate are the most widely studied three representatives, whose recent progresses are summarized as follows.

2.5.1 Synthesis and photocatalytic application of bismuth oxyhalides

2.5.1.1 Crystal and electronic structure

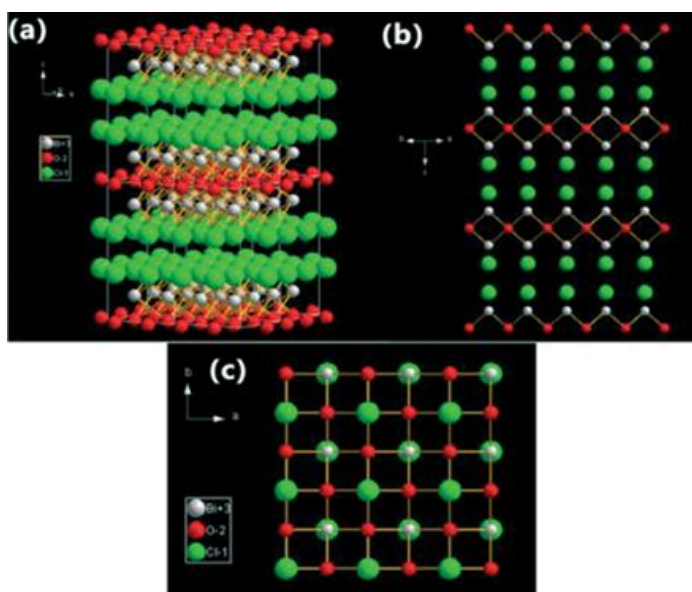


Figure 2.24. Schematic diagram of model structure for BiOI crystals (a) three-dimensional projection; (b) {110} facets; and (c) {001} facets [150]. Acknowledgement to Royal Society of Chemistry.

Bismuth oxyhalides compounds BiOX ($\text{X}=\text{Cl}, \text{Br}, \text{I}$) have been confirmed to possess outstanding photocatalytic activities owing to their unique structure as well as excellent physicochemical and optical properties [147-149]. It features a tetragonal matlockite structure,

a layered structure of $[\text{Bi}_2\text{O}_2]$ slabs, which are interwaved by double slabs of certain halogen atoms as illustrated in Figure 2.24. The internal static electric field is believed to promote the efficient separation of photo-induced electrons and holes for enhanced photocatalytic activity. As the atomic numbers increases from Cl to I, their band gaps become narrower from BiOCl (~3.2 eV) to BiOI (~1.7 eV), which falls into the responsive range of both UV and visible light. The hybridization and engineering of BiOX compounds could lead to a maximum enhancement of their photocatalytic activity and optimal utilization of visible light.

2.5.1.2 Photoactivity enhancement via modification

Pioneeringly, Zhang et al. [151] demonstrated the exceptional photocatalytic performance of BiOCl for photodegradation of MO dye under UV light, far exceeding the performance of commercial P25. Since then, numerous interests have been centered on the morphological modulation, semiconductor hybridization, defects control and tuning of facets exposure for BiOX photocatalysts with their applications in energy and environmental management. Normally, high efficient nanostructure of BiOX photocatalyst is comprised of binary or ternary hybridized heterostructure due to synergistic effects. Among which, semiconductor/BiOX hybrids have been most intensely studied recently [152-154].

The engineering design of constructing BiOI/BiOX (X=Cl, Br) composites has been addressed in the past few years [155-157]. Pure BiOI boasts for its narrow band gap which is favorable for visible light absorption. However, the high recombination rate of photo-generated electron-hole pairs will restrain its practical utilization of solar energy due to a low quantum efficiency. Huang's group [155] has synthesized BiOI/BiOBr composites by a one-pot solvothermal process with enhanced photocatalytic bacteriostatic activity under visible light. Yang et. al prepared BiOI/BiOCl composites via a facile ultrasonic approach assisted by ionic liquid. The obtained composites with 40% content of BiOI exhibits the highest photocatalytic activity towards degradation of RhB, tetracycline and other dye pollutants [156]. Due to the formation of the BiOI/BiOCl heterojunction, the photo-excited electrons from BiOI under visible light will transfer from the new formed CB of BiOI to lower level CB of BiOCl, while the holes will make the opposite transfer. The efficient separation and utilization of electron-hole pairs will contribute to the drastic enhancement of photocatalytic degradation activity for this BiOI/BiOCl heterostructure. The schematic diagram of synthesis procedure and the photocatalytic reaction mechanism are illustrated in Figure 2.25. Wang's group [157] synthesized 3D BiOI/BiOX(X=Cl, Br) nanohybrids with enhanced O_2 evolution performance from water splitting as well as visible-light photocatalytic activity towards dyes degradation.

Wu's group [158] had different findings with as-synthesized BiOX and their composites $\text{BiO}_x\text{B}_{1-x}$ via a microwave-assisted solvothermal technique. Among all the materials, BiOI displayed the highest photocatalytic H_2 evolution activity because of its narrow band gap and sufficiently negative conduction band to drive water reduction under visible light irradiation. On the contrary, the $\text{BiO}_x\text{B}_{1-x}$ composites demonstrated a relatively low performance for H_2 evolution, probably due to their wide band gap and inappropriate electronic band structure.

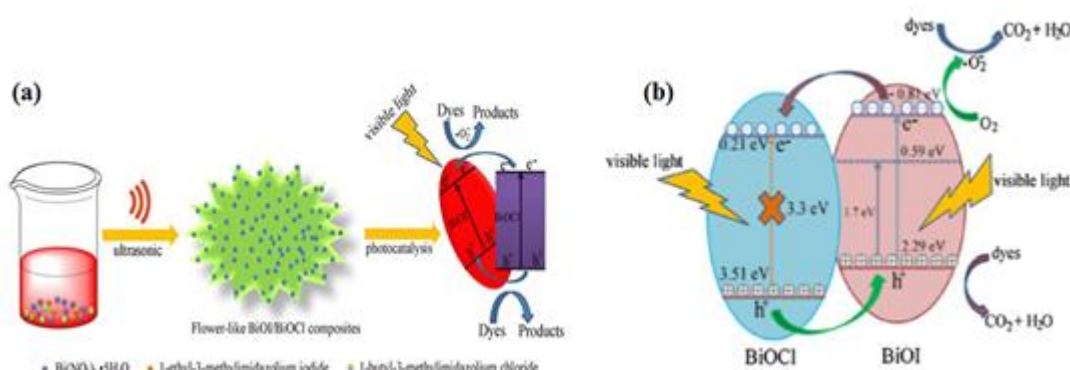


Figure 2.25. (a) The schematic diagram for fabrication of flower-like BiOI/BiOCl; (b) Schematic illustration of photocatalytic reaction process over BiOI/BiOCl heterostructure [156]. Reproduced with permission from Elsevier.

In addition, BiOX hybridized with other semiconductors have also been reported as promising visible light photocatalysts. Lee et al. [152] found that as-prepared BiOCl/ Bi_2O_3 heterostructure by a chemical etching process displayed superior photocatalytic activity than P25 for degradation of both aqueous and gaseous organic contaminants. Homogeneous C-doped $\text{Bi}_3\text{O}_4\text{Cl}$ nanosheets could boost an excellent photocatalytic OER activity under visible light without any cocatalyst and sacrificial agent [159]. Besides, WO_3/BiOCl [153], $\text{NaBiO}_3/\text{BiOCl}$ [160], $\text{BiOCl/BiNbO}_4/\text{TiO}_2$ [161], and $\text{Bi}_{12}\text{O}_{17}\text{Cl}_2/\text{MoS}_2$ [162] have been fabricated and proven to show efficient photocatalytic activity driven by visible light.

Most recently, more and more researchers showed their interests to point defects control as well as specific facet tailoring of BiOX crystals as main strategies for structural engineering. Facet tailoring of crystals is usually achieved via adopting acids as a capping agent to regulate the exposure of crystal facets with a high catalytic activity, leading to the optimized photoelectrochemical properties of the catalyst. Once the H^+ ions bind strongly with the terminated oxygen atoms, which are densely distributed on the surface of {001} facet, the crystal growth along c axis will be suppressed. Jiang et al. [163] adopted a simple hydrothermal approach to obtain the {001} facet-dominant BiOCl nanosheets tailored by self-generated H^+ ions. The exposure percentage of different facets could be achieved by adjusting pH value of

the solution. As presumed, the {001} facet-dominant BiOCl nanosheets exhibited superior photocatalytic activity towards MO degradation than the {010} facet-dominant analogues for direct photo-excitation process.

The introduction of point defects such as oxygen or metal vacancies is normally conducted under thermal conditions or protection of reducing atmosphere such as Ar. Thus, the electronic band levels, transport of charge carriers and light absorption capabilities could be varied accordingly. Those vacancies can also serve as traps for charge carriers. BiOCl nanosheets with oxygen vacancies have been obtained by exposing the white BiOCl powder to UV light irradiation under protection of Ar gas [164]. As shown in Figure 2.26, the color of BiOCl is changed to black due to formation of oxygen vacancies, which will contribute to the defect state lying below the conduction band. This new state will serve as the electron traps and promote faster separation of charge carriers for enhanced photocatalytic activity. Thus, its band structure has been tuned as an efficient visible light responsive photocatalyst.

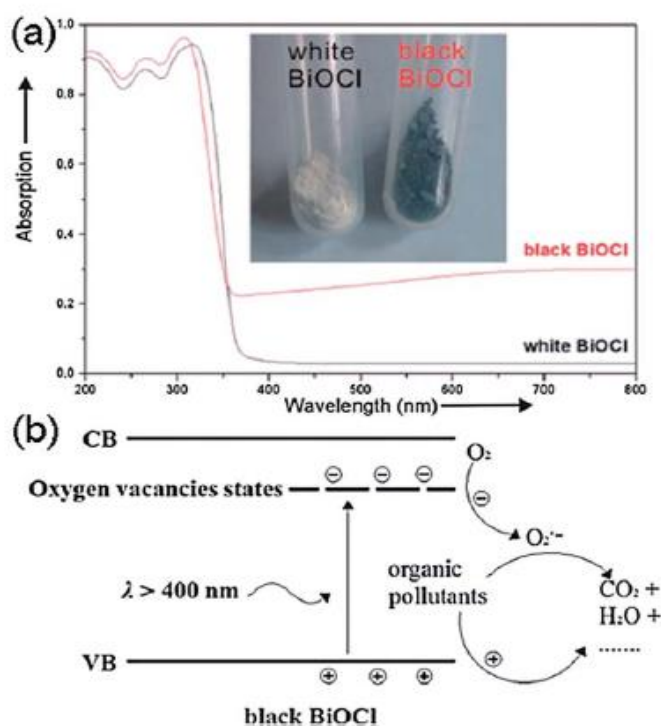


Figure 2.26. (a) UV-vis DRS spectra for the as-synthesized BiOCl samples; and (b) Schematic diagram of band structure and photocatalytic reaction process over black BiOCl [164]. Acknowledgement to Royal Society of Chemistry.

2.5.1.3 Summary and outlook

Except for the applications in photocatalytic degradation of pollutants, photocatalytic water splitting and photocatalytic disinfection, BiOX has also been proven to be a promising catalyst in photocatalytic CO₂ reduction [165], photocatalytic nitrogen fixation [166] and photocatalytic organic synthesis [167]. Still, there are some arguments concerning the detailed photocatalytic mechanism for BiOX. Deep exploration for understanding the active sites in photocatalytic reactions are much needed. In addition, more efforts should be put to control the atomic thickness, porous or hollow structure during the synthesis of BiOX. The advancing of nanotechnology will undoubtedly bring more opportunities to guide the rational design of highly efficient photocatalysts. Assisted with computational calculation and advanced in-situ characterization techniques such as infrared spectroscopy, realistic experimental study over BiOX-based photocatalysts will definitely achieve more fruitful results and broader applications in the future.

2.5.2 Synthesis and photocatalytic application of bismuth ferrite perovskites

2.5.2.1 Crystal and electronic structure

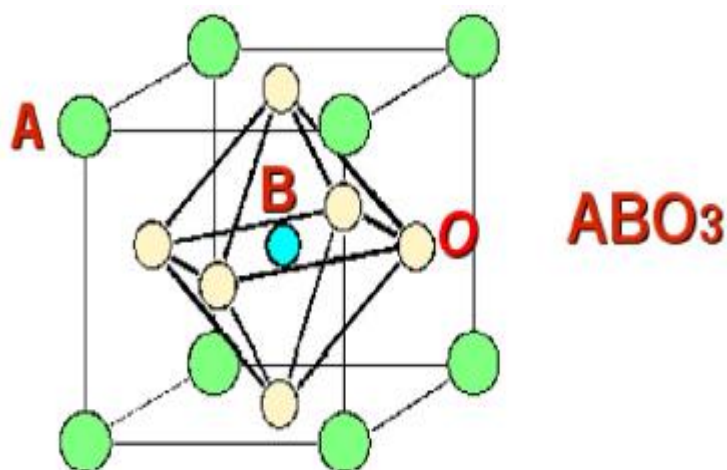


Figure 2.27. Schematic illustration of ABO₃ perovskite structure[171]. Reproduced with permission from Elsevier.

Recently, bismuth ferrite perovskites (BiFeO₃) have emerged as another new class of visible-light driven photocatalysts in degradation of aqueous organic pollutants owing to their unique ferroelectric and magnetic properties[142, 168-170]. The basic chemical formula of the perovskite compound is ABO₃. Generally, the A site is filled with a cation with a larger size than B, typically an alkali metal, an alkaline earth metal and a rare earth metal ion, which

locates in the center of a tetradecahedron composed of 12 oxygen atoms; while the B site is a small-sized transition metal ion which locates in the center of an octahedron composed of six oxygen ions. The ideal ABO_3 perovskite possesses a cubicsymmetry with oxygen ions in the center of the faces as shown in Figure 2.27.

Basically, the A-site ion will not be involved in the reaction directly. To maintain the electrical neutrality and stability of the unit cell, it can adjust the valence state and dispersion state of the B-site ion as the active component. However, if it is replaced by other ion with a different valence state, the valence state of the B-site ions will change accordingly and the unusual valence ions will become stable. Also, lattice defects may occur and lead to the change of the chemical position of the lattice oxygen. In addition, the combination of the A site ion with the O^{2-} carries the characteristics of an ionic bond. When the A site ion is substituted by a higher valence ion, the A ion vacancy may be generated or the valence state of the B site ion may be lowered in order to meet the charge balance. When the A site ion is substituted by a lower valence ion, an oxygen vacancy will be generated or the valence state of the B site is lifted, which favors for the enhancement of photocatalytic activity. Meanwhile, the lattice distortions from ABO_3 perovskite will lead to the transfer between the various crystal phases, which also accounts for the variance in optical and electronic characteristics. By tuning different combination of A and B ions, there is a large scope for engineering and designing optimal ABO_3 perovskite with satisfying optical and physicochemical properties. The catalytic activity of the perovskite-type photocatalyst depends on the energy gap between the B-site cation and O^{2-} which is formed due to the interaction between B - O - B. Therefore, the role and the selection of the B-site cation are crucial. When the B-site ions are replaced by ions of different valence states, it will produce lattice vacancies or the valence alteration of other ions in the B-site, thus the adsorbed oxygen on the catalyst surface will be significantly increased or decreased. Moreover, some synergistic effects will also take place. When the energy gap becomes narrower, the mobility of electrons will be enhanced, and so does the photocatalytic activity. The reduction of the energy gap is beneficial to the absorption of visible light and the utilization of solar energy.

Among all ABO_3 perovskites, $BiFeO_3$ attracts extensive attention as a photocatalyst because of its narrow band gap that responds to visible light excitation as well as multiferroic and magnetic behavior, which are favorable in practical photocatalytic applications. It has been widely studied since 2007, owing to its prominent photocatalytic performance. Most of the fabrication techniques for pure $BiFeO_3$ fall into wet chemical methods such as hydrothermal

[172-174], co-precipitation [175-176] and ultrasonic approach [177-178], etc. Specifically, the hydrothermal process at a low temperature is most attractive for fabrication of BiFeO₃ with desired phase and high purity as well as controllable morphology [179-181]. Meso-scale BiFeO₃ octahedral crystals were fabricated via a hydrothermal approach with tunable KOH concentrations [182]. Seen from the SEM image in Figure 2.28, octahedral BiFeO₃ nanoparticles are covered by eight {001}_{hex} crystal facets. A self-assembly and crystal-plane-selected ripening mechanism is proposed in Figure 2.27(c). The pioneering work by Gao et al. [183] reported that polycrystalline BiFeO₃ nanoparticles with a size of 80-120 nm were obtained by a simple sol-gel method, demonstrating high efficiencies in decomposing organic pollutants under visible light irradiations. It has been proven to display obvious advantage utilizing the visible light, compared to normal TiO₂. Furthermore, it also exhibits weak ferromagnetism at room temperature, which favours the easy removal of the catalysts after the reactions.

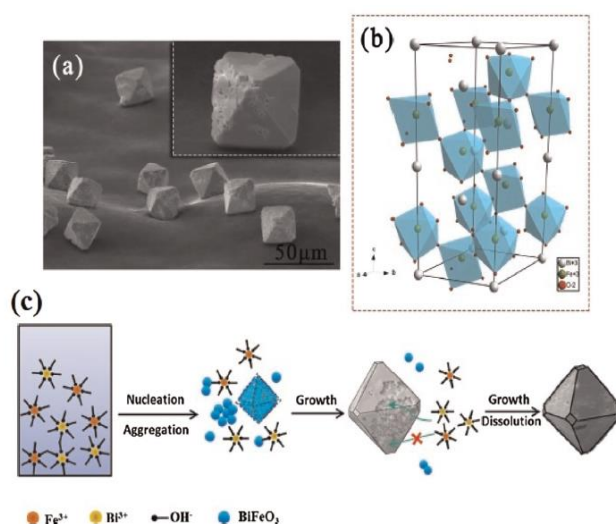


Figure 2.28. (a) SEM image of BiFeO₃ octahedral particles; (b) schematic diagram of model structure for BiFeO₃ with R3c space and (c) illustration of formation process for BiFeO₃ octahedral particles during hydrothermal synthesis[182]. Reproduced with permission from Elsevier.

2.5.2.2 Photoactivity enhancement via modification

Although BiFeO₃ shows a great potential as a promising visible light photocatalyst, it suffers from the high recombination rate of electron-hole pairs and the relatively low conduction band level. Therefore, many researchers focus on further improvement of its photoactivity through tremendous efforts on modification strategies such as morphology and facets control, constructing of heterojunction composites and introduction of oxygen vacancies [184-186].

Most recently, achieving preferential exposure of highly reactive facets via morphological control has become a research hotspot towards many novel photocatalysts. The new insights lie in the discovery that the shifting the photo-induced electron-hole pairs to various crystal planes is closely related to their resultant orientation and optical characteristics [187]. Usually, a surfactant like PVP or PEG will be added during the hydrothermal reaction process under alkaline conditions. Wang et al. [188] adopted a one-pot hydrothermal approach to synthesize uniform BiFeO₃ crystallites with pure phase assisted by KOH and PEG. Tunable BiFeO₃ crystallites could be obtained with various predominantly-exposed facets by altering the alkaline conditions of the precursor solutions. Moreover, the {111}_c facet-dominant pills and rods demonstrate superior visible light response than that of the {100}_c facet-dominant cubes.

Constructing heterojunction with a noble metal dopant or another semiconductor has always been an effective strategy to separate and transfer electron-hole pairs for the enhancement of photoactivity. M@BFO (M=Ag, Au) bowl arrays were synthesized via a thermal evaporation process assisted by a template, demonstrating a much higher efficacy than pure BFO in degrading RhB. The enhancement of photocatalytic efficiency could be attributed to the localized surface plasmon resonance (SPR) induced by noble metals, which increases the separation of charge carriers and also the absorption of visible light [189]. As for semiconductor heterojunctions, construction of TiO₂/BiFeO₃ heterostructures have attracted most attention within the past few years [168,170,190-193]. Wang's group [193] successfully prepared BiFeO₃@TiO₂ nanocomposites with a p-n heterojunction and a core-shell structure, displaying enhanced photocatalytic performance for photodegradation of methyl violet (MV) under both UV and visible light irradiation. Specifically, BiFeO₃@TiO₂ nanocomposite with mass ratio of 1:1 (TiO₂ shell thickness around 50-100 nm) outperforms analogues with other ratios due to optimal loading of TiO₂ shells with suitable thickness. The main attributes for constructing such a BiFeO₃@TiO₂ nanocomposite lie in the internal electric field built at the junction interface, which will drive the faster separation and migration of photogenerated electrons and holes. Additionally, the inner ferroelectric property of BiFeO₃ assists in facilitating the transport of charge carriers due to its internal dipolar field. This unique core-shell nanostructure with p-n junction promotes easier and faster charge transfer with enlarged contact area, enhanced visible light absorption and inhibited charge recombination, presenting new perspectives for designing more efficient BiFeO₃-based nanocomposite heterojunctions in future studies.

Humayun et al. [168] fabricated highly efficient visible-light photocatalysts of porous-BiFeO₃/nanocrystalline TiO₂ nanocomposites with a p-n junction formed at the interface. The

enhanced visible light photoactivity regarding gas-phase degradation of acetaldehyde, liquid-phase degradation of phenol and water reduction for H₂ evolution were attributed to the dimensional transfer of high energy electrons from porous-BiFeO₃ to TiO₂, which leads to the much more efficient separation of charge carriers for the enhanced photoactivity. As illustrated in Figure 2.29, an internal electric field has been built between p-type BiFeO₃ and n-type TiO₂, driving photo-generated electrons to migrate from conduction band (CB) of BiFeO₃ to that of TiO₂, which has been verified through the surface photovoltage (SPV) method including detection of the steady-state surface and transient-state surface photovoltage responses. Also, BiFeO₃ coupled with other semiconductors have been reported with improved photoactivity within the visible light range, such as g-C₃N₄/BiFeO₃ [169], Fe₂O₃/BiFeO₃ [194], and SrTiO₃/BiFeO₃ [195] nanocomposites, for the applications in photocatalytic degradation of organic pollutants and photocatalytic H₂ evolution from water.

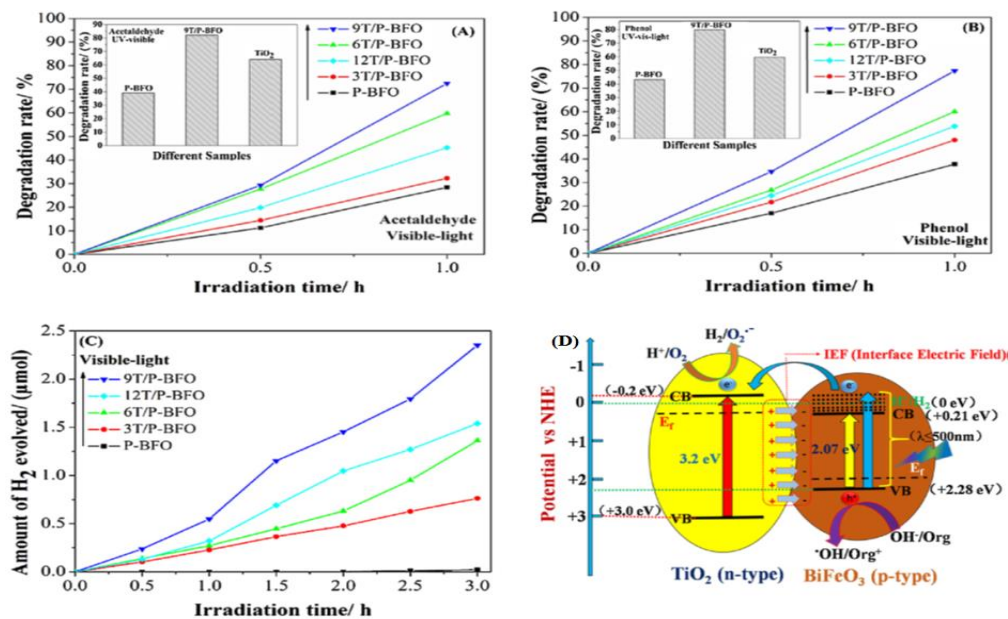


Figure 2.29. Comparison of P-BFO and T/P-BFO composites under visible light (inserts showing UV-visible light photoactivity over different samples) for (A) degradation of acetaldehyde in gas; (B) degradation of phenol, (C) vis-light photocatalytic H₂ evolution; and (D) Schematic diagram of possible charge transfer mechanism for T/P-BFO heterojunction nanocomposites [168]. Reproduced with permission from Elsevier.

Silimar to bismuth oxyhalides (BiOX), introduction of oxygen vacancies is another strategy, which has been employed for modification of BiFeO₃ in very recent years. For the first time, Wang et al. [196] introduced oxygen vacancies onto surface of BiFeO₃ nanoparticles via a hydrogenation approach under high pressure (2.0 MPa), contributing to the enhanced light absorption ability in the visible light region as well as a decrease in band gap energy. The

concentration of oxygen vacancies could be tuned by controlling different hydrogenation temperature, which will further affects its photocatalytic activity. As a result, the hydrogenated BiFeO₃ sample demonstrates a much higher visible-light photocatalytic performance towards the degradation of methyl orange. Further reports by Chen et al. [197] also confirm the effective technique of formation of oxygen vacancies via hydrogenation treatment under high pressure and established inherent correlation between the concentration of oxygen vacancies and improved photocatalytic activity. The presence of oxygen vacancies would enhance light absorption, reduce band gap and also serve as electrons trap to promote faster separation and transfer of charge carriers, leading to a remarkably enhanced photoactivity.

2.5.2.3 Summary and outlook

Undeniably, bismuth ferrite perovskite (BiFeO₃) exhibits a great potential in photocatalytic degradation of organic contaminants and water splitting hydrogen evolution owing to its narrow band gap as well as intrinsic ferroelectric and ferromagnetic attributes. Specifically, it is easy for catalysts to get recycled and reused after wastewater treatment without any concern for nano toxicity. Current modification strategies center around morphology and facets control, heterostructures (core-shell, composites, etc.) and introduction of oxygen vacancies with great progress. However, scalable application other than lab trials is still a big challenge facing the researchers. Several issues need to be addressed in the future to attain stimulating results in the practical applications: (1) design of more efficient BiFeO₃-based nanocomposites with a high porosity and surface area; (2) computational technique should be combined with novel characterization approaches to take a further in-depth study into the reaction mechanism; (3) the evaluation system should step into various types of pollutants other than dyes in aqueous phases; and (4) BiFeO₃-assisted photo-fenton reaction is also a promising process which requires more in-depth investigations.

2.5.3 Synthesis and photocatalytic application of bismuth tungstates

2.5.3.1 Crystal and electronic structure

Usually two crystalline phases can be found in Bi₂WO₆ in an orthorhombic phase and monoclinic phase. While most of the Bi₂WO₆ structures discussed in the present research belong to orthorhombic phase with the crystal structure depicted in Figure 2.30, which manifests a layered structure composed by WO₆ octahedral layers interleaved with [Bi₂O₂]²⁺ layers like a sandwich [198]. Obviously, each W atom is surrounded by six O atoms to constitute a WO₆ octahedron.

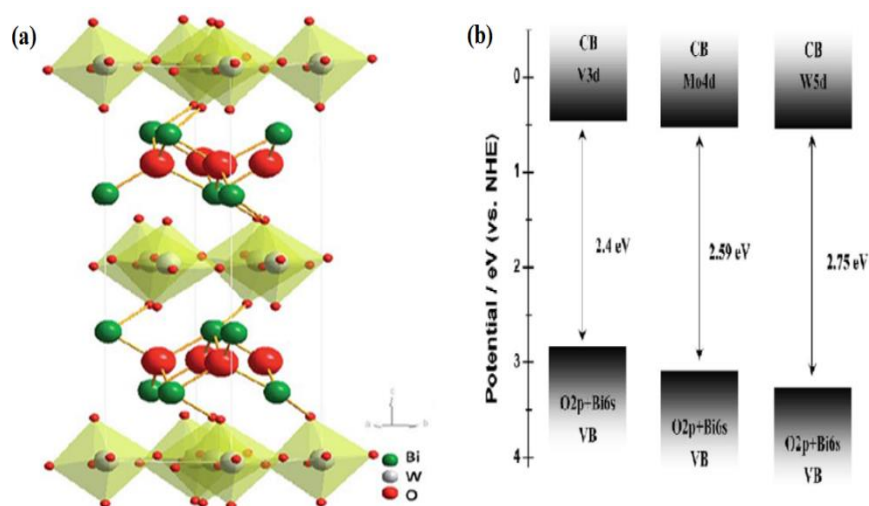


Figure 2.30. (a) Crystal structure illustration of orthorhombic Bi_2WO_6 ; (b) Band structure diagram and theoretical band potentials of BiVO_4 , Bi_2WO_6 and Bi_2MoO_6 [198]. Acknowledgement to Royal Society of Chemistry.

The crystal distortion originated from W and Bi ions evidenced by six various W-O bond length can impact the electronic structure of the crystal and further influence the photocatalytic activity. Based on the calculations from Density Functional Theory (DFT), Bi_2WO_6 is considered to possess a direct band gap of 2.75 eV. The valence band is mainly composed of Bi 6s and O 2p levels, while the conduction band is mainly composed of W 5d levels [199]. The Bi 6s lonely pair electrons are of great importance to reducing the band gap and enhancing hole conductivity. As such, the Bi or O site is considered to be an oxidation site while the W site is believed to act as a reduction site. Inferred from its crystal structure and electronic structure, Bi_2WO_6 can have the potential to act as a promising photocatalyst for degradation of organic pollutants and water splitting for O_2 production under visible light irradiation.

2.5.3.2 Photoactivity enhancement via modification

Early in 1999, Bi_2WO_6 was discovered to possess activity for photocatalytic O_2 evolution from silver nitrate aqueous solution under visible light excitation [200]. Later, Zhu et al. [201] reported that nanosized Bi_2WO_6 exhibited high photocatalytic activity for degradation of RhB under visible light. After these pioneering reports, many researchers focus on consistent enhancement of photocatalytic performance of bismuth tungstate as visible-light-responsive photocatalysts. Various techniques including structural and morphological control, surface modification and constructing of nanocomposites have been proposed and investigated in the

past few years. Hydrothermal method has been proven to be a simple and moderate procedure to obtain flower-like bismuth tungstate with tunable shapes and sizes. In detail, the morphology of as-synthesized Bi_2WO_6 nanoparticles via the hydrothermal process could be controlled through adjusting the pH value of the precursor solution or adding surfactants [202]. As shown in Figure 2.31, the flower-like hierarchical microstructure demonstrated much higher photocatalytic performance in degrading organic pollutants than the bulk samples due to its large surface area and easy separation and migration of charge carriers. These 3D flower-like structures are built by self-assembling and aggregation of thin 2D nanoplates of Bi_2WO_6 [202]. Some other methods such as ultrasonic or microwave-assisted solvothermal or hydrothermal process are also explored to obtain Bi_2WO_6 with hollow spheres, nanoplates or nanoflake morphologies.

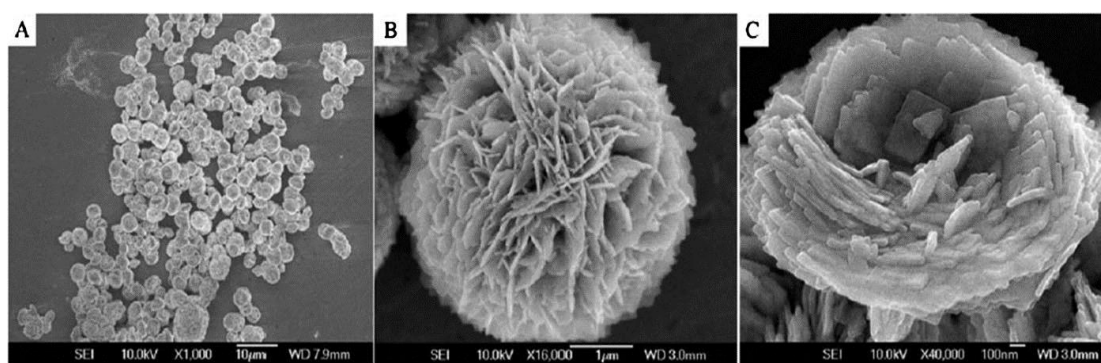


Figure 2.31. Typical SEM images of flower-like microstructures of Bi_2WO_6 [202]. Acknowledgement to Royal Society of Chemistry.

Surface acidification and fluorination are two effective strategies to modify the surface properties of Bi_2WO_6 . The introduced acidic sites could facilitate a strong linkage between the catalyst surface and the pollutant to lead to a faster and easier transfer of charge carriers. In addition, the introduction of F-containing group on the surface could also act as electron traps to improve the interfacial transfer rate of electrons. Surface hybridization with C_{60} has been proposed for enhanced photogenerated electron mobility by Zhu et al. [203]. After being modified on surface of Bi_2WO_6 , C_{60} could serve as an electron collector for efficient transfer and migration of photogenerated electrons, thanks to its delocalized conjugated π structure.

Designing composite nanostructure also provides an effective and achievable way to take advantage of the possible synergistic effect to extend the light absorption capability as well as inhibiting the recombination rate of charge carriers. The constructed composite material can be a metal (Pt, Ag or Au etc.), a carbon material (C_{60} , GO or carbon nanotube etc.) or a semiconductor. So far, the most widely reported composite photocatalyst is $\text{Bi}_2\text{WO}_6/\text{TiO}_2$,

which benefits from well-matched band potentials of Bi_2WO_6 and TiO_2 with an intimate contact heterojunction between them. It shows much enhanced photocatalytic activity towards removal of various environmental contaminants including acetaldehyde, methylene blue, and stearic acid, etc. [204-206]. The limitation lies in the UV-responsive inherence of TiO_2 , which could be substituted by other visible-light-driven semiconductors such as g- C_3N_4 , WO_3 , Co_3O_4 , Bi_2O_3 , and CdS, etc [207-214]. Constructing these semiconductors with Bi_2WO_6 would lead to the enhanced photocatalytic efficiency and extended visible light excitation as well.

2.5.3.3 Summary and outlook

As stated above, significant progresses have been achieved in the development of highly efficient bismuth tungstates as photocatalysts with applications in environmental purification and solar energy conversion. Still, there are a few challenges and difficulties to be conquered on the way for scalable applications. The most weakening point is the poor reduction ability for the photo-induced electrons lying in the relatively low conduction band of Bi_2WO_6 , which is the main obstacle for faster separation of electron-hole pairs. During the fabrication of an efficient nanosized photocatalyst, quantum size effects should be taken into consideration to obtain bismuth tungstates with a smaller size and a better performance. Last but not least, surface defects and crystal facet tailoring are anticipated to receive more attention in the future study. Combining these with computational calculations, in-depth mechanism and principles of photocatalytic process can be revealed clearly.

2.6 Conclusions and perspectives

Over the past few decades, photocatalysis has been proven to provide a feasible route to solve two worldwide critical issues of environmental pollution and energy crisis. Specifically, hydrogen evolution via the photocatalytic process from water splitting or PEC process is a promising technique, which draws enormous attention recently. The approach of photocatalytic water splitting is potentially economical and scalable to directly convert sustainable solar energy to hydrogen fuels by virtue of highly efficient photocatalysts. Herein, bismuth-based and g- C_3N_4 -based photocatalysts were systematically examined as two visible-light-responsive representatives for achieving promising photocatalytic performances. Main fabrication techniques and modification strategies have been elaborated based on the present research findings. Recent research hotspots mainly focus on the morphology and facets control, construction of heterojunction composites and introduction of surface defects such as oxygen

vacancies. Charge transfer mechanism for most of the constructed heterostructure composites follows a type-II or Z-scheme heterojunction principle for a drastically facilitated separation and migration of electron-hole pairs to enhance the photocatalytic efficiency.

Although significant achievements have been made during the past few years, there are still full of challenges to meet the realization of scalable production of as-synthesized quantum sized nanoparticles in practical applications. Future studies should attach more importance to the following aspects: (1) exploring in-depth mechanism to understand the active sites in photocatalytic reactions; (2) combining theoretical calculation with innovative approaches for the design of site-selective loading of co-catalysts and crystal facet tailoring of photocatalysts; (3) developing new strategies for exploiting efficient visible light absorption to higher wavelength (above 500 nm) to mimic the natural photosynthesis process; (4) discovering green and simple synthesis techniques without any secondary hazards; and (5) establishing robust and stable linkage between photocatalyst and cocatalyst with easy reuse and recycle. Looking into the future, it is highly anticipated that the objectives of creating a clean environment and conquering the energy crisis could be achieved with green and efficient photocatalysts.

References

- [1] O. K. Varghese, M. Paulose, T. J. LaTempa and C. A. Grimes, *Nano Lett.*, 2009, **9**, 731-737.
- [2] J. Y. Liu, B. Garg and Y. C. Ling, *Green Chem.*, 2011, **13**, 2029-2031.
- [3] A. Houas, H. Lachheb, M. Ksibi, E. Elaloui, C. Guillard, J.-M. Herrmann, *Appl. Catal.B: Environ.*, 2001, **31**, 145-157.
- [4] D.S. Bhatkhande, V.G. Pangarkar, A.A. Beenackers, *J. Chem. Technol. Biotechnol.*, 2002, **77**, 102-116.
- [5] Z. Zhang, C. Shao, X. Li, Y. Sun, M. Zhang, J. Mu, P. Zhang, Z. Guo, Y. Liu, *Nanoscale*, 2013, **5**, 606-618.
- [6] X. Wu, G. Q. Lu, L. Wang, *Energ. Environ. Sci.*, 2011, **4**, 3565-3572.
- [7] Y. Hou, Z. Wen, S. Cui, X. Guo, J. Chen, *Adv. Mater.*, 2013, **25**, 6291-6297.
- [8] M. Li, W. Luo, D. Cao, X. Zhao, Z. Li, T. Yu, Z. Zou, *Angew. Chem., Int. Ed.*, 2013, **52**, 11016-11020.
- [9] Y. Li, T. Takata, D. Cha, K. Takanabe, T. Minegishi, J. Kubota, K. Domen, *Adv. Mater.*, 2013, **25**, 125-131.
- [10] J. Zhang, F. Guo, X. Wang, *Adv. Funct. Mater.*, 2013, **23**, 3008-3014.
- [11] S. Yang, Y. Gong, J. Zhang, L. Zhan, L. Ma, Z. Fang, R. Vajtai, X. Wang, P. M. Ajayan, *Adv. Mater.*, 2013, **25**, 2452-2456.
- [12] Y. Hou, A. B. Laursen, J. Zhang, G. Zhang, Y. Zhu, X. Wang, S. Dahl, I. Chorkendorff, *Angew. Chem., Int. Ed.* 2013, **52**, 3621-3625.
- [13] S.-I. In, D. D. Vaughn, R. E. Schaak, *Angew. Chem., Int. Ed.*, 2012, **51**, 3915-3918.

- [14] Y. Li, H. Zhang, P. Liu, D. Wang, Y. Li, H. Zhao, *Small*, 2013, **9**, 3336-3344.
- [15] S. Kumar, T. Surendar, A. Baruah, V. Shanker, *J. Mater. Chem. A*, 2013, **1**, 5333-5340.
- [16] Y.-S. Jun, E. Z. Lee, X. Wang, W. H. Hong, G. D. Stucky, A. Thomas, *Adv. Funct. Mater.*, 2013, **23**, 3661-3667.
- [17] Y. Wang, R. Shi, J. Lin, Y. Zhu, *Energy Environ. Sci.*, 2011, **4**, 2922-2929.
- [18] W. Wang, Moses O. Tadé, Z. P. Shao. *Chem. Soc. Rev.*, 2015, **44**, 5371-5408.
- [19] K. L. Chopra, P. D. Paulson, V. Dutta. *Prog. Photovolt: Res. Appl.*, 2004, **12**, 69-92.
- [20] M. K. Nazeeruddin, E. Baranoff, M. Gratzel. *Solar Energ.*, 2011, **85**, 1172-1178.
- [21] A. Hagfeldt, G. Boschloo, L. Sun, L. Kloo and H. Pettersson, *Chem. Rev.*, 2010, **110**, 6595-6663.
- [22] T. Inoue, A. Fujishima, S. Konishi and K. Honda, *Nature*, 1979, **277**, 637-638.
- [23] Q. Liu, Y. Zhou, J. H. Kou, X. Y. Chen, Z. P. Tian, J. Gao, S. C. Yan and Z. G. Zou, *J. Am. Chem. Soc.*, 2010, **132**, 14385-14387.
- [24] (a) X. C. Wang, K. Maeda, A. Thomas, K. Takanabe, G. Xin, J. M. Carlsson, K. Domen and M. Antonietti, *Nat. Mater.*, 2009, **8**, 76-80; (b) G. Liu, P. Niu, C. H. Sun, S. C. Smith, Z. G. Chen, G. Q. Lu and H. M. Cheng, *J. Am. Chem. Soc.*, 2010, **132**, 1642-11648; (c) D. H. Wang, Y. W. Zhang and W. Chen, *Chem. Commun.*, 2014, **50**, 1754-1756; (d) J. H. Li, B. A. Shen, Z. H. Hong, B. Z. Lin, B. F. Gao and Y. L. Chen, *Chem. Commun.*, 2012, **48**, 12017-12019; (e) Y. D. Hou, A. B. Laursen, J. S. Zhang, G. G. Zhang, Y. S. Zhu, X. C. Wang, S. Dahl and I. Chorkendorff, *Angew. Chem., Int. Ed.*, 2013, **52**, 3621-3625; (f) J. S. Zhang, M. W. Zhang, G. G. Zhang and X. C. Wang, *ACS Catal.*, 2012, **2**, 940-948.
- [25] J. Mao, T. Y. Peng, X. H. Zhang, K. Li, L. Q. Ye and L. Zan, *Catal. Sci. & Technol.*, 2013, **3**, 1253-1260.
- [26] W. J. Ong, L. L. Tan, Y. H. Ng, S. T. Yong and S. P. Chai, *Chem Rev*, 2016, **116**, 7159-7329.
- [27] M. R. Hoffmann, S. T. Martin, W. Choi, D. W. Bahnemann, *Chem. Rev.* 1995, **95**, 69-96.
- [28] T. Sano, S. Tsutsui, K. Koike, T. Hirakawa, Y. Teramoto, N. Negishi, K. Takeuchi, *J. Mater. Chem. A*, 2013, **1**, 6489-6496.
- [29] F. Dong, Z. Zhao, T. Xiong, Z. Ni, W. Zhang, Y. Sun, W. K. Ho, *ACS Appl. Mater. Interfaces*, 2013, **5**, 11392-11401.
- [30] Q. Li, N. Zhang, Y. Yang, G. Wang, D. H. Ng, *Langmuir*, 2014, **30**, 8965-8972.
- [31] Y. Cui, Z. Ding, P. Liu, M. Antonietti, X. Fu, X. Wang, *Phys. Chem. Chem. Phys.* 2012, **14**, 1455-1462.
- [32] G. Xie, K. Zhang, B. Guo, Q. Liu, L. Fang, J. R. Gong, *Adv. Mater.*, 2013, **25**, 3820-3839.
- [33] A. Kudo, Y. Miseki, *Chem. Soc. Rev.*, 2009, **38**, 253-278.
- [34] J. Liu, Y. Liu, N. Liu, Y. Han, X. Zhang, H. Huang, Y. Lifshitz, S.-T. Lee, J. Zhong, Z. Kang, *Science*, 2015, **347**, 970-974.
- [35] G. Zhang, Z.-A. Lan, L. Lin, S. Lin, X. Wang, *Chem. Sci.*, 2016, **7**, 3062-3066.
- [36] H. Sun, G. Zhou, Y. Wang, A. Suvorova, S. Wang, *ACS Appl. Mater. Interfaces*, 2014, **6**, 16745-16754.
- [37] J. Ran, J. Zhang, J. Yu, M. Jaroniec, S. Z. Qiao, *Chem. Soc. Rev.*, 2014, **43**, 7787-7812.

- [38] M. G. Walter, E. L. Warren, J. R. McKone, S. W. Boettcher, Q. Mi, E. A. Santori, N. S. Lewis, *Chem. Rev.* 2010, **110**, 6446.
- [39] M. S. Dresselhaus, I. L. Thomas, *Nature* 2001, **414**, 332.
- [40] V. Artero, M. Chavarot-Kerlidou and M. Fontecave, *Angew. Chem., Int. Ed.*, 2011, **50**, 7238-7266.
- [41] A. Marshall, B. Borresen, G. Hagen, M. Tsyppkin and R. Tunold, *Energy*, 2007, **32**, 431-436.
- [42] M. Wang, L. Chen and L. Sun, *Energy Environ. Sci.*, 2012, **5**, 6763-6778.
- [43] V. S. Thoi, Y. Sun, J. R. Long and C. J. Chang, *Chem. Soc. Rev.*, 2013, **42**, 2388-2400.
- [44] J. A. Turner, *Science*, 1999, **285**, 687-689.
- [45] X. Zou, Y. Zhang, *Chem. Soc. Rev.*, 2015, **44**, 5148-5180.
- [46] Y.-J. Tang, Y. Wang, X.-L. Wang, S.-L. Li, W. Huang, L.-Z. Dong, C.-H. Liu, Y.-F. Li, Y.-Q. Lan, *Adv. Energy Mat.*, 2016, **6**, 1600116.
- [47] W. Fu, H. He, Z. Zhang, C. Wu, X. Wang, H. Wang, Q. Zeng, L. Sun, X. Wang, J. Zhou, Q. Fu, P. Yu, Z. Shen, C. Jin, B.I. Yakobson, Z. Liu, *Nano Energy*, 2016, **27**, 44-50.
- [48] J. Xie, H. Zhang, S. Li, R. Wang, X. Sun, M. Zhou, J. Zhou, X.W. Lou, Y. Xie, *Adv Mater*, 2013, **25**, 5807-5813.
- [49] Y. Pan, Y. Lin, Y. Chen, Y. Liu, C. Liu, *J. Mater. Chem. A*, 2016, **4**, 4745-4754.
- [50] C. Wu, Y. Yang, D. Dong, Y. Zhang, J. Li, *Small*, 2017, **13**, 1602873.
- [51] P. Xiao, X. Ge, H. Wang, Z. Liu, A. Fisher, X. Wang, *Adv. Funct. Mater.*, 2015, **25**, 1520-1526.
- [52] B. Cao, G. M. Veith, J. C. Neuefeind, R. R. Adzic, P. G. Khalifah, *J. Am. Chem. Soc.*, 2013, **135**, 19186-19192.
- [53] D.H. Youn, S. Han, J.Y. Kim, J.Y. Kim, H. Park, S.H. Choi, J.S. Lee, *ACS Nano*, 2014, **8**, 5164-5173.
- [54] Y. Ito, W. Cong, T. Fujita, Z. Tang, M. Chen, *Angew. Chem. Int. Ed.*, 2015, **54**, 213.
- [55] Y. Zheng, Y. Jiao, Y. Zhu, L. H. Li, Y. Han, Y. Chen, A. Du, M. Jaroniec, S. Z. Qiao, *Nat. Commun.* 2014, **5**, 3783.
- [56] X. Ren, L. Pang, Y. Zhang, X. Ren, H. Fan, S. Liu, *J. Mater. Chem. A*, 2015, **3**, 10693-10697.
- [57] G. Zhang, Z.A. Lan, X. Wang, *Chem Sci*, 2017, **8**, 5261-5274.
- [58] Y. Zheng, L. Lin, B. Wang and X. Wang, *Angew. Chem., Int. Ed.*, 2015, **54**, 12868-12884.
- [59] H. Zhao, Y. Dong, P. Jiang, H. Miao, G. Wang, J. Zhang, *J. Mater. Chem. A*, 2015, **3**, 7375-7381.
- [60] J. Wen, X. Li, H. Li, S. Ma, K. He, Y. Xu, Y. Fang, W. Liu, Q. Gao, *Appl. Surf. Sci.*, 2015, **358**, 204-212.
- [61] L. Lin, H. Ou, Y. Zhang, X. Wang, *ACS Catal.*, 2016, **6**, 3921-3931.
- [62] X. Zong, H. Yan, G. Wu, G. Ma, F. Wen, L. Wang, C. Li, *J. Am. Chem. Soc.*, 2008, **130**, 7176-7177.
- [63] S.N.H. Jaafar, L.J. Minggu, K. Arifin, M.B. Kassim, W.R.D. Wan, *Renew. Sust. Energ. Rev.*, 2017, **78**, 698-709.

- [64] Fujishima A, Honda K, *Nature*, 1972, **37**, 238.
- [65] L. Ye, D. Wang, S. Chen, *ACS Appl Mater Interfaces*, 2016, **8**, 5280-5289.
- [66] O. Monfort, L.-C. Pop, S. Sfaelou, T. Plecenik, T. Roch, V. Dracopoulos, E. Stathatos, G. Plesch, P. Lianos, *Chem. Eng. J.*, 2016, **286**, 91-97.
- [67] Z. Li, W. Luo, M. Zhang, J. Feng and Z. Zou, *Energy Environ. Sci.*, 2013, **6**, 347-370.
- [68] R. Li, *Chin. J. Catal.*, 2017, **38**, 5-12.
- [69] J. V. Liebig, *Ann. Pharm.* 1834, **10**, 10.
- [70] S.R.G. Naraharisetty, V.M. Kasyanenko, J. Zimmermann, M.C. Thielges, F.E. Romesberg, I.V. Rubtsov, *J. Phys. Chem. B*, 2009, **113**, 4940-4946.
- [71] H. Xiao, W. Wang, G. Liu, Z. Chen, K. Lv, J. Zhu, *Appl. Surf. Sci.*, 2015, **358** (Part A), 313-318.
- [72] Y. Zhang, J. Liu, G. Wu, W. Chen, *Nanoscale*, 2012, **4**, 5300-5303.
- [73] M. C. Liu, D. W. Jing, Z. H. Zhou and L. J. Guo, *Nat. Commun.*, 2013, **4**, 2278.
- [74] Y. Zhang, J. Liu, G. Wu, W. Chen, *Nanoscale*, 2012, **4**, 5300-5303.
- [75] F. Dong, L. Wu, Y. Sun, M. Fu, Z. Wu, S. C. Lee, *J. Mater. Chem.* 2011, **21**, 15171-15174.
- [76] J. Liu, T. Zhang, Z. Wang, G. Dawson, W. Chen, *J. Mater. Chem.* 2011, **21**, 14398-14401.
- [77] F. Dong, Z. Wang, Y. Sun, W.-K. Ho, H. Zhang, *J. Colloid Interface Sci.* 2013, **401**, 70-79.
- [78] J. Jiang, O. Lei, L. Zhu, A. Zheng, J. Zou, X. Yi, H. Tang, *Carbon*, 2014, **80**, 213-221.
- [79] X. Wang, K. Maeda, A. Thomas, K. Takanabe, G. Xin, J.M. Carlsson, K. Domen, M. Antonietti, *Nat. Mater.*, 2009, **8**, 76-80.
- [80] G. Zhang, S. Zang, X. Wang, *ACS Catal.*, 2015, **5**, 941-947.
- [81] Z. Lin, X. Wang, *Angew. Chem.*, 2013, **125**, 1779-1782.
- [82] J. Qin, S. Wang, H. Ren, Y. Hou, X. Wang, *Appl. Catal. B: Environ.*, 2015, **179**, 1-8.
- [83] G. Zhang, Z.-A. Lan, X. Wang, *ChemCatChem*, 2015, **7**, 1422-1423.
- [84] R. Kuriki, K. Sekizawa, O. Ishitani, K. Maeda (Eds.), *Angew. Chem. Int.* 2015, **54**, 2406-24-9.
- [85] Y. Cui, Z. Ding, P. Liu, M. Antonietti, X. Fu, X. Wang, *Phys. Chem. Chem. Phys.* 2012, **14**, 1455-1462.
- [86] Y. Zhang, J. Liu, G. Wu, W. Chen, *Nanoscale*, 2012, **4**, 5300-5303.
- [87] G. Zhang, J. Zhang, M. Zhang, X. Wang, *J. Mater. Chem.* 2012, **22**, 8083-8091.
- [88] J. Xu, H. Wu, X. Wang, B. Xue, Y. Li, Y. Cao, *Phys. Chem. Chem. Phys.* 2013, **15**, 4510-4517.
- [89] J. Xu, Y. Wang, Y. Zhu, *Langmuir*, 2013, **29**, 10566-10572.
- [90] L. Gu, J. Wang, Z. Zou, X. Han, *J. Hazard. Mater.*, 2014, **268C**, 216-223.
- [91] S. Kumar, T. Surendar, A. Baruah, V. Shanker, *J. Mater. Chem. A*, 2013, **1**, 5333-5340.

- [92] Y. Wang, R. Shi, J. Lin, Y. Zhu, *Energy Environ. Sci.*, 2011, **4**, 2922-2929.
- [93] C. A. Caputo, L. Wang, R. Beranek, E. Reisner, *Chem. Sci.*, 2015, **6**, 5690-5694.
- [94] J. Yu, S. Wang, J. Low, W. Xiao, *Phys. Chem. Chem. Phys.*, 2013, **15**, 16883-16890.
- [95] K. Sridharan, E. Jang, T. J. Park, *Appl. Catal., B: Environ.*, 2013, **142-143**, 718-728.
- [96] C. Han, L. Ge, C. Chen, Y. Li, X. Xiao, Y. Zhang, L. Guo, *Appl. Catal. B: Environ.*, 2014, **147**, 546-553.
- [97] H. Zhang, W. Tian, X. Guo, L. Zhou, H. Sun, M.O. Tade, S. Wang, *ACS Appl Mater Interfaces*, 2016, **8**, 35203-35212.
- [98] H. Zhang, W. Tian, L. Zhou, H. Sun, M. Tade, S. Wang, *Appl. Catal. B: Environ.*, 2018, **223**, 2-9.
- [99] D. Chen, K. Wang, T. Ren, H. Ding, Y. Zhu, *Dalton Trans.*, 2014, **43**, 13105-13114.
- [100] Y. Li, X. Wei, X. Yan, J. Cai, A. Zhou, M. Yang and K. Liu, *Phys. Chem. Chem. Phys.*, 2016, **18**, 10255-10261.
- [101] X.-j. Wang, W.-y. Yang, F.-t. Li, Y.-b. Xue, R.-h. Liu, Y.-j. Hao, *Indus. Eng. Chem. Res.*, 2013, **52**, 17140-17150.
- [102] H. J. Li, Y. Zhou, W. G. Tu, J. H. Ye, Z. G. Zou, *Adv. Funct. Mater.*, 2015, **25**, 998-1013.
- [103] J. Yu, S. Wang, J. Low, W. Xiao, *Phys Chem Chem Phys*, 2013, **15**, 16883-16890.
- [104] Y. Li, J. Wang, Y. Yang, Y. Zhang, D. He, Q. An, G. Cao, *J. Hazard. Mater.*, 2015, **292**, 79-89.
- [105] D. Lu, G. Zhang, Z. Wan, *Appl. Surf. Sci.*, 2015, **358 (Part A)**, 223-230.
- [106] K. Dai, L. Lu, C. Liang, Q. Liu, G. Zhu, *Appl. Catal., B: Environ.*, 2014, **156-157**, 331-340.
- [107] Y. Zang, L. Li, Y. Xu, Y. Zuo, G. Li, *J. Mater. Chem. A*, 2014, **2**, 15774-5780.
- [108] Y. Zhang, J. Liu, G. Wu, W. Chen, *Nanoscale*, 2012, **4**, 5300-5303.
- [109] J. Liu, J. Ke, Y. Li, B. Liu, L. Wang, H. Xiao, S. Wang, *Appl. Catal., B: Environ.*, 2018, **236**, 396-403.
- [110] J. Ding, Q. Liu, Z. Zhang, X. Liu, J. Zhao, S. Cheng, B. Zong, W.-L. Dai, *Appl. Catal., B: Environ.*, 2015, **165**, 511-518.
- [111] S. Kumar, S. T. B. Kumar, A. Baruah, V. Shanker, *J. Phys. Chem. C*, 2013, **117**, 26135-26143.
- [112] J. Chen, S. Shen, P. Guo, M. Wang, P. Wu, X. Wang, L. Guo, *Appl. Catal., B: Environ.*, 2014, **152-153**, 335-341.
- [113] L. Huang, H. Xu, R. Zhang, X. Cheng, J. Xia, Y. Xu, H. Li, *Appl. Surf. Sci.*, 2013, **283**, 25-32.
- [114] K. Sridharan, T. Kuriakose, R. Philip, T. J. Park, *Appl. Surf. Sci.* 2014, **308**, 139-147.
- [115] S. Xu, D. Li, P. Wu, *Adv. Func. Mat.*, 2015, **25**, 1127-1136.
- [116] H. Zhao, Y. Dong, P. Jiang, H. Miao, G. Wang, *J. Mater. Chem. A*, 2015, **3**, 7375-7381.
- [117] Q. Li, N. Zhang, Y. Yang, G. Wang, D.H. Ng, *Langmuir*, 2014, **30**, 8965-8972.
- [118] X. Jin, X. Fan, J. Tian, R. Cheng, M. Li, L. Zhang, *RSC Adv.*, 2016, **6**, 52611-52619.

- [119] J. Li, E. Liu, Y. Ma, X. Hu, J. Wan, L. Sun, J. Fan, *Appl. Surf. Sci.*, 2016, **364**, 694-702.
- [120] Y. Liu, H. Zhang, J. Ke, J. Zhang, W. Tian, X. Xu, X. Duan, H. Sun, M. O Tade, S. Wang, *Appl. Catal. B: Environ.*, 2018, **228**, 64-74.
- [121] Y. Liu, X. Xu, J. Zhang, H. Zhang, W. Tian, X. Li, M.O. Tade, H. Sun, S. Wang, *Appl. Catal. B: Environ.*, 2018, **239**, 334-344.
- [122] S.-W. Cao, Y.-P. Yuan, J. Fang, M.M. Shahjamali, F.Y.C. Boey, J. Barber, S.C. Joachim Loo, C. Xue, *Int J of Hydrogen Energ.*, 2013, **38**, 1258-1266.
- [123] Q. Fan, Y. Huang, C. Zhang, J. Liu, L. Piao, Y. Yu, S. Zuo, B. Li, *Catal. Today*, 2016, **264**, 250-256.
- [124] J. Zhang, Y. Wang, J. Jin, J. Zhang, Z. Lin, F. Huang, J. Yu, *ACS Appl Mater Interfaces*, 2013, **5**, 10317-10324.
- [125] L. Ge, F. Zuo, J. Liu, Q. Ma, C. Wang, D. Sun, L. Bartels, P. Feng, *J. Phys. Chem. C*, 2012, **116**, 13708-13714.
- [126] Y. Hou, Y. Zhu, Y. Xu, X. Wang, *Appl. Catal. B: Environ.*, 2014, **156-157**, 122-127.
- [127] J. Hong, Y. Wang, Y. Wang, W. Zhang and R. Xu, *ChemSusChem*, 2013, **6**, 2263-2268.
- [128] Y. Shi, S. Jiang, K. Zhou, B. Wang, B. Wang, Z. Gui, Y. Hu, R. K. K. Yuen, *RSC Adv.*, 2014, **4**, 2609-2613.
- [129] M. Liu, L. Wang, G. Lu, X. Yao, L. Guo, *Energ & Environ Sci.*, 2011, **4**, 1372.
- [130] M. Liu, D. Jing, Z. Zhou, L. Guo, *Nat Commun*, 2013, **4**, 2278.
- [131] S. Cao, Y. Chen, C.-C. Hou, X.-J. Lv and W.-F. Fu, *J. Mater. Chem. A*, 2015, **3**, 6096-6101.
- [132] X. Yue, S. Yi, R. Wang, Z. Zhang and S. Qiu, *Small*, 2017, **13**, 1603301.
- [133] D. Zeng, W.-J. Ong, Y. Chen, S.Y. Tee, C.S. Chua, D.-L. Peng, M.-Y. Han, *Part & Part Syst Char*, 2018, **35**, 1700251.
- [134] S.-S. Yi, J.-M. Yan, B.-R. Wulan, S.-J. Li, K.-H. Liu, Q. Jiang, *Appl. Catal. B: Environ.*, 2017, **200**, 477-483.
- [135] Z. Pan, Y. Zheng, F. Guo, P. Niu, X. Wang, *ChemSusChem*, 2017, **10**, 87-90.
- [136] J. Ryu, N. Jung, J. H. Jang, H.-J. Kim and S. J. Yoo, *ACS Catal.*, 2015, **5**, 4066-4074.
- [137] P. Ye, X. Liu, J. Iocozzia, Y. Yuan, L. Gu, G. Xu, Z. Lin, *J. Mater. Chem. A*, 2017, **5**, 8493-8498.
- [138] L. Bi, X. Gao, L. Zhang, D. Wang, X. Zou, T. Xie, *ChemSusChem*, 2018, **11**, 276-284.
- [139] Y. Dong, L. Kong, P. Jiang, G. Wang, N. Zhao, H. Zhang, B. Tang, *ACS Sustain. Chem. & Eng.*, 2017, **5**, 6845-6853.
- [140] Z. Huang, Z. Chen, Z. Chen, C. Lv, H. Meng, C. Zhang, *ACS Nano*, 2014, **8**, 8121-8129.
- [141] W. Zhao, Y. Liu, Z. Wei, S. Yang, H. He, C. Sun, *Appl. Catal. B: Environ.*, 2016, **185**, 242-252.
- [142] Y. Zhang, A.M. Schultz, L. Li, H. Chien, P.A. Salvador, G.S. Rohrer, *Acta Mater.* 2012, **60**, 6486-6493.
- [143] J. Ke, J. Liu, H. Sun, H. Zhang, X. Duan, P. Liang, X. Li, M.O. Tade, S. Liu, S. Wang, *Appl. Catal. B: Environ.*, 2017, **200**, 47-55.

- [144] J. Ke, X. G. Duan, S. Luo, H.Y. Zhang, H. Q. Sun, J. Liu, M. Tade, S. B. Wang, *Chem. Eng. J.*, 2017, **313**, 1447-1453.
- [145] L. Ye, L. Zan, L. Tian, T. Peng, J. Zhang, *Chem. Commun.*, 2011, **47**, 6951–6953.
- [146] C. Zhang, G. Chen, C. Li, J. Sun, C. Lv, S. Fan, W. Xing, *ACS Sustain. Chem. & Eng.*, 2016, **4**, 5936-5942.
- [147] H. Cheng, B. Huang, Z. Wang, X. Qin, X. Zhang, Y. Dai, *Chem. Eur. J.* 2011, **17**, 8039-8043.
- [148] Y. Lei, G. Wang, S. Song, W. Fan, H. Zhang, *CrystEngComm* 2009, **11**, 1857-1862.
- [149] Z. Jia, F. Wang, F. Xin, B. Zhang, *Ind. Eng. Chem. Res.*, 2011, **50**, 6688–6694.
- [150] L. Ye, Y. Su, X. Jin, H. Xie, C. Zhang, *Environ. Sci.: Nano*, 2014, **1**, 90.
- [151] K. L. Zhang, C. M. Liu, F. Q. Huang, C. Zheng and W. D. Wang, *Appl. Catal. B: Environ.*, 2006, **68**, 125-129.
- [152] S. Y. Chai, Y. J. Kim, M. H. Jung, A. K. Chakraborty, D. Jung and W. I. Lee, *J. Catal.*, 2009, **262**, 144-149.
- [153] S. Shamaila, A. K. L. Sajjad, F. Chen and J. L. Zhang, *J. Colloid Interface Sci.*, 2011, **356**, 465–472.
- [154] L. Zhang, W. Z. Wang, L. Zhou, M. Shang and S. M. Sun, *Appl. Catal. B: Environ.*, 2009, **90**, 458-462.
- [155] Y. Wang, L. Lin, F. Li, L. Chen, D. Chen, C. Yang, M. Huang, *Photochem Photobiol Sci*, 2016, **15**, 666-672.
- [156] C. Yang, F. Li, M. Zhang, T. Li, W. Cao, *J. Mol. Catal. A*, 2016, **423**, 1-11.
- [157] Y. Liu, J. Xu, L. Wang, H. Zhang, P. Xu, X. Duan, H. Sun, S. Wang, *Nanomaterials (Basel)*, 2017, **7**, 63.
- [158] G.-J. Lee, Y.-C. Zheng, J.J. Wu, *Catal. Today*, 2018, **307**, 197-204.
- [159] J. Li, L.J. Cai, J. Shang, Y. Yu, L.Z. Zhang, *Adv. Mater.*, 2016, **28**, 4059-4064.
- [160] X. F. Chang, G. Yu, J. Huang, Z. Li, S. F. Zhu, P. F. Yu, C. Cheng, S. B. Deng and G. B. Ji, *Catal. Today*, 2010, **153**, 193-199.
- [161] H. H. Gan, G. K. Zhang and Y. D. Guo, *J. Colloid Interface Sci.*, 2012, **386**, 373-380.
- [162] J. Li, G.M. Zhan, Y. Yu, L.Z. Zhang, *Nat. Commun.* 2016, **7**, 11480.
- [163] J. Jiang, K. Zhao, X.Y. Xiao, L.Z. Zhang, *J. Am. Chem. Soc.*, 2012, **134**, 4473-4476.
- [164] L. Q. Ye, K. J. Deng, F. Xu, L. H. Tian, T. Y. Peng and L. Zan, *Phys. Chem. Chem. Phys.*, 2012, **14**, 82-85.
- [165] L. Zhang, W.Z. Wang, D. Jiang, E.P. Gao, S.M. Sun, *Nano Res.* 2015, **8**, 821-831.
- [166] H. Li, J. Shang, Z.H. Ai, L.Z. Zhang, *J. Am. Chem. Soc.*, 2015, **137**, 6393-6399.
- [167] Y.H. Wu, B. Yuan, M.R. Li, W.H. Zhang, Y. Liu, C. Li, *Chem. Sci.*, 2015, **6**, 1873-1878.
- [168] M. Humayun, A. Zada, Z. Li, M. Xie, X. Zhang, Y. Qu, F. Raziq, L. Jing, *Appl. Catal. B:Environ.*, 2016, **180**, 219-226.
- [169] X. Wang, W. Mao, J. Zhang, Y. Han, C. Quan, Q. Zhang, T. Yang, J. Yang, X. Li, W. Huang, *J Colloid Interface Sci*, 2015, **448**, 17-23.
- [170] L. Gong, Z. Zhou, S. Wang, B. Wang, *Mat. Sci. in Semicon. Proc.*, 2013, **16**, 288-294.

- [171] C. Ponraj, V. G. J. Daniel, *Environ. Nanotechnol. Monit. Manage.*, 2017, **7**, 110-120.
- [172] T. Gao, Z. Chen, F. Niu, D.T. Zhou, Q.L. Huang, Y.X. Zhu, L.S. Qin, X.G. Sun, Y.X. Huang, *J. Alloy Compd.*, 2015, **648**, 564-570.
- [173] J.Z. Jiang, J. Zou, M.N. Anjum, J.C. Yan, L. Huang, Y.X. Zhang, J.F. Chen, *Solid State Sci.*, 2011, **13**, 1779-1785.
- [174] X.F. Wang, W.W. Mao, Q.X. Zhang, Q. Wang, Y.Y. Zhu, J. Zhang, T. Yang, J.P. Yang, X.A. Li, W. Huang, *J. Alloys Compd.* 2016, **677**, 288-293.
- [175] T. Xian, H. Yang, J.F. Dai, Z.Q. Wei, J.Y. Ma, W.J. Feng, *Mater. Lett.* 2011, **65**, 1573-1575.
- [176] Z.K. Liu, Y.J. Qi, C.J. Lu, *J. Mater. Sci. Mater. Electron.* 2010, **21**, 380-384.
- [177] T. Soltani, M.H. Entezari, *Chem. Eng. J.* 2013, **223**, 145-154.
- [178] T. Soltani, M.H. Entezari, *J. Mol. Catal. A: Chem.* 2013, **377**, 197-203.
- [179] L.F. Fei, J.K. Yuan, Y.M. Hu, C.Z. Wu, J.L. Wang, Y. Wang, *Cryst. Growth Des.* 2011, **11**, 1049-1053.
- [180] X.Q. Xu, Q.R. Xu, Y.J. Huang, X.X. Hu, Y.Q. Huang, G.Y. Wang, X.L. Hun, N.F. Zhuang, *J. Cryst. Growth*, 2016, **437**, 42-48.
- [181] Y.G. Wang, G. Xu, L.L. Yang, Z.H. Ren, X. Wei, W.J. Weng, P.Y. Du, G. Shen, G.R. Han, *Ceram. Intern.* 2009, **35**, 1285-1287.
- [182] L. Hou, Z.Y. Lu, Y.C. Dai, K.H. Zuo, Y.F. Xia, Z.M. Ren, J. Wu, X.G. Lu, Y.P. Zeng, X. Li, *J. Cryst. Growth*, 2016, **434**, 42-46.
- [183] F. Gao, X. Chen, K. Yin, S. Dong, Z. Ren, F. Yuan, T. Yu, Z. Zou, J.M. Liu. *Adv. Mater.*, 2007, **19**, 2889-2892.
- [184] S. Mohan, B. Subramanian, G. Sarveswaran, *J. Mater. Chem. C*, 2014, **2**, 6835-6842.
- [185] S. Mohan, B. Subramanian, I. Bhaumik, P.K. Gupta, S.N. Jaisankar, *RSC Adv.*, 2014, **4**, 16871-16878.
- [186] S. Mohan, B. Subramanian, *RSC Adv.*, 2013, **3**, 23737-23744.
- [187] G.G. Liu, T. Wang, W. Zhou, X.G. Meng, H.B. Zhang, H.M. Liu, T. Kako, J.H. Ye, *J. Mater. Chem. C.*, 2015, **3**, 7538-7542.
- [188] L.F. Fei, J.K. Yuan, Y.M. Hu, C.Z. Wu, J.L. Wang, Y. Wang, *Cryst. Growth Des.*, 2011, **11**, 1049-1053.
- [189] X. Zhang, B. Wang, X. Wang, X. Xiao, Z. Dai, Z.W. Wu, J. Zheng, F. Ren, C.Z. Jiang, *J. Am. Ceram. Soc.*, 2015, **98**, 2255-2263.
- [190] A. Zhu, Q. Zhao, X. Li, Y. Shi, *ACS Appl Mater Interfaces*, 2014, **6**, 671-679.
- [191] S. Li, Y.-H. Lin, B.-P. Zhang, J.-F. Li, C.-W. Nan, *J. Appl. Phys.*, 2009, **105**, 054310.
- [192] Y. Zhang, A.M. Schultz, P.A. Salvador, G.S. Rohrer, *J. Mater. Chem.*, 2011, **21**, 4168-4174.
- [193] Y. Liu, S. Ding, J. Xu, H. Zhang, S. Yang, X. Duan, H. Sun, S. Wang, *Chin. J. Catal.*, 2017, **38**, 1052-1062.
- [194] W.J. Tseng, R.D. Lin, *J. Colloid Interface Sci.*, 2014, **428**, 95-100.
- [195] J.H. Luo, P.A. Maggard, *Adv. Mater.*, 2006, **18**, 514-517.

- [196] S. Wang, D. Chen, F. Niu, N. Zhang, L.S. Qin, Yuexiang Huang, *J. Alloy Compd.*, 2016, 688, 399-406.
- [197] D. Chen, F. Niu, L. Qin, S. Wang, N. Zhang, Y. Huang, *Sol. Energy Mater. Sol. Cells*, 2017, **171**, 24-32.
- [198] S. Sun, W. Wang, *RSC Adv.*, 2014, **4**, 47136-47152.
- [199] A. Walsh, Y. Yan, M. N. Huda, M. M. Al-Jassim and S. H. Wei, *Chem. Mater.*, 2009, **21**, 547-551.
- [200] A. Kudo and S. Hijii, *Chem. Lett.*, 1999, **28**, 1103-1104.
- [201] H. B. Fu, C. S. Pan, W. Q. Yao and Y. F. Zhu, *J. Phys. Chem. B*, 2005, **109**, 22432-22439.
- [202] L. Zhang, W. Wang, Z. Chen, L. Zhou, H. Xu and W. Zhu, *J. Mater. Chem.*, 2007, **17**, 2526-2532.
- [203] Y. F. Zhu, S. B. Zhu, T. G. Xu, H. B. Fu and J. C. Zhao, *Environ. Sci. Technol.*, 2007, **41**, 6234-6239.
- [204] G. Colón, S. M. López, M. C. Hidalgo and J. A. Navío, *Chem. Commun.*, 2010, **46**, 4809-4811.
- [205] Y. Zhang, L. Fei, X. Jiang, C. Pan and Y. Wang, *J. Am. Ceram. Soc.*, 2011, **94**, 4157-4161.
- [206] Q. C. Xu, D. V. Wellia, Y. H. Ng, R. Amal and T. T. Y. Tan, *J. Phys. Chem. C*, 2011, **115**, 7419-7428.
- [207] M. Ge, Y. Li, L. Liu, Z. Zhou and W. Chen, *J. Phys. Chem. C*, 2011, **115**, 5220-5225.
- [208] X. Li, R. Huang, Y. Hu, Y. Chen, W. Liu, R. Yuan and Z. Li, *Inorg. Chem.*, 2012, **51**, 6245-6250.
- [209] M. S. Gui, W. D. Zhang, Q. X. Su and C. H. Chen, *J. Solid State Chem.*, 2011, **184**, 1977-1982.
- [210] Y. Wang, X. Bai, C. Pan, J. He and Y. Zhu, *J. Mater. Chem.*, 2012, **22**, 11568-11573.
- [211] L. Ge, C. Han and J. Liu, *Appl. Catal. B: Environ.*, 2011, **108-109**, 100-107.
- [212] M. S. Gui, W. D. Zhang, Y. Q. Chang and Y. X. Yu, *Chem. Eng. J.*, 2012, **197**, 283-288.
- [213] Q. Xiao, J. Zhang, C. Xiao and X. Tan, *Catal. Commun.*, 2008, **9**, 1247-1253.
- [214] L. Ge and J. Liu, *Appl. Catal., B: Environ.*, 2011, **105**, 289-297.

Every reasonable effort has been made to acknowledge the owners of copyright material. I would be pleased to hear from any copyright owner who has been omitted or incorrectly acknowledged.

**Chapter 3. Preparation of p-n Heterojunction of
BiFeO₃@TiO₂ with a Core-Shell Structure for Visible
Light Photocatalytic Degradation**

Abstract

Recently, bismuth-based visible light photocatalysts have attracted much attention due to their high photocatalytic activity and stability. Magnetically separable BiFeO₃ nanoparticles were fabricated by a citrate self-combustion method and then coated with TiO₂ by hydrolysis of Ti(OBu)₄ to form bismuth ferrite@TiO₂ core-shell nanocomposites with different mass ratios. The photocatalytic performances of the catalysts were comprehensively investigated via photocatalytic oxidation of methyl violet (MV) under both UV and visible light irradiations. The BiFeO₃@TiO₂ samples exhibited better photocatalytic performances than either BiFeO₃ or TiO₂, and the BiFeO₃@TiO₂ (mass ratio of 1:1) sample with TiO₂ shell of 50-100 nm thickness showed the highest photo-oxidation activities. The enhancement of photocatalytic activities could be ascribed to the formation of p-n junction of BiFeO₃/TiO₂ with improved charge separation efficiency as well as strong light absorption ability. The photoelectrochemical Mott-Schottky (M-S) measurements show that the charge carrier transportation and donor density of BiFeO₃ were drastically enhanced after introduction of TiO₂. The mechanism of MV degradation is mainly attributed to hydroxyl radicals and photo-generated electrons based on energy band theory and the building of an internal electrostatic field. In addition, its unique core-shell structure also favors the charge transfer at the BiFeO₃/TiO₂ interface via increasing the contact area between BiFeO₃ and TiO₂. Finally, its photocatalytic activity was further evaluated by degradation of other industrial dyes under visible light irradiations.

3.1 Introduction

Rapid consumption of fossil fuels will lead to both environmental pollution and energy crisis. One promising solution falls into the efficient utilization of solar energy, which is abundant and clean [1]. So far, it has been widely used for solar cells [2], water splitting [3-5], photocatalytic CO₂ reduction and hydrogen production [6-9], as well as removal of environmental pollutants [10-13]. Among various photocatalysts, TiO₂ has been proven to be one of the most popular catalysts in solar-energy utilization due to its high chemical stability, low toxicity, and low cost [14]. However, its wide band gap ($E_g=3.2$ eV) has limited its performance to UV light irradiation, which occupies only 4% of solar radiation. Therefore,

fabrication of efficient visible-active photocatalysts with a high visible light absorption capacity is of great importance. Another key bottleneck limiting the practical application of photocatalysis is the low quantum yield due to easy recombination of the photogenerated electron-hole pairs [15]. Therefore, various modification strategies have been developed to overcome the above barriers, for example, dye sensitization [16] and impurity doping [17, 18] as well as metal oxide coupling [19]. Among all these strategies, heterogeneous coupling has been proved to be a promising and practical way to improve photocatalytic activity by lowering the recombination rate of photo-generated carriers [20-22]. Luo et al. [23] used Fe_2O_3 and BiFeO_3 to sensitize SrTiO_3 shell to visible light and the core-shell structured nanocomposites with some magnetic materials as a core and TiO_2 as a shell are attracting research interest [24-26].

As a typical perovskite material, BiFeO_3 exhibits both ferroelectric and magnetic polarization [27-30]. Its internal polarization will usually lead to band bending and subsequently drive photogenerated carriers in opposite directions [31-33] to inhibit the recombination, thus enhancing photocatalytic efficiency. In addition, BiFeO_3 has been reported to be a typical visible-light-responsive photocatalyst due to its relatively narrow band gap ($E_g = 2.2\text{-}2.7$ eV) [34]. Zhang et al. fabricated $\text{TiO}_2/\text{BiFeO}_3$ heterostructures, suggesting that BiFeO_3 has helped weaken the recombination of photogenerated electrons and holes [35]. Li et al. had synthesized a unique $\text{BiFeO}_3@\text{TiO}_2$ core-shell structure via a hydrothermal method and this nanocomposite showed a higher photocatalytic activity than pure BiFeO_3 under visible light irradiation. It is inferred that some heterojunction structures have been formed so that the interfacial charge transfer has been promoted accordingly [36]. Zhu et al. [37] prepared $\text{BiFeO}_3/\text{TiO}_2$ nanotube array composite electrode and found that the surface modification by BiFeO_3 nanoparticles can efficiently improve the photochemical properties of TiO_2 nanotubes due to further utilization of visible light. However, the exact mechanism of $\text{BiFeO}_3@\text{TiO}_2$ core-shell nanocomposite is not clear, further experimental and theoretical studies need to be conducted to better understand the intrinsic relations between its high photocatalytic activity and interfacial structures.

In this chapter, core-shell structured $\text{BiFeO}_3@\text{TiO}_2$ nanocomposites were synthesized by a citrate self-combustion and TiO_2 coating procedure controlled by the hydrolysis of $\text{Ti}(\text{O}i\text{Bu})_4$ with different mass ratios. The crystal structure, optical properties and morphologies of the nanocomposites were systematically characterized and investigated. The photocatalytic performances of the powders were studied via photocatalytic oxidation of methyl violet (MV) under both UV and visible light irradiations. The photoelectrochemical properties of the

heterojunction system were studied to confirm the formation of p-n heterojunction interface between p-BiFeO₃ and n-TiO₂ with enhanced charge carrier transportation and donor densities. Furthermore, a series of quenching tests were conducted to investigate the mechanism for dye photodegradation. Moreover, the optimal reaction conditions were studied for MV degradation under visible light irradiations. Finally, the core-shell structured BiFeO₃@TiO₂ nanocomposites were also applied for degradation of other dye pollutants.

3.2 Experimental section

3.2.1 Materials

Methyl violet, methyl orange and congo red (AR, Tianjin Chemical Company, China) were chosen as the model pollutants.

Bismuth nitrate pentahydrate (Bi(NO₃)₃·5H₂O, 99%, AR, Xilong Chemical Corporation), iron nitrate non-anhydrate (Fe(NO₃)₃·9H₂O, 98.5%, AR, Nanjing Chemical Company), anhydrous ethanol (C₂H₅OH, 99.7%, Jiuyi Chemical Reagent Co. Ltd., China), nitric acid, ammonium hydroxide (AR, Nanjing Chemical Company), citric acid (AR, Guoyao Group Chemical Reagent Co. Ltd.), PEG (CP, Xilong Chemical Corporation), tetrabutyl orthotitanate (Ti(OBu)₄; AR, Jiangsu Yonghua Chemical Company), and acetylacetone (AR, Jiangsu Yonghua Chemical Company) were employed for fabrication of BiFeO₃@TiO₂ catalysts and deionized (DI) water were used in all the experiments. Benzoquinone (98%, p-BQ), ammonium oxalate monohydrate (AO, 99.0%) and *tert*-butyl alcohol (TBA, 99.5%) were purchased from Sigma-Aldrich.

3.2.2 Sample Preparation

BiFeO₃ nanoparticles were fabricated by a citrate-nitrate combustion method [38]. In a typical synthesis, equal moles of Fe(NO₃)₃·9H₂O and Bi(NO₃)₃·5H₂O were dissolved in 100 mL of nitric acid solution (volume ratio of nitric acid and distilled water is 1:5) adjusted its pH to about 4-5 by adding nitric acid and ammonium hydroxide, and then equal molar citric acid was added to the above solution with continually stirring for half an hour at 50 °C. Then certain amount of PEG was added to the mixed solution (0.5 g PEG equals to 2.5 mmol Bi(NO₃)₃·5H₂O) and followed by 0.5 h ultrasonication. Subsequently, this suspension was heated at 80 °C to obtain the BiFeO₃ xerogel powders. Then the xerogel powders were annealed at 500 °C for 2 h and the BiFeO₃ nanoparticles were obtained.

TiO₂ coating is controlled via hydrolysis of Ti(OBu)₄ in the presence of BiFeO₃ powders according to the published method with minor modification [36]. The starting reaction mixture comes from two solutions of A and B. Solution A contains suitable amounts of Ti(OBu)₄ (nominal mass ratios of BiFeO₃:TiO₂=1:2,1:1,2:1, respectively) and 2.5 mL acetylacetone in a solvent mixture containing 100 mL ethanol and 2 mL DI water. Solution B is composed of 100 mL ethanol mixed with 1.2 g of dispersed BiFeO₃ powder. The pH value was adjusted to about 5-6 by HNO₃. Then solution A was slowly added to solution B under vigorous stirring for 2 h in an ultrasonic bath. Subsequently, this suspension was heated under reflux at 80 °C for 2 h to improve the cross-linking of Ti(OH)₄ on the surface of BiFeO₃ nanoparticles. Then the products were washed and dried at 70 °C for 24 h. Finally, the as-prepared powders were calcined at 500 °C for 2 h in air. Meanwhile, pure TiO₂ nanoparticles were obtained by hydrolysis of the Ti(OBu)₄ solution under the same experimental conditions in the absence of BiFeO₃ powders.

3.2.3 Characterization Techniques

X-ray diffraction analysis (XRD) for crystal structure of the samples was conducted with Cu K α radiation in a X'TRA diffractometer (ARL Company, Swiss). The surface morphology and structure of the catalysts were studied via scanning electron microscopy (SEM) on QUANTA FEG 250. Transmission electron microscopy (TEM) was operated using 200CX (JEOL Company, Japan) to observe the morphologies. UV-Visible diffuse reflectance spectra (DRS) of the solid materials were performed on a SHIMADZU UV-2401 UV-Vis spectrophotometer equipped with an integrated sphere attachment. The photoluminescence (PL) spectra of the samples were measured on a Horiba Fluorolog 3-22 type fluorescence spectrophotometer.

3.2.4 Evaluation of Photocatalytic Activity

The photocatalytic activities were evaluated by the degradation of methyl violet (MV) in aqueous solutions under UV light (CEL-LAX Xe lamp 400W; cut-off filter < 400 nm; light intensity at 268 mW/cm²) and visible light (CEL-LAX Xe lamp, 400W; cut-off filter 350~680 nm; light intensity at 405 mW/cm²), the concentrations of the dye solutions were measured by a UV-vis spectrometer (Perkin-Elmer Lambda 900UV/vis/NIR, Waltham, MA). The reactor was a Pyrex top-irradiation vessel equipped with a flow of circling water to control the reaction temperature. Prior to irradiation, the suspensions were magnetically stirred in the dark for 1.0 h to ensure the establishment of an adsorption/desorption equilibrium. Quenching tests were

carried out with addition of radical scavengers of TBA, AO and BQ under the same conditions. All the measurements were performed at room temperature.

3.2.5 Photoelectrochemical Measurements

The photoelectrochemical characterization was carried out on a Zahner Zennium electrochemical workstation with a standard three-electrode system. The prepared samples were deposited onto the as-washed FTO glass (controlled area of 1 cm²) using a dip-coating method to serve as the working photoanode. Pt wire and Hg/Hg₂Cl₂/saturated KCl (SCE) were applied as the counter and reference electrodes, respectively. A Na₂SO₄ aqueous solution (0.05M, pH=6.8) was used as the electrolyte. A 300 W Xenon lamp (Philip) coupled with an AM 1.5 G filter was employed as the simulated sunlight source ($I_0=100 \text{ mW. cm}^{-2}$).

3.3 Results and Discussion

3.3.1 Morphology and Structure

XRD analysis

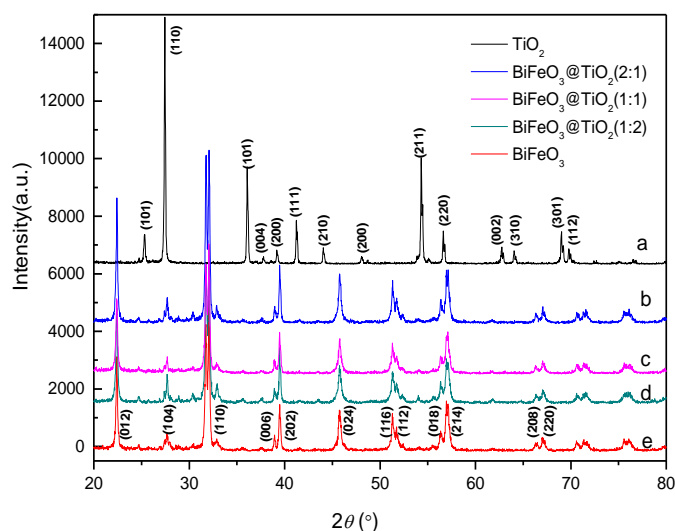


Figure 3.1. XRD patterns of the as-prepared samples.

Figure 3.1 shows the crystal structures of the as-synthesized BiFeO₃, TiO₂, and BiFeO₃@TiO₂ nanocomposites with different mass ratios. The obtained TiO₂ sample consists of both anatase ([101], [004] and [200] planes) and rutile phases ([110], [211] and [220] planes). All the diffraction peaks in Figure 3.1e should be ascribed to a perovskite phase BiFeO₃ [39] with a high diffraction intensity. Furthermore, the average crystalline size was calculated to be

39 nm from the Scherrer's formula [40], assuming that the small crystallite size is the only reason for line broadening of XRD peaks. As for the $\text{BiFeO}_3@ \text{TiO}_2$ nanocomposites with different mass ratios, they possess more typical peak characteristics of BiFeO_3 than TiO_2 nanoparticles, and no impurity peaks can be observed, which confirms that there is no impurity phase formation in the interface between TiO_2 shell and BiFeO_3 core. Additionally, with an increase in TiO_2 content, the relative intensity of the peaks of TiO_2 increased obviously, especially for rutile [110] crystal plane.

TEM analysis

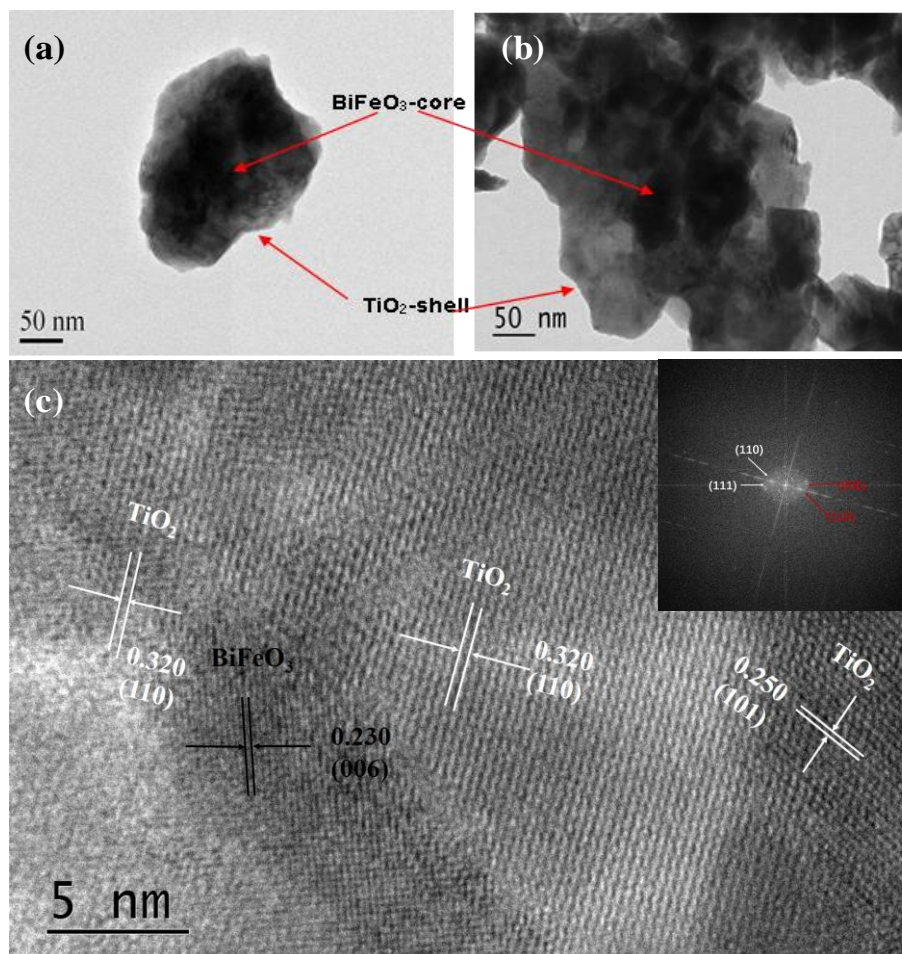


Figure 3.2. TEM (a), (b) and HRTEM(c) images of $\text{BiFeO}_3/\text{TiO}_2$ nanocomposites (mass ratio of 1:1). Inset in (c): SAED pattern. (red lines represent BiFeO_3 while white lines represent TiO_2 .)

TEM analysis has been carried out to further investigate the $\text{BiFeO}_3@ \text{TiO}_2$ interaction. The TEM photographs of $\text{BiFeO}_3@ \text{TiO}_2$ (mass ratio=1:1) are shown in Figure 3.2a and 3.2b. The contrast between dark core and gray shell can be clearly observed, indicating that the TiO_2 -coated BiFeO_3 nanoparticles have formed in a BiFeO_3 core/ TiO_2 shell structure, that is, the

BiFeO_3 particles have been encapsulated uniformly by TiO_2 nanocrystalline shells. The thickness of TiO_2 shell edge on the core BiFeO_3 particles are in the range of 50-100 nm. At higher magnification of HRTEM in Figure 3.2c, the lattice spacings for the crystalline planes were measured to be 0.230, 0.250 and 0.320 nm, corresponding to the (006) plane of perovskite BiFeO_3 , (101) and (110) planes of rutile TiO_2 , respectively, which is in good agreement with the previous report [41]. It can be further observed in the HRTEM image in Figure 3.2c that BiFeO_3 core is surrounded by the TiO_2 structures with distinct junction interface. Selective-area electron diffraction (SAED) pattern (inset of Figure 3.2c) indicates that typical crystal planes of TiO_2 correspond with XRD results of Figure 3.1a.

SEM analysis

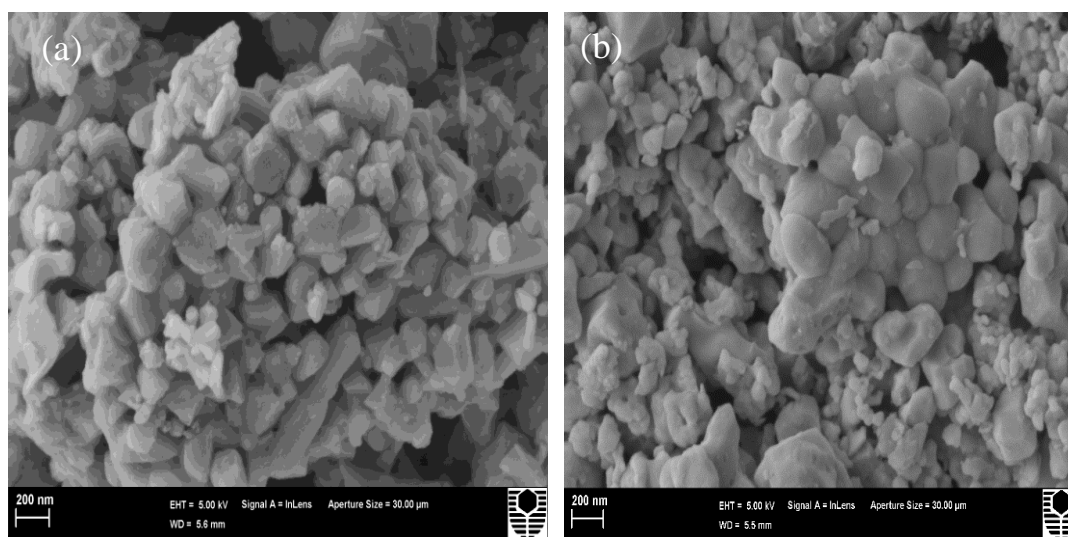


Figure 3.3. SEM image of (a) pure BiFeO_3 and (b) $\text{BiFeO}_3@ \text{TiO}_2$ (mass ratio=1:1).

The surface morphology and structure of the as-prepared BiFeO_3 and $\text{BiFeO}_3@ \text{TiO}_2$ (mass ratio=1:1) were studied by SEM analysis. Figure 3.3a reveals that pure BiFeO_3 nanoparticles show irregular shapes and uneven surface with agglomeration to some extent. As for $\text{BiFeO}_3@ \text{TiO}_2$ (mass ratio=1:1), it could be found in Figure 3.3b that BiFeO_3 particles have been coated with TiO_2 films with uniform spherical particles and relatively smooth surface.

3.3.2. Optical Properties

UV-vis analysis

UV-vis diffuse reflectance spectra of TiO_2 , BiFeO_3 and $\text{BiFeO}_3@ \text{TiO}_2$ (mass ratio=1:1) catalysts are shown in Figure 3.4. The results demonstrate that the broad band gap of pure TiO_2

shows narrow absorption edges below 385 nm. While BiFeO₃ semiconductor is a visible light responsive photocatalyst with a narrow band gap. It can be clearly seen that the TiO₂-coated BiFeO₃ nanocomposites show a red shift and increase in the optical absorption. The spectral response in the visible region of the BiFeO₃@TiO₂ is mainly attributed to the photosensitization of BiFeO₃. When the two semiconductors are in contact, electronic interaction occurs at their contact point. The internal spontaneous polarization within the ferroelectric domains of BiFeO₃ leads to band bending, which will drive photo-induced electrons and holes in opposite directions and effectively inhibit their later recombination with enhanced photocatalytic efficiency [35]. A further observation indicates that, within UV light range, pure TiO₂ shows the highest light absorption capacity, while for visible light range, BiFeO₃@TiO₂ (mass ratio=1:1) owns much more excellent photo-absorption, leading to higher production of electron-hole pairs. The optical band gap energy E_g of TiO₂, BiFeO₃ as well as BiFeO₃@TiO₂ (mass ratio=1:1) were estimated to be around 2.96, 1.68 and 1.77 eV, respectively, by extrapolating the linear portion of their UV-vis spectra to zero in Figure 3.5 (a-c), in which the plots of $(\eta h\nu)^{1/2}$ vs. $h\nu$ (Kubelka-Munk) were transformed based on UV-vis DRS spectra in Figure 3.4. TiO₂ is a blend phase of both anatase and rutile with the rutile phase predominating in the composition, its band gap is also consistent with the reported data [42].

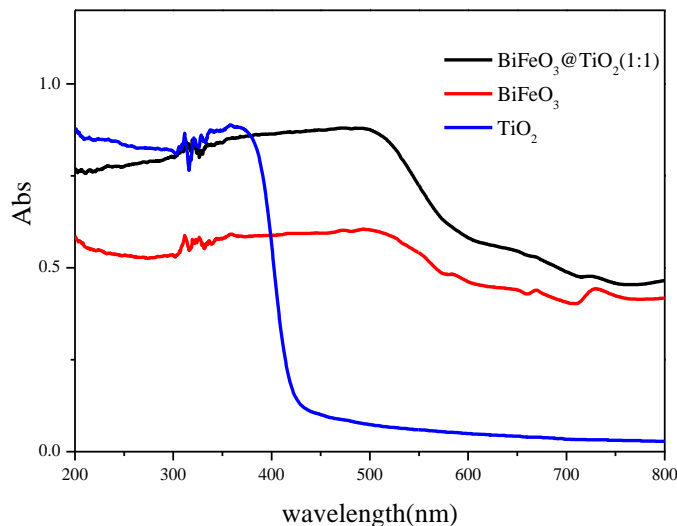


Figure 3.4. UV-vis diffuse reflectance spectra of TiO₂, BiFeO₃ and BiFeO₃@TiO₂ (mass ratio=1:1).

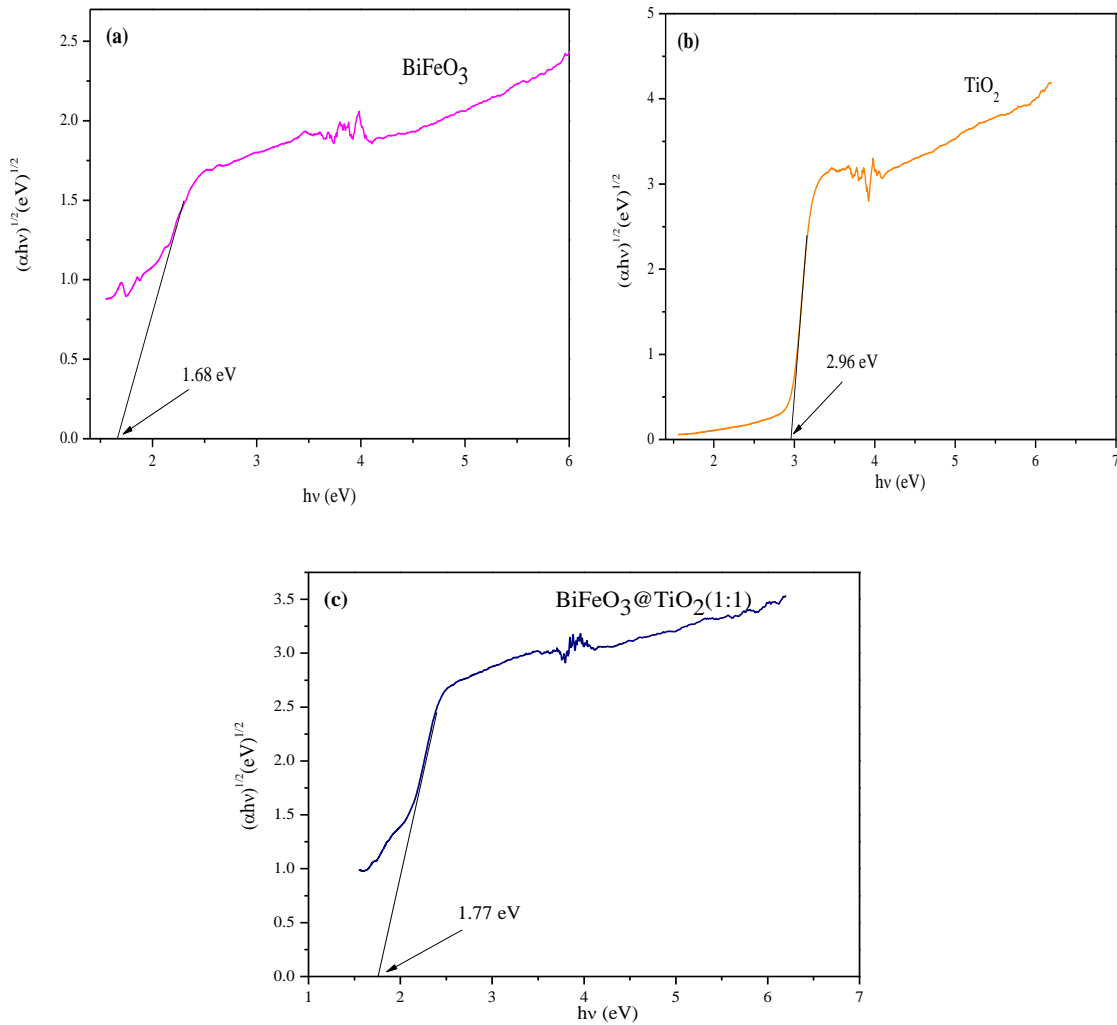


Figure 3.5. The plots of $(\alpha h\nu)^{1/2}$ versus band gap energy ($h\nu$) of (a) BiFeO_3 , (b) TiO_2 and (c) $\text{BiFeO}_3@TiO_2(1:1)$.

Photoluminescence spectrum

Figure 3.6 shows the photoluminescence spectra of TiO_2 (blue line) and BiFeO_3 nanoparticles (black line) as well as the core-shell nanocomposites of $\text{BiFeO}_3@TiO_2$ (mass ratio=1:1) (red line) measured at an excitation wavelength of 350 nm. Two main emission peaks could be found at about 519 nm and 564 nm for pure TiO_2 nanocrystallites, which should be attributed to shallow traps of oxygen vacancies (OVs) [43]. As for pure BiFeO_3 sample, the main peak was centered at about 566 nm, which could be attributed to oxygen vacancies also [44, 45]. Once BiFeO_3 is coupled with TiO_2 , the photoluminescence drops markedly, which

could be due to the efficient transfer of photo-excited holes and electrons between BiFeO₃ and TiO₂, leading to a low recombination probability for electron-hole pairs.

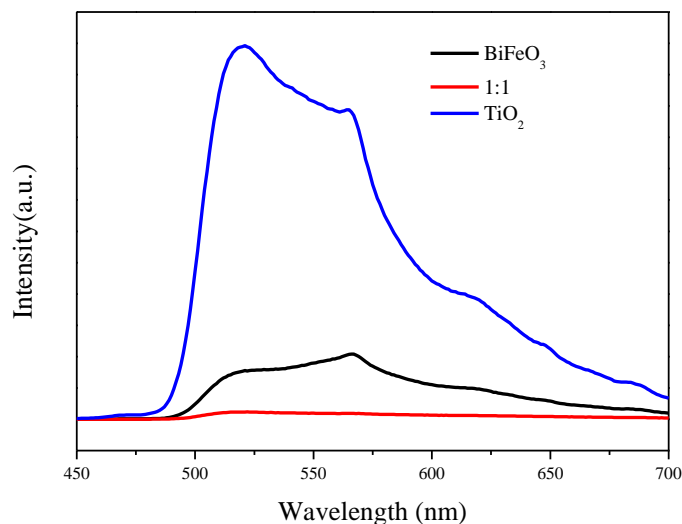


Figure 3.6. PL spectrum of TiO₂, BiFeO₃ and BiFeO₃@TiO₂ (mass ratio=1:1).

3.3.3 Photocatalytic Degradation of Methyl Violet

Comparison of Photocatalytic Activity

The photocatalytic activity of the as-synthesized samples was studied using MV as a substrate under UV and visible irradiation, respectively. All the reactions were conducted under the same conditions: initial concentration of 15 mg/L, catalyst dosage of 1 g/L, pH=5 with solution volume of 300 mL. Figure 3.7a represents the photocatalytic degradation of MV using the following catalysts: BiFeO₃@TiO₂ nanocomposites with mass ratio of 1:2, 2:1 and 1:1; pure TiO₂ as well as pure BiFeO₃ under UV irradiation condition. From Figure 3.7a, it can be seen that only 30% of MV can be removed without any catalysts. Pure TiO₂ nanoparticles show high performance in degrading MV molecules, achieving 89% removal rate after 180 min of reaction, showing that TiO₂ is a high efficient UV absorbing material with high photocatalytic activity. In addition, TiO₂ possesses the highest degradation rate among all photocatalysts including BiFeO₃@TiO₂ (with mass ratio of 1:1), especially during the first 90 min, which confirms that TiO₂ is an excellent UV light responsive photocatalyst. As for BiFeO₃@TiO₂(with mass ratio of 1:1), the initial degradation rate for MV is slower than that of pure TiO₂, but its final removal rate achieves 93%, exhibiting extremely high photocatalytic activity under UV irradiation, which is in accordance with UV-vis absorption spectra.

According to pseudo-first-order kinetics [46], the apparent first-order rate constants (k_{app}) were obtained as a comparative parameter for photocatalytic activity of different catalysts.

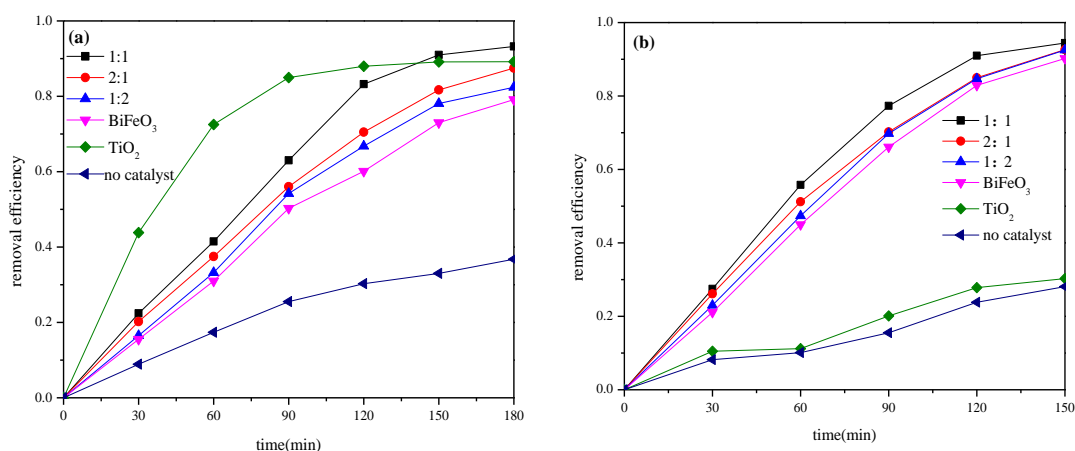


Figure 3.7. Comparison of photocatalytic activity of different samples for $C_0 = 15$ mg/L, catalyst 1g/L, pH=5 with MV under (a) UV light irradiation; (b) visible light irradiation.

The calculation results based on Figure 3.7a and Figure 3.7b are presented in Table 3.1. This result underlines that light absorption capacity of the photocatalyst stands out to be a major factor in determining its final photocatalytic performance. Apparent first-order rate constants (k_{app}) for different photocatalysts under visible light irradiation (Table 3.1) suggest TiO₂ was severely hindered due to its wide band gap, while BiFeO₃ exhibits much better performance with a narrower band gap [47].

It can be seen from Figure 3.7b that all the composite catalysts possess a higher activity than pure TiO₂ or BiFeO₃. In addition, their photocatalytic activity for degrading MV is in the following order as 1:1 > 2:1 > 1:2. BiFeO₃@TiO₂ (with a mass ratio of 1:1) demonstrated nearly 95% of MV removal after 150 min. The reason that BiFeO₃@TiO₂ (with a mass ratio of 1:1) outperforms the other ratios will be explained in later sections. As a typical perovskite material, BiFeO₃ exhibits both ferroelectric and spontaneous polarization properties that give rise to the efficient separation of charge carriers. The built internal fields in BiFeO₃ effectively inhibit the recombination of the charge carriers, leading to an enhanced photocatalytic efficiency. More specifically, the number of separated carriers will increase with the broadened space-charge width, which will enlarge the dielectric constant of BiFeO₃ [48]. The synthesized BiFeO₃ in this work is different from the catalysts in previous reports. Firstly, the band gap of the BiFeO₃ in this study was measured to be narrower (1.68 eV) than those from previous reports of 2.1-2.5 eV [49, 50]. This tuned reduction in band-gap energy could be due to the distortion induced

in Fe-O octahedral rearrangement of molecular orbitals [51]. Besides, the particle size of the catalyst presented here was much smaller with an average crystalline size of 39 nm [50]. These two features bring in larger surface areas as well as greater numbers of electrons excited from valence band, which are favorable for generation of reactive species for photodegradation [52]

Table 3.1 Photodegradation rate constants of various catalysts under UV and visible light.

Light Irradiation	Photocatalysts	K_{app} (min^{-1})	R^2
UV	TiO ₂	0.0153	0.954
	BiFeO ₃ @TiO ₂ (1:1)	0.0145	0.980
	BiFeO ₃ @TiO ₂ (2:1)	0.0108	0.989
	BiFeO ₃ @TiO ₂ (1:2)	0.0094	0.991
	BiFeO ₃	0.0083	0.992
Visible	BiFeO ₃ @TiO ₂ (1:1)	0.0184	0.984
	BiFeO ₃ @TiO ₂ (2:1)	0.0157	0.982
	BiFeO ₃ @TiO ₂ (1:2)	0.0155	0.977
	BiFeO ₃	0.0142	0.979
	TiO ₂	0.0025	0.988

Photocatalytic mechanism of BiFeO₃@TiO₂ heterojunction

The core-shell structured BiFeO₃@TiO₂ shows a much higher photocatalytic activity, which is mainly due to the suppression of charge recombination, strong photo-absorption ability as well as the unique core-shell structure geometry. The reduced electron-hole recombination rate should be ascribed to the new electronic-accumulation centers formed by electronic interaction of the two semiconductors, which will effectively separate the electrons and holes, leading to high quantum efficiency. In addition, the obvious redshift on photo-absorption spectrum is mainly induced by Fe or Bi/Ti inter-diffusion on the interfaces. Theoretically, an inner electric field with the direction from TiO₂ to BiFeO₃ will be constructed simultaneously when p-type BiFeO₃ and n-type TiO₂ come in contact and form the p-n heterojunction interface [53-54]. Driven by the inner electric field, the holes and electrons will flow towards the opposite direction, thus leading to the efficient separation of the photo-generated electrons and holes with enhanced photocatalytic activity.

To further explore the nature of the p-n heterojunction, Mott-Schottky (M-S) measurements were performed to study flat band potentials of the semiconductors [55]. The

details of testing process were depicted in experimental section. All three plots were shown in Figure 3.8(a-c). According to equation (3.1) [56], the flat band potentials at the electrode-electrolyte interface could be estimated from the plots.

$$1/C^2 = (2/\epsilon_r\epsilon_0eN_dA^2) [(V-V_{fb})-kT/e] \quad 3.1$$

When plotting $1/C^2$ (C is the specific capacity) versus V (V is the applied potential), V_{fb} (the flat band potential) could be easily found by extrapolating the linear portion of the plots to zero. It can be seen from Figure 3.8(a) and Figure 3.8(b) that, as-synthesized TiO_2 is a typical n-type semiconductor with a positive slope of the M-S plot. While for pure BiFeO_3 , a p-type semiconductor is observed with a negative slope of the plot. The flat band potentials of n-type TiO_2 and p-type BiFeO_3 were calculated from the x-axis intercept to be 0.25 V and 1.51 V vs. RHE, respectively [55]. More interestingly, once they were coupled to form a heterojunction, an inverted ‘V-shape’ appeared for Figure 3.8(c), suggesting a p-n heterojunction characteristic has been formed with two different electronic behavior [55]. Based on above equation (3.1), the density of charge carriers could be calculated from the slopes of the M-S plots. The doping densities of n-type TiO_2 , p-type BiFeO_3 and $\text{BiFeO}_3@ \text{TiO}_2$ were measured to be 9.43×10^{18} , 1.969×10^{18} and 3.773×10^{18} in the dark, respectively. The increase of doping densities indicates that charge carrier transportation of BiFeO_3 nanoparticles have been efficiently enhanced after being coated with TiO_2 films, which helped to prove the creation of p-n heterojunction interface as a sufficient space charge layer.

To further explore the mechanism of MV degradation, quenching tests were conducted to verify roles of different reactive species in Figure 3.9. As a typical $\cdot\text{O}_2^-$ scavenger, benzoquinone (BQ) was added to the reaction system. The results showed that the reaction rate did not decrease with the addition of BQ compared with the reaction without any scavenger, considering dark adsorption amount in the first 60 min. This result shows that no $\cdot\text{O}_2^-$ radicals were produced in the reaction solution. Furthermore, TBA and ammonium oxalate (AO) were adopted to trap $\cdot\text{OH}$ radicals and holes, respectively. The degradation rate of MV decreased a little with addition of 0.01 M TBA as a scavenger of $\cdot\text{OH}$ radicals, which indicates that the photocatalytic activity of $\text{BiFeO}_3@ \text{TiO}_2$ heterojunction is suppressed by the addition of TBA. However, addition of AO has promoted the faster degradation of MV with degradation rate constant increasing from 0.0195 min^{-1} to 0.0254 min^{-1} , which can be inferred that dye

degradation did not achieve via holes. According to studies with similar findings [57-59], MV degradation should be ascribed mainly to electrons and $\cdot\text{OH}$ radicals as well. The trapping of holes by AO has effectively inhibited the recombination of electrons and holes. Obviously, photo-generated electrons play the most important role in the photodegradation process.

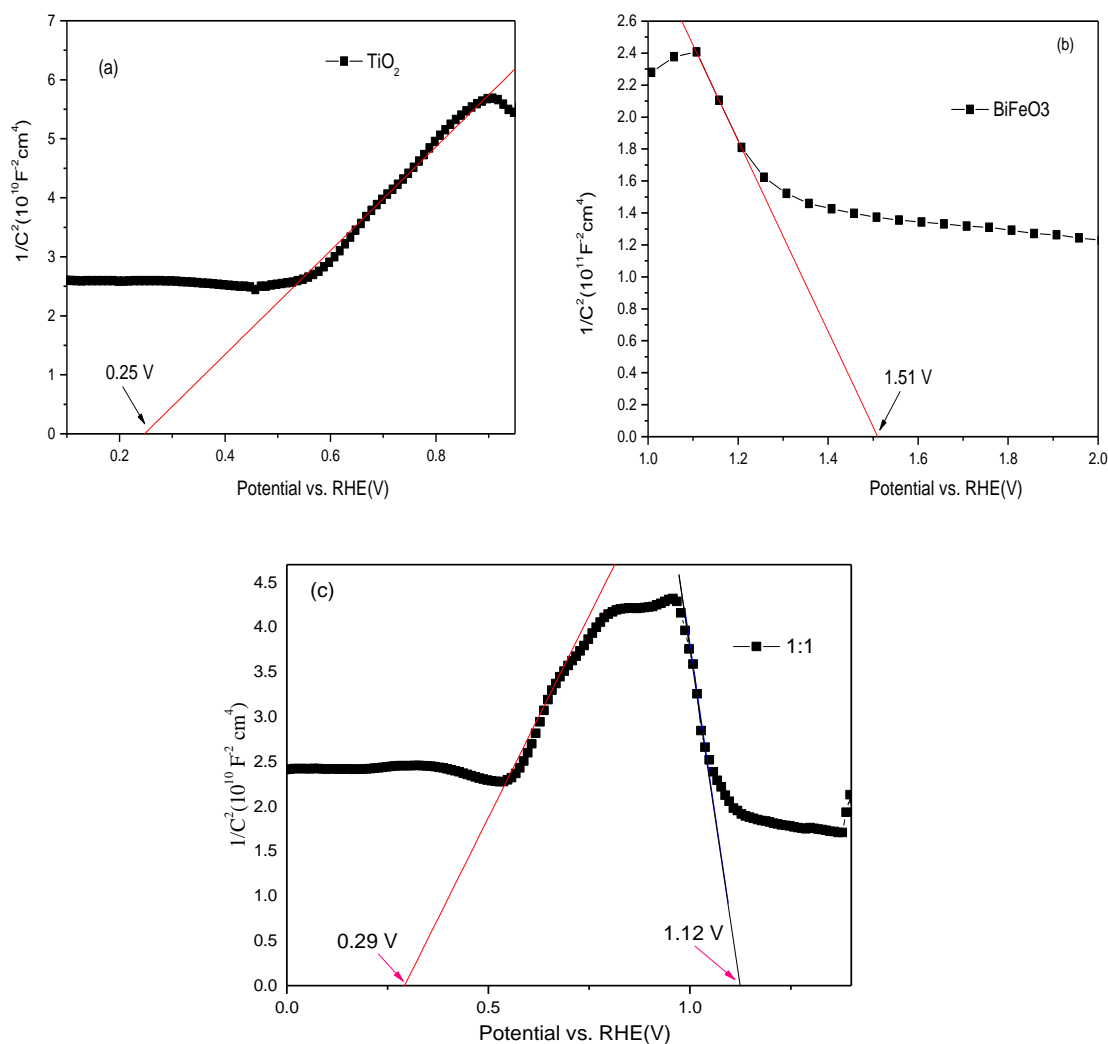


Figure 3.8. Mott-Schottky curves of (a) TiO_2 , (b) BiFeO_3 and (c) $\text{BiFeO}_3/\text{TiO}_2$ (1:1).

Based on above photo-physical as well as electrochemical characterization results, energy band structure and photocatalytic mechanism are illustrated in Figure 3.10, Assuming the gap between flat band potential and bottom edge of conduction band (top edge of valence band for p type) is negligible for n-type semiconductors [60-61], the conduction band position of TiO_2 and the valence band position of BiFeO_3 could be estimated as indicated in Figure 3.10. Given the obtained optical band gap values, it is not difficult to calculate the valence band position of TiO_2 as well as the conduction band position of BiFeO_3 . BiFeO_3 has a relatively high

conduction band due to Ti doping [23, 36], therefore, electrons can be excited from the partially filled d orbitals of Fe^{3+} to the Ti 3d orbitals of TiO_2 even under visible light. According to the energy band structure theory, electrons from the CB of BiFeO_3 will be transferred to the lower lying CB of TiO_2 to form an electron center, while the holes from the VB of TiO_2 will be transferred opposite to the VB of BiFeO_3 to form a hole center. After coupling of these two semiconductors, an internal electrical field (E_{internal}) will be formed with direction from TiO_2 to BiFeO_3 , leading to much more efficient charge separation. As illustrated in Figure 3.10, the Fermi level of n- TiO_2 is close to its conduction band, whereas for p- BiFeO_3 , the Fermi level is close to its valence band. After the formation of p-n heterojunctions between these two semiconductors, their respective valence bands as well as conduction bands will be realigned due to thermal equilibrium of their different Fermi levels [55].

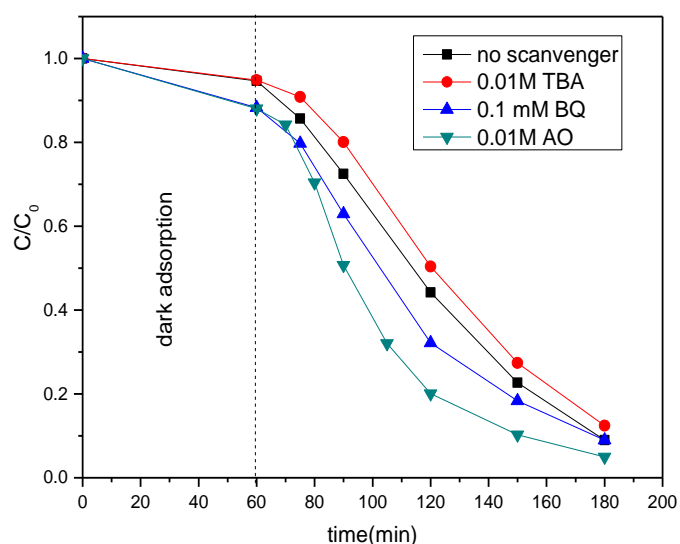


Figure 3.9. The quenching tests with addition of TBA, benzoquinone (BQ) and ammonium oxalate (AO) for $C_0=15$ mg/L, catalyst 1g/L, pH=5 with MV under visible light irradiation.

These separated e^- and h^+ can participate in the photocatalytic reactions to directly or indirectly decompose organic compounds such as MV, involving partially oxidizing H_2O to $\cdot\text{OH}$ by h^+ . Compared with the standard reduction potential of $\cdot\text{OH}/\text{H}_2\text{O}$ (2.27 eV) or $\cdot\text{OH}/\text{OH}^-$ (2.38 eV) [54], the VB potential of BiFeO_3 is only 1.51 eV vs. RHE (1.11 vs. NHE), indicating that most of h^+ on the surface of BiFeO_3 cannot oxidize H_2O or OH^- into $\cdot\text{OH}$. Fortunately, the VB potential of TiO_2 is 3.21 eV vs. RHE (2.81 vs. NHE), which is positive enough to oxidize H_2O or OH^- into $\cdot\text{OH}$ radicals. Furthermore, the reduction potential of $\text{O}_2/\cdot\text{O}_2^-$ is -0.33 eV [54],

the CB edge potential of TiO₂ (0.25 eV vs. RHE or -0.15 vs. NHE) is not negative enough to reduce O₂ to ·O₂⁻ radicals. Most of the electrons will induce dye degradation due to retardation of electron-hole recombination, which also confirms the results from quenching tests.

Therefore, the enhanced photocatalytic activities of the BiFeO₃@TiO₂ nanocomposite can be mainly ascribed to the efficient charge separation and transfer at the junction interfaces formed between the two semiconductors assisted by the inner electric field with matching band potentials of the two components. As a consequence, it effectively inhibits the recombination of the photo-generated electrons and holes, which is also in accordance with the photoluminescence testing results.

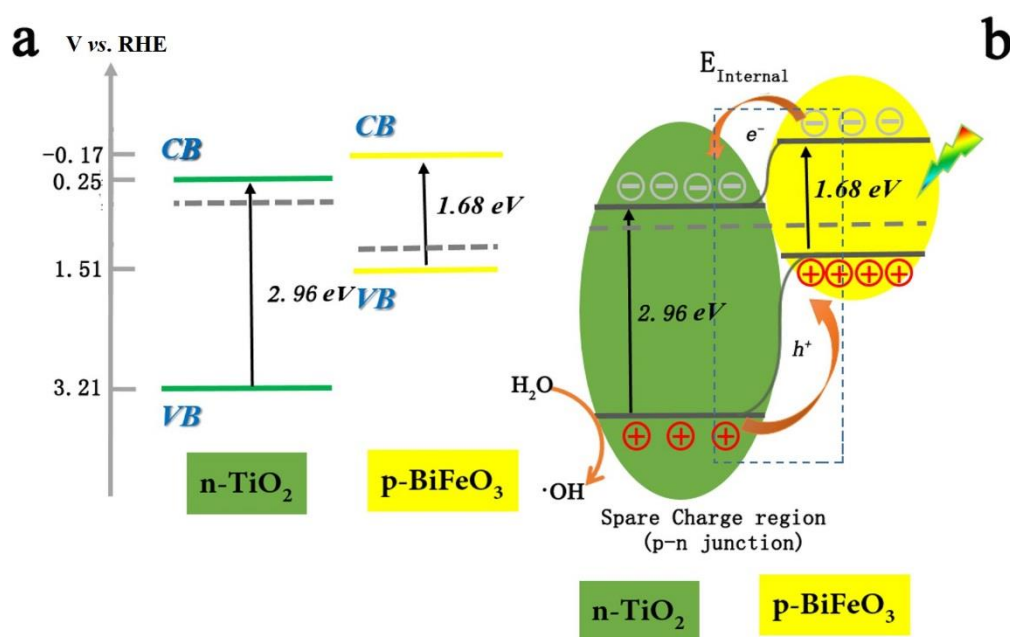


Figure 3.10. Schematic diagram of energy band structure and proposed mechanism (a) before contact; (b) after formation of TiO₂ and BiFeO₃ p-n heterojunction.

Another driving force may come from BiFeO₃ as a ferroelectric semiconductor. It has internal dipolar fields that will help facilitate the migration of electrons and holes and may reduce recombination. Electrons generated in BiFeO₃ can be transported to the surface of TiO₂, which is favored in the ferroelectric domains with a positive polarization pointed toward the surfaces and helps enhance the photocatalytic oxidation efficiency [35]. Furthermore, UV-vis diffuse reflectance spectra show that BiFeO₃@TiO₂ exhibits much higher light absorption ability with its absorption edge reaching further out in the visible region, leading to production of more electron-hole pairs, which is another factor for enhancing the photocatalytic activity of semiconductors. In addition, the enhanced contact area between semiconductors of TiO₂ and

BiFeO₃ is partly due to its unique core-shell structure, which also speeds up the charge transfer at the BiFeO₃/TiO₂ interface. It can be inferred that different thickness of TiO₂ shell can be achieved by changing the loading amount of TiO₂ in the synthesis process. It is known that BiFeO₃ is deposited with suitable amounts of TiO₂ only, both BiFeO₃ and TiO₂ can efficiently form the p-n heterojunction interface to speed up the photocatalytic process. Also, TiO₂ at too high or too low concentration is not favorable to form a BiFeO₃@TiO₂ core-shell structure with high efficient charge transfer. These theoretic analyses also coincided with the photocatalytic activity, which proves that BiFeO₃@TiO₂ (at a mass ratio of 1:1) shows the optimal photocatalytic performance. When the content of TiO₂ increases, the excess amounts of TiO₂ in the sample may also shield the photocatalyst from visible light, resulting in the decrease in the photocatalytic activity. The exact mechanism is not very clear, further experimental and theoretical work is desirable to understand the interfacial electronic structures as well as the detailed effect of TiO₂ shell loading on the formation of heterojunction interface.

Influences of reaction conditions on MV degradation

a. Effect of catalyst dosage

The effect of catalyst dosage of BiFeO₃@TiO₂ (with a mass ratio of 1:1) on MV decomposition was studied in Figure 3.11(a) with the catalyst dosage ranged from 0.5 to 1.5 g/L. The best degradation efficiency was observed when the catalyst dosage was increased to 1 g/L. Increasing amount of TiO₂ particles dispersed in the solution may weaken the penetration of the incident light, and thus lead to reduction in the percentage of dye decomposition. Note that only appropriate amount of catalyst could facilitate the generation of active species, thus speeding up the rate of dye degradation with high transparency. Based on this study, 1.0 g/L BiFeO₃@TiO₂(with a mass ratio of 1:1) was chosen as the optimal catalyst dosage under the reaction conditions.

b. Effect of Initial concentration of MV

Degradation of MV with initial concentration from 10 to 20 mg/L in the photocatalytic process is depicted in Figure 3.11(b). It can be seen that with the increase of initial dye concentration, the degradation efficiency gradually decreases. It seems that this catalyst was efficient in degrading MV polluted water with concentration less than 20 mg/L with degradation rate over 80%. Considering the practical application of the catalyst itself as well as for better decolorization efficiency, 15 mg/L was chosen as the initial concentration for MV in this study.

C. Effect of pH of initial solution

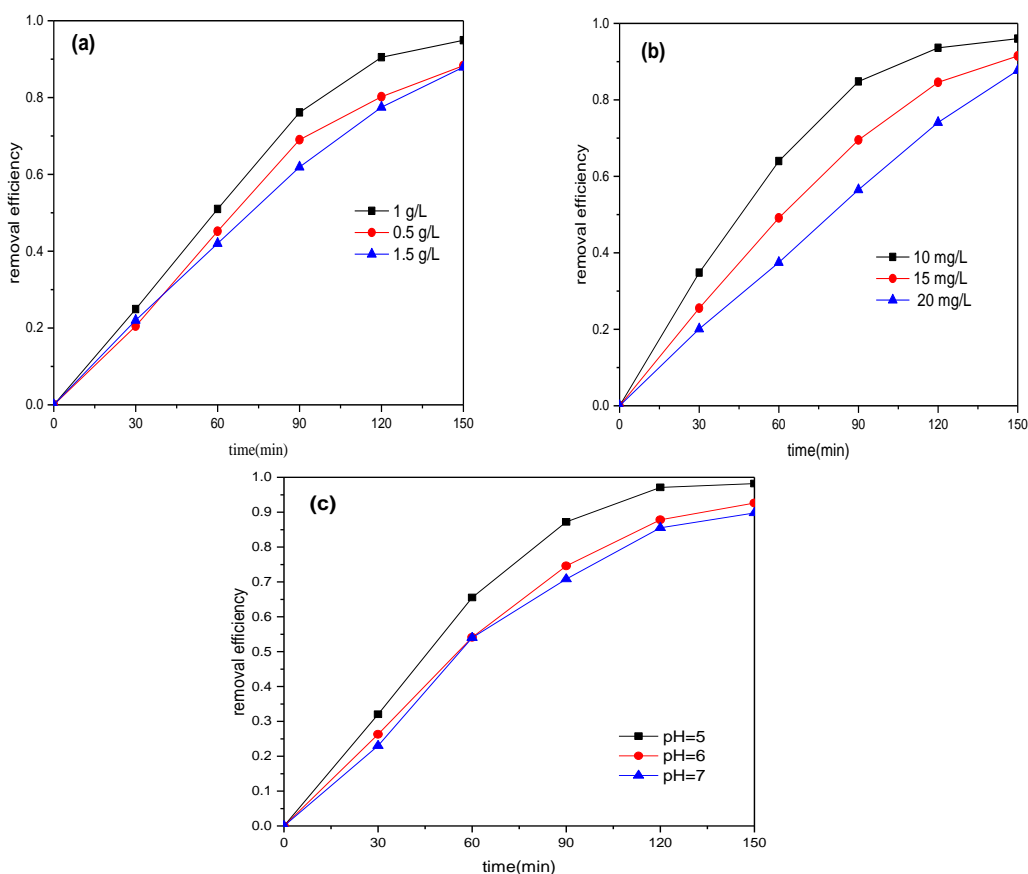


Figure 3.11. Effects of (a) different catalyst dosage, $C_0=15$ mg/L, pH=5 (b) initial concentration of MV, catalyst= 1g/L, pH=5 (c) pH of initial solution, $C_0=15$ mg/L, catalyst= 1g/L on MV degradation with $\text{BiFeO}_3@ \text{TiO}_2$ (1:1) under visible light irradiation.

The effect of MV solution pH on photocatalytic reaction is depicted in Figure 3.11(c). As the increase of pH value from 5 to 7, degradation rate of MV drops, which could be ascribed to the structure of MV as well as surface charge of the catalyst powder. Some studies [62] showed that there are certain competitive relations between phenoxide ions and hydroxyls on surface of TiO_2 particles. Other studies found that the adsorption of the substrate onto TiO_2 surface will have a direct impact on the adsorption between MV molecules and hydroxyls, leading to different photocatalytic degradation rate. In addition, isoelectric points of TiO_2 particles and BiFeO_3 ceramics in water are around pH=6.8 [63] and pH=5.1 [64], respectively. Under acidic conditions, the catalyst will easily get protonized and carry positive charges, which would accelerate the transferring process of photo-generated electrons to the surface of the catalyst. When pH value comes above the isoelectric point of the catalyst, its surface will become negatively charged, and the number of adsorption sites may decrease accordingly.

3.3.4. Photocatalytic Degradation of Other Dyes with $\text{BiFeO}_3@\text{TiO}_2$ (mass ratio 1:1)

To further prove the superior photocatalytic activity as well as practical applications for the $\text{BiFeO}_3@\text{TiO}_2$ (mass ratio 1:1), several experiments were run for other dye pollutants, methyl orange (MO) and congo red (CR), under the same reaction conditions. As can be seen in Figure 3.12, both MO and CR underwent minor changes with visible light irradiation only. $\text{BiFeO}_3@\text{TiO}_2$ (mass ratio 1:1) plays a key role in degrading the dyes. After irradiation for 150 min, the degradation rates of MO and CR reach 56% and 76%, respectively. As shown in the inset image of Figure 3.12, after each cycle of reaction, the as-synthesized $\text{BiFeO}_3@\text{TiO}_2$ nanoparticles can be attracted towards the black magnet strongly, demonstrating its excellent performance on magnetic recycling as pure BiFeO_3 . It shows that this core-shell structured $\text{BiFeO}_3@\text{TiO}_2$ (mass ratio 1:1) could be widely used in dye degradations as an optimal visible light photocatalyst. Based on the analysis of the molecular structures of the three dyes, it could be deduced that the degradation efficiency of the dyes was closely related to the azo functional groups. All the dye molecular structures are listed in Table 3.2. Methyl violet contains no azo group in its structure, while methyl orange and congo red are mono-azo and di-azo dyes,

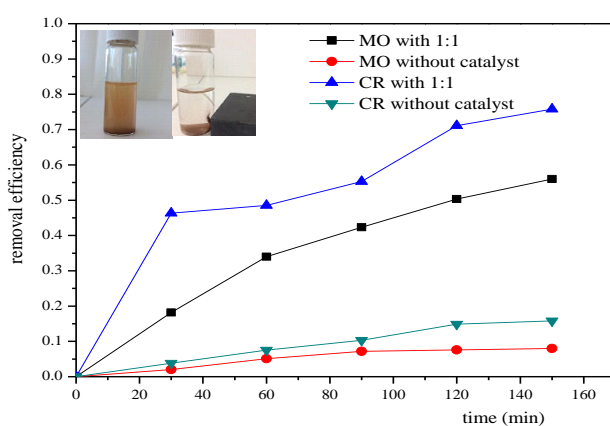
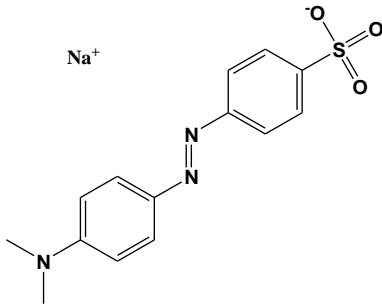
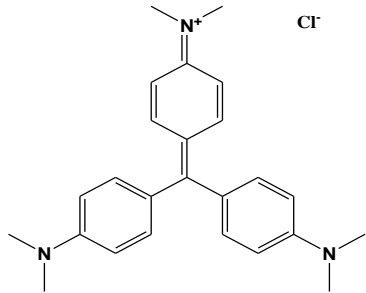
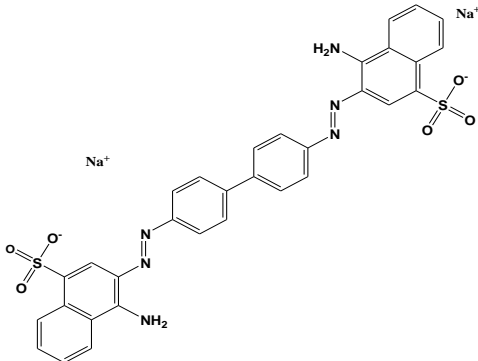


Figure 3.12. Degradation of other dyes with $\text{BiFeO}_3@\text{TiO}_2(1:1)$ for $C_0=15$ mg/L, catalyst= 1g/L, pH=5 under visible light irradiations.

respectively. The cleavage of the $\text{N}=\text{N}$ bond leads to the decoloration of the azo compounds, which is the first step of the oxidative process [65]. Besides the characteristics of the dye structures, the degradation of dyes also depend on other parameters such as pH value and catalyst concentration of the solution [66].

Table 3.2. Molecular Structures and characteristics of the dyes.

Dye	Molecular structure	Application	safety
Methyl Orange		pH indicator	mutagenic properties
Methyl Violet		purple dye for textiles	mutagen and mitotic poison
Congo Red		pH indicator	carcinogenicity & reproductive toxicity

3.4. Conclusions

A citrate self-combustion approach combined with a hydrolysis precipitation process was developed to synthesize nanocomposite photocatalyst $\text{BiFeO}_3@\text{TiO}_2$ with a core-shell structure. The $\text{BiFeO}_3@\text{TiO}_2$ heterojunction (with mass ratio of 1:1) exhibited much higher photocatalytic oxidation of different dyes (MV, MO and CO) under visible light irradiation, attributing to the efficient inhibition of charge recombination, strong light absorption ability as well as its core-shell structure geometry. The photoelectrochemical results confirm the formation of p-n heterojunction interface between p- BiFeO_3 and n- TiO_2 , which enhances the charge carrier transportation and donor density, leading to the enhancement of the quantum efficiency. The mechanism of MV degradation was attributed to hydroxyl radicals and photo-

generated electrons. The nanocomposites provide a new perspective in designing novel p-n heterojunction nanomaterials for practical application related to solar energy conversion.

References

- [1] J. Y. Liu, B. Garg and Y. C. Ling, *Green Chem.*, 2011, **13**, 2029-2031.
- [2] X. Wu, G. Q. Lu and L. Z. Wang, *Energ Environ. Sci.*, 2011, **4**, 3565-3572.
- [3] Y. Hou, Z. H. Wen, S. M. Cui, X. R. Guo and J. H. Chen, *Adv. Mater.*, 2013, **25**, 6291-6297.
- [4] M. X. Li, W. J. Luo, D. P. Cao, X. Zhao, Z. S. Li, T. Yu and Z. G. Zou, *Angew. Chem. Int. Ed.*, 2013, **52**, 11016-11020.
- [5] Y. B. Li, T. Takata, D. Cha, K. Takanabe, T. Minegishi, J. Kubota and K. Domen, *Adv. Mater.*, 2013, **25**, 125-131.
- [6] J. S. Zhang, F. S. Guo and X. C. Wang, *Adv. Funct. Mater.*, 2013, **23**, 3008-3014.
- [7] S. B. Yang, Y. J. Gong, J. S. Zhang, L. Zhan, L. L. Ma, Z. Y. Fang, R. Vajtai, X. C. Wang and P. M. Ajayan, *Adv. Mater.*, 2013, **25**, 2452-2456.
- [8] Y. D. Hou, A. B. Laursen, J. S. Zhang, G. G. Zhang, Y. S. Zhu, X. C. Wang, S. Dahl and I. Chorkendorff, *Angew. Chem. Int. Ed.*, 2013, **52**, 3621-3625.
- [9] S. I. In, D. D. Vaughn and R. E. Schaak, *Angew. Chem. Int. Ed.*, 2012, **51**, 3915-3918.
- [10] Y. B. Li, H. M. Zhang, P. R. Liu, D. Wang, Y. Li and H. J. Zhao, *Small*, 2013, **9**, 3336-3344.
- [11] S. Kumar, T. Surendar, A. Baruah and V. Shanker, *J. Mater. Chem. A*, 2013, **1**, 5333-5340.
- [12] Y. S. Jun, E. Z. Lee, X. C. Wang, W. H. Hong, G. D. Stucky and A. Thomas, *Adv. Funct. Mater.*, 2013, **23**, 3661-3667.
- [13] Y. J. Wang, R. Shi, J. Lin and Y. F. Zhu, *Energ Environ. Sci.*, 2011, **4**, 2922-2929.
- [14] X. Chen and S. S. Mao, *Chem. Rev.*, 2007, **107**, 2891-2959.
- [15] W. Choi, A. Termin, and M. R. Hoffmann, *Angew. Chem.*, 1994, **106**, 1148-1149.
- [16] V. H. Houlding and M. Graetzel, *J. Am. Chem. Soc.*, 1983, **105**, 5695-5696.
- [17] R. Asahi, T. Morikawa, T. Ohwaki, K. Aoki and Y. Taga, *Science*, 2001, **293**, 269-271.
- [18] W. Choi, A. Termin, and M. R. Hoffmann, *J. Phys. Chem.*, 1994, **98**, 13669-13679.
- [19] N. Serpone, P. Maruthamuthu, P. Pichat, E. Pelizzetti and H. Hidaka, *J. Photochem. Photobiol. A*, 1995, **85**, 247-255.
- [20] D. L. Liao, C. A. Badour and B. Q. Liao, *J. Photochem. Photobiol. A*, 2008, **194**, 11-19.
- [21] Y. H. Fan, C. H. Ma, W. G. Li and Y. S. Yin, *Mater. Sci. Semicond. Process.*, 2012, **15**, 582-585.

- [22] H. M. Yang, R. R. Shi, K. Zhang, Y. H. Hu, A. D. Tang and X. W. Li, *J. Alloy. Compd.*, 2005, **398**, 200-202.
- [23] J. H. Luo and P. A. Maggard, *Adv. Mater.*, 2006, **18**, 514-517.
- [24] M. S. Islam, Y. Kusumoto, M. Abdulla-Al-Mamun, Y. J. Horie, *Catal. Commun.*, 2011, **16**, 39-44.
- [25] W. Y. Fu, H. B. Yang, M. H. Li, L. X. Chang, Q. J. Yu, J. Xu and G. T. Zou, *Mater. Lett.*, 2006, **60**, 2723-2727.
- [26] H. M. Xiao, X. M. Liu and S. Y. Fu, *Compos. Sci. Technol.*, 2006, **66**, 2003-2008.
- [27] X. Zou, L. You, W. G. Chen, H. Ding, D. Wu, T. Wu, L. Chen and J. Wang, *Acs Nano*, 2012, **6**, 8997-9004.
- [28] R. Moubah, O. Rousseau, D. Colson, A. Artemenko, M. Maglione and M. Viret, *Adv. Funct. Mater.*, 2012, **22**, 4814-4818.
- [29] J. J. Zhang, X. D. Su, M. R. Shen, Z. H. Shen, L. J. Zhang, X. Y. Zhang, W. X. Cheng, M. Y. Cao and G. Zou, *Sci. Rep.*, 2013, **3**, 12109.
- [30] J. R. Teague, R. Gerson and W. J. James, *Solid State Commun.*, 1970, **8**, 1073-1074.
- [31] P. S. Brody, *Solid State Commun.*, 1973, **12**, 673-676.
- [32] P. S. Brody, *J. Solid State Chem.*, 1975, **12**, 193-200.
- [33] V. M. Fridkin, *Ferroelectrics*, 1984, **53**, 169-187.
- [34] S. Li, Y. H. Lin, B. P. Zhang, Y. Wang and C. W. Nan, *J. Phys. Chem. C*, 2010, **114**, 2903-2908.
- [35] Y. L. Zhang, A. M. Schultz, P. A. Salvador and G. S. Rohrer, *J. Mater. Chem.*, 2011, **21**, 4168-4174.
- [36] S. Li, Y. H. Lin, B. P. Zhang, J. F. Li and C. W. Nan, *J. Appl. Phys.*, 2009, **105**, 054310.
- [37] A. S. Zhu, Q. D. Zhao, X. Y. Li and Y. Shi, *ACS Appl. Mater. Interfaces*, 2014, **6**, 671-679.
- [38] Y. B. Yao, B. Ploss, C. L. Mak and K. H. Wong, *Appl. phys. A Mater.*, 2010, **99**, 211-216.
- [39] JCPDS Card No. 86-1518.
- [40] G. Arya, and N. Negi, *J. Phys. D: Appl. Phys.*, 2013, **46**, p. 095004.
- [41] L. X. Gong, Z. F. Zhou, S. M. Wang and B. Wang, *Mater. Sci. Semicond. Process*, 2013, **16**, 288-294.
- [42] D. Reyes-Coronado, G. Rodriguez-Gattorno, M. E. Espinosa-Pesqueira, C. Cab, R. de Coss and G. Oskam, *Nanotechnology*, 2008, **19**, 145605- 145614.
- [43] Y. Lei, L. D. Zhang, G. W. Meng, G. H. Li, X. Y. Zhang, C. H. Liang, W. Chen and S. X. Wang, *Appl. Phys. Lett.*, 2001, **78**, 1125-1127.
- [44] A. J. Hauser, J. Zhang, L. Mier, R. A. Ricciardo, P. M. Woodward, T. L. Gustafson, L. J. Brillson, F. Y.

- Yang, *Appl. Phys. Lett.*, 2008, **92**, 222901/1-222901/3.
- [45] R. Moubah, G. Schmerber, O. Rousseau, D. Colson and M. Viret, *Appl. Phys. Express.*, 2012, **5**, 035802/1-035802/3.
- [46] Y. Z. Liu, S. G. Yang, J. Hong and C. Sun, *J. Hazard. Mater.*, 2007, **142**, 208-215.
- [47] F. Gao, Y. Yuan, K. F. Wang, X. Y. Chen, F. Chen and J. M. Liu, *Appl. Phys. Lett.*, 2006, **89**, 102506/1-102506/3.
- [48] S. Irfan, Y. Shen, S. Rizwan, H.C. Wang, S.B. Khan and C.W. Nan, *J. Am. Ceram. Soc.*, 2017, **100**, 31-40.
- [49] F. Gao, X. Y. Chen, K.B. Yin, S. Dong, Z. F. Ren, F. Yuan, T. Yu, Z.G. Zou and J. M. Liu, *Adv. Mater.*, 2007, **19**, 2889-2892.
- [50] M. Arora, P. C. Sati, S. Chauhan, S. Chhoker, A.K. Panwar and M. Kumar, *J. Supercond. Nov. Magn.*, 2013, **26**, 443-448.
- [51] C. Hengky, X. Moya, N.D. Mathur and S. Dunn, *RSC Adv.*, 2012, **2**, 11843-11849.
- [52] X. Wang, Y. Lin, Z. C. Zhang and J. Y. Bian, *J. Sol-Gel Sci. Technol.*, 2011, **60**, 1-5.
- [53] W. Zhao, Y. Liu, Z. B. Wei, S. G. Yang, H. He and C. Sun, *Appl. Catal. B: Environ.*, 2016, **185**, 242-252.
- [54] J. Ke, J. Liu, H. Q. Sun, H. Y. Zhang, X. G. Duan, P. Liang, X. Y. Li, M. O. Tade, S. M. Liu and S. B. Wang, *Appl. Catal. B: Environ.*, 2017, **200**, 47-55.
- [55] A. A. Dubale, W. N. Su, A. G. Tamirat, C. J. Pan, B. A. Aragaw, H. M. Chen, C. H. Chen, B. J. Hwang, *J. Mater. Chem. A*, 2014, **2**, 18383-18397.
- [56] P. Liang, C. Zhang, H. Q. Sun, S. M. Liu, M. O. Tade and S. B. Wang, *RSC Adv.*, 2016, **6**, 95903-95909.
- [57] M. Samadi, H. A. Shivaee, A. Pourjavadi and A. Z. Moshfegh, *Appl. Catal. A*, 2013, **466**, 153-160.
- [58] Y. Wang and P. Zhang, *J. Hazard. Mater.*, 2011, **192**, 1869-1875.
- [59] S. J. Hong, S. Lee, J. S. Jang and J. S. Lee, *Energ Environ. Sci.*, 2011, **4**, 1781-1787.
- [60] J. Premkumar, *Chem. Mater.*, 2004, **16**, 3980-3981.
- [61] T. Y. Wei and C. C. Wan, *J. Photochem. Photobiol. A*, 1992, **69**, 241-249.
- [62] C. C. Chen and C. S. Lu, *Environ. Sci. Technol.*, 2007, **41**, 4389-4396.
- [63] J. Zhang, M. A. Gondal, W. Wei, T. N. Zhang, Q. Y. Xu and K. Shen, *J. Alloys Compd.*, 2012, **530**, 107-110.
- [64] N.J. Bejarano-Perez, and M.F. Suarez-Herrera, *Ultrason. Sonochem.*, 2007, **14**, 589-95.

[65] I.K. Konstantinou, and T.A. Albanis, *Appl. Catal. B: Environ.*, 2004, **49**, 1-14.

Every reasonable effort has been made to acknowledge the owners of copyright material. I would be pleased to hear from any copyright owner who has been omitted or incorrectly acknowledged.

**Chapter 4. Three-Dimensional BiOI/BiOX (X = Cl or Br)
Nanohybrids for Enhanced Visible-Light Photocatalytic
Activity**

Abstract

As typical bismuth-based complex oxides, three-dimensional flower-like BiOI/BiOX (X = Br or Cl) hybrids were synthesized via a facile one-pot solvothermal approach. With systematic characterizations by X-ray diffraction (XRD), scanning electron microscopy (SEM), transmission electron microscopy (TEM), the Brunauer-Emmett-Teller (BET) specific surface area, X-ray photoelectron spectroscopy (XPS), and UV–vis diffuse reflectance spectra (DRS), the BiOI/BiOCl composites showed a fluffy and porous 3-D architecture with a large specific surface area (SSA) and high capability for light absorption. Among all the BiOX (X = Cl, Br, I) and BiOI/BiOX (X = Cl or Br) composites, BiOI/BiOCl stands out as the most efficient photocatalyst under both visible light and UV light irradiations for methyl orange (MO) oxidation. The reaction rate of MO degradation on BiOI/BiOCl was 2.1 times higher than that on pure BiOI under visible light. Moreover, BiOI/BiOCl exhibited enhanced water oxidation efficiency for O₂ evolution, which was 1.5 times higher than BiOI. The enhancement of photocatalytic activity could be attributed to the formation of a heterojunction between BiOI and BiOCl, with a nanoporous structure, a larger SSA, and a stronger light absorbance capacity especially in the visible-light region. The in situ electron paramagnetic resonance (EPR) revealed that BiOI/BiOCl composites could effectively evolve superoxide radicals and hydroxyl radicals for photodegradation, and the superoxide radicals are the dominant reactive species. The superb photocatalytic activity of BiOI/BiOCl could be utilized for the degradation of various industrial dyes under natural sunlight irradiation which is of high significance for the remediation of industrial wastewater in the future.

4.1 Introduction

In the past few decades, intensive research has been focused on the efficient utilization of solar energy as a promising and sustainable strategy to address the energy crisis and environmental contamination. Solar energy is a natural resource which is inexhaustible as well as environmentally-friendly [1–3]. Among the solar energy conversion and applications, such as photocatalytic decomposition of organic pollutants [4–6], solar cells [7], water splitting [8–10], as well as catalytic CO₂ reduction [11–13], the rational development of efficient

semiconductors and construction of optimal heterojunction nanocomposites to enhance the utilization of solar energy have turned out to be the two most effective techniques. Among the popular photocatalysts, TiO_2 has been widely investigated due to its superb photocatalytic activity, good chemical stability, relatively low toxicity, and cost [14]. However, TiO_2 can only absorb and respond to ultraviolet light due to its wide band gap (3.2 eV), which severely limits its practical applications in solar energy conversion. Recently, photocatalysts containing bismuth with high visible-light-induced activity have attracted considerable attention in designing novel photocatalysts, such as BiFeO_3 [15], BiVO_4 [16], Bi_2MoO_6 [17], Bi_2WO_6 [18], etc. Bismuth oxyhalides, BiOX ($X = \text{Cl}, \text{Br}, \text{I}$), have shown remarkable photocatalytic activity due to their unique structure and physicochemical properties [19–22]. The bismuth oxyhalides comprise of a layered structure of $[\text{Bi}_2\text{O}_2]$ slabs interleaved by double slabs of halogen atoms with an internal static electric field, which could facilitate the rapid separation of photo-generated electrons and holes. Among these new family members, BiOI shows the highest absorption capacity for visible light irradiation due to its relatively narrow band gap. However, the photocatalytic degradation of organics on pure BiOI is still unsatisfactory due to the high recombination rate of the photo-generated carriers, which constrains the photocatalytic activity for solar energy utilization.

Heterogeneous coupling has been adopted as a fantastic strategy to improve photocatalytic activity by minimizing the recombination rate of photogenerated carriers. Meanwhile, a nanoporous structure with a large surface area is especially attractive for heterogeneous photocatalysis due to the multiple scattering effects [23]. Three-dimensional microstructure hybrids fabricated from nanoscaled building blocks may further contribute to the enhancement of catalytic performance by providing abundant transport paths for the reactants to arrive at the active sites. For the hybrid catalysts constructed with a heterojunction, both of the semiconductors would adjust their bandgaps to obtain the composite valence band (VB) and conduction band (CB), which could be tuned to be more suitable for visible light excitation. However, the intrinsic mechanism of the photocatalytic process over BiOI/BiOX ($X = \text{Cl}$ or Br) composites is still uncertain.

In this chapter, a simple one-pot solvothermal process was adopted to synthesize 3D BiOI/BiOX ($X = \text{Cl}$ or Br) flower-like microspheres with a high specific surface area and superior visible light photo-absorption ability. The performances of the BiOI/BiOX ($X = \text{Cl}$ or Br) composites and pure BiOX ($X = \text{Cl}, \text{Br}, \text{I}$) were evaluated by photo-oxidation of methyl orange (MO) under both UV and visible light irradiations. The BiOI/BiOCl composites also demonstrated an excellent activity for water oxidation under simulated solar light irradiations.

In addition, the information about the composite band structure and the reactive oxygen species in the photocatalytic process was unveiled for an in-depth mechanistic study. The composite was finally assessed for practical remediation of versatile industrial dyes under natural sunlight irradiations.

4.2 Experimental Section

4.2.1 Materials

Bismuth (III) nitrate pentahydrate ($\text{Bi}(\text{NO}_3)_3 \cdot 5\text{H}_2\text{O}$) was purchased from Sinopharm Chemical Reagent Co. Ltd, Shanghai, China. Ethylene glycol ($\text{HOCH}_2\text{CH}_2\text{OH}$), potassium iodide (KI), sodium bromide (NaBr), potassium chloride (KCl), and ethanol ($\text{CH}_3\text{CH}_2\text{OH}$, absolute) were obtained from Nanjing Chemical Reagent Co. Ltd, Nanjing, China. Methyl orange and methyl violet were purchased from Shanghai Sansi Co. Ltd, Shanghai, China. Direct black 38 was purchased from Tokyo Chemical Industry Co. Ltd. 5,5-dimethyl-1-pyrroline N-oxide (DMPO, $\geq 98.0\%$) was purchased from Sapphire Bioscience Pty. Ltd., (Redfern, NSW, Australia). Silver nitrate ($\geq 99.0\%$) and lanthanum (III) oxide ($\geq 99.9\%$) were purchased from Sigma-Aldrich (Castle Hill, NSW, Australia). All the chemicals are analytical reagents and were received without further treatment.

4.2.2 Synthesis of BiOX ($X = \text{Cl}, \text{Br}, \text{I}$)

The BiOX was synthesized via a simple solvothermal method. More specifically, 3.88 g $\text{Bi}(\text{NO}_3)_3 \cdot 5\text{H}_2\text{O}$ and 1.33 g KI were dissolved in a 40 mL ethylene glycol solution, separately. Then the $\text{Bi}(\text{NO}_3)_3$ solution was dropped into the KI solution gradually with vigorous stirring for 5 min using a magnetic stirrer on a hotplate to form a homogeneous mixture. Then the solution was transferred to a 120 mL Teflon-lined autoclave, sealed, and treated in an oven at 160 °C for 12 h and cooled down naturally. The precipitate was filtered and washed with deionized water and ethanol three times each, and finally dried in the oven at 60 °C for 24 h. BiOCl and BiOBr were prepared following the same protocol based on a mole ratio of $\text{Bi}(\text{NO}_3)_3 \cdot 5\text{H}_2\text{O}:\text{NaBr}(\text{KCl}) = 1:1$.

4.2.3 Synthesis of BiOI/BiOX ($X = \text{Cl}, \text{Br}$)

The BiOI/BiOCl and BiOI/BiOBr composites were prepared via a similar procedure according to a previous report with minor modifications [24]. In a typical procedure, 1.96 g $\text{Bi}(\text{NO}_3)_3 \cdot 5\text{H}_2\text{O}$ was dissolved in 80 mL ethylene glycol with vigorous stirring for 30 min to form a transparent solution. Then, 0.6 g KI and 0.03 g KCl were added into the above solution and continued to stir for another 2 h. Afterward, the mixed solution was transferred to a 120 mL Teflon-lined autoclave, sealed, and treated in an oven at 160 °C for 12 h and cooled down naturally. The precipitate was filtered and washed with deionized water and ethanol three times each, and finally dried in the oven at 60 °C for 24 h. Thus, BiOI/BiOCl was obtained. The synthesis of BiOI/BiOBr followed the same procedure based on a molar ratio of KI:NaBr = 9:1.

4.2.4 Characterization Techniques

The crystal structures of the as-synthesized catalysts were characterized via X-ray diffraction analysis (XRD) with Cu $K\alpha$ radiation in a X'TRA diffractometer (ARL Company, Swiss, Basel, Switzerland). Scanning electron microscopy (SEM, X650, Hitachi Company, Tokyo, Japan) and transmission electron microscopy (TEM, 200CX, JEOL Company, Tokyo, Japan) were employed to study the surface morphology and structure of the catalysts. The specific surface areas were measured using N_2 adsorption/desorption isotherms on a Micromeritics ASAP 2020, and the pore size distribution was calculated from the desorption isotherm. UV-visible diffuse reflectance spectra (DRS) were performed on a Shimadzu UV-2401 UV-Vis spectrophotometer equipped with an integrated sphere attachment. X-ray photoelectron spectroscopy with Al $K\alpha$ X-ray radiation (PHI 5000 VersaProbe, ULVAC-PHI, Kanagawa, Japan) was adopted to investigate the surface elemental composition. Electron paramagnetic resonance (EPR) was performed on a Bruker EMX plus spectrometer (Bruker Company, Rheinstetten, Germany) under the conditions of modulation amplitude (8 G), modulation frequency (100 kHz), microwave frequency (9.48 GHz), and non-saturating microwave power (1.02 mW). DMPO was utilized as a chemical probe to capture the produced radicals from photocatalysis. In the EPR tests, 0.2 g/L BiOI/BiOCl was first mixed with a 40 μL DMPO solution. Then the mixed solution was extracted via the capillary and tested under both dark and simulated solar light irradiation after 5 min. The superoxide radicals ($\cdot\text{O}_2^-$) were captured by changing the solution to methanol to quench the hydroxyl radicals.

4.2.5 Evaluation of the Photocatalysts

The photocatalytic activities were evaluated by the degradation of organic dyes in aqueous solution under UV light (CEL-LAX Xe lamp 300 W; cut-off filter <400 nm) with a light intensity of 268 mW/cm² and visible light (CEL-LAX Xe lamp, 300 W; cut-off filter 350–680 nm) with a light intensity of 405 mW/cm². Specifically, 0.05 g of photocatalyst was suspended into 250 mL MO solution (20 mg/L). Prior to irradiation, the suspensions were magnetically stirred in the dark for 30 min to ensure the establishment of an adsorption/desorption equilibrium. During the photocatalytic process, 3 mL of the reaction solution was extracted every 30 min and centrifuged at 13,000 rpm for 15 min to remove the particles. Then the concentration of the MO solution was measured by a UV-Vis spectrometer (Perkin-Elmer Lambda 900UV/Vis/NIR, Waltham, MA, USA) at the maximum absorbance wavelength of 465 nm.

The catalysts were also evaluated in a water oxidation process for oxygen evolution. The reaction was processed in a black jacket reactor with a 300 W Xenon lamp as the light source. Silver nitrate was selected as the electron scavenger. In a typical procedure, 0.1 g of catalyst was added to 200 mL of solution including AgNO₃ (0.03 M) and La₂O₃ (0.2 g). The suspensions were mixed under vigorous stirring for 30 min in the dark and degassed to remove the air prior to irradiation. The produced O₂ was in situ analyzed by gas chromatography (Agilent 490 Micro GC, NSW, Australia) equipped with a thermal conductive (TCD) detector (Agilent 490 Micro GC, NSW, Australia).

4.3 Results and Discussion

4.3.1 Morphology and Structure

Figure 4.1 shows the phase structures of the as-synthesized samples of pure BiOX (X = Cl, Br and I) as well as BiOI/BiOX (X = Cl and Br) composites. The diffraction peaks of a, b, and e in Figure 4.1 can be fully indexed to the tetragonal BiOBr phase (JCPDS card No. 78-0348), tetragonal BiOCl phase (JCPDS card No. 73-2060), and tetragonal BiOI phase (JCPDS card No. 73-2062) with no impurities. The BiOI/BiOCl and BiOI/BiOBr composites exhibit the characteristic peaks of pure BiOI whereas no obvious peaks for BiOCl and BiOBr were discovered, possibly due to their low loading amount. Comparing the profiles of d with e, it can be seen that all diffraction peaks slightly shift to the higher angles, corresponding to a smaller spacing distance between the different planes. The same phenomenon could be

observed for BiOI/BiOBr. Moreover, the diffraction peaks of the composites are broader than the corresponding peaks of pure BiOI, indicating that the crystallite sizes of BiOI/BiOCl and BiOI/BiOBr become smaller during heterogeneous growth based on Scherrer's formula $D=0.9\lambda/\beta\cos\theta$ (D - crystallite size; λ -X ray wavelength; θ -diffraction angle; β - the full width at half maximum intensity of the peak), which is in good accordance with the literature [25–27].

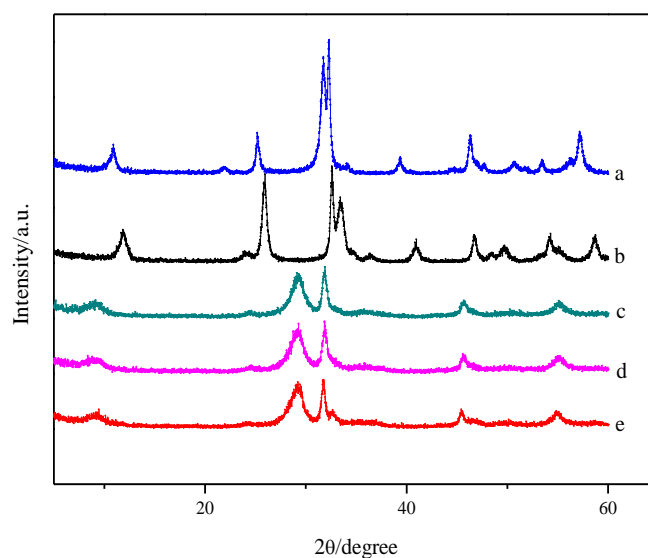


Figure 4.1. X-ray diffraction (XRD) patterns of (a) BiOBr, (b) BiOCl, (c) BiOI/BiOBr, (d) BiOI/BiOCl, and (e) BiOI.

SEM images of the photocatalysts are presented in Figure 4.2. All the BiOX samples present as microspheres with different diameters, morphologies, and microstructures. Among them, BiOBr shows the largest particle size with a diameter between 1.5 and 2.1 μm , which is larger than that of BiOCl (0.4-1 μm) and BiOI (0.1-0.5 μm). High-magnification images in Figure 4.2b,d,f indicate that all the microspheres are composed of nanoplates with a thickness of 25 nm, which were aggregated at the core compactly. Moreover, the nanoplates in BiOI in Figure 4.2b were closely packed together to form irregular microspheres with no obvious gaps. For BiOCl, the microsphere particles are presented with regular shapes with multilayers in Figure 4.2d. The microspheres of BiOBr in Figure 4.2f are constructed of diverse diameters with regular shapes and large gaps. As seen from Figure 4.2g-j, the nanocomposites of BiOI/BiOX ($X = \text{Br}, \text{I}$) with diameters around 2-8 μm exhibit three-dimensional micro/nano-architectures aggregated by monolithic or monomeric particles, which are larger than the pure BiOX ($X = \text{Cl}, \text{Br}, \text{I}$). More interestingly, compared to the compact BiOI/BiOBr clusters,

BiOI/BiOCl composites appear as more loose and fluffy agglomerates. The hierarchical 3D micro-hybrid with a porous structure may lead to a high specific surface area and surface-to-volume ratio, as well as abundant transport paths for charge-carrier separation, which could be favorable for a photocatalytic process [28].

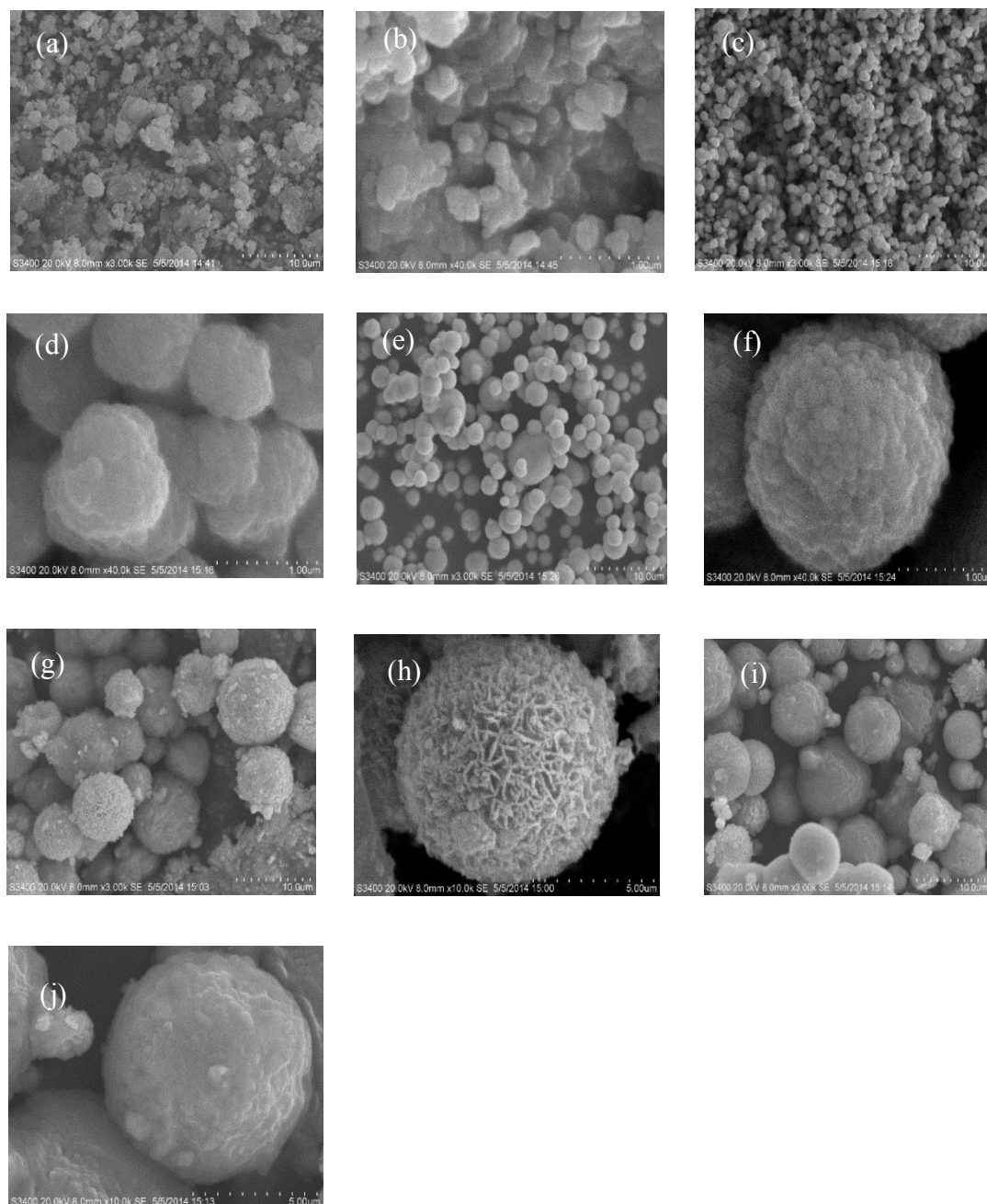


Figure 4.2. Scanning electron microscopy (SEM) images of (a,b) BiOI; (c,d) BiOCl; (e,f) BiOBr; (g,h) BiOI/BiOCl and (i,j) BiOI/BiOBr with different magnification levels.

TEM images further unveiled the morphological structure of the BiOI/BiOCl and BiOI/BiOBr composites. Figure 4.3a,c exhibits flower-like 3D architectures and BiOI/BiOBr show a more compact microstructure. Both of the nanoplates in Figure 4.3b,d are very thin

with a thickness of around 20 nm. The TEM image in Figure 4.3b (BiOI/BiOCl) shows a more regular morphology with smaller particle size than that of BiOI/BiOBr in Figure 4.3d. In addition, two different lattices of BiOCl can be observed from the high resolution transmission electron microscopy (HRTEM) image in Figure 4.3e with the d-spaces of 0.301 nm for the (102) plane of BiOI and 0.275 nm for the (110) plane. Figure 4.3f also exhibits two different crystalline structures with d-spaces of 0.282 nm and 0.277 nm, which can be assigned to the (110) plane of BiOI and the (110) plane of BiOBr, respectively. The structures of the composites revealed in the TEM images are in agreement with the SEM images.

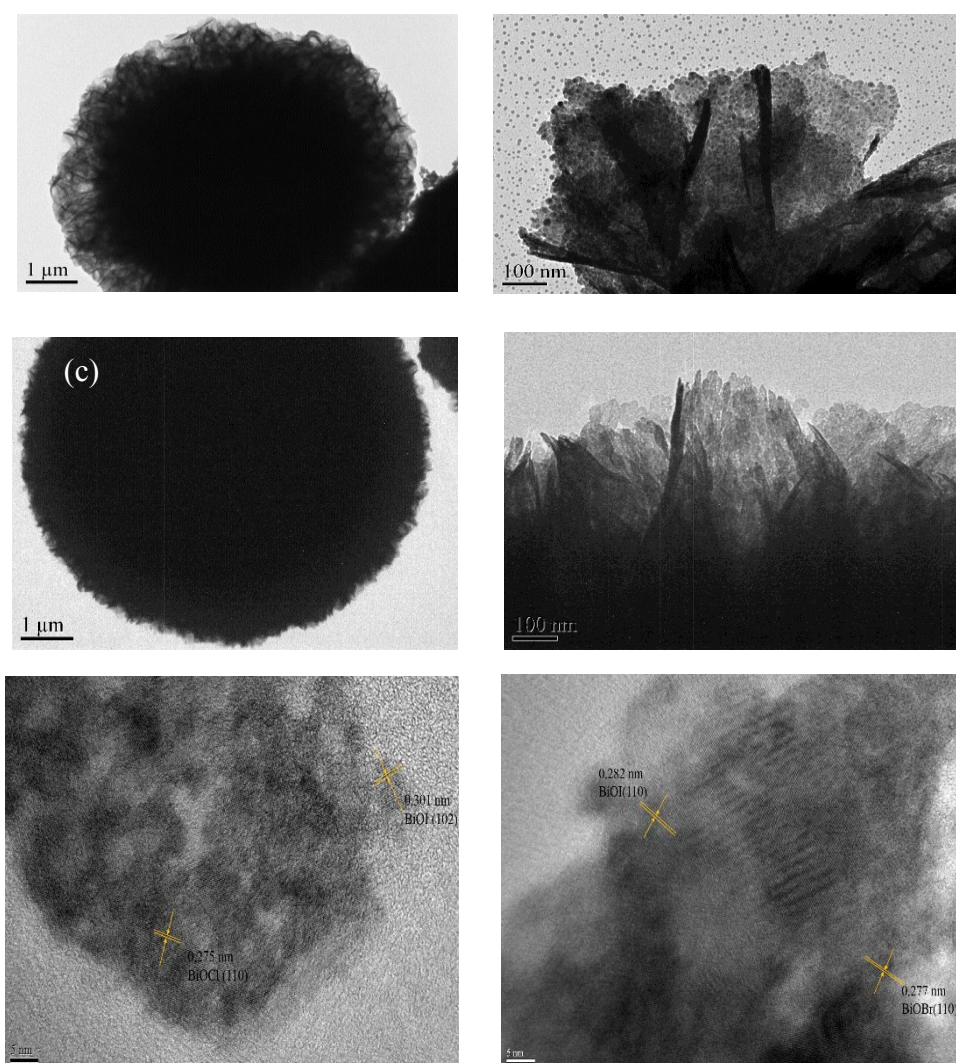


Figure 4.3. Transmission electron microscopy (TEM) images of (a,b) BiOI/ BiOCl; (c,d) BiOI/ BiOBr samples and High resolution transmission electron microscopy (HRTEM) images of (e) BiOI/BiOCl; (f) BiOI/BiOBr.

4.3.2 Optical Properties

The band gap structure and electronic states of a semiconductor photocatalyst are of crucial importance to determine the photoabsorption capacity and catalytic performance. Figure 4.4a displays the UV-Vis diffuse reflectance spectra of the BiOX (X = Cl, Br, I) as well as BiOI/BiOX (X = Br, Cl) composites. BiOCl is only responsive to UV light with an absorption edge at approximately 375 nm, while BiOI exhibits typical optical absorbance in the visible light region with the absorption edge at about 630 nm. BiOBr shows great absorption capacity in both UV and visible light regions with the absorption edge at 450 nm. Compared to BiOX, BiOI/BiOX (X = Br, Cl) composites exhibit enhanced photoabsorption capacity with a slight shift to the lower wavelength. The optical band gap energy can be evaluated based on the plots of $(\alpha h\nu)^{1/2}$ vs. photon energy [24,26] shown in Figure 4.4b. By extrapolating the linear portion of the plots to zero, the band gap energy E_g of BiOCl, BiOBr, BiOI, BiOI/BiOCl, and BiOI/BiOBr were estimated to be 3.25, 2.85, 1.93, 2.09, and 2.01 eV, respectively, with the color transition from off-white to brick red with the red shift of the bandgap (Figure 4.4a, insert). The results are consistent with previously reported values [25, 29, 30]. Meanwhile, the band gap of BiOI/BiOCl is located between BiOI and BiOCl due to the formation of a solid solution, which is also observed for BiOI/BiOBr.

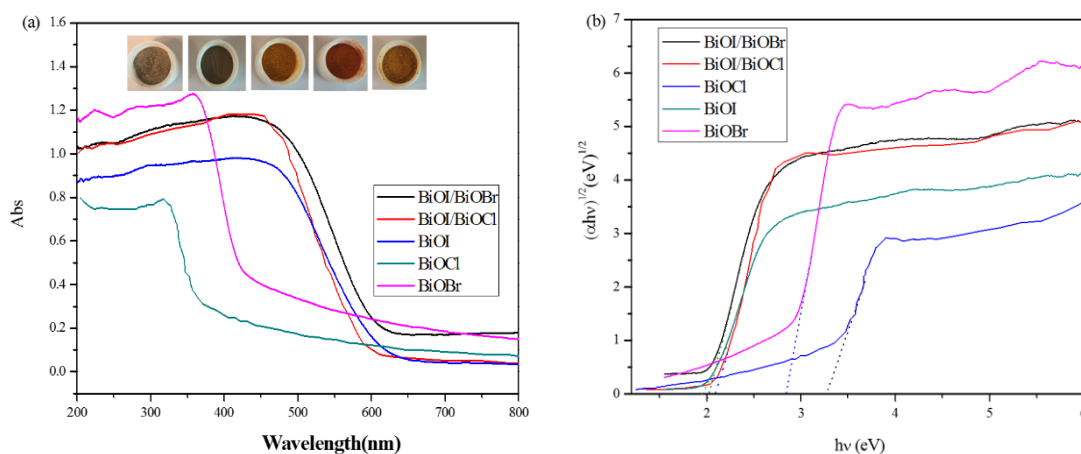


Figure 4.4. Ultraviolet-visible diffuse reflectance spectra (UV-Vis DRS) of (a) as-prepared samples and (b) the plotting of $(\alpha h\nu)^{1/2}$ vs. photon energy.

4.3.3 XPS Analysis

To further analyze the surface chemical composition of the BiOI/BiOCl composite, X-ray photoelectron spectroscopy (XPS) were conducted. The XPS survey in Figure 4.5a shows that BiOI/BiOCl contains major elements of Bi, O, I and Cl as well as a certain amount of C (the

adventitious carbon from the XPS instruments [25,31]). In Figure 4.5b, the two peaks with the binding energies of 158.67 and 163.99 eV are attributed to Bi 4f_{7/2} and Bi 4f_{5/2}, respectively, which represent the typical Bi³⁺ in BiOI/BiOCl composite. The high-resolution O 1s scan is presented in Figure 4.5c. The dominant peak at 529.63 eV can be assigned to the lattice oxygen in the (BiO)₂²⁺ slabs of the BiOI/BiOCl layered structure, and the other peak at 532.49 eV may

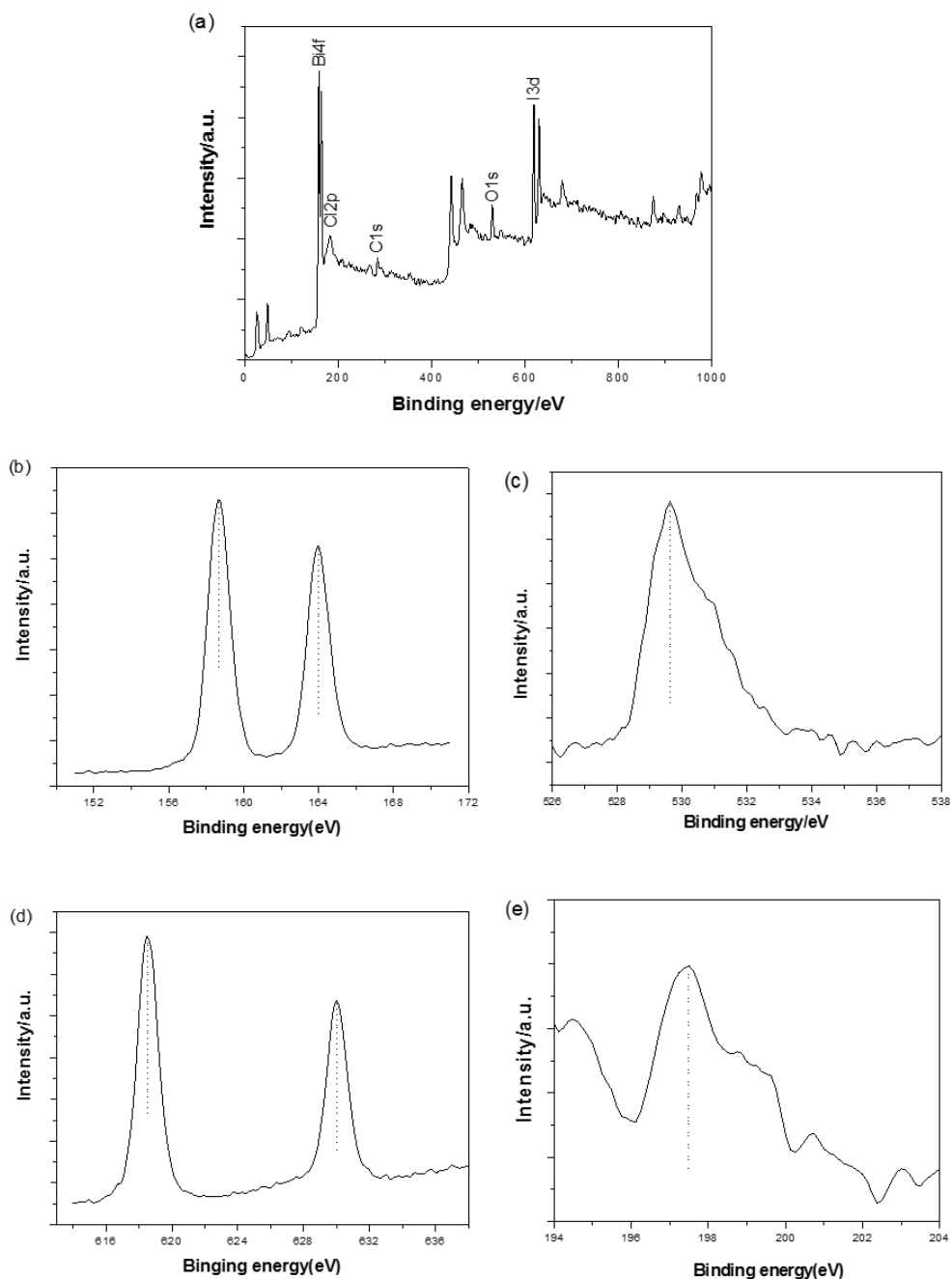


Figure 4.5. (a) X-ray photoelectron spectroscopy (XPS) spectra survey and high-resolution scan of (b) Bi 4f; (c) O 1s; (d) I 3d and (e) Cl 2p of BiOI/BiOCl composite.

be attributed to the surface hydroxyl groups [32]. The peaks of I 3d in Figure 4.5d can be found at 630.02 and 618.53 eV, which could be attributed to I 3d_{3/2} and I 3d_{5/2}, respectively, corresponding to I⁻ in the BiOI/BiOCl composite. The high-resolution scan of Cl 2p is shown in Figure 4.5e with one peak centered at 197.47 eV, which is ascribed to Cl 2p_{3/2}. The overall surface chemical compositions including atomic concentrations of the major elements are listed in Table 4.1. It is noted that the atomic ratio of I/Cl on the surface of the composite catalyst is about 2.9:1, which is much lower than 9:1 applied during the catalyst preparation, indicating a high concentration of chlorine ions on the surface.

Table 4.1. Surface chemical composition and concentration of the BiOI/BiOCl catalyst.

Element	O 1s	Cl 2p	Bi 4f	I 3d
Atomic%	30.57	2.44	22.03	7.09

4.3.4 Specific Surface Areas and Pore Structure

A large specific surface area of a photocatalyst is beneficial to the enhancement of the photocatalytic performance. Nitrogen adsorption/desorption isotherms and pore size distributions of the BiOI, BiOCl, and BiOI/BiOCl composites (with a mole ratio of I⁻:Cl⁻ = 9:1) are estimated as shown in Figure 4.6a,b. The isotherms of all the three samples fall into type IV isotherms with a distinct hysteresis loop observed in the range of 0.6 -1.0 P/P_0 , suggesting the formation of capillary condensation related to mesopores between closely-packed spherical particles [33]. The presence of a small amount of Cl⁻ in the BiOI exerted obvious influence on the BET surface areas and pore structure (Table 4.2). The BET surface area decreases a little from 42.5 to 37.7 m²·g⁻¹ with the average pore size increased from 15.7 to 16.8 nm. Both of the isotherms of BiOI and BiOI/BiOCl manifest much higher adsorption capacity than BiOCl at high relative pressure (P/P_0 in the range of 0.8-1.0), indicating that larger inter-aggregated pores were generated and became predominant with larger total pore volumes and a higher adsorption capacity, due to the aggregation of sheet-like nanoparticles [24]. This could be confirmed by the SEM and TEM images with the flower-like 3D microstructure interwoven by very thin nanoplates.

Table 4.2. The Brunauer-Emmett-Teller (BET) surface areas and pore structures of the photocatalysts.

Catalyst	Surface Area/m ² ·g ⁻¹	Pore Volume (cm ³ ·g ⁻¹)	Pore Size (nm)
BiOI	42.4	0.20	15.7
BiOCl	17.0	0.046	8.8
BiOCl/BiOI	37.7	0.20	16.8

Compared with pure BiOI, the BiOI/BiOCl composites also exhibited a larger hysteresis loop with a similar shape in the isotherms. In addition, the pore-size distribution of BiOI/BiOCl composites became more uniform. The pure BiOI sample contained a bimodal mesopore size distribution from ca. 2.1 nm to ca. 14.7 nm. In contrast, the larger mesopores in the BiOI/BiOCl composites occupied the main portion of the total pore volume with a maximum pore diameter of 18.2 nm, which may be produced from the inter-aggregated secondary particles and the stack of nanoplates.

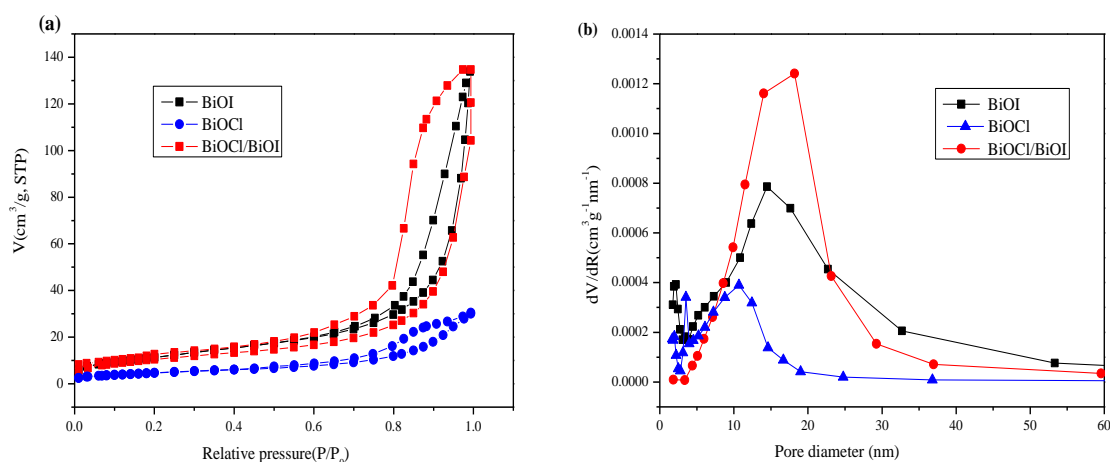


Figure 4.6. (a) Nitrogen sorption isotherms of BiOI, BiOCl, and BiOI/BiOCl; (b) Pore size distributions of BiOI, BiOCl, and BiOI/BiOCl.

4.3.5. Photocatalytic Degradation of MO

Adsorption of MO

All the adsorption experiments were conducted in the dark with an initial concentration of 20 ppm MO and a catalyst dosage of 0.2 g/L [34]. As shown in Figure 4.7, both BiOCl and BiOBr achieved adsorption equilibrium after 30 min with 10% dye adsorption. The pure BiOI

and the composites (BiOI/BiOX, X = Br, Cl) exhibited a higher adsorption capacity of about 25% dye removal in 30 min.

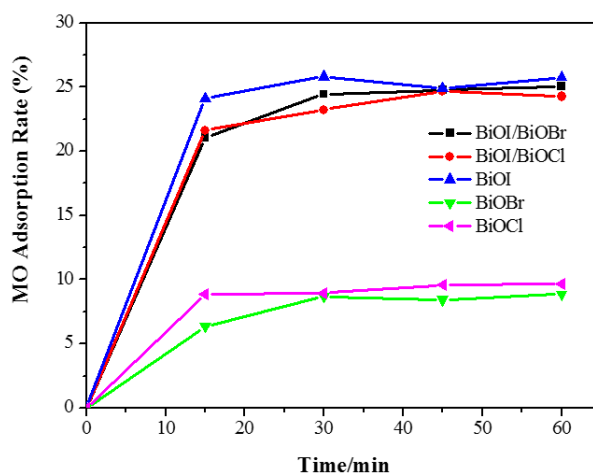


Figure 4.7. Adsorbed MO in the dark for BiOX (X = Cl, Br, I) and BiOI/BiOX (X = Br, Cl) composites ($C_0 = 20$ ppm, catalyst dosage = 0.2 g/L).

Pure BiOI shows the highest adsorption rate of 25.7% MO removal after 60 min, which could be due to the highest BET surface area among the photocatalysts. The greater dye adsorption rate would contribute to faster dye degradation as the larger surface area would be more favourable for dye molecules to adsorb onto the active sites of the photocatalyst, giving rise to an enhanced photocatalytic activity. Overall, when 0.05 g of catalyst was introduced into the 20 ppm methyl orange solution, the adsorption removal efficiencies of all of the catalysts are less than 30% after adsorption equilibrium in 30 min. In this case, adsorption will not exhibit a considerable influence on the investigation of photodegradation efficiency.

Comparison of Photocatalytic Activity

All the photocatalysts were tested under both visible and UV irradiations as shown in Figures 4.8 and 4.9. Figure 4.8a demonstrates that only 12% of MO was removed after 2.5 h for visible-light irradiation without any catalyst, suggesting that MO is chemically stable and refractory to decomposition by photolysis. Both of the composite semiconductors BiOI/BiOCl and BiOI/BiOBr had higher photocatalytic activity than pure BiOI under visible-light irradiation. Among all the catalysts, the BiOI/BiOCl composite gave 78% MO removal after 150 min, which was 25% higher than the pure BiOI. The lattice of single BiOI was expanded

by the coupling of BiOX (X = Cl, Br), leading to the recombination between the lattices to form a three-dimensional spherical structure with heterojunction interfaces, which will contribute to the efficient separation of photogenerated electron-hole pairs. As shown in Figure 4.4, the band edges of both pure BiOI and BiOI/BiOX (X = Cl, Br) fall into the visible light region, with the composites showing even higher light absorption capacity than the pure BiOI. The photocatalytic activity enhancement of BiOI/BiOX (X = Cl, Br) could be ascribed to the retardation of electron-hole recombination with improved interfacial charge transfer efficiency as well as a stronger light absorption ability.

Relative to BiOX (X = Cl, Br), BiOI has a narrow band gap of around 1.9 eV, which can be excited by visible light with a more efficient utilization of solar energy. Additionally, BiOI and its composite (BiOI/BiOCl) with larger specific surface areas (SSAs) can not only supply more active sites for pollutant degradation but also promote the separation of the electron-hole pairs [35]. Nevertheless, BiOCl is severely limited for visible light adsorption due to its wide bandgap (3.25 eV) which caused a poor catalytic performance in the visible light region. In Figure 4.8, BiOCl exhibits the lowest photodegradation activity among all the catalysts under visible light irradiation. According to pseudo-first-order kinetics [36], the apparent pseudo-first-order rate constants (k_{app}) were obtained as a comparative parameter for the photocatalytic activity of different catalysts.

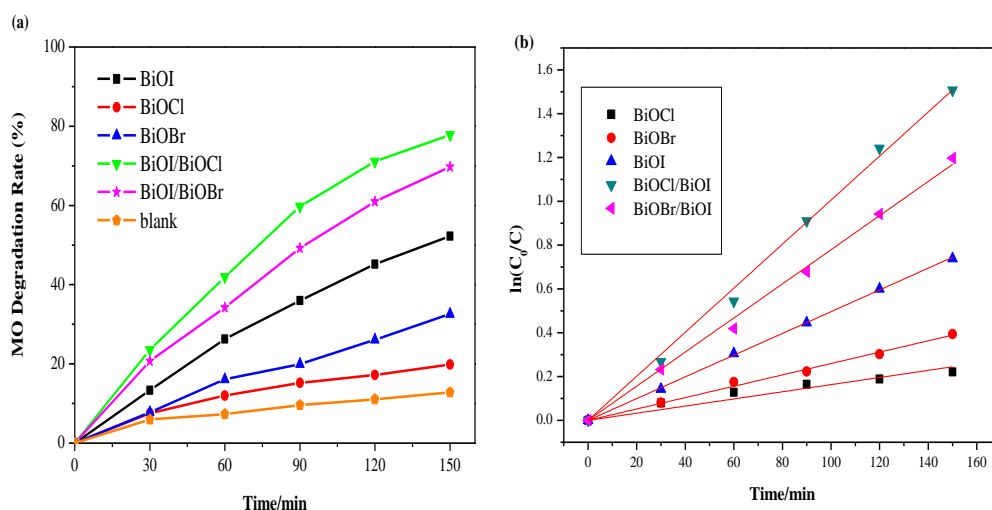


Figure 4.8. (a) Comparison of photodegradation efficiencies of different samples under visible irradiation; (b) pseudo-first-order kinetics curves of Methyl orange (MO) degradation over different samples under visible irradiation.

$$\ln\left(\frac{C_0}{C}\right) = kKt = k_{app}t \quad \text{or} \quad C_t = C_0 e^{-k_{app}t} \quad 4.1$$

where C_0 is the original concentration of the dyes and C is the concentration at the reaction time t ; k is the reaction rate constant; K is the adsorption coefficient of the reactant. The linear time dependence of $\ln(C_0/C)$ with t is plotted in Figures 4.8b and 4.9b correspondingly.

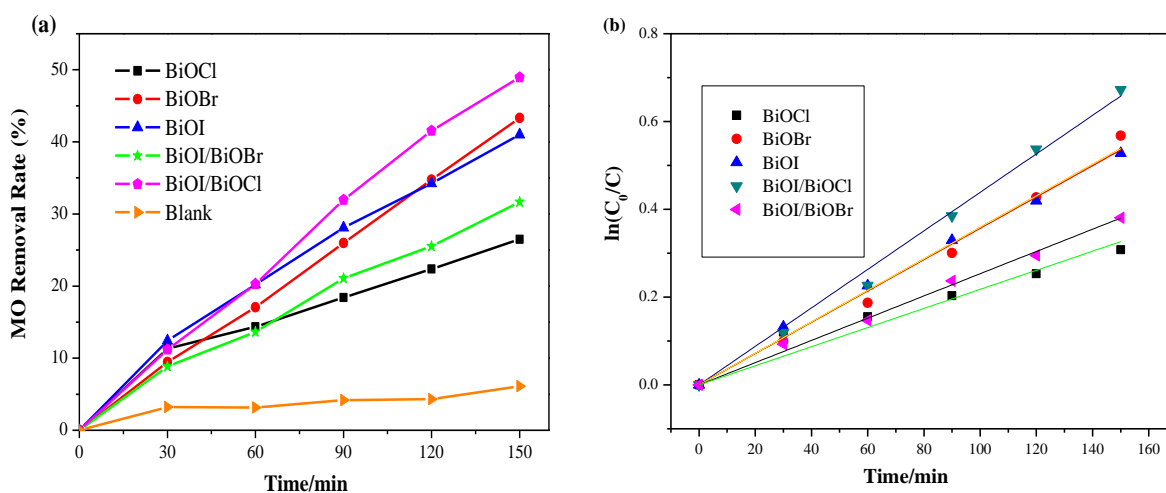


Figure 4.9. (a) Comparison of photodegradation efficiencies of different samples under UV irradiation; (b) pseudo-first-order kinetics curves of MO degradation over different samples under UV irradiation.

Based on the curves from Figures 4.8b and 4.9b, the calculated values of k_{app} and R^2 are displayed in Table 4.3. As observed in Figure 4.9b and Table 4.3, the BiOI/BiOCl composite demonstrates the highest photodegradation efficiency under UV light irradiation with almost 50% MO removal in 150 min, compared with the pure BiOI catalyst of 40%. Given the performances under visible light irradiation, BiOBr turns out to be an excellent UV responsive photocatalyst, as BiOBr shows good UV light absorption capacity according to Figure 4.4. The BiOI/BiOBr composites present an outstanding photocatalytic activity under visible light irradiation, yet an inferior activity under UV light irradiation. In summary, BiOI/BiOCl exhibits the highest photocatalytic performance both under UV and visible light irradiation, indicating that the intimate interaction between BiOI and BiOCl is crucial for the formation of a charge-separation heterojunction [37]. However, BiOCl shows the lowest activity under both UV and visible irradiations, due to the poor light-absorption capability and a low specific surface area.

Table 4.3. Photodegradation rate constants of various catalysts under UV and visible light.

Light Irradiation	Photocatalysts	K_{app} (min^{-1})	R^2
UV	BiOCl	0.0022	0.979
	BiOBr	0.0036	0.996
	BiOI	0.0036	0.998
	BiOI/BiOBr	0.0025	0.998
	BiOI/BiOCl	0.0044	0.998
Visible	BiOCl	0.0016	0.976
	BiOBr	0.0026	0.998
	BiOI	0.0050	0.999
	BiOI/BiOBr	0.0078	0.999
	BiOI/BiOCl	0.0100	0.999

Figure 4.10a shows a typical UV-Vis absorption spectrum of the MO solution during degradation by the BiOI/BiOCl composite at different time intervals. As the irradiation proceeded, the absorption peak at 465 nm showed a blue-shift and becomes broadened simultaneously, implying that the decomposition of MO molecules is due to the demethylation reaction in which the methyl group is substituted by a hydrogen atom after the homolytic breaking of the nitrogen-carbon bond [38].

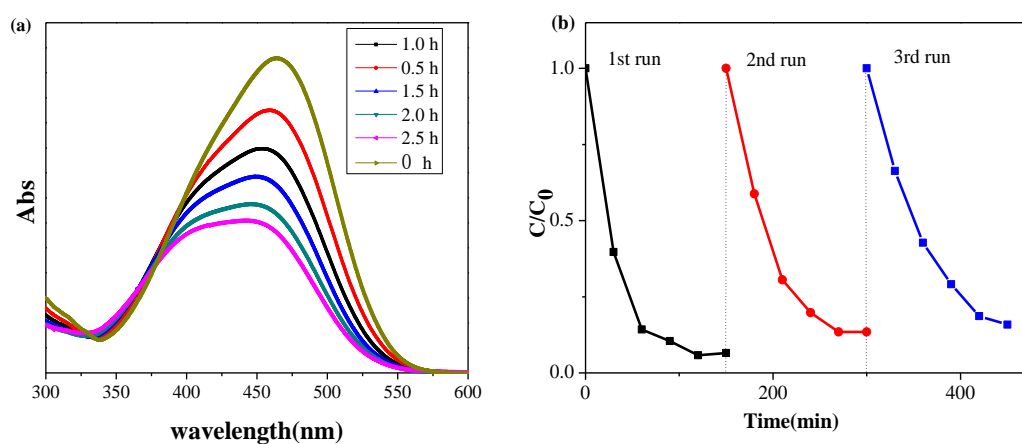


Figure 4.10. (a) Temporal evolution of the spectra during the photodegradation of MO mediated by BiOI/BiOCl composite; (b) Cycling run in the photocatalytic degradation of MO with BiOI/BiOCl as the photocatalyst under visible light irradiation.

Except for high photocatalytic activity, the lifetime of the photocatalyst is also a key parameter for the practical application of the catalytic process. To observe sample stabilities, recycling experiments were conducted with the BiOI/BiOCl composite photocatalyst to degrade MO under visible light irradiation using a MSR 575/2 metal halide lamp (575 W, Philips, N.J., USA) with the intensity at 250 mW/cm² (400–1050 nm). As shown in Figure 4.10b, the photocatalytic degradation was 93.5%, 86.6%, and 84.2% for the first, second, and third runs, respectively. Thus, the sample exhibits good stability without a remarkable decline of photocatalytic activity.

According to the previous studies, the valence band energies of BiOI and BiOCl were calculated to be 2.42 and 3.44 eV, respectively [24,25], both of which are more positive than the standard redox potential of H₂O/O₂ (1.23 eV vs. reversible hydrogen electrode (RHE) at pH = 0) [39]. Theoretically, both BiOI and BiOCl including their composites can oxidize H₂O to produce O₂. Therefore, BiOI/BiOCl with the highest photocatalytic activity was chosen to explore the potential for photocatalytic water oxidation. Figure 4.11 describes the time dependence of O₂ evolution from water over the synthesized catalysts. As can be seen, the O₂ evolution rate is 7.57 μmol/h for BiOI/BiOCl, which is 1.55 and 1.53 times higher than that of pure BiOI (4.87 μmol/h) and BiOCl (4.96 μmol/h) accordingly after 1 h of simulated solar light irradiation. It is also observed that the water oxidation rates rapidly speeded up in the first 20 min, then went through a plateau afterwards. This result indicates that an effective heterojunction has been constructed between BiOI and BiOCl, which leads to an enhancement of charge transfer and separation efficiency.

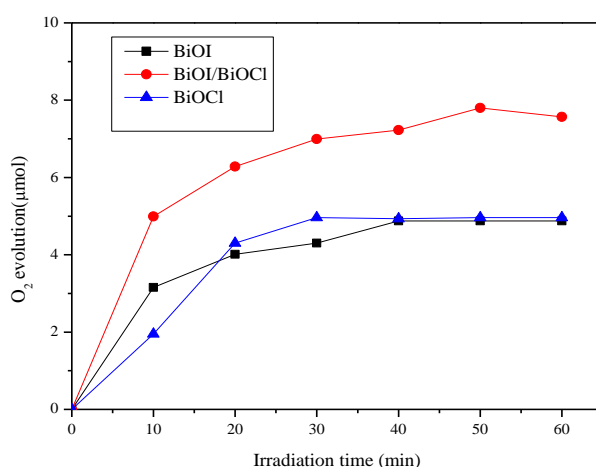


Figure 4.11. The photocatalytic O₂ evolution of BiOI, BiOCl, and BiOI/BiOCl composites.

Photocatalytic Mechanism of the BiOI/BiOCl Composite

Given the results above, it could be concluded that the photocatalytic performance of BiOI is highly promoted after coupling with BiOCl to form an effective heterojunction. To further explore the in-depth mechanism, in situ electron paramagnetic resonance (EPR) technology was used to probe the reactive oxygen species in the photodegradation. Both hydroxyl ($\cdot\text{OH}$) and superoxide radicals ($\cdot\text{O}_2^-$) were detected with characteristic peaks as shown in Figure 4.12. The nitroxide 5,5-dimethyl-pyrrolidone-(2)-oxyl-(1) (DMPOX) represents oxidized DMPO impurities due to a long-time irradiation. In Figure 4.12a, the weak signals of hydroxyl radicals ($\cdot\text{OH}$) were observed after irradiation for 5 min, indicating that the photo-generated holes might combine with adsorbed H_2O molecules to produce a small amount of $\cdot\text{OH}$. Figure 4.12b revealed that the characteristic peaks of superoxide radicals ($\cdot\text{O}_2^-$) with strong intensities were detected, indicating that the superoxide radicals could be the main reactive oxygen species during the photocatalytic reaction process. According to recent studies [40–43], surface peroxy species could be formed via the disproportionation of the superoxide radicals or coupling of hydroxyl radicals, and become the primary intermediates of photocatalytic reactions, which will be involved in the photocatalytic reaction processes including photodegradation of organic pollutants and oxygen evolution. The detailed mechanism involving peroxy species requires further exploration in future studies.

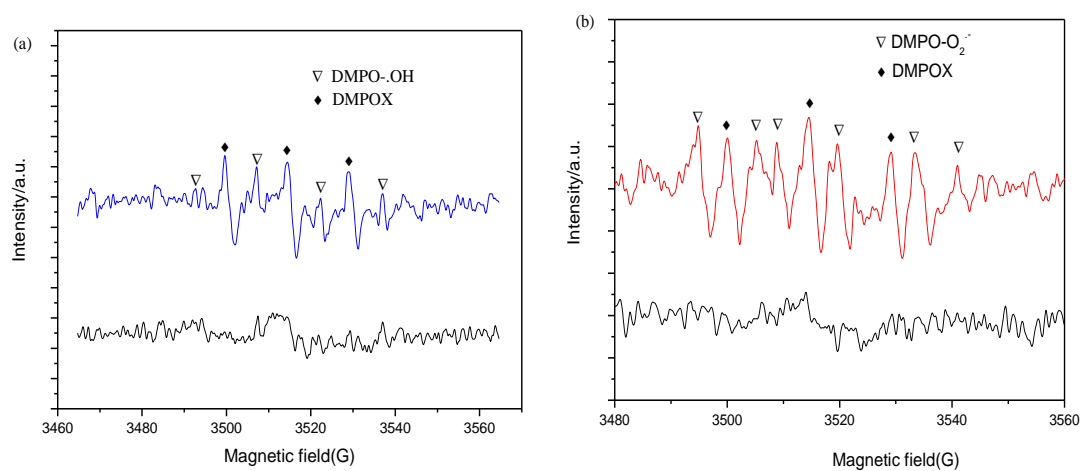


Figure 4.12. Electron paramagnetic resonance (EPR) spectra of hydroxyl (a) and superoxide (b) radicals over the BiOI/BiOCl sample under solar light irradiation (DMPOX was denoted as oxidized 5,5-dimethyl-1-pyrroline N-oxide (DMPO)).

According to the semi-empirical equation (Equation (4.2)) based on the Mulliken electronegativity theory [44], both the conduction band potential (CB) and valence band potential (VB) of BiOI and BiOCl were calculated.

$$E_{VB} = X - E_e + 0.5 \times E_g \quad 4.2$$

where E_g is the band gap potential, E_e is the energy of free electrons on the hydrogen scale (4.5 eV), and X is the absolute electronegativity of the constituent atoms.

According to the UV-Vis diffuse spectra, the values of E_g of pure BiOCl and BiOI were calculated to be 3.25 and 1.93 eV, respectively. The calculated VB positions of BiOCl and BiOI were estimated as 3.44 and 2.39 eV accordingly. Thus, the CB positions of BiOCl and BiOI were obtained to be 0.19 and 0.46 eV.

Based on analysis and discussion above, a schematic illustration was proposed to unravel the formation of the BiOI/BiOCl heterojunction structure in Figure 4.13. Under visible light irradiation, only BiOI with a narrow band gap of 1.93 eV could be excited, with photo-generated electrons in the valence band being excited to a higher potential edge than the original one to form a new conduction band [27], which is even higher than the CB of BiOCl. According to energy band structure theory, electrons from the CB of BiOI will be transferred to the lower lying CB of BiOCl to generate an electron center; meanwhile, the holes from the VB of BiOCl will be transferred oppositely to the VB of BiOI to create a hole center. Herein, the photo-excited electrons and holes could be efficiently separated with a lengthened lifetime. Moreover, since the new conduction band of BiOI is more negative than the reduction potential of $O_2/\cdot O_2^-$ (-0.33 eV) [16], the oxygen molecules could be reduced to $\cdot O_2^-$ radicals by the electrons, which is further supported by the EPR results. Compared with the standard reduction potential of $\cdot OH/H_2O$ (2.27 eV) or $\cdot OH/OH^-$ (2.38 eV) [16], the VB potential of BiOI is 2.39 eV, indicating that oxidative holes (h^+) on the surface of BiOI experienced difficulty in directly oxidizing H_2O or OH^- into $\cdot OH$. Instead, most of the h^+ would react with dye molecules directly and synergistically promote the dye decomposition. However, the VB potential of BiOCl is 3.44 eV, which is positive enough to oxidize H_2O or OH^- into $\cdot OH$ radicals. Thus, the small amount of h^+ left in the VB of BiOCl could produce some hydroxyl radicals, contributing to the dye degradation as well. In summary, the unique heterojunction between BiOI and BiOCl could render the charge carrier separation and transport more efficiently, which are the key factors for improved photocatalytic performance, compared to the pure BiOI.

The strong light absorption capacity of the BiOI/BiOCl composite as well as the enlarged specific surface area also account for the excellent photodegradation efficiency.

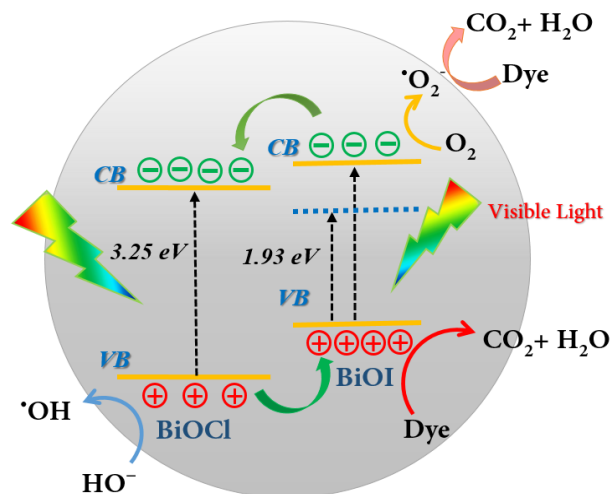


Figure 4.13. Proposed mechanistic diagram of the photocatalytic process for the BiOI/BiOCl photocatalyst under visible light irradiation.

Photodegradation of Dyes under Natural Solar Light Irradiation

To further investigate the practical application of the optimal photocatalysts, two other typical dyes of methyl violet (MV) and direct black (DB) together with methyl orange were studied for the estimation of the photodegradation effectiveness of the BiOI and BiOI/BiOCl composites under natural solar light irradiation. All of the experiments were performed simultaneously outdoor (Nanjing, China) at noon (11:30 a.m.–3:00 p.m.) in the summer season of June, under the same conditions listed in Section 4.3.5.2 except for the light source. The degradation efficiency results are depicted in Figure 4.14. Among the three dye pollutants, methyl violet is most vulnerable to sunlight irradiation on the catalysts. 100% MV degradation could be achieved in 210 min under natural sunlight irradiation on the BiOI/BiOCl composite. Moreover, the degradation of methyl violet attained a superior reaction rate in the first 60 min. Overall, the degradation rate was enhanced by using BiOI/BiOCl as the photocatalyst rather than the pure BiOI for MO and MV. Based on the analysis of the molecular structure of the three dyes, it could be deduced that the degradation efficiency of the dyes was closely related to the azo functional groups in the molecular structure. All the dye molecular structures are listed in Table 4.4. Zero, one, and three azo groups were functionalized in methyl violet, methyl orange, and direct black, respectively, which might account for the reason that direct black is refractory to decompose on both the BiOI and BiOI/BiOCl catalysts.

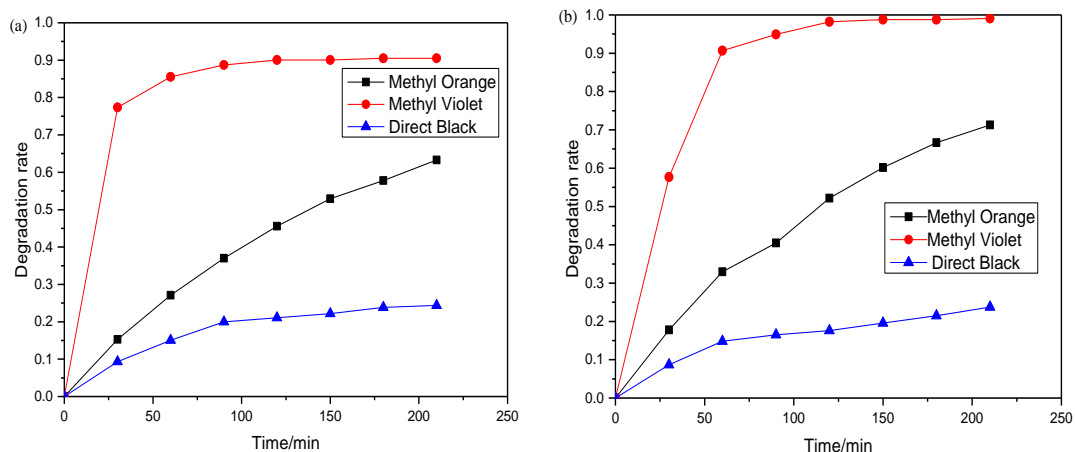


Figure 4.14. Photocatalytic degradation of typical dyes under natural solar light irradiation with (a) BiOI and (b) BiOI/BiOCl.

Table 4.4. Molecular structures and characteristics of the dyes.

Dye	Molecular Structure	Application	Safety
Methyl Orange		pH indicator	mutagenic properties
Methyl Violet		purple dye for textiles	mutagen and mitotic poison
Direct Black		silk dyeing/printing/leather shading	carcinogenicity and reproductive toxicity

4.4 Conclusions

In summary, flower-like 3D BiOI/BiOX (X = Br or Cl) hybrids have been successfully fabricated via a facile one-pot solvothermal approach. The BiOI/BiOCl hybrids present fluffy and porous 3D microspheres with large specific surface areas and high light absorption abilities. Under visible light irradiation, both of the composites exhibited significant enhancement of the photocatalytic oxidation performance compared to pure BiOI. The apparent reaction rate for MO degradation is 2.1 times higher over BiOI/BiOCl, and 1.6 times higher over BiOI/BiOBr than that of pure BiOI. Moreover, BiOI/BiOCl demonstrated a slight promotion under UV light irradiation, which is 1.3 times higher than pure BiOI. Moreover, the BiOI/BiOCl composite also displayed excellent water oxidation ability with enhanced O₂ evolution from the water. The enhancement of photocatalytic activity could be attributed to the formation of a heterojunction between BiOI and BiOCl, which facilitates the separation and transportation of charge carriers more efficiently with a rationally-engineered energy band structure. In addition, the nanoporous structure, larger specific surface area, and the stronger light absorption capacity both in the visible and UV region also contributed to the excellent photocatalytic activity of the BiOI/BiOCl composites. The photodegradation was evidenced to be ascribed to the superoxide radicals, oxidative holes, and a minor amount of hydroxyl radicals. This study deepens the understanding of BiOI/BiOCl composites for enhanced photodegradation and water oxidation. The rational design of hybrid materials in photocatalysis will provide promising candidates for further applications in photocatalysis and solar energy conversion.

References

1. Z. Zhang, C. Shao, X. Li, Y. Sun, M. Zhang, J. Mu, P. Zhang, Z. Guo and Y. Liu, *Nanoscale*, 2013, **5**, 606-618.
2. D.S. Bhatkhande and V.G. Pangarkar, A.A. Beenackers, *J. Chem. Technol. Biot.*, 2002, **77**, 102-116.
3. J. Ke, J. Liu, H. Sun, H. Zhang, X. Duan, P. Liang, X. Li, M.O. Tade, S. Liu and S. Wang, *Appl. Catal. B: Environ.*, 2017, **200**, 47-55.
4. Y.B. Li, H.M. Zhang, P.R. Liu, D. Wang, Y. Li and H.J. Zhao, *Small*, 2013, **9**, 3336-3344.

5. S. Kumar, T. Surendar, A. Baruah and V. Shanker, *J. Mater. Chem. A.*, 2013, **1**, 5333-5340.
6. Y.S. Jun, E.Z. Lee, X. Wang, W.H. Hong, G.D. Stucky and A. Thomas, *Adv. Funct. Mater.* 2013, **23**, 3661-3667.
7. X. Wu, G.Q.M. Lu and L. Wang, *Energ Environ. Sci.*, 2011, **4**, 3565-3572.
8. Y. Hou, Z. Wen, S. Cui, X. Guo and J. Chen, *Adv. Mater.*, 2013, **25**, 6291-6297.
9. M. Li, W. Luo, D. Cao, X. Zhao, Z. Li, T. Yu and Z. Zou, *Angew. Chem. Int. Ed.*, 2013, **52**, 11016-11020.
10. Y. Li, T. Takata, D. Cha, K. Takanabe, T. Minegishi, J. Kubota and K. Domen, *Adv. Mater.*, 2013, **25**, 125-131.
11. J. Zhang, F. Guo and X. Wang, *Adv. Funct. Mater.*, 2013, **23**, 3008-3014.
12. S.I. In, D.D. Vaughn and R.E. Schaak, *Angew. Chem. Int. Ed.*, 2012, **51**, 3915-3918.
13. J. Mao, T. Peng, X. Zhang, K. Li, L. Ye and L. Zan, *Catal. Sci. Technol.*, 2013, **3**, 1253-1260.
14. X. Chen and S.S. Mao, *Chem. Rev.*, 2007, **107**, 2891-2959.
15. Y. Zhang, A.M. Schultz, L. Li, H. Chien, P.A. Salvador and G.S. Rohrer, *Acta Mater.*, 2012, **60**, 6486-6493.
16. W. Zhao, Y. Liu, Z. Wei, S. Yang, H. He and C. Sun, *Appl. Catal. B: Environ.*, 2016, **185**, 242-252.
17. J. Ke, X.G. Duan, S. Luo, H.Y. Zhang, H.Q. Sun, J. Liu, M. Tade and S.B. Wang, *Chem. Eng. J.*, 2017, **313**, 1447-1453.
18. G.-Q. Zhang, N. Chang, D.-Q. Han, A.-Q. Zhou, X.-H. Xu, *Mater. Lett.*, 2010, **64**, 2135-2137.
19. Y. Lei, G. Wang, S. Song, W. Fan, H. Zhang, *CrystEngComm*, 2009, **11**, 1857-1862.
20. L. Ye, L. Zan, L. Tian, T. Peng, J. Zhang, *Chem. Commun.*, 2011, **47**, 6951-6953.
21. A. Iwase and A. Kudo, *J. Mater. Chem.*, 2010, **20**, 7536-7542.
22. H. Cheng, B. Huang, Z. Wang, X. Qin, X. Zhang and Y. Dai, *Chem. Eur. J.*, 2011, **17**, 8039-8043.
23. G.J.D.A. Soler-Illia, C. Sanchez, B. Lebeau, J. Patarin, *Chem. Rev.*, 2002, **102**, 4093-4138.
24. Z. Jia, F. Wang, F. Xin and B. Zhang, *Ind. Eng. Chem. Res.*, 2011, **50**, 6688-6694.
25. F. Dong, Y. Sun, M. Fu, Z. Wu and S.C. Lee, *J. Hazard. Mater.*, 2012, **219-220**, 26-34.
26. X. Xiao, R. Hao, M. Liang, X. Zuo, J. Nan, L. Li and W. Zhang, *J. Hazard. Mater.*, 2012, **233-234**, 122-130.

27. C. Yang, F. Li, M. Zhang, T. Li and W. Cao, *J. Mol. Catal. A*, 2016, **423**, 1-11.
28. J. Li, G. Lu, Y. Wang, Y. Guo and Y. Guo, *J. Colloid Interface Sci.*, 2012, **377**, 191-196.
29. X. Zhang, Z. Ai, F. Jia and L. Zhang, *J. Phys. Chem. C*, 2008, **112**, 747-753.
30. T.B. Li, G. Chen, C. Zhou, Z.Y. Shen, R.C. Jin and J.X. Sun, *Dalton Trans.*, 2011, **40**, 6751-6758.
31. R. Asahi, T. Morikawa, T. Ohwaki, K. Aoki and Y. Taga, *Science*, 2001, **293**, 269-271.
32. Z. Ai, W. Ho, S. Lee and L. Zhang, *Environ. Sci. Technol.*, 2009, **43**, 4143-4150.
33. K.S. Sing, *Pure Appl. Chem.*, 1985, **57**, 603-619.
34. J. Xu, Y.Z. Liu, L.Q. Wang and F. Ye, *Environ. Prot. Sci.*, 2015, **41**, 79-82.
35. Y. Huang, Z. Ai, W. Ho, M. Chen and S. Lee, *J. Phys. Chem. C*, 2010, **114**, 6342-6349.
36. Y.Z. Liu, S.G. Yang, J. Hong and C. Sun, *J. Hazard. Mater.*, 2007, **142**, 208-215.
37. Y. Hou, A.B. Laursen, J. Zhang, G. Zhang, Y. Zhu, X. Wang, S. Dahl and I. Chorkendorff, *Angew. Chem. Int. Ed.*, 2013, **52**, 3621-3625.
38. K. Dai, H. Chen, T. Peng, D. Ke, H. Yi, *Chemosphere*, 2007, **69**, 1361-1367.
39. J. Liu, Y. Liu, N. Liu, Y. Han, X. Zhang, H. Huang, Y. Lifshitz, S.T. Lee, J. Zhong and Z. Kang, *Science*, 2015, **347**, 970-974.
40. C.C. Chen, P.X. Lei, H.W. Ji, W.H. Ma, J.C. Zhao, *Environ. Sci. Technol.*, 2004, **38**, 329-337.
41. J.M. Wu, T.W. Zhang, Y.W. Zeng, S. Hayakawa, K. Tsuru and A. Osaka, *Langmuir*, 2005, **21**, 6995-7002.
42. J.X. Yang, D.G. Wang, X. Zhou, C. Li, *Chem. Eur. J.*, 2013, **19**, 1320-1326.
43. R. Nakamura, A. Imanishi, K. Murakoshi and Y. Nakato, *J. Am. Chem. Soc.*, 2003, **125**, 7443-7450.
44. W. Zhao, Y. Guo, S. Wang, H. He, C. Sun and S. Yang, *Appl. Catal. B: Environ.* 2015, **165**, 335-343.

Every reasonable effort has been made to acknowledge the owners of copyright material. I would be pleased to hear from any copyright owner who has been omitted or incorrectly acknowledged.

Chapter 5. 0D (MoS₂)/2D (g-C₃N₄) Heterojunctions in Z-Scheme for Enhanced Photocatalytic and Electrochemical Hydrogen Evolution

Abstract

Apart from bismuth-based visible light photocatalysts from previous two chapters, graphitic carbon nitride ($g\text{-C}_3\text{N}_4$) rises up as another promising semiconductor photocatalyst because of its environmental-friendly and metal-free attributes as well as simple fabrication process. In this chapter, MoS_2 quantum dots (MSQDs) with a high and stable dispersion ability in water were prepared via a facile one-pot hydrothermal process. The MSQDs were then applied to decorate graphitic carbon nitride ($g\text{-C}_3\text{N}_4$, CN) nanosheets to obtain modified $g\text{-C}_3\text{N}_4$ photocatalysts (MSQD-CN). Compared to pristine $g\text{-C}_3\text{N}_4$, the hybrid photocatalysts showed a slight red shift and stronger light absorption with remarkably improved photocatalytic activity in water splitting to generate hydrogen. The hydrogen-evolution rate over 0.2 wt% MSQD-CN increased by 1.3 and 8.1 times as high as that of 0.2 wt% Pt-CN and $g\text{-C}_3\text{N}_4$, respectively. With deposition of 2 wt% Pt as a cocatalyst, 5 wt% MSQD-CN exhibited the highest photocatalytic efficiency with an average hydrogen evolution reaction (HER) rate of $577 \mu\text{mol}\cdot\text{h}^{-1}\cdot\text{g}^{-1}$. Photoluminescence spectra (PL) and photoelectrochemical measurements inferred that MSQDs introduction drastically promoted the electron transfer for more efficient separation of charge carriers, which could lower HER overpotential barriers and enhance the electrical conductivity. In addition, the well-matched band potentials of the MSQD-CN hybrid with an intimate contact interface of p-n heterojunction also inhibited the recombination of photo-generated carriers, leading to enhanced photocatalytic HER performance. A direct Z-scheme charge transfer mechanism of the MSQD-CN hybrid was proposed to further elaborate the synergic effect between MSQDs, Pt and $g\text{-C}_3\text{N}_4$. This work underlines the importance of heterojunction interface and presents a feasible protocol for rational construction of $g\text{-C}_3\text{N}_4$ based photocatalysts for various photocatalytic applications.

5.1 Introduction

Energy crisis and environmental problems have always been considered as challenging and critical issues over the past decades. Solar energy conversion into chemical energies by photocatalysis has emerged as a sustainable and efficient route. Hydrogen, as an ultimate clean energy with a much higher fuel value (143 kJ/g), is considered as an ideal candidate to replace fossil fuels in the future with wide applications in chemical industries[1]. Since Fujishima and Honda reported a photoelectrochemical hydrogen evolution process from water in 1972[2],

photocatalytic H₂ evolution over earth-abundant semiconductors combined with co-catalysts for water splitting has received considerable attention[3-5]. This shows more significances to the environmental remediation by photocatalytic process[6, 7]. In practice, stable and highly efficient photocatalysts are of vital importance to the production of H₂. Tremendous efforts have thus been focused on the development of effective surface junctions between semiconductors and co-catalysts with a matched band structure and electron affinity, which could optimize light capture capacity and increase the charge separation to achieve overall enhanced photocatalytic performance[8].

As a metal-free semiconductor, graphitic carbon nitride (g-C₃N₄) has attracted much attention because of its layered graphite-like structure, suitable electronic structure for water redox catalysis as well as its simple synthesis from earth abundant elements and chemical stability[9, 10]. However, pristine g-C₃N₄ has a relatively narrow light response range with bandgap energy at 2.7 eV[11], suffering from the fast recombination of photo-generated electron/hole pairs. Moreover, it is also restricted by low electrocatalytic activity, severely detrimental to the water splitting process. Integration of a co-catalyst, such as platinum or other noble metals, helps promote the charge separation with a prolonged lifetime for electrons to transfer over the surface, as well as to lower the overpotentials for H₂ evolution with an improved electrical conductivity[12].

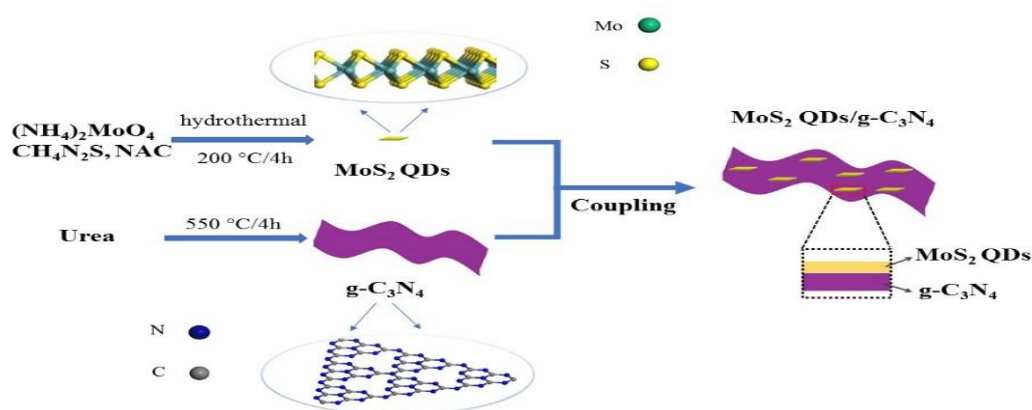
Recent studies show that molybdenum sulfide (MoS₂) stands out to be a promising catalyst for hydrogen-evolution reaction (HER) with a satisfactory electrocatalytic activity originated from its unique structure[13-15]. MoS₂ has a similar layered structure to g-C₃N₄, which could achieve better lattice matching and promote the growth of MoS₂ slabs on the surface of g-C₃N₄[16]. Moreover, the unsaturated atoms of both Mo and S at the edges will foster an favorable edge activity during the catalytic process[17]. Serving as an efficient co-catalyst, MoS₂ has already exhibited a promoting effect in photocatalytic H₂ evolution[18-21]. So far, most of MoS₂ was fabricated in 2D nanosheets to construct a hybrid with thin-layered nanojunctions[22-25]. Few studies, however, have been reported focusing on the fabrication and application of MoS₂ quantum dots (MoS₂ QDs) on g-C₃N₄. With more exposed edges as catalytically active sites than MoS₂ sheets, MoS₂ QDs appear to be a more favorable candidate as the co-catalyst in photocatalytic HER.

Herein, water-dispersible MoS₂ QDs were synthesized via a facile one-pot hydrothermal process and were then used to decorate g-C₃N₄ nanosheets by a simple impregnation method. The prepared MoS₂ QDs/g-C₃N₄ (MSQD-CN) composites showed remarkably enhanced photocatalytic H₂ evolution activities compared to pristine g-C₃N₄ and Pt/g-C₃N₄. The effect

of MoS₂ QDs content on H₂ evolution rate was comprehensively studied, confirming the formation of a p-n heterojunction interface. In addition, a possible mechanism for photocatalytic H₂ evolution process over MSQD-CN composites was proposed, providing insights into designing organic-inorganic hybrid photocatalysts.

5.2 Experimental Section

5.2.1 Synthesis of Photocatalysts



Scheme 5.1. Schematic illustration of a synthetic route for MSQD-CN.

Urea (AR) was purchased from Chem-Supply, Australia. Ammonium molybdate (99.98%), N-acetyl-L-cysteine (NAC, $\geq 99\%$), thiourea ($\geq 99.0\%$), chloroplatinic acid hexahydrate ($\geq 37.5\%$ Pt basis), ethanol, methanol and acetone were supplied by Sigma-Aldrich, Australia. All the reagents were used directly without any further purification.

The overall formation process of MSQD-CN composites is depicted in Scheme 5.1 and more detailed information is given as follows.

Metal-free g-C₃N₄ powders were synthesized via the following procedure: 10 g of urea was placed in a furnace, heated to 550 °C at a rate of 15 °C min⁻¹ and kept at 550 °C for 4 h in air.

Water soluble MoS₂ QDs were prepared by a facile hydrothermal approach[26] with minor revision. Ammonium molybdate (4.25×10^{-3} M) and N-acetyl-L-cysteine (10.2×10^{-3} M) were mixed in 40 mL ultrapure water in an ice-water bath and stirred for a while. Then thiourea (8.5×10^{-3} M) was dissolved in the above solution with further stirring for 1 h under N₂ protection. The mixture was subsequently transferred into a 100-mL Teflon-lined stainless steel autoclave which was already de-aired with N₂ flow and kept at 200 °C for 4 h to get a high

yield of MoS₂ QDs without any black sediments. After centrifuge at 13000 rpm for 20 min, the QDs were washed with ethanol and deionized (DI) water. Finally, the QDs were transferred and dispersed in 20 mL DI water, which was able to maintain in a long-term homogeneous phase.

For synthesis of MSQD-CN, certain amounts of MoS₂ QDs solutions were sonicated for 30 min to achieve complete dispersion of the MoS₂ QDs. The as-synthesized g-C₃N₄ (0.1 g) was milled into fine powder and added to the above solution, followed by ultrasonication for 1 h. Then 10 mL acetone was added to the solution to make MoS₂ QDs deposit onto the surface of g-C₃N₄ with vigorous stirring for 24 h. After that, the precipitates were collected by centrifugation, washed with ethanol and distilled water successively, and dried at 80 °C overnight. The samples were further heated under N₂ flow at 300 °C for 1 h and noted as x wt% MSQD-CN, where x = 0, 0.2, 2.5, 5, and 7.5, respectively, representing different weight percentages of MoS₂ QDs at 0, 0.2, 2.5, 5, and 7.5 wt%. For comparison, one sample of 5 wt% MSQD-CN was synthesized following the same procedures except for the final heat treatment under N₂ flow at 120 °C for 1 h and noted as 5 wt% MSQD-CN-120 °C.

Moreover, MoS₂ nanosheets were prepared based on a previous report[19]. Ammonium molybdate (32.2 mg) and thiourea (25.12 mg) were dissolved in 40 mL distilled water followed by vigorous stirring for 1 h. Next, the homogeneous solution was transferred into a 100 mL Teflon-lined autoclave and maintained at 210 °C for 24 h. After centrifugation, the black precipitate was collected and washed with distilled ethanol and water successively, followed by drying at 80 °C. The assembly of MoS₂ nanosheets on g-C₃N₄ was achieved following the same route as 5 wt% MSQD-CN, and noted as 5 wt% MSNS-CN. Pt co-catalyst at 2.0 wt% was loaded by dissolving H₂PtCl₆ into the suspension directly, followed by ultrasonication for 10 min.

5.2.2 Characterization Techniques

Powder X-ray diffraction (XRD) patterns were obtained on an Empyrean multipurpose research diffractometer (Panalytical Empyrean XRD) utilizing Cu K α radiation ($\lambda = 1.5418 \text{ \AA}$) with a current of 40 mA and a voltage of 40 kV. Images of scanning electron microscopy (SEM) were recorded on a FEI Verios XHR SEM microscope. Transition electron microscopy (TEM) images and selective area electron diffraction (SAED) were received with a JEOL 2100 TEM microscope. High angle annular dark field scanning transmission electron microscopy image (HAADF-STEM) mapping was obtained under a FEI TITAN G2 (200 kV). X-ray

photoelectron spectroscopy (XPS) and valence band XPS (VB XPS) were conducted on a Thermo Escalab 250 spectrometer with an Al K α X-ray. A Shirley background was first subtracted followed by component fitting using Voigt functions with a 30% Lorentzian component. Fourier transformed infrared (FTIR) spectra were collected on a PerkinElmer Spectrum Two FT-IR spectrometer. UV-visible diffuse reflectance spectra (DRS) were obtained on an Agilent Cary 100 UV-Visible spectrophotometer equipped with an integrated sphere attachment. Photoluminescence (PL) spectra of the samples were measured on a Cary Eclipse Fluorescence Spectrophotometer (Agilent, US).

5.2.3 Photocatalytic Activity Evaluation

Photocatalytic H₂ production experiments were carried out in a customized airtight stainless steel cell covered by a quartz window at ambient temperature. A 300 W Xenon lamp (Newport) was used as a light source with irradiation intensity centered at 35 mW/cm² for UV light and 320 mW/cm² for visible light using a light cutoff filter ($\lambda > 420$ nm). Typically, 50 mg of photocatalyst was dispersed in an aqueous solution (120 mL) containing methanol (25% by volume). The loading of 2.0 wt% Pt co-catalyst was conducted by directly dissolving H₂PtCl₆ into the suspension. Before irradiation, the suspensions were mixed under vigorous stirring for 30 min in the dark and the reaction vessel was degassed for anaerobic conditions by purging with N₂ for 30 min. The produced H₂ was in situ analyzed by a gas chromatography (Agilent 490 Micro GC) using a thermal conductivity detector.

5.2.4 Photoelectrochemical Measurements

Photocurrent, electrochemical impedance spectroscopy (EIS) and Mott-Schottky curve measurements were conducted on a Zennium electrochemical workstation (Zahner, Germany) in a standard three-electrode framework with a 0.05 M Na₂SO₄ (pH = 6.8) electrolyte solution, adopting a Pt wire as the counter electrode and a saturated calomel electrode (SCE) as the reference electrode. As for the photoanode, the sample film was fabricated on fluorine-doped tin oxide (FTO) glasses, which were ultrasonically cleaned in acetone and ethanol for 20 min in sequence, then dried at 60 °C. To be specific, 10 mg of the catalyst was mixed with 500 μ L of absolute ethanol and 25 μ L of Nafion solution homogeneously. The obtained slurry was then dropped onto the pretreated FTO glass via a dip-coating method with a controlled area of 1 cm², followed by drying in air for 2 h to form a film electrode. Photocurrents were obtained using a 300 W Xenon arc lamp with light passing through an AM 1.5 G filter into an optical

fiber (output $I_0 = 100 \text{ mW} \cdot \text{cm}^{-2}$). Mott-Schottky analysis was performed at a frequency of 1 kHz.

5.2.5 Electrocatalytic Hydrogen Evolution

Electrochemical measurements were carried out at room temperature on a Zennium electrochemical station (Zahner, Germany) in a standard three-electrode system, loading the samples on a glassy carbon electrode (GCE, 5 mm in diameter) as the working electrode, a Ag/AgCl electrode as the reference and a Pt wire as the counter electrode. The electrolyte was 0.5 M H_2SO_4 purged with N_2 gas (99.999%). Specifically, the catalysts of 5 mg were dispersed in 600 μL ethanol absolute and 50 μL 5% Nafion via ultrasonication for 1 h to form a homogeneous ink. Then 5 μL of the slurry was deposited on the glassy carbon electrode with a catalyst loading of $0.196 \text{ mg} \cdot \text{cm}^{-2}$. The HER performance was tested by linear sweep voltammetry (LSV) at a scan rate of $10 \text{ mV} \cdot \text{S}^{-1}$. All the polarization curves were obtained without the ohmic potential drop (iR) correction.

5.3 Results and Discussion

5.3.1 Phase Structure, Morphology and Composition of Catalysts

Figure 5.1a displays XRD patterns of MSQD-CN samples with different MoS_2 QD contents (0 - 7.5 wt%). Both pristine g- C_3N_4 and MSQD-CN had two apparent diffraction peaks. The one centering at 27.7° can be indexed to the stacking of the conjugated double bonds for graphitic materials as the (002) crystal plane, corresponding to an interplanar distance of g- C_3N_4 at 0.336 nm, while the weak one at 12.9° represents the (100) plane of g- C_3N_4 , corresponding to the in-planar ordering of tri-s-triazine units of 0.675 nm[27]. These results confirm the formation of g- C_3N_4 with a typical graphitic, layered structure as in the previous reports[20, 28]. As shown in Figure 5.1c for bare MoS_2 QDs, the appearance of a strong (002) reflection and a weak (110) reflection confirm the presence of MoS_2 quantum dots with hexagonal 2H- MoS_2 structure of JCPDS No. 37-1492[13]. While the other peaks could be ascribed to the reflections from the substrate of quartz glass. In contrast, no apparent peaks of MoS_2 could be observed from the MSQD-CN samples, illustrating that the g- C_3N_4 nanosheet structure maintained unchanged with MoS_2 modification, possibly due to the small amount and well dispersed MoS_2 QDs on the g- C_3N_4 surface.

The elemental composition and chemical states of 5 wt% MSQD-CN sample were investigated by XPS (Figure 5.1b and Figure 5.2). Figure 5.1b presents the XPS survey spectrum of the composite, containing elements of C, N, O and also a small amount of Mo and S. Typical peaks could be observed at binding energies of 282.6 (C 1s), 393.4 (N 1s), 527.1 (O 1s), 226.4 (Mo 3d) and 163.7 eV (S 2p). The C 1s peak in Figure 5.2a can be deconvoluted into two peaks at 288.1 and 284.6 eV. The strong one at 288.1 eV could be ascribed to sp^2 carbon bonded to the three nitrogen atoms in the carbon nitride lattice[28-30], and the weak one corresponds to unavoidably loaded graphitic carbon atoms[31, 32]. Four asymmetrical peaks at 393.9, 395.0, 396.5 and 399.8 eV can be fitted for N1s in Figure 5.2b, which can be ascribed to C–N=C sp^2 -bonded N atoms in graphite-like $g-C_3N_4$ structure, tertiary (N–(C)3) groups, amino functional groups (C–N–H), and a typical π -excitation accordingly [27, 33-35].

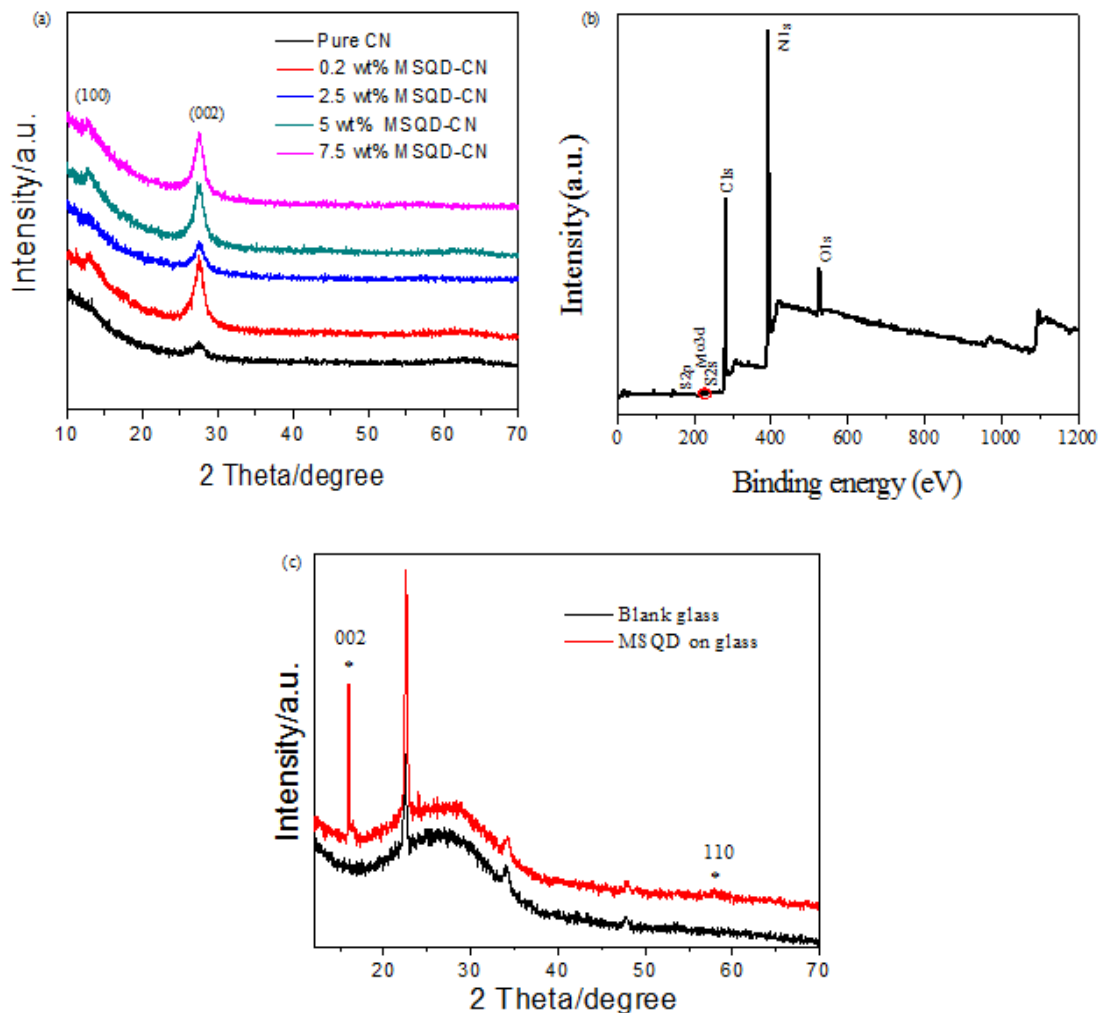


Figure 5.1. (a) XRD patterns of MSQD-CN composite samples and pure $g-C_3N_4$. (b) XPS survey of 5 wt% MSQD-CN. (c) XRD patterns of MoS_2 QDs sample.

The observed peaks of Mo 3d at 227.6 (3d_{5/2}) and 230.7 eV (3d_{3/2}) in Figure 5.2c indicate that Mo element exists predominantly as Mo⁴⁺ in the composite sample. No oxidation of Mo from Mo⁴⁺ state in the MoS₂ to Mo⁶⁺ in MoO₃ occurred. The S 2p spectrum (Figure 5.2d) gives two main peaks at 162.8 and 164.3 eV, corresponding to the S 2p_{3/2} and S 2p_{1/2}, respectively, demonstrating the existence of S²⁻ state in the composite sample[18]. The high-resolution spectra further confirmed the existence of MoS₂ QDs in the as-synthesized 5 wt% MSQD-CN sample.

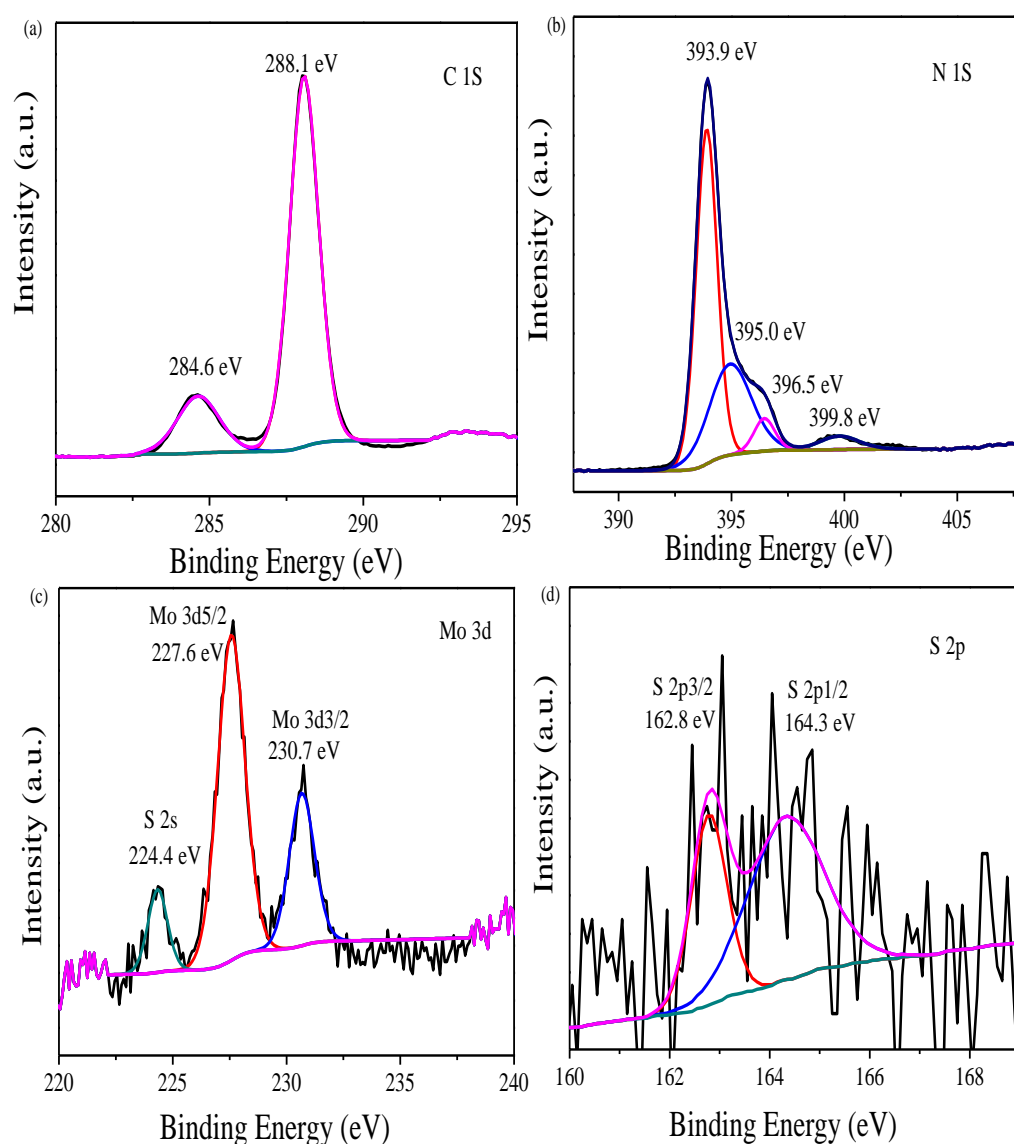


Figure 5.2. (a) C 1s (b) N 1s (c) Mo 3d and (d) S 2p spectra of 5 wt% MSQD-CN.

Figure 5.3 shows the typical SEM and TEM images of a light yellow fluffy powder of g-C₃N₄, exhibiting a typical layered sheet-like structure. The microstructure and morphology of

MoS₂ QDs was revealed by transmission electron microscopy (TEM). Figure 5.4a shows that the mean diameter of MoS₂ QDs particles is about 1.7 nm. According to the inset graph of particle size distribution, total up to 89.2% MoS₂ QDs distributes within the range of 1.5~2.5 nm, which are homogeneous without obvious aggregation. A typical hexagonal lattice structure with high crystallinity can be observed with ordered lattice fringe (103) from the high-resolution transmission electron microscopy (HRTEM) image in Figure 5.4b, showing a lattice spacing of 0.230 nm in the inset amplified image[36]. TEM images of the 5 wt% MSQD-CN composite sample (Figure 5.4c) reveal that thin and sheet-like g-C₃N₄ was decorated with crystallized MoS₂ QDs in random distribution. As shown in Figure 5.4d, the lattice distance of g-C₃N₄ crystallites was measured to be 0.34 nm, corresponding to the (002) plane of hexagonal g-C₃N₄ (JCPDS 87-1526) and in conformity with the XRD results. Meanwhile, the lattice spacing of 0.59 nm (JCPDS 37-1492), corresponding to the (002) facet of MoS₂ QDs, was also observed. Thus, the MoS₂ QDs were proved to be closely attached to the g-C₃N₄ nanostructure via their (002) crystal planes with intimate interfacial contact, which might be favorable for promoting the charge separation in the electron-transfer process for photocatalytic H₂ evolution. In addition, the HAADF-STEM elemental mapping (Figure 5.4e) of 5 wt% MSQD-CN sample further proves that MoS₂ QDs were immersed well into a broader g-C₃N₄ matrix with the elements of Mo and S exhibiting a low density at the same location.

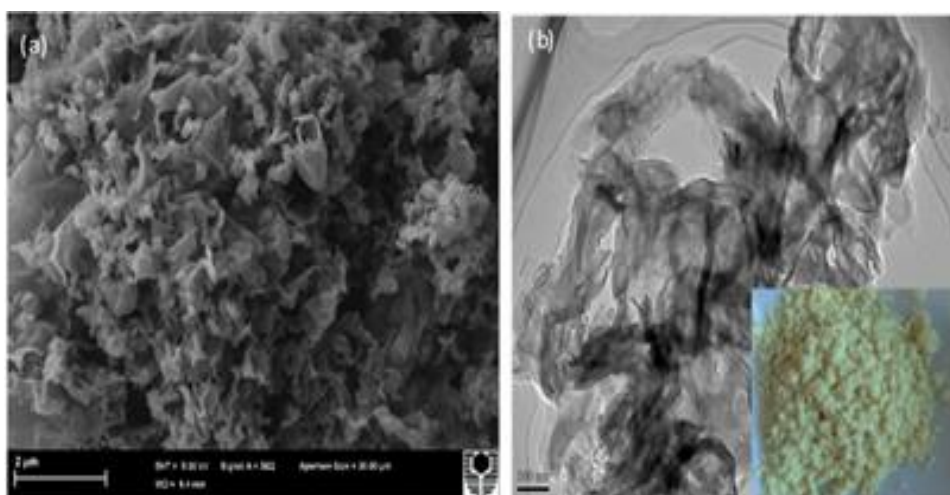


Figure 5.3. (a) SEM image and (b) TEM image and photograph (inset) of g-C₃N₄.

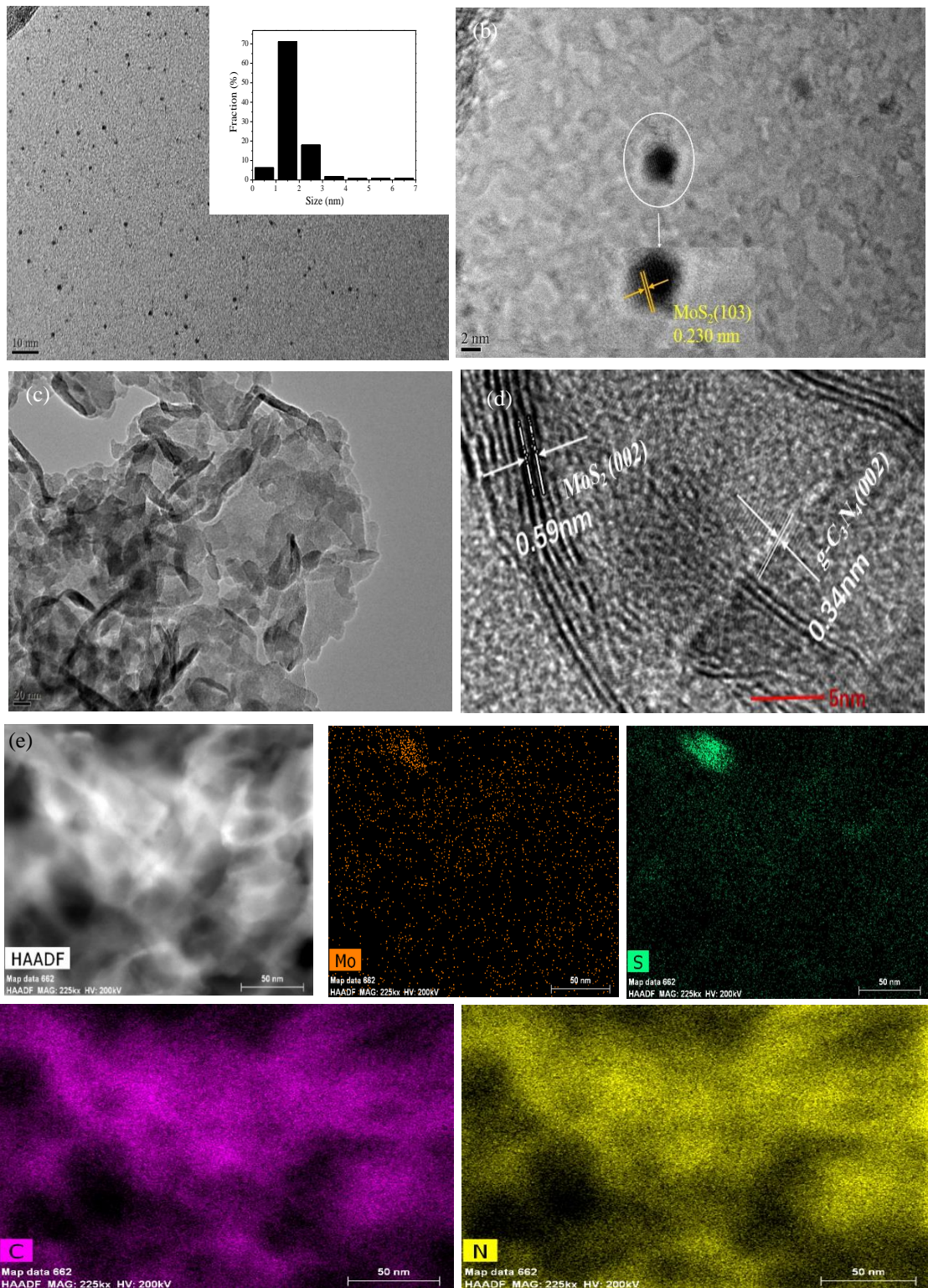


Figure 5.4. TEM and HRTEM images of (a-b) MoS₂ QDs (insert shows corresponding particle size distribution); (c-d) 5 wt% MSQD-CN; (e) High angle annular dark field scanning TEM image and corresponding EDX elemental mapping of 5 wt% MSQD-CN sample.

5.3.2 Optical Properties

The optical absorption properties of g-C₃N₄, MoS₂ QDs and MSQD-CN composites are shown in Figure 5.5. For the MoS₂ QDs, it can be observed from Figure 5.5c that the peaks at 207 and 230 nm show excitonic features of MoS₂ quantum dots[36, 37]. The peaks at 380 and 367 nm should be assigned to excitonic absorption bands due to direct band-gap transition at K point with energy split from valence band spin-orbital coupling[26]. Compared to the absorption edge of bulk MoS₂ and monolayer MoS₂ nanosheets in previous reports[19, 38], a large blue-shift was observed due to the strong quantum confinement effect[39] of MoS₂ QDs as the majority of the particles are within the size of 2-5 nm. The inset image in Figure 5c exhibits the high stability and good dispersion of MoS₂ QDs in water without noticeable agglomeration for two months. As can be seen from Figure 5.5a, the steep edge at around 380 nm should be assigned to the band gap transition of g-C₃N₄ [40]. For the composite samples, all of their absorption edges present a slight red-shift. In addition, the introduction of MoS₂ QDs enhanced both UV and visible light absorption capacity of the composite samples. It is worth noting that 5 wt% MSQD-CN outperformed other samples, which might lead to enhanced production of electron-hole pairs and thus a possibly higher photocatalytic activity. The band-gap energies of all the samples were estimated based on the Kubelka-Munk theory [9, 40, 41] following the equation of $(\alpha h\nu)^n = k (h\nu - E_g)$ (where α , ν , k and E_g represents absorption factor, light frequency, proportionality constant and band gap energy respectively). Based on the UV-vis diffuse reflectance spectra in Figure 5.5a and Figure 5.5c, $(\alpha h\nu)^n$ ($n = 2$ for direct-gap semiconductors and $n=1/2$ for indirect-gap semiconductors) versus $h\nu$ was then plotted in Figure 5.5b and Figure 5.5c (inset) with values shown in Table 5.1. The decreased band-gap energy of the composite with the increasing content of MoS₂-QDs proves that the MoS₂ QDs decoration changed the semiconductor composite properties of g-C₃N₄ due to mutual interaction. The direct band-gap energy for pure MoS₂-QDs has been determined to be 3.41 eV. As for pristine g-C₃N₄, the band-gap value of 2.90 eV is larger than bulk g-C₃N₄, and much closer to g-C₃N₄ nanosheets according to previous reports[42-44], which proved that the g-C₃N₄ prepared in this study exhibits a thin, sheet-like structure. This enlarged band-gap energy of nanostructured semiconductor compared to its bulk counterpart is also attributed to

the well-known quantum confinement effect, shifting its absolute conduction and valence band in opposite directions[45].

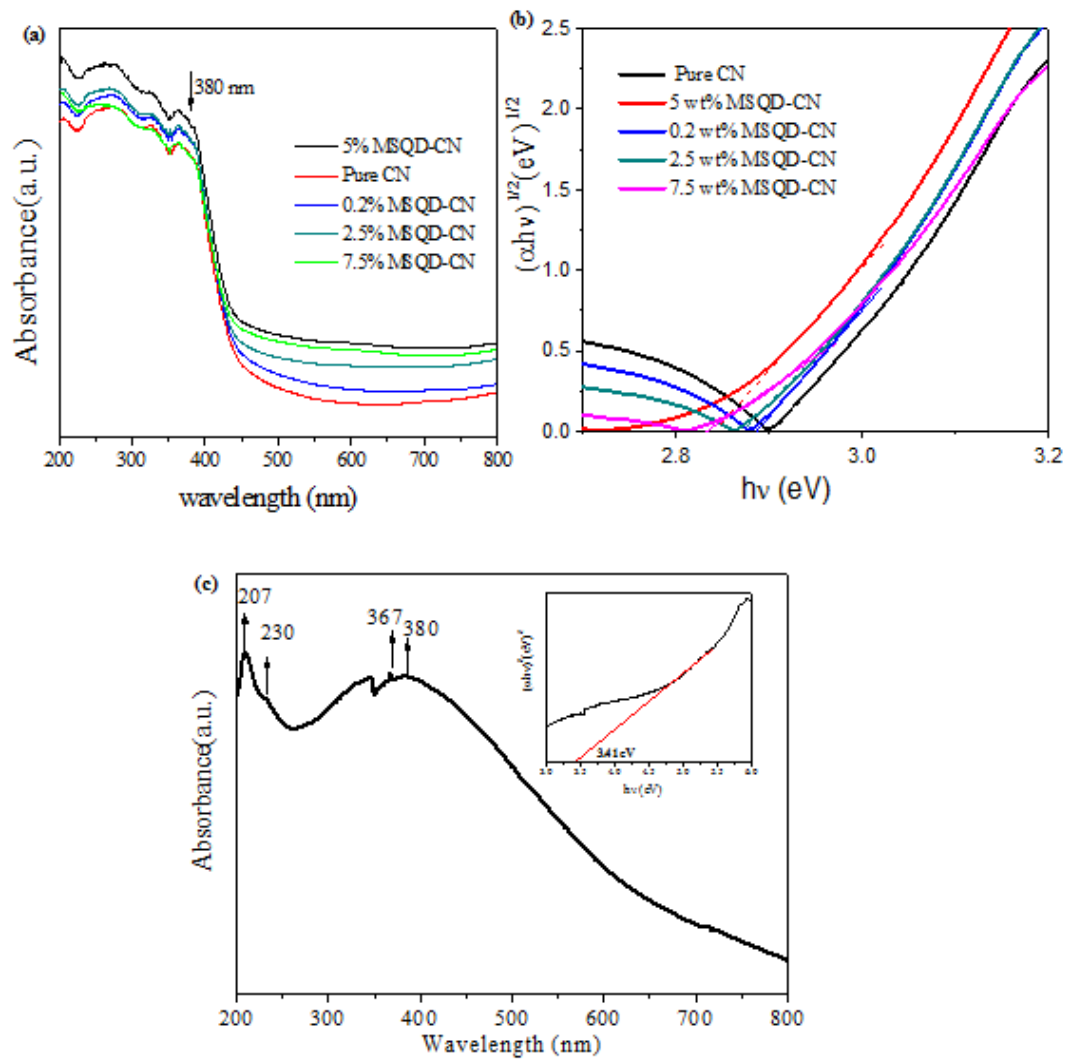


Figure 5.5. (a) UV-vis diffuse reflectance spectra, (b) the plots of $(\alpha hv)^{1/2}$ versus band-gap energy ($h\nu$) of $g\text{-C}_3\text{N}_4$ and different MSQD-CN samples. (c) UV-vis absorption spectrum of MoS_2 QDs. Left insert: photograph (inset) of MoS_2 QDs aqueous solution; right insert: the plots of $(\alpha hv)^2$ versus band-gap energy ($h\nu$).

Table 5.1. Band-gap energy of $g\text{-C}_3\text{N}_4$ and MSQD-CN composites.

Sample	Band-gap (eV)
$g\text{-C}_3\text{N}_4$	2.90

0.2 wt%MSQD-CN	2.88
2.5 wt%MSQD-CN	2.87
5 wt%MSQD-CN	2.84
7.5 wt%MSQD-CN	2.83
MSQD	3.41

To investigate the charge carrier separation, transferring, and trapping in pure g-C₃N₄ and MSQD-CN composite samples, the photoluminescence (PL) was conducted (Figure 5.6a). All the photocatalysts exhibit similar emission trends at an excitation wavelength of 325 nm at room temperature. The main emission peak centered at around 460 nm for pure g-C₃N₄ is attributed to the recombination of the photoexcited electron-hole pairs originating from the intrinsic HOMO–LUMO transition [27, 32]. The main emission peaks of the MSQD-CN composites shift slightly to the left, compared with the spectrum of pure g-C₃N₄. This blue shift of fluorescence emission spectrum further confirmed the enlarged band-gap energy after introduction of MoS₂ QDs. The only exception is for the sample of 0.2 wt% MSQD-CN, which might be due to extremely low content of MoS₂ QDs. Looking into the peak intensities around 640 nm, both 5 wt% MSQD-CN and 2.5 wt% MSQD-CN show a lower PL intensity relative to g-C₃N₄. This observation indicated that the quantum-sized MoS₂ and its heterojunction with g-C₃N₄ induced efficient charge transfer at the interface, suppressing the recombination of photogenerated electrons and holes. The PL results were in agreement with UV-vis absorption behavior and the corresponding photocatalytic H₂ evolution activities shown in the next section. In addition, the PL spectra of pure MoS₂ QD were also investigated under different excitation wavelengths at room temperature (Figure 5.6b). Similarly, it also shows a marked blue-shift in comparison with those of monolayer MoS₂ nanosheets[26]. With the increase of the excitation wavelength from 220 to 400 nm, a red shift of emission peaks from 440 to 800 nm was observed, while its intensity decreased noticeably over the excitation wavelength ranging from 300 to 400 nm. This may be ascribed to the direct excitonic transitions from the K point of the Brillouin zone, the presence of polydispersity and various trap states in MoS₂ quantum dots [26, 36, 46-49]. The strongest emission peak occurs at excitation wavelength of 300 nm, which should result from the transition at K point with energy split of valence band [26]. Further on, it is observed that the emission wavelength of the PL also depends on the particle size of the MoS₂ QDs, possibly due to the quantum size effect. Based on previous studies [48], medium-

sized MoS₂ QDs (1.5-3 nm) usually emit visible light within the range of 400–700 nm, which is in accordance with the particle size measurements in TEM for MoS₂ QDs synthesized in this paper.

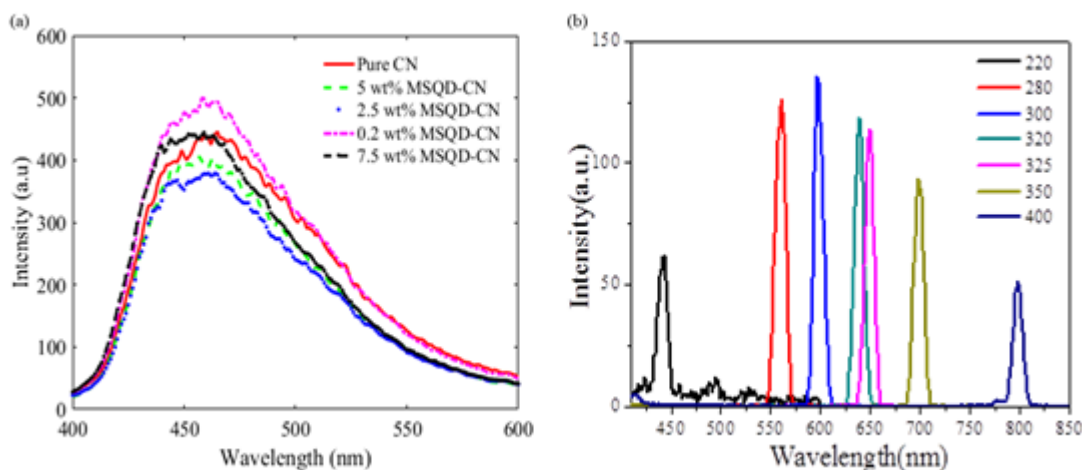


Figure 5.6. (a) PL spectra of pure g-C₃N₄ and different MSQD-CN samples. (b) PL spectra of MoS₂ QD aqueous solution excited by different wavelengths shifting from 220 to 400 nm.

5.3.3 Photocatalytic H₂-Production Activity and Stability

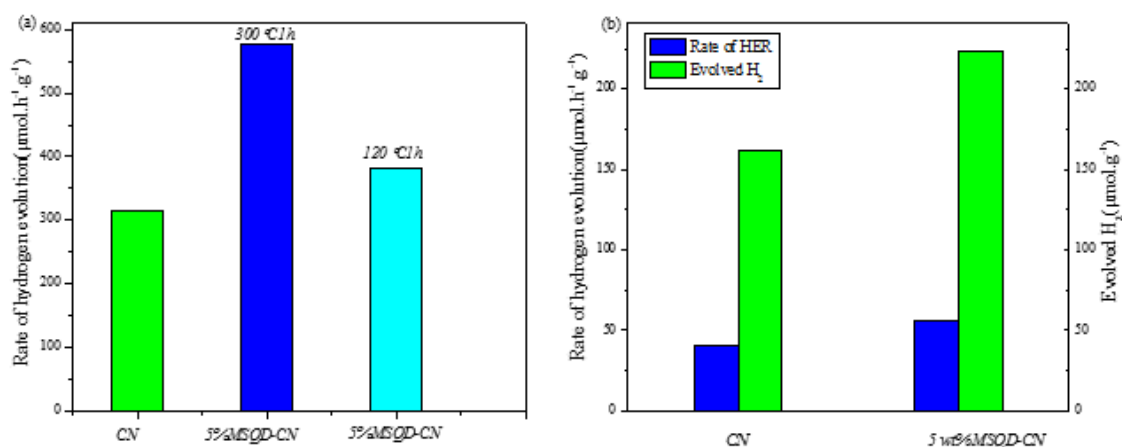


Figure 5.7. (a) Average rate of H₂ evolution for samples annealed at different temperatures. (b) Photocatalytic H₂ evolution over pure CN and 5 wt% MSQD-CN under visible light irradiation during 4 h (25 vol% methanol, 2.0 wt% Pt, 0.05g catalyst in 120 mL aqueous solution).

H₂ evolution on pure g-C₃N₄ and 5 wt% MSQD-CN samples annealed at different temperatures (120 and 300 °C) were tested (Figure 5.7a). The photocatalytic H₂-evolution rates

of 5 wt% MSQD-CN-300 °C and 5 wt% MSQD-CN-120 °C were elevated to approximately 1.8 and 1.5 times of the pristine g-C₃N₄, which might be ascribed to the establishment of efficient heterojunction between g-C₃N₄ and MoS₂ QDs.

The photocatalytic water reduction using different amount of MoS₂ QDs decorated g-C₃N₄ at 300 °C were further investigated (Figure 5.8). As a traditional and efficient co-catalyst, Pt is adopted to reduce the overpotential required for water splitting to H₂ evolution. Control experiments show no H₂ was detected with Pt or pure MoS₂ QDs only, indicating that Pt or MoS₂ QDs alone is not active for photocatalytic H₂ evolution. After 240 min of light irradiation, total hydrogen evolution over pure g-C₃N₄ reached 62.9 μmol. After impregnation with MoS₂ QDs, the photocatalytic H₂ evolution activity was significantly enhanced. The rate of H₂ evolution reached the maximum of 577 μmol.h⁻¹.g⁻¹ at 5 wt% MoS₂ QDs, which ranks among the top photocatalytic H₂ evolution activities based on recent studies as shown in Table 5.2. A further increase in MoS₂ QDs loading led to a drop in the photocatalytic hydrogen evolution. It is reported that excessive loading of MoS₂ may not be favorable for photo-redox catalytic reaction due to the blocking effect to hinder the light absorption of g-C₃N₄ [50]. This hypothesis conforms to the results from UV-vis spectra. Previous reports showed that MoS₂ with thin layers could improve charge transport across the layers by shortening the path and speeding up the transportation process for photo-generated electrons to enhance photocatalytic efficiency for hydrogen generation [15, 51]. Additionally, 5 wt% MSNS-CN exhibits a higher hydrogen-evolution rate than pure g-C₃N₄, but much lower than that on 5 wt% MSQD-CN. Compared with thin-layered MoS₂ nanosheet, which has been recognized as an effective HER catalyst [14, 52], MoS₂ quantum dots possess a higher quantum confinement and smaller-size, providing more opportunity for their unsaturated bonds to connect with other atoms to form an intimate contact between MoS₂ and g-C₃N₄. MoS₂ QDs also boost a superior HER activity by lowering activation barriers with a high electrical conductivity [21], leading to a higher photocatalytic H₂-evolution activity.

Table 5.2. Photocatalytic HER activities of graphitic carbon nitride modified with different cocatalysts.

Catalyst	Cocatalyst	Electron donor	λ (nm)	Hydrogen Evolution	Reference
----------	------------	----------------	-----------	-----------------------	-----------

				$(\mu\text{mol}\cdot\text{h}^{-1}\cdot\text{g}^{-1})$		
g-C ₃ N ₄	2.89 wt% MoS ₂	triethanolamine	sunlight	320	[53]	
g-C ₃ N ₄	1.5 polypyrrole+3 wt% Pt	acetic acid	Xe lamp	154	[54]	
g-C ₃ N ₄	0.15 wt% CoTiO ₃ + 3 wt% Pt	ethanol	Xe lamp	858	[55]	
g-C ₃ N ₄	3 wt% Pt	methanol	Xe lamp	300	[56]	
g-C ₃ N ₄	0.5%CB-1.0%NiS	TEOA	Xe lamp	366.4	[27]	
g-C ₃ N ₄	3 wt% CoP+3 wt% Pt	methanol	Xe lamp	1125	[57]	
g-C ₃ N ₄	5 wt% MSQD+ 2 wt% Pt	methanol	Xe lamp	576.6	This work	

As for visible light irradiation, it can be noticed in Figure 5.7b that 5 wt% MSQD-CN exhibited a slightly better photocatalytic H₂-evolution performance than pure g-C₃N₄. After 240 min of visible light irradiation, the total hydrogen evolution over g-C₃N₄ and 5 wt% MSQD-CN reached 162.2 and 222.9 $\mu\text{mol}\cdot\text{g}^{-1}$, respectively.

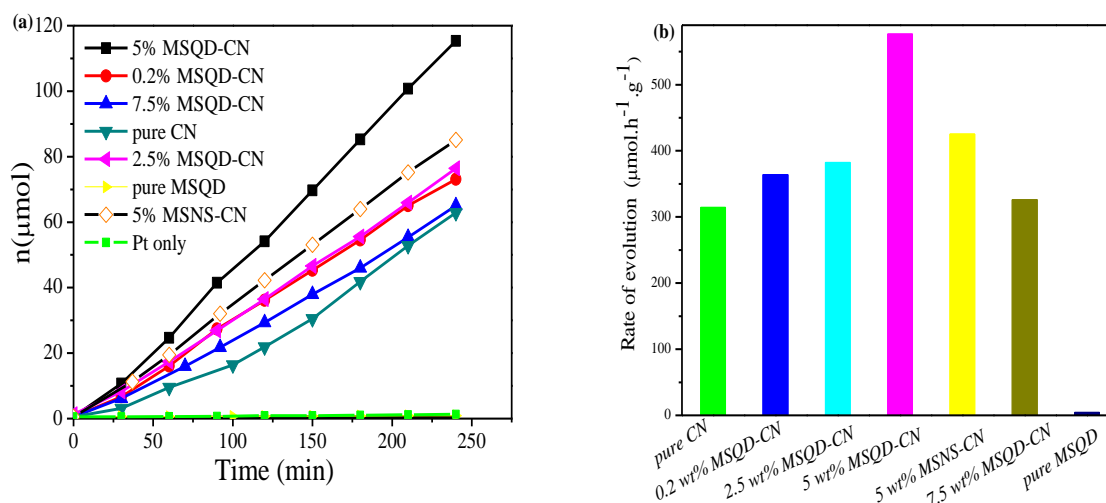


Figure 5.8. (a) Photocatalytic activity for H₂ evolution and (b) average photocatalytic H₂ evolution rate over different samples under simulated solar light irradiation. (25 vol% methanol, 2.0 wt% Pt, 0.05g catalyst in 120 mL aqueous solution)

In addition, it can be seen from Figure 5.9a that the as-synthesized 0.2 wt% MSQD-CN without Pt deposition showed a higher activity in photocatalytic H₂ evolution than 0.2 wt% Pt-

CN with an enhancement about 20%. The photocatalytic H₂ evolution was very low (only 3.29 μmol after 240 min) on g-C₃N₄ without loading any co-catalyst. An ideal co-catalyst often provides relatively low activation potentials for H₂ evolution and also promotes prompt transportation of photo-induced charge carriers, serving as the active sites for photocatalytic H₂ evolution [50]. As a noble metal, Pt is recognized as one of the best co-catalysts to promote H₂ evolution [58], but in this study the rate of H₂ evolution over 0.2 wt% Pt-CN is lower than that of 0.2 wt% MSQD-CN. This result proves that MoS₂ quantum dots could serve as an efficient co-catalyst with the potential to replace noble metals, constructing effective surface junctions with g-C₃N₄ with a structural and electronic compatibility, which is crucial for enhancing photocatalytic activity.

As mentioned above, no H₂ was detected on pure MoS₂-QDs. While the decoration of MoS₂-QDs on g-C₃N₄ was able to drastically improve the H₂ evolution from 16.45 μmol · h⁻¹ · g⁻¹ on pure g-C₃N₄ to 132.68 μmol · h⁻¹ · g⁻¹ on 0.2 wt% MSQD-CN in the absence of Pt. When Pt was loaded on the catalyst of 0.2 wt% MSQD-CN as an electron collector, the H₂ yield was further improved to 363.9 μmol · h⁻¹ · g⁻¹.

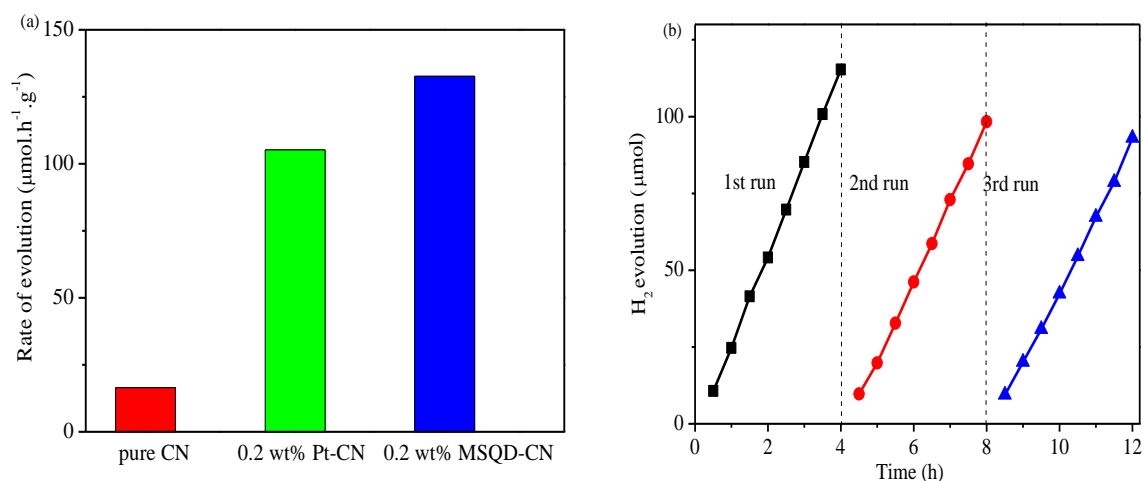


Figure 5.9. (a) Rate of H₂ production over CN loaded with different co-catalysts and (b) Cycle runs for the photocatalytic H₂ production on 5 wt% MSQD-CN (25 vol% methanol, 0.05 g catalyst in 120 mL aqueous solution).

The stability of 5 wt% MSQD-CN photocatalyst was further investigated in recycling photocatalytic experiments. Figure 5.9b displays the H₂ evolution in a 12 h photocatalytic run with 4 h intermittence over the sample of 5 wt% MSQD-CN. Only a slight decrease of

photocatalytic H₂ evolution was detected for 5 wt% MSQD-CN composite after three recycling runs. The XRD and FT-IR profiles in Figure 5.10 reveal that no apparent change occurred on 5 wt% MSQD-CN before and after the three cycles of photocatalytic H₂ evolution reactions. It is inferred that the small loss of activity might be attributed to the oxidation or corrosion of MoS₂ by photo-induced holes during the reaction process[50]. These results confirm that the MSQD-CN composites possess sufficient stability without structural change during the photocatalytic reaction process.

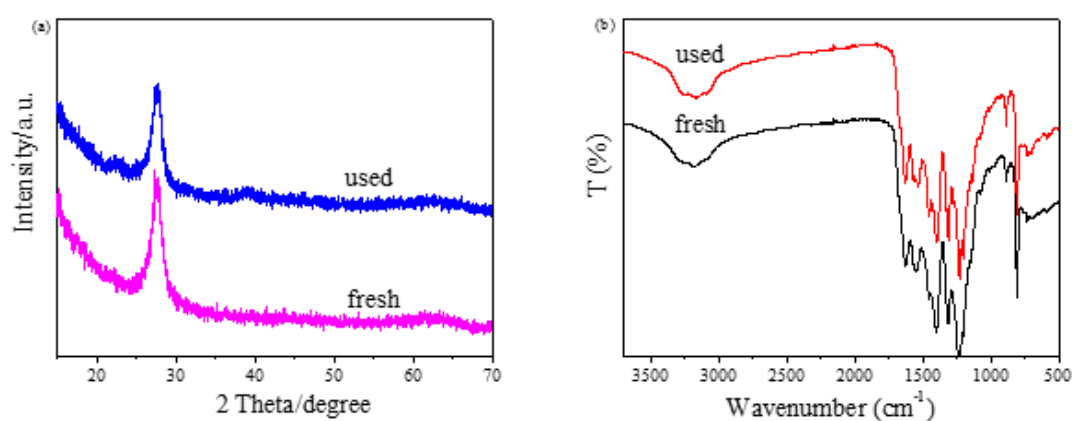


Figure 5.10. (a) XRD patterns and (b) FT-IR spectra for 5 wt% MSQD-CN before and after three cycles of reactions.

5.3.4 Photocatalytic Mechanism

Photoelectrochemical properties of the catalysts were explored concerning the charge transfer and separation rates for photocatalytic mechanism. Transient photocurrents of g-C₃N₄ and 5 wt% MSQD-CN were studied (Figure 5.11). Compared with g-C₃N₄, the photocurrent intensity of 5 wt% MSQD-CN decreased but exhibited a higher stability after four cycles. The photocurrent was obtained by guiding photo-induced electrons moving to external circuit. The density of photocurrent depends on many factors, such as the quality of working electrode, light harvesting ability of samples, and transfer efficiency of electrons. Therefore, the measured photocurrent intensity is not closely correlated with its photocatalytic performance. To further verify the relationship between photoactivity and electrochemical properties, electrochemical impedance spectroscopy (EIS) was adopted to complement the photocurrent curves as a more convincing and powerful technique in studying the interfacial charge transport behavior and efficiency [59, 60]. EIS measurements were performed and recorded in the semicircular Nyquist diagram as shown in Figure 5.12a. It is observed that the arc radius of the Nyquist plot of 5 wt% MSQD-CN is much smaller compared to that of pure g-C₃N₄ and MoS₂ quantum dots,

indicating a lower charge transfer resistance with improved charge separation efficiency. This result further confirms that the decoration of MoS₂ quantum dots on g-C₃N₄ could accelerate charge separation and transportation with a much slower recombination rate of photo-generated electron/hole pairs, which is a key contributor to the enhancement of photocatalytic H₂ production and also in agreement with the above PL results.

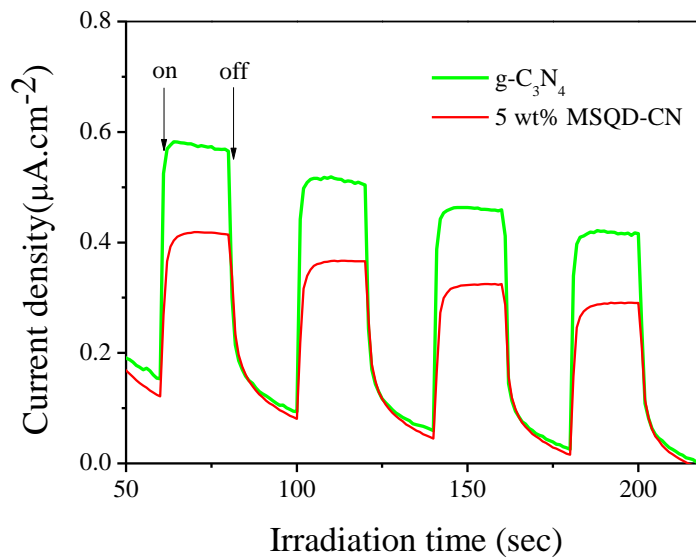


Figure 5.11. Transient photocurrent of g-C₃N₄ and 5 wt% MSQD-CN.

To gain further insights into the intrinsic properties of the heterojunction between MoS₂ QDs and g-C₃N₄, Mott-Schottky (M-S) measurements were conducted to determine the flat band potential values as well as electronic band structure shifts (Figure 5.12b-d), which can be estimated from the plots based on equation (5.1),

$$1/C^2 = (2/\epsilon_r \epsilon_0 e N_d A^2) [(V - V_{fb}) - kT/e] \quad 5.1$$

where V_{fb} (the flat band potential) can be obtained from the intercept of the plot tangents on X-axis when plotting $1/C^2$ (C is the specific capacity) versus V (V is the applied potential). The positive slope of the tangent lines in Figure 5.12b indicates that g-C₃N₄ is an n-type semiconductor, for which the lowest potential of conduction band (CB) can be extremely close to its flat-band potential. While for MoS₂ QDs, a typical p-type semiconductor was observed with a negative slope of the plot in Figure 5.12c, whose highest potential of valence band (VB)

could be estimated from its flat-band potential accordingly. The flat band potentials of n-type g-C₃N₄ and p-type MoS₂ QDs were calculated to be -1.10 V vs. SCE (-0.86 V vs. NHE) and 0.99 V vs. SCE (1.23 V vs. NHE), respectively[61]. It is worth noting that an inverted ‘V-shape’ is present in Figure 5.12d, confirming that a p-n heterojunction forms at the interface between g-C₃N₄ and MoS₂ QDs with distinct electronic behavior [61]. Therefore, an internal electrical field (E_{internal}) will be formed with a direction from n-type g-C₃N₄ to p-type MoS₂, leading to much more efficient charge separation of the photo-generated electrons and holes. The formation of p-n junction could help to explain the decrease of photocurrent in Figure 5.11 due to possible existence of short-circuit as opposed to flowing photoelectrons to some extent. To better elucidate the photocatalytic mechanism and draw the schematic diagram of energy band structure, the exact CB and VB positions for g-C₃N₄, MoS₂ QDs and 5 wt% MSQD-CN were also verified by valence band (VB) XPS spectra measurement, which could give detailed information related to the total density of states (DOS) of the valence band of the samples [62-64] with results presented in Figure 5.13. As shown, the maximum VB energies of 5 wt% MSQD-CN, g-C₃N₄ and MoS₂ QDs could be calculated at about 1.88 eV, 2.05 eV and 1.23 eV respectively. Combined with band gap energy of 2.90 eV for g-C₃N₄ in Table 5.1, the minimum conduction band (CB) energy could be calculated to be at about -0.85 eV. Both of the results conform well with the flat band potential values estimated in Figure 5.12.

To further identify the roles of MoS₂ QDs as a co-catalyst in promoting H₂ evolution activity during the photocatalytic process, electrochemical polarization curves were obtained in a typical three electrode cell. Figure 5.14a depicts the electrocatalytic H₂-evolution activity for g-C₃N₄, MoS₂ QDs and different MSQD-CNs, showing an obvious cathodic current in the range of -0.4 ~ -1.0 V (versus Ag/AgCl) with respect to H₂ evolution reaction (HER). Clearly, MoS₂ QDs exhibited the lowest onset potential for H₂ evolution (only -0.44 V vs Ag/AgCl, obtained via the intercept of the plot tangents on horizontal axis) with the highest HER performance, while pure g-C₃N₄ showed the lowest HER activity with an onset potential of -0.54 V vs Ag/AgCl. After introduction of MoS₂ QDs, MSQD-CN sample exhibited proper onset potentials for H₂ evolution, revealing that the MoS₂ QDs plays a key role in decreasing the onset potential and improving electrocatalytic efficiency by acting as an active site. Consequently, the HER performance of MSQD-CN was enhanced with the lowering of activation barriers and improved kinetics for H₂ evolution. In addition, 5 wt% MSQD-CN sample (-0.47 V vs Ag/AgCl) outperforms 2.5 wt% MSQD-CN sample (-0.51 V vs Ag/AgCl) with a lower onset potential, which agrees well with the tests of photocatalytic H₂ evolution activity.

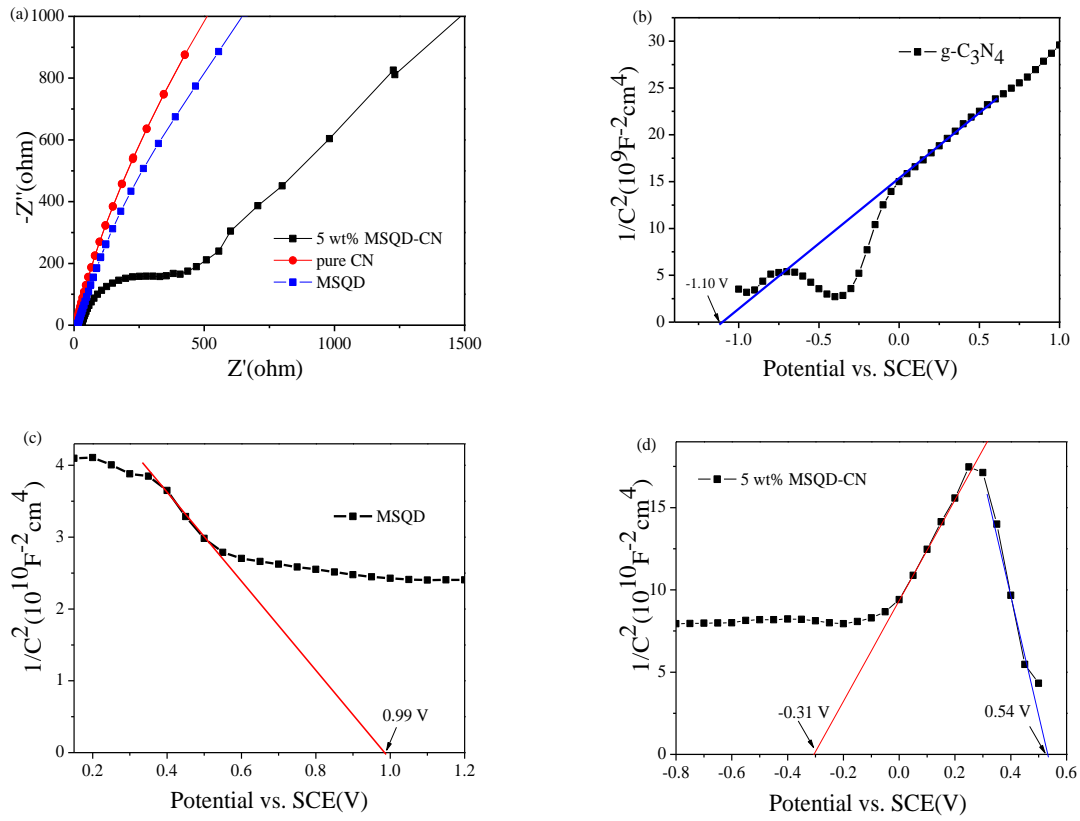


Figure 5.12. Nyquist plots of electrochemical impedance spectroscopy (EIS) with different electrodes in dark (a); Mott–Schottky curves collected on g-C₃N₄ (b), MoS₂ QDs (c) and 5 wt% MSQD-CN (d).

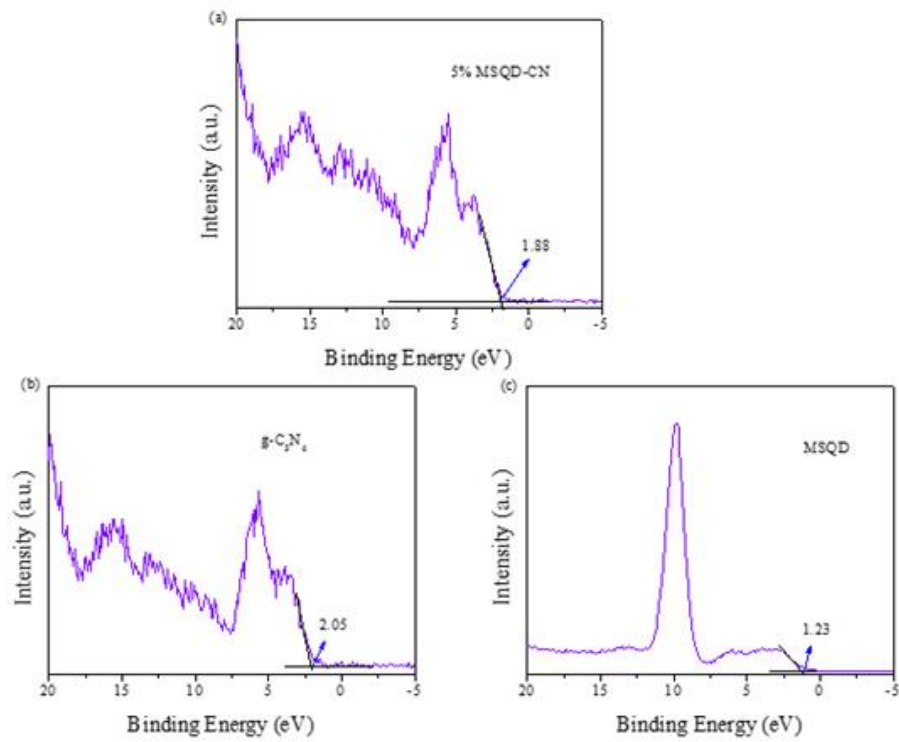


Figure 5.13. VB XPS spectra of (a) 5 wt% MSQD-CN, (b) g-C₃N₄ and (c) MoS₂ QDs.

Meanwhile, Figure 5.14b shows the electrocatalytic H₂-evolution activities of g-C₃N₄, as-synthesized MoS₂ nanosheets and 5 wt% MSNS-CN. Unlike the MSQD-CN, after introduction of MoS₂ nanosheets, the HER performance of 5 wt% MSNS-CN dropped significantly with an even higher onset potential. These results indicate that effective and intimate contact at the nanojunction of MoS₂ and g-C₃N₄ is of vital importance to lower activation barriers as well as electron transport, which may account for the inferior photocatalytic H₂ production on 5 wt% MSNS-CN to 5 wt% MSQD-CN.

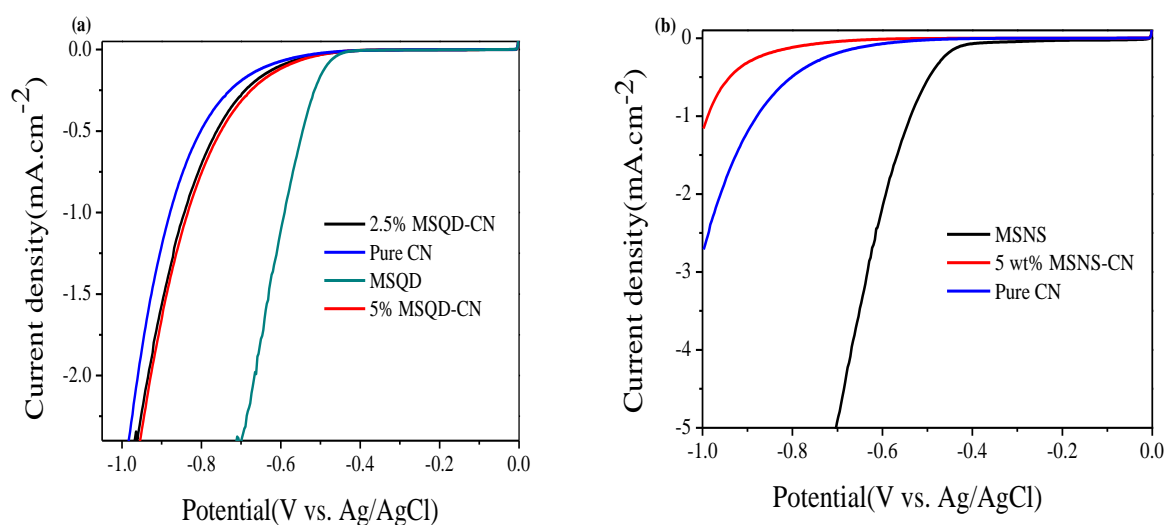


Figure 5.14. Polarization curves of g-C₃N₄, MoS₂ QDs and different composite photocatalysts (a); g-C₃N₄, MoS₂ nanosheets and 5 wt% MSNS-CN composite (b).

Based on the results and discussions above, it is concluded that the improved photocatalytic H₂-evolution activity of the MSQD-CN composites could be ascribed to the enhancement of light absorption capacity as well as much more efficient separation of photogenerated electron/hole pairs. It was reported that the distance between electrons and holes is crucial to the inhibition of efficient recombination and prolonged lifetime of charge carriers. As a co-catalyst, MoS₂ QDs cooperating with g-C₃N₄ could increase light absorption and lower the activation barriers for H₂ evolution, facilitating faster electron transfer across the interface with improved photocatalytic activity. However, thick layered MoS₂ nanosheet leads to the light blocking effect, not favorable for light utilization by g-C₃N₄. Optimal loading of 5 wt% MoS₂ QDs achieves the superior balance between light harvesting in g-C₃N₄ and charge transfer between g-C₃N₄ and MoS₂ QDs.

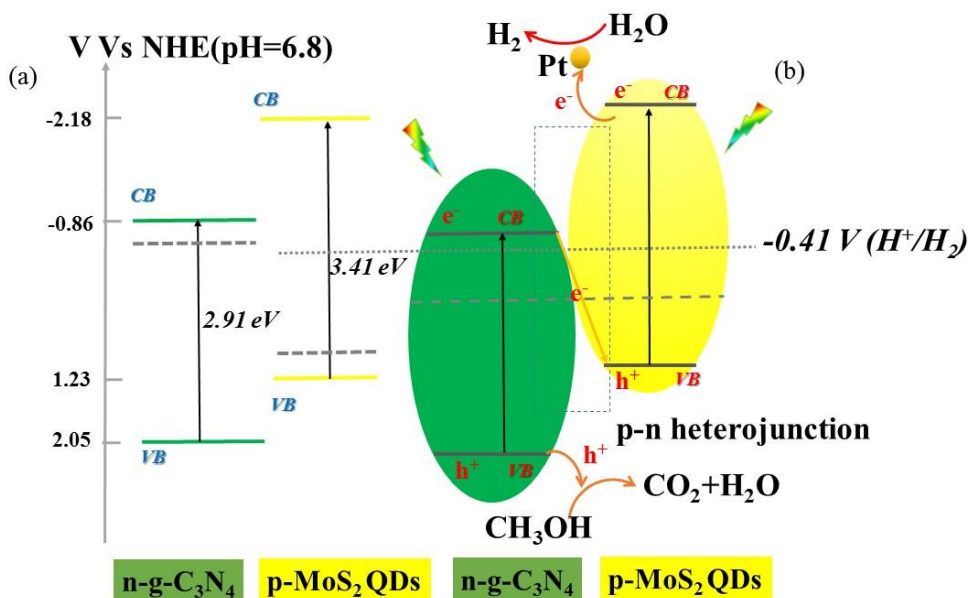


Figure 5.15. Schematic diagram of energy band structure and proposed mechanism (a) before contact; (b) after formation of g-C₃N₄ and MoS₂ QDs p-n heterojunction.

The energy band structure and photo-generated charge transfer scheme are illustrated in Figure 5.15. It is shown that the conduction band of MSQD-CN is properly positioned above the reduction level of H₂, which allows electrons to transfer for water reduction. From the band gap structures of MoS₂ QDs and g-C₃N₄, traditional heterojunction-transfer mechanism [24, 65-67] may not well interpret the results illustrated in Figure 5.15. In the traditional heterojunction-transfer mechanism, the photoexcited electrons will inevitably being transferred from the CB of MoS₂ QDs (-2.18 eV) to the CB of g-C₃N₄ (-0.86 eV), leading to the drop in electron reduction potential. As such, the electrons accumulated on the CB of g-C₃N₄ will experience difficulty in reducing H⁺ into H₂, especially in case of no Pt as cocatalyst (Figure 5.9a). According to recent reports[56, 68-70], the enhanced photocatalytic H₂-evolution activity could be properly explained following the PS-PS system of Z-scheme charge transfer mechanism for the MSQD-CN system. Under solar light irradiation, both of the electrons from the VB of MoS₂ QDs and g-C₃N₄ will be excited to the CB of MoS₂ QDs and g-C₃N₄ correspondingly. Owing to the short electron-migration distance between MoS₂ QDs and g-C₃N₄ nanosheets, the photogenerated electrons from CB of g-C₃N₄ will combine rapidly with the photogenerated holes from VB of MoS₂ QDs at the formed ohmic contact in the solid-solid interface. Therefore, more oxidative holes and reductive electrons will be retained in VB of g-

C₃N₄ and CB of MoS₂ QDs separately, leading to the enhancement of overall photocatalytic performance. Meanwhile, after coupling g-C₃N₄ and MoS₂ QDs, the internal electrical field was formed at the interfacial phases as a p-n heterojunction, promoting much more efficient charge separation of e⁻/h⁺ pairs[41]. MoS₂ QDs possess a more negative E_{CB} with strong reducibility as an electron collector with unsaturated active S atoms at the exposed edges and will easily reduce the bonded H⁺ to H₂[53]. Moreover, some electrons in the CB of MoS₂ QDs will also transfer to metallic Pt and then get involved in H₂ evolution. At this point, MoS₂ QDs boosts the H₂-evolution surface active sites over g-C₃N₄ nanosheets owing to its much lower electrocatalytic H₂-evolution overpotentials[21]. In a word, 5 wt% MSQD-CN exhibits an excellent photocatalytic H₂-evolution activity with enhanced light absorption ability, a smaller onset potential with a higher electrical conductivity and a stronger reductive capability. In addition, it is plausible to explain why the 5 wt% MSQD-CN sample shows a slightly higher photocatalytic H₂-evolution activity than pure g-C₃N₄ under visible light only. Under the visible light irradiation ($\lambda > 420$ nm), MoS₂ QDs with a large band gap energy of 3.41 eV can hardly get photoexcited, while only g-C₃N₄ with a smaller band gap energy can respond to visible light with photo-generated electrons and holes in the CB and VB of g-C₃N₄ respectively. As a result, the recombination without fast separation via Z-scheme charge transfer mechanism would thus occur.

5.4 Conclusions

In summary, uniform water-soluble MoS₂ QDs with sizes of 2-5 nm were prepared via a facile one-pot hydrothermal process and were employed to modify g-C₃N₄ nanosheets for MoS₂ QDs/g-C₃N₄ photocatalysts with high photocatalytic and electrochemical H₂ evolution activities. The introduction of MoS₂ QDs results in a red shift and stronger light absorption capability in comparison with pure g-C₃N₄. Owing to quantum confinement effect, MoS₂ QDs facilitate a faster electron transfer and efficiently prevent the charge recombination via lowering overpotential barriers and charge-transfer resistance. In addition, the well-matched band-structure of MSQD-CN composite conforms to Z-scheme charge transfer mechanism with a higher reductive capability, leading to the enhancement of photocatalytic H₂ evolution activity. The highest photocatalytic H₂ evolution activity was found on 5 wt% MSQD-CN, superior to the as-synthesized 5 wt% MSNS-CN. This study provides a novel strategy for designing p-n heterostructured photocatalysts for solar hydrogen production in the future.

References

- [1] N.S. Lewis and D.G. Nocera, *PNAS*, 2006, **103**, 15729-15735.
- [2] A. Fujishima, *Nature*, **1972**, 238, 37-38.
- [3] J. Liu, Y. Liu, N. Liu, Y. Han, X. Zhang, H. Huang, Y. Lifshitz, S.-T. Lee, J. Zhong and Z. Kang, *Science*, 2015, **347**, 970-974.
- [4] Y. Li, T. Takata, D. Cha, K. Takanabe, T. Minegishi, J. Kubota and K. Domen, *Adv. Mater.*, 2013, **25**, 125-131.
- [5] A. Kudo and Y. Miseki, *Chem. Soc. Rev.*, 2009, **38**, 253-278.
- [6] G.L. Zhou, H.Q. Sun, S.B. Wang, H.M. Ang and M.O. Tade, *Sep. Purif. Technol.* 2011, **80**, 626-634.
- [7] H.Q. Sun, Y. Bai, H.J. Liu, W.Q. Jin, N.P. Xu, G.J. Chen and B.Q. Xu, *J. Phys. Chem. C*, 2008, **112**, 13304-13309.
- [8] M.G. Walter, E.L. Warren, J.R. McKone, S.W. Boettcher, Q. Mi, E.A. Santori and N.S. Lewis, *Chem. Rev.*, 2010, **110**, 6446-6473.
- [9] H. Sun, G. Zhou, Y. Wang, A. Suvorova and S. Wang, *ACS Appl. Mater. Interfaces.*, 2014, **6**, 16745-16754.
- [10] L. Zhou, H.Y. Zhang, H.Q. Sun, S.M. Liu, M.O. Tade, S.B. Wang and W.Q. Jin, *CATAL SCI TECHNOL*, 2016, **6**, 7002-7023.
- [11] X. Wang, K. Maeda, A. Thomas, K. Takanabe, G. Xin, J.M. Carlsson, K. Domen and M. Antonietti, *Nat. Mater.*, 2008, **8**, 76.
- [12] K. Maeda, K. Teramura, D. Lu, T. Takata, N. Saito, Y. Inoue and K. Domen, *Nature*, 2006, **440**, 295-295.
- [13] J. Xie, H. Zhang, S. Li, R. Wang, X. Sun, M. Zhou, J. Zhou, X.W. Lou and Y. Xie, *Adv. Mater.*, 2013, **25**, 5807-5813.
- [14] Y. Hou, Z. Wen, S. Cui, X. Guo and J. Chen, *Adv. Mater.*, 2013, **25**, 6291-6297.
- [15] Y. Yang, H. Fei, G. Ruan, C. Xiang and J.M. Tour, *Adv. Mater.*, 2014, **26**, 8163-8168.
- [16] Y.J. Hong, T. Fukui and *ACS nano*, 2011, **5**, 7576-7584.
- [17] L.S. Byskov, J.K. Nørskov, B.S. Clausen and H. Topsøe, *J. Catal.* 1999, **187**, 109-122.
- [18] Q. Xiang, J. Yu and M. Jaroniec, *J. Am. Chem. Soc.*, 2012, **134**, 6575-6578.
- [19] W. Zhou, Z. Yin, Y. Du, X. Huang, Z. Zeng, Z. Fan, H. Liu, J. Wang and H. Zhang, *Small*, 2013, **9**, 140-147.
- [20] J. Li, E. Liu, Y. Ma, X. Hu, J. Wan, L. Sun and J. Fan, *Appl. Surf. Sci.*, 2016, **364**, 694-702.
- [21] F. Li, J. Li, Z. Cao, X. Lin, X. Li, Y. Fang, X. An, Y. Fu, J. Jin and R. Li, *J. Mater. Chem. A*, 2015, **3**, 21772-21778.
- [22] H. Xu, J. Yi, X. She, Q. Liu, L. Song, S. Chen, Y. Yang, Y. Song, R. Vajtai, J. Lou, H. Li, S. Yuan and J. Wu, P.M. Ajayan, *Appl. Catal., B: Environ.*, 2018, **220**, 379-385.
- [23] W. Fu, H. He, Z. Zhang, C. Wu, X. Wang, H. Wang, Q. Zeng, L. Sun, X. Wang, J. Zhou, Q. Fu, P. Yu, Z. Shen, C. Jin, B.I. Yakobson and Z. Liu, *NANO ENERGY*, 2016, **27**, 44-50.

- [24] S.A. Ansari and M.H. Cho, *Sci. Rep.*, 2017, **7**, 43055.
- [25] D. Zheng, G. Zhang, Y. Hou and X. Wang, *Appl. Catal., A: General*, 2016, **521**, 2-8.
- [26] H. Huang, C. Du, H. Shi, X. Feng, J. Li, Y. Tan and W. Song, *PART PART SYST CHAR*, 2015, **32**, 72-79.
- [27] J. Wen, J. Xie, Z. Yang, R. Shen, H. Li, X. Luo, X. Chen and X. Li, *ACS Sustain. Chem. Eng.*, 2017, **5**, 2224-2236.
- [28] L. Ge, F. Zuo, J. Liu, Q. Ma, C. Wang, D. Sun, L. Bartels and P. Feng, *J. Phys. Chem. C*, 2012, **116**, 13708-13714.
- [29] A. Thomas, A. Fischer, F. Goettmann, M. Antonietti, J.-O. Müller, R. Schlögl and J.M. Carlsson, *J. Mater. Chem.*, 2008, **18**, 4893-4908.
- [30] V.N. Khabashesku, J.L. Zimmerman and J.L. Margrave, *Chem. Mater.*, 2000, **12**, 3264-3270.
- [31] S. Yan, Z. Li and Z. Zou, *Langmuir*, 2009, **25**, 10397-10401.
- [32] X. Jin, X. Fan, J. Tian, R. Cheng, M. Li and L. Zhang, *RSC Adv.*, 2016, **6**, 52611-52619.
- [33] J. Duan, S. Chen, M. Jaroniec and S.Z. Qiao, *ACS nano*, 2015, **9**, 931-940.
- [34] J. Wen, X. Li, H. Li, S. Ma, K. He, Y. Xu, Y. Fang, W. Liu and Q. Gao, *Appl. Surf. Sci.*, 2015, **358**, 204-212.
- [35] L. Shi, L. Liang, F. Wang, M. Liu, K. Chen, K. Sun, N. Zhang and J. Sun, *ACS Sustain. Chem. Eng.*, 2015, **3**, 3412-3419.
- [36] X. Ren, L. Pang, Y. Zhang, X. Ren, H. Fan and S.F. Liu, *J. Mater. Chem. A*, 2015, **3**, 10693-10697.
- [37] V. Chikan and D. Kelley, *J. Phy. Chem. B: Environ.*, 2002, **106**, 3794-3804.
- [38] W. Ho, J.C. Yu, J. Lin, J. Yu and P. Li, *Langmuir*, 2004, **20**, 5865-5869.
- [39] H. Shi, R. Yan, S. Bertolazzi, J. Brivio, B. Gao, A. Kis, D. Jena, H.G. Xing and L. Huang, *ACS Nano*, 2013, **7**, 1072-1080.
- [40] H. Zhang, W. Tian, L. Zhou, H. Sun, M. Tade and S. Wang, *Appl. Catal., B: Environ.*, 2017, **223**, 2-9.
- [41] W. Zhao, Y. Liu, Z. Wei, S. Yang, H. He and C. Sun, *Appl. Catal., B: Environ.*, 2016, **185**, 242-252.
- [42] J. Tong, L. Zhang, F. Li, M. Li and S. Cao, *Phys. Chem. Chem. Phys.*, 2015, **17**, 23532-23537.
- [43] P. Niu, L. Zhang, G. Liu and H.-M. Cheng, *Adv. Funct. Mater.*, 2012, **22**, 4763-4770.
- [44] X. Wang, K. Maeda, A. Thomas, K. Takanebe, G. Xin, J.M. Carlsson, K. Domen and M. Antonietti, *Nat. Mater.*, 2009, **8**, 76-80.
- [45] A.P. Alivisatos, *Science*, 1996, **271**, 933.
- [46] D. Gopalakrishnan, D. Damien and M.M. Shaijumon, *ACS Nano*, 2014, **8**, 5297-5303.
- [47] Y. Wang and Y. Ni, *Anal. Chem.*, 2014, **86**, 7463-7470.
- [48] V. Stengl and J. Henych, *Nanoscale*, 2013, **5**, 3387-3394.
- [49] J.Z. Ou, A.F. Chrimes, Y. Wang, S.-y. Tang, M.S. Strano and K. Kalantar-zadeh, *Nano Lett.*, 2014, **14**, 857-863.

- [50] Y. Hou, A.B. Laursen, J. Zhang, G. Zhang, Y. Zhu, X. Wang, S. Dahl and I. Chorkendorff, *Angew. Chem., Int. Ed.*, 2013, **52**, 3621-3625.
- [51] X. Zong, H. Yan, G. Wu, G. Ma, F. Wen, L. Wang and C. Li, *J. Am. Chem. Soc.*, 2008, **130**, 7176-7177.
- [52] M.A. Lukowski, A.S. Daniel, F. Meng, A. Forticaux, L. Li, and S. Jin, *J. Am. Chem. Soc.*, 2013, **135**, 10274-10277.
- [53] H. Zhao, Y. Dong, P. Jiang, H. Miao, G. Wang and J. Zhang, *J. Mater. Chem. A*, 2015, **3**, 7375-7381.
- [54] Y. Sui, J. Liu, Y. Zhang, X. Tian and W. Chen, *Nanoscale*, 2013, **5**, 9150-9155.
- [55] R. Ye, H. Fang, Y.Z. Zheng, N. Li, Y. Wang and X. Tao, *ACS Appl. Mater. Interfaces*, 2016, **8**, 13879-13889.
- [56] G. Zhang, Z.-A. Lan, L. Lin, S. Lin and X. Wang, *Chem. Sci.*, 2016, **7**, 3062-3066.
- [57] Z. Pan, Y. Zheng, F. Guo, P. Niu and X. Wang, *ChemSusChem*, 2017, **10**, 87-90.
- [58] Y.-J. Tang, Y. Wang, X.-L. Wang, S.-L. Li, W. Huang, L.-Z. Dong, C.-H. Liu, Y.-F. Li and Y.-Q. Lan, *Adv. Energy Mater.*, 2016, **6**, 1600116.
- [59] J.G. Yu, J. Jin, B. Cheng and M. Jaroniec, *J. Mater. Chem. A*, 2014, **2**, 3407-3416.
- [60] X.P. Xiao, J.H. Wei, Y. Yang, R. Xiong, C.X. Pan and J. Shi, *ACS Sustain. Chem. Eng.*, 2016, **4**, 3017-3023.
- [61] J. Ke, J. Liu, H. Sun, H. Zhang, X. Duan, P. Liang, X. Li, M.O. Tade, S. Liu and S. Wang, *Appl. Catal., B: Environ.*, 2017, **200**, 47-55.
- [62] K. Shen, X. Xue, X. Wang, X. Hu, H. Tian and W. Zheng, *RSC Adv.*, 2017, **7**, 23319-23327.
- [63] X. Chen, L. Liu, P.Y. Yu and S.S. Mao, *Science*, 2011, **331**, 746-750.
- [64] J. Zhang, X. An, N. Lin, W. Wu, L. Wang, Z. Li, R. Wang, Y. Wang, J. Liu and M. Wu, *Carbon*, 2016, **100**, 450-455.
- [65] Y. Liu, S. Ding, J. Xu, H. Zhang, S. Yang, X. Duan, H. Sun and S. Wang, *CHINESE J CATAL*, 2017, **38**, 1052-1062.
- [66] Y. Liu, J. Xu, L. Wang, H. Zhang, P. Xu, X. Duan, H. Sun and S. Wang, *Nano Sci. Nano Technol. Indian J.*, 2017, **7**, 64.
- [67] M. Li, L. Zhang, X. Fan, M. Wu, Y. Du, M. Wang, Q. Kong, L. Zhang and J. Shi, *Appl. Catal., B: Environ.*, 2016, **190**, 36-43.
- [68] D. Lu, H. Wang, X. Zhao, K.K. Kondamareddy, J. Ding, C. Li and P. Fang, *ACS Sustain. Chem. Eng.*, 2017, **5**, 1436-1445.
- [69] J.C. Wang, H.C. Yao, Z.Y. Fan, L. Zhang, J.S. Wang, S.Q. Zang and Z.J. Li, *ACS Appl. Mater. Interfaces*, 2016, **8**, 3765-3775.
- [70] P. Zhou and J. Yu, M. Jaroniec, *Adv. Mater.*, 2014, **26**, 4920-4935.

Every reasonable effort has been made to acknowledge the owners of copyright material. I would be pleased to hear from any copyright owner who has been omitted or incorrectly acknowledged.

**Chapter 6. Flower-Like MoS₂ on Graphitic Carbon
Nitride for Enhanced Photocatalytic and Electrochemical
Hydrogen Evolutions**

Abstract

In the last chapter, we presented the fabrication of 0D (MoS₂)/2D (g-C₃N₄) heterojunctions with excellent photocatalytic H₂ evolution performances. To verify if a novel 3D (MoS₂)/2D (g-C₃N₄) superstructure would facilitate a prominently enhanced activity in both solar hydrogen evolution and electrochemical hydrogen generation from water splitting, flower-like MoS₂ nanoparticles with thin-layers were fabricated using a one-pot hydrothermal process and were further attached to g-C₃N₄ nanosheets via their (002) crystal planes to form an intimate face-to-face contact. The hybrid catalysts exhibited a red-shift to the visible light region with an enhanced absorption capacity. At the optimal loading of 0.5 wt% MoS₂, MoS₂/g-C₃N₄ exhibited the highest photocatalytic H₂ evolution rate of 867.6 μmol·h⁻¹·g⁻¹ under simulated sunlight irradiations, which is 2.8 times as high as that of pure g-C₃N₄. Furthermore, the average photocatalytic H₂ evolution rate was elevated to ca. 5 times as high as that of pure g-C₃N₄ under visible light irradiations. The synergistic effect responsible for the enhanced HER (hydrogen evolution reaction) performance might be originated from the intimate interface between the light-harvesting g-C₃N₄ and MoS₂ as the active sites with the decreased overpotential, lowered charge-transfer resistance and increased electrical conductivity, leading to a more efficient charge separation and a higher reductive potential. In addition, the lower overpotential and smaller Tafel slope on 0.5 wt% MoS₂/g-C₃N₄ lead to the enhancement of electrochemical HER performance compared to pure g-C₃N₄. This chapter provides a feasible protocol for rational design of three-dimensional (3D)/two-dimensional (2D) nanoarchitectures as highly efficient HER electrocatalysts and photocatalysts towards future energy innovation.

6.1 Introduction

As a clean and renewable energy carrier, hydrogen has been extensively acknowledged as an ideal source to mitigate the severe global energy crisis and environmental deterioration[1, 2]. Photocatalytic H₂ evolution utilizing solar energy as well as electrochemical H₂ evolution reaction (HER) via water splitting has aroused significant research interests worldwide[3-7]. Since Fujishima and Honda for the first time developed a TiO₂-based photoelectrochemical water splitting cell in 1972[8], numerous catalytic systems composed of an earth-abundant light-harvesting photocatalyst with an electronic conductive co-catalyst, especially noble-metal, have been constructed to achieve highly efficient photocatalytic H₂ evolution[9-12].

Most recently, two-dimensional (2D) semiconductors with a unique structure have triggered broad interests owing to their unprecedented optical and electronic properties [13, 14]. Among them, graphitic carbon nitride (g-C₃N₄) has attracted overwhelming research focus because of its narrow band gap, strong photoreduction capability as well as easy production from nitrogen-rich precursors[15-17]. Despite these fascinating merits, pure g-C₃N₄ still suffers from several shortfalls such as limited light absorption, easy recombination of electron/hole pairs and sluggish electrical conductivity. To resolve these bottlenecks, a strategy of incorporating 2D g-C₃N₄ with another co-catalysts with lamellar structures to form hybrid nanocomposites with an intimate contact interface has been proven to be highly effective with practical capabilities[18, 19]. Meanwhile, an ideal co-catalyst might also serve as the active sites to decrease the overpotentials for electrocatalytic H₂ evolution and lower the charge-transfer resistance to enhance the HER performance of g-C₃N₄[20]. Among a variety of layered materials, molybdenum sulfide (MoS₂) has demonstrated its excellent HER performance and can act as an efficient co-catalyst for solar-to-H₂ conversion[21-23]. The similarity of the layered structures between MoS₂ and g-C₃N₄ poses positive effects on charge transfer and formation of a newly built electric field at the interface between MoS₂ and g-C₃N₄ modulates the electronic band structures. Moreover, the unsaturated Mo and S atoms at the exposed edges will also promote the sulfur edge activity functioning as active sites[24]. So far, most of the reported MoS₂/g-C₃N₄ hybrids were constructed as either 2D (MoS₂)/2D (g-C₃N₄) or 0D (MoS₂)/2D (g-C₃N₄) heterojunctions via a complicated impregnation-sulfidation approach or under harsh reaction conditions[14, 25-27]. However, 2D MoS₂ layers tend to restack or aggregate due to van der Waals interaction. It is suggested that a three-dimensional flower-like MoS₂ consisting of few-layer nanosheets may suppress the sheets stacking to expose more active edge planes[24], exhibiting a larger surface area with shorter transport paths, higher interfacial transfer, and much enhanced photoactivity[28, 29]. Thus, a simple and green technology for the fabrication of such hybrid nanocomposites with greatly enhanced electrocatalytic and photocatalytic activities is needed to be demonstrated.

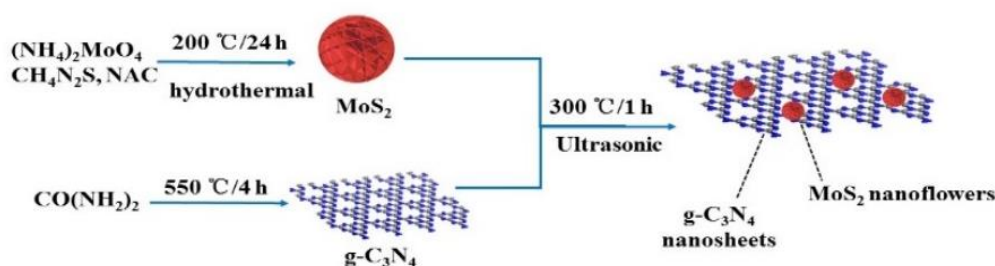
Herein, a functional hybrid of 3D (MoS₂)/2D (g-C₃N₄) nanojunction with an intimate face contact was fabricated via a feasible and sustainable ultrasonic approach. In which, a unique flower-like MoS₂ with self-assembled ultrathin nanosheets with exposed (103) and (002) facets was synthesized using a facile, one-pot hydrothermal process, assisted by N-acetyl-L-cysteine as a biomolecular capping reagent to control the morphology and growth of MoS₂ nanosheets for the first time. The as-prepared hybrids exhibited drastically enhanced photocatalytic and electrocatalytic H₂-evolution activities, compared to pure g-C₃N₄, 2D (MoS₂)/2D (g-C₃N₄) and

0D (MoS_2)/2D ($\text{g-C}_3\text{N}_4$). The optimal 0.5% 3D (MoS_2)/2D ($\text{g-C}_3\text{N}_4$) hybrid demonstrated superior photocatalytic activity and stability for H_2 evolution under solar and visible lights. Moreover, the 0.5% 3D (MoS_2)/2D ($\text{g-C}_3\text{N}_4$) also showed an excellent electrocatalytic HER activity with a low overpotential and substantial current densities. Finally, the in-depth probe on photocatalytic mechanism reveals that the intimate contact interface contributes to a higher photoreductive potential, a faster interfacial charge separation and electrons transfer from $\text{g-C}_3\text{N}_4$ to MoS_2 to facilitate the overall photocatalytic H_2 evolution reaction.

6.2 Experimental Section

6.2.1 Materials

Urea ($\geq 99.5\%$, pellets), ammonium molybdate (99.98%), N-acetyl-L-cysteine (NAC, $\geq 99\%$), thiourea ($\geq 99.0\%$), chloroplatinic acid hexahydrate ($\geq 37.5\%$ Pt basis), anhydrous ethanol, and methanol were supplied by Sigma-Aldrich, Australia. All the reagents were directly used as received.



Scheme 6.1. Synthesis process of 3D (MoS_2)/2D ($\text{g-C}_3\text{N}_4$) nanocomposites.

6.2.2 Synthesis of the Catalysts

The 3D (MoS_2)/2D ($\text{g-C}_3\text{N}_4$) binary photocatalysts with the unique structure were successfully fabricated via a facile and reliable ultrasonic approach as illustrated in Scheme 6.1.

Metal-free $\text{g-C}_3\text{N}_4$ (CN) powders were synthesized using urea as the precursor. Typically, 10 g of urea was placed in a furnace with a cover, heated to $550\text{ }^\circ\text{C}$ at a rate of $5\text{ }^\circ\text{C min}^{-1}$ and kept at $550\text{ }^\circ\text{C}$ for 4 h in air.

MoS_2 nanostructured (MSNS) particles were synthesized based on a facile one-pot hydrothermal approach[30] with prolonged reaction time. Ammonium molybdate (33.32 mg)

and N-acetyl-L-cysteine (66.58 mg) were dissolved in 40 mL ultrapure water in an ice-water bath. Thiourea (25.88 mg) was added to the above solution with further stirring for 1 h under N₂ protection. The mixture was subsequently transferred into a 100-mL Teflon-lined stainless steel autoclave which was already de-aired with N₂ flow, and kept at 200 °C for 24 h to form black sediments of MoS₂. Afterwards, the black precipitates were filtered and washed with ethanol and deionized (DI) water, followed by drying overnight at 80 °C.

Binary MSNS-CN composites were synthesized by an ultrasonic chemical approach. The as-synthesized g-C₃N₄ powder (0.1 g) and a certain amount of MoS₂ were dispersed in 10 mL anhydrous ethanol with ultrasonic shaking for 1 h, followed by vigorous stirring for 10 h before being dried at 80 °C to remove the solvent. At last, the samples were further heated under N₂ flow at 300 °C for 1 h to strengthen the interaction between the MoS₂ nanostructure and g-C₃N₄ matrix. The weight ratios of MoS₂ to g-C₃N₄ were varied from 0 to 2.5% and noted as x% MSNS-CN, where x = 0, 0.1, 0.2, 0.5, and 2.5 representing different weight ratios of MoS₂ at 0, 0.1 wt%, 0.2 wt%, 0.5 wt%, and 2.5 wt%, respectively.

6.2.3 Characterization Techniques

Thermogravimetric analysis (TGA) was performed on a TGA 4000 analyzer (Perkin Elmer) with a heating rate of 10 °C min⁻¹. X-ray diffraction (XRD) patterns were obtained on Panalytical Empyrean multipurpose research diffractometer utilizing a Cu K α radiation ($\lambda = 1.5418 \text{ \AA}$). Scanning electron microscopy (SEM) images were recorded on a FEI Verios XHR SEM microscope. Transition electron microscopy (TEM) and high-resolution transmission electron microscopy images were collected on a JEOL 2100 TEM microscope. The high angle annular dark field scanning transmission electron microscopy (HAADF-STEM) images were recorded with FEI TITAN G2 (200 kV). Fourier transform infrared (FTIR) spectra were recorded on a PerkinElmer Spectrum 100 spectrometer in the range of 500 - 2000 cm⁻¹. X-ray photoelectron spectroscopy (XPS) measurements were conducted on a Thermo Escalab 250 with an Al K α X-ray. A Shirley background was first subtracted followed by component fitting using Voigt functions with a 30% Lorentzian component. Raman spectra were obtained on a confocal microscopic Raman spectrometer (WITec alpha 300RA+) using a 785 nm laser as irradiation light. UV-visible diffuse reflectance spectra (DRS) were recorded on an Agilent Cary 100 UV-Visible spectrophotometer equipped with an integrated sphere attachment. Photoluminescence (PL) spectra of the samples were obtained on an Agilent Cary Eclipse Fluorescence Spectrophotometer.

6.2.4 Evaluation of Photocatalytic Activity

The photocatalytic hydrogen evolution experiments were conducted in a stainless steel vessel sealed with a quartz window for top-irradiation. Please refer to 5.2.3 of Chapter 5 concerning testing conditions and procedures details.

6.2.5 Photoelectrochemical Measurements

Photocurrent, electrochemical impedance spectroscopy (EIS) and Mott-Schottky curve measurements were performed on a Zahner Zennium electrochemical workstation in a standard three-electrode framework with a 0.05 M Na₂SO₄ (pH = 6.8) electrolyte solution, adopting a Pt wire as the counter electrode and a saturated calomel electrode (SCE) as the reference electrode. As for the photoanode, the sample film was fabricated on a fluorine-doped tin oxide (FTO) glass, which was ultrasonically cleaned in acetone and ethanol for 20 min in sequence, then dried at 60 °C. The specific details for electrode preparation and testing process could be found in 5.2.4 of Chapter 5.

6.2.6 Electrocatalytic Hydrogen Evolution

Electrochemical measurements were carried out at room temperature on a Zennium electrochemical station (Zahner, Germany) in a standard three-electrode system, using the samples on the glassy carbon electrode (GCE, 5 mm in diameter) as the working electrode, an Ag/AgCl electrode as the reference and a Pt wire as the counter electrode. The electrolyte was 0.5 M H₂SO₄ purged with N₂ gas (99.999%). Details for electrodes preparation and testing process of linear sweep voltammetry (LSV) could be found in 5.2.5 of Chapter 5.

6.3 Results and Discussion

6.3.1 Crystal Structure, Morphology and Composition

Thermogravimetric analysis (TGA) was implemented to determine the actual mass ratios of MSNS-CN samples. All of the TGA curves in Figure 6.1 show similar profiles. Compared to pure g-C₃N₄, the TGA curves of all MSNS-CN samples exhibit significant decay at lower temperature for both starts and ends, suggesting that the obtained MSNS-CN samples possess lower thermal stability, probably due to the crystallization disturbance from MoS₂ [31]. The weight loss under 400 °C could be ascribed to the oxidation process from MoS₂ to MoO₃ [31, 32]. The rapid decay above 450 °C represents the thermal decomposition of g-C₃N₄. Assuming that the final product after 550 °C is pure MoO₃, MoS₂ contents were calculated to be 0.12%,

0.18%, 0.36% and 0.92%, corresponding to 0.1%, 0.2%, 0.5% and 2.5% MSNS-CN as-synthesized samples, respectively.

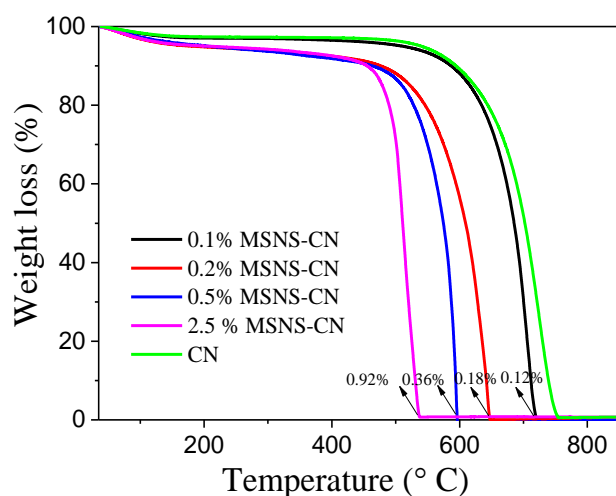


Figure 6.1. TGA curves of as-synthesized MSNS-CN samples.

XRD was used to investigate the crystal structures of pure MoS₂ and hybrid MSNS-CN samples at varying MoS₂ contents of 0-2.5 wt% (Figure 6.2a). All the MSNS-CN samples follow the similar pattern of pure g-C₃N₄ with two distinct diffraction peaks at 27.6° and 13.1°, representing the interplanar stacking of the conjugated double bonds for graphitic materials as the (002) crystal plane and the in-planar ordering of tri-s-triazine units as the (100) plane [33], respectively. As for pure MoS₂, all the diffraction peaks conform to the typical pattern of hexagonal 2H-MoS₂ structure (JCPDS No. 37-1492) [21] with apparent broadening and shortening of all the peaks, suggesting a smaller average crystallite size and less layers of MoS₂ nanosheets with a well-stacked lamellar structure, compared to bulk MoS₂ [34-36]. The MSNS-CN composite samples exhibit strong diffraction peaks of g-C₃N₄, and some tiny peaks of MoS₂ due to the low contents, confirming the existence of both phases. It can be seen that the modification with MoS₂ does not pose any noticeable impact on the bulk structure and chemical skeleton of g-C₃N₄ nanosheet.

The chemical state and surface elemental composition of the 0.5% MSNS-CN sample were examined by XPS (Figure 6.2b-e). Figure 6.2b gives a XPS full survey spectrum, indicating the existence of elements of C, N, O with a small amount of Mo and S. Corresponding peaks could be observed at binding energies of 287.5 (C 1s), 397.5 (N 1s), 531.5 (O 1s), 231.0 (Mo 3d) and 170.5 eV (S 2p). An atomic C/N proportion of 0.64 was detected in the sample, consistent with the theoretical value of pure g-C₃N₄ at 0.75 [37]. Oxygen at 7.7 at.% was also

present, which can be ascribed to the prolonged annealing of g-C₃N₄ in the air as well as the adsorbed water molecules [38]. To achieve stronger signal-noise ratio for more convincing evidence, peaks from 2.5% MSNS-CN were also studied in detail after deconvolution, apart from the sample of 0.5% MSNS-CN. For pure g-C₃N₄, the C 1s peak in Figure 6.2c can be deconvoluted into two peaks at binding energies of ~284.6 and ~287.8 eV, respectively. The former can be assigned to unavoidably loaded graphitic or amorphous carbon atoms adsorbed on the surface (C-C/C=C bonding) [39, 40], and the latter is associated with sp²-hybridized carbon in the triazine rings of carbon nitride lattice (N-C=N bonding)[41-44]. As observed, the existence of C elements on surface of MoS₂ could be ascribed to some graphitic carbon residual from the precursors during synthesis process, which might explain that the peak intensity of 284.6 eV increased compared to pure g-C₃N₄. Depicted in Figure 6.2d, three prominent peaks at 398.16, 398.60, and 400.14 eV can be obtained for pure g-C₃N₄ by deconvoluting N1s (Figure 6.1d), corresponding to sp²-bonded N atoms of C-N=C, tertiary (N-(C)3) groups and amino functional groups (C-N-H)[10, 33, 45, 46]. This further confirms the existence of graphite-like g-C₃N₄ structure. After modification, all the N 1s peaks shift to a higher binding energy with increasing content of MoS₂. Looking into Figure 6.2e, peaks of Mo 3d and S 2s are observed at binding energies of 231.5 (Mo 3d_{5/2}), 234.6 eV (Mo 3d_{3/2}) and 228.5 eV (S 2s) for pure MoS₂, which are the typical values of Mo⁴⁺ peak in MoS₂, convincing the predominant existence of Mo⁴⁺ state. It is further presented in Figure 6.2f that two strong peaks in S 2p spectrum appear at 164.2 and 165.5 eV, which are assigned to S 2p_{3/2} and S 2p_{1/2}, respectively, indicating the presence of S²⁻ in MoS₂[47]. Two weak bands at 237.5 eV (Figure 6.2e) and 171.2 eV (Figure 6.2f) suggests the possible presence of Mo⁶⁺ and S⁶⁺ respectively, owing to the small amount of oxide species during the calcination process. Compared with pure MoS₂, both of Mo 3d and S 2p peaks of 2.5% MSNS-CN shift to a lower binding energy, indicating the change of chemical microenvironment of Mo and S atoms after g-C₃N₄ hybridizes with MoS₂. The opposite shifting tendency between N 1s and Mo 3d (S 2p) suggests that the total electron density has migrated from g-C₃N₄ to MoS₂ due to the stronger electronegativity of S atoms, thus facilitating the change of bonding and the formation of interface. The high-resolution spectra of XPS further confirmed the existence of MoS₂ in the hybridized samples.

The morphology and microstructure of the as-synthesized samples of MoS₂, g-C₃N₄ and 0.5% MSNS-CN were investigated by SEM. As shown in Figure 6.3a and Figure 6.3b, pure MoS₂ particles demonstrate a 3D flower-like nanostructure with diameters about 400-600 nm and are consisted of thin nanosheets showing thickness around 10 nm. Interestingly, the tiny plate-like subunits interconnected with each other by sharing one edge to form the three-dimensional

flower-like networks. The rippled nanoplates in ultrathin features self-assembled to constitute the loose porous architecture to avoid a disordered stacking of MoS₂ layers, which might be beneficial in exposing more edges as active sites and enlarging specific surface area to shorten the diffusion path for both reactant molecules and surface charges[28]. Different from the sheet-like structure of pure g-C₃N₄ in Figure 6.3d, the MoS₂/g-C₃N₄ (0.5 wt%) composite in Figure 6.3c exhibits more loose and fluffy microstructure, indicating the incorporation and coating of MoS₂ nanoflowers into the matrix of g-C₃N₄ nanosheets. The intimate contact of the 3D MoS₂ superstructure with 2D g-C₃N₄ nanosheets might facilitate the enhancement of photoactivity with the controllable porous nanostructure.

TEM and magnified HRTEM images of g-C₃N₄, MoS₂ and 0.5% MSNS-CN are shown in Figure 6.4. Derived directly from urea, this pristine g-C₃N₄ exhibits a typical silk-like morphology of thin nanosheets (Figures 6.4e & 6.4f), which could facilitate a faster charge transfer and separation than that on densely stacked layers [11]. Figure 6.4a shows flower-like MoS₂ nanostructure with the high-resolution TEM (HRTEM) image as shown in Figure 6.4b. The constituents of the ultrathin nanosheets show crumpling and bending flakes with thickness of 5-10 nm, which agrees well with the SEM observations. Ordered lattice fringe (103) together with commonly observed lattice fringe (002) can be observed clearly, showing a lattice spacing of 0.23 nm and 0.62 nm with a good crystallinity [7, 48]. This is in accordance with the XRD results in Figure 6.4a for MoS₂ nanostructure. The specific exposed crystal planes other than the chemically inert basal plane of (002) could benefit the exposure of more active sites for HER performance [49].

TEM and HRTEM images of 0.5% MSNS-CN sample are shown in Figure 6.4c-d, revealing that the crystallized MoS₂ with thin-layers has covered the surface of g-C₃N₄ with a similar layered structure. As can be seen in Figure 6.4d, approximately 5-8 slabs of MoS₂ have been uniformly deposited on g-C₃N₄, forming intimate junctions during the impregnation and calcination process. According to previous reports [48, 50], the similarity of layered structures between g-C₃N₄ and MoS₂ might bring in an advantage to the junction formation, promoting the growth of MoS₂ slabs on the surface of g-C₃N₄. Most of nanosheets in the MoS₂ nanoflowers (Figure 6.4d) are relatively thin (averagely 3.7 nm), even thinner than that of pure MoS₂ observed in Figure 6.4b. This is probably because of the ultrasonic or calcination process during the synthesis of the composite sample [19, 21]. Owing to the electron-tunneling effect, thinner layers composing the 3D nanoflowers could facilitate higher charge transport efficiency across the interface than multi-layers of MoS₂ deposited on the surface of g-C₃N₄.

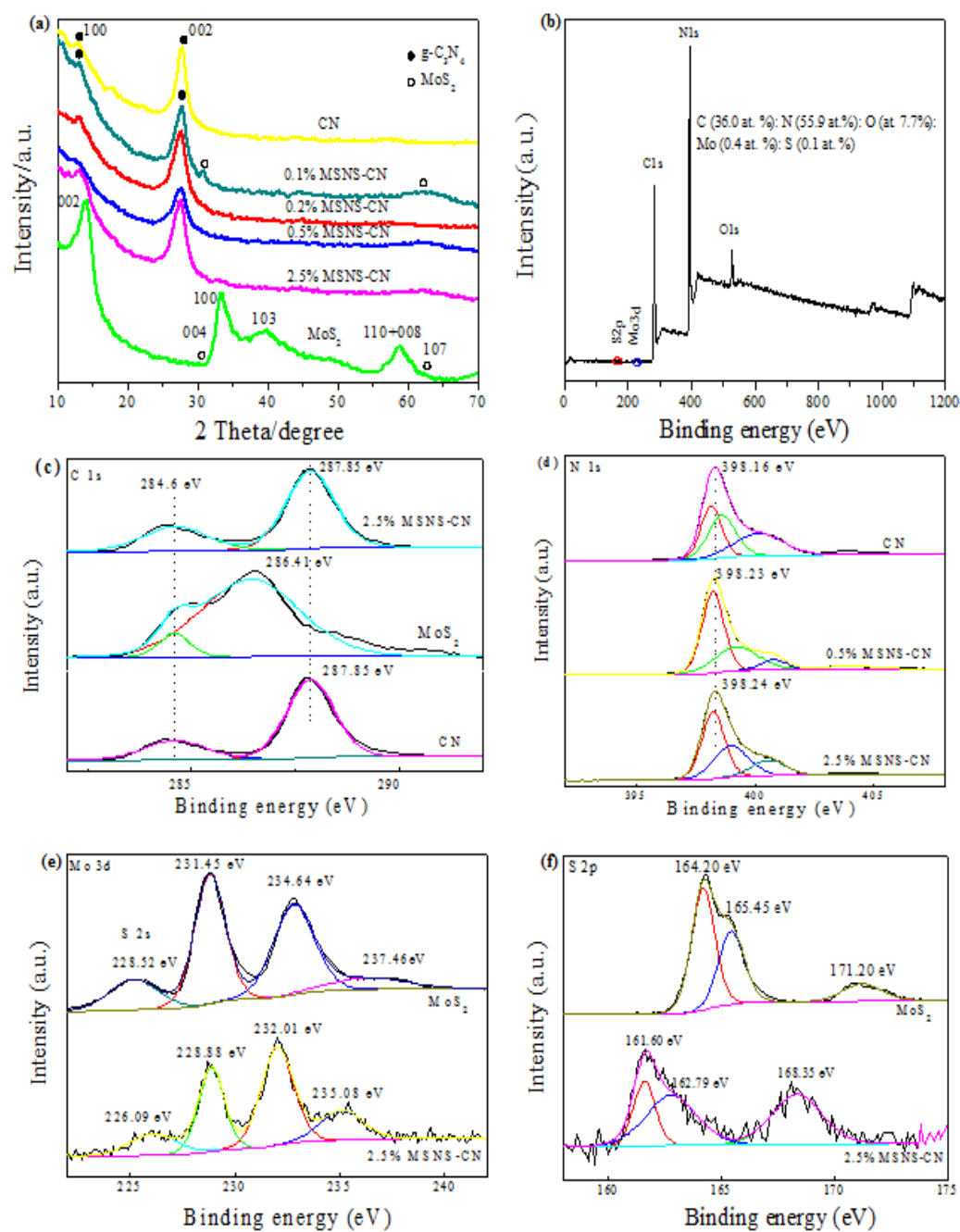


Figure 6.2. (a) XRD patterns of pure $g\text{-C}_3\text{N}_4$ and MSNS-CN composite samples; (b) XPS survey of 0.5% MSNS-CN; High-resolution XPS spectra of (c) C 1s (d) N 1s (e) Mo 3d and (f) S 2p for all samples.

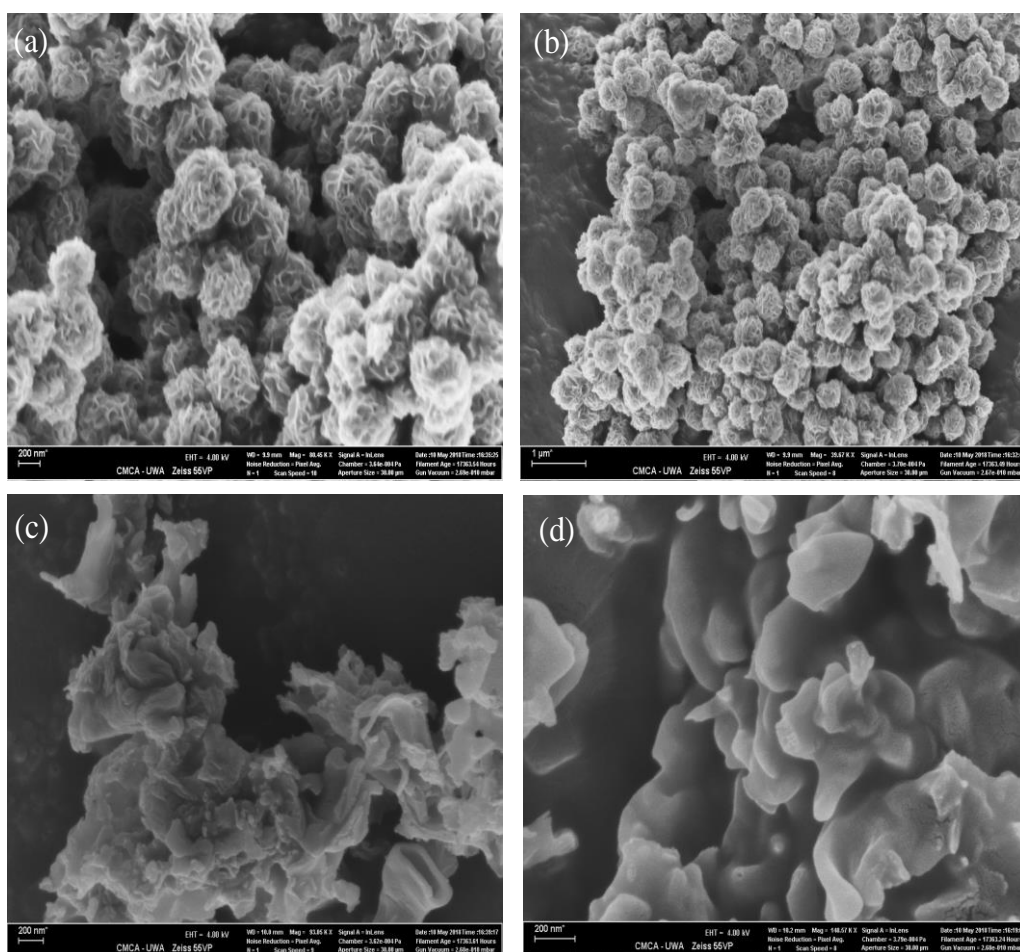


Figure 6.3. SEM images of (a-b) MoS₂; (c) 0.5% MSNS-CN; (d) g-C₃N₄.

Thus, the MoS₂ nanostructure was proven to be closely attached to the g-C₃N₄ nanosheets via their (002) crystal planes (interlayer spacings of 0.62 nm) with an intimate interfacial contact, which contributes to efficient hydrogen evolution by means of a shorter charge transport distance, faster separation of electron-hole pairs on thin nanosheets both internally and externally. STEM-EDX elemental mapping was also implemented to investigate the distribution patterns of elements more intuitively. EDX spectrum (Figure 6.5a) and high angle annular dark field scanning TEM (HAADF-STEM) image with corresponding elemental mapping images of 0.5% MSNS-CN (Figure 6.5b) confirm the existence of the four major elements (C, N, Mo and S) with uniform distribution and intimate contact. Further observation reveals that flower-like MoS₂ particles are densely deposited into the broader matrix of g-C₃N₄.

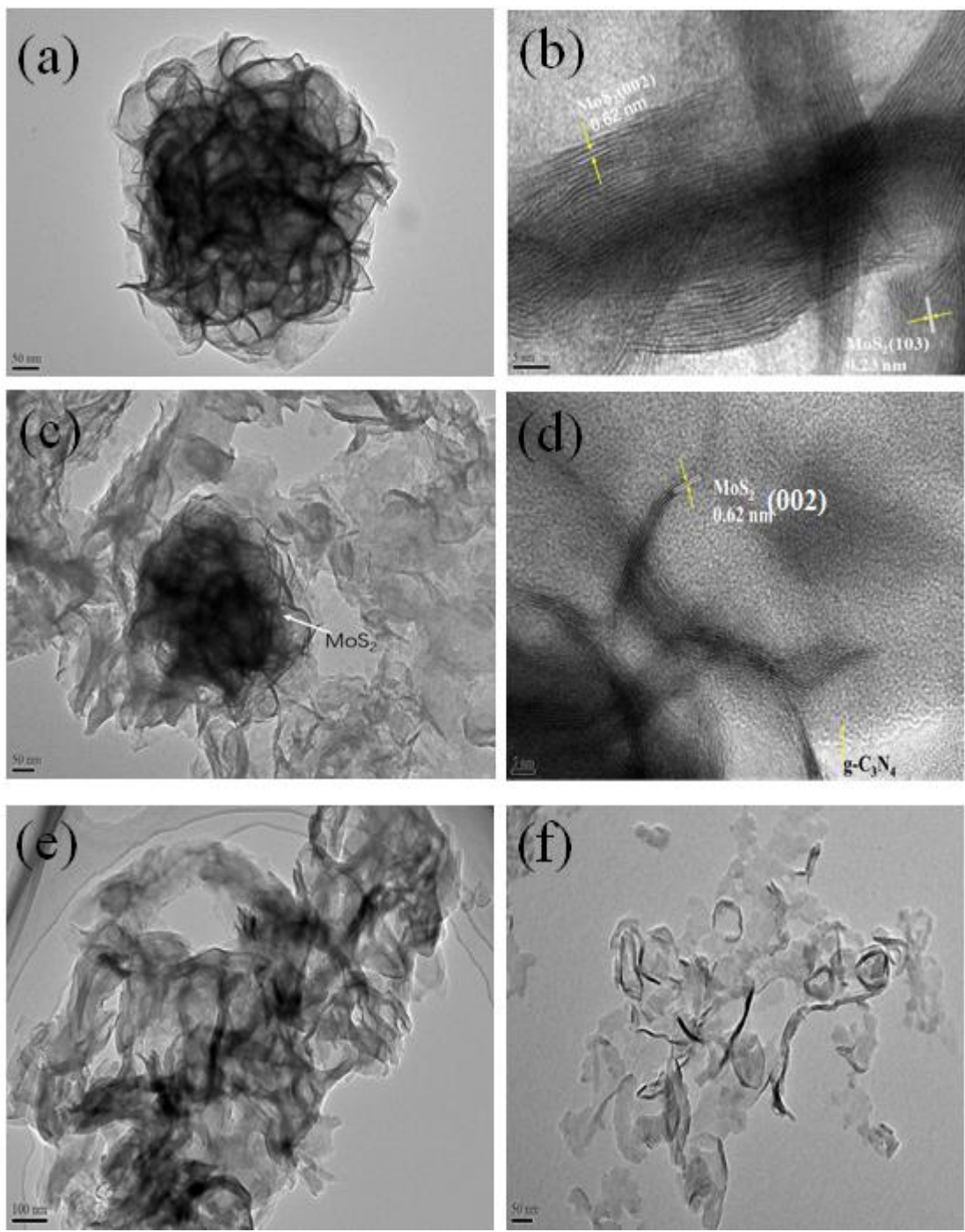


Figure 6.4. TEM images of MoS₂ (a) and 0.5% MSNS-CN (c); HRTEM images of MoS₂ (b); 0.5% MSNS-CN (d); TEM images of g-C₃N₄ (e) (f).

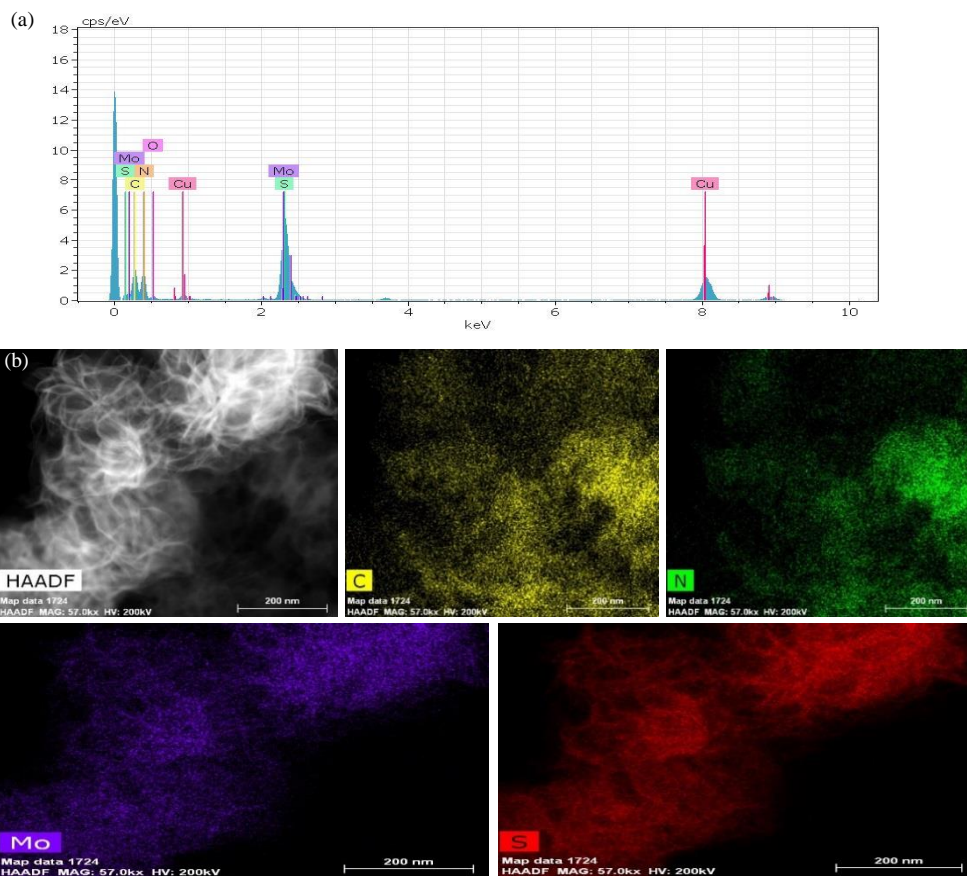


Figure 6.5. (a) EDX spectrum and (b) STEM-EDX elemental mapping of the optimum 0.5% MSNS-CN composite.

To gain detailed morphology information of the sample with Pt deposition, TEM images of g-C₃N₄ decorated with both MoS₂ and Pt nanoparticles are well illustrated in Figure 6.6. Clearly, the sample exhibits well-dispersed ultrafine Pt nanoparticles of ~2.5 nm on thin g-C₃N₄ nanosheets. Observation from HRTEM reveals that photodeposition of Pt was further confirmed by the (111) crystal plane with lattice spacing of ~0.222 nm.

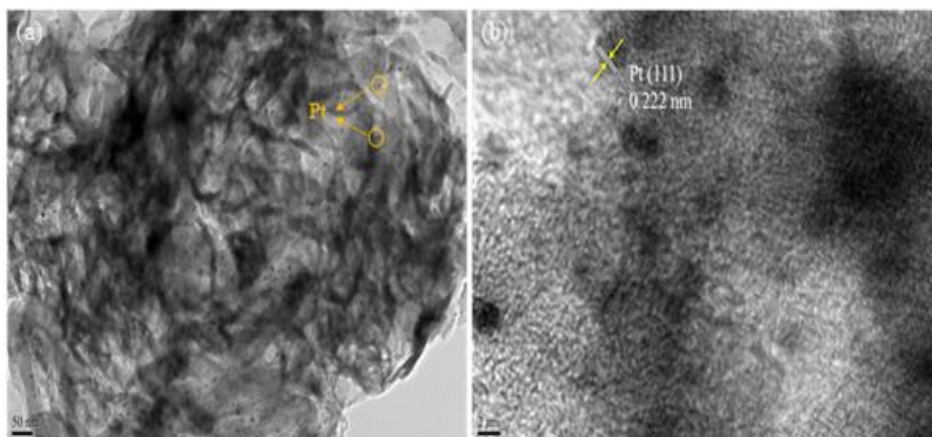


Figure 6.6. (a) TEM; (b) HRTEM image of the optimum 0.5% MSNS-CN composite after in-situ photodeposition with 2% Pt.

As shown in Figure 6.7a, Raman spectra were recorded to investigate the vibrational properties of the samples. Clearly, two Raman bands at ~ 382 and ~ 412 cm^{-1} could be observed for MoS_2 sample, corresponding to the in-plane (E_{2g}^1) and the out-of-plane (A_{1g}) mode vibrations of Mo-S bond [32], respectively. Both pure $g\text{-C}_3\text{N}_4$ and 2.5% MSNS-CN exhibit similar band profiles due to disordered graphitic carbons and other surface defects[51], except for the newly observed Raman bands at 380 cm^{-1} as a representative E_{2g}^1 mode of MoS_2 . In addition, two typical peaks at 1355 and 1570 cm^{-1} correspond to the “D” and “G” band profiles with their band intensities (I_D/I_G) increased after the modification of MoS_2 , indicating a lower graphitic carbon content in the composite sample [51]. The Raman results help convince the successful decoration of MoS_2 on the surface of $g\text{-C}_3\text{N}_4$, suggesting the intimate contact between the MoS_2 and $g\text{-C}_3\text{N}_4$.

FT-IR spectra of all the samples are illustrated in Figure 6.7b, and all the MSNS-CN composite samples follow the similar chemical skeleton of pure $g\text{-C}_3\text{N}_4$ with no obvious peaks of MoS_2 detected, in good agreement with previous XRD analysis. The absorption bands dominate in the range of $1200\text{-}1700$ cm^{-1} , presenting characteristic peaks at 1228 , 1329 , 1427 , 1567 and 1632 cm^{-1} . These peaks can be ascribed to typical stretching modes of CN heterocyclic compounds [52]. Meanwhile the sharp peak appearing at 805 cm^{-1} represents the vibration mode of the tri-s-triazine (melem) unit. It can be seen that there is apparent decrease of peak intensity or red shift in peak location with increasing MoS_2 content. These changes might be attributed to the hydrogen bonding interactions of $\text{S}\cdots\text{H}-\text{N}$ after modification with sulfur atoms of MoS_2 , helping to proving the formation of strong interfacial interactions between MoS_2 and $g\text{-C}_3\text{N}_4$ [53, 54].

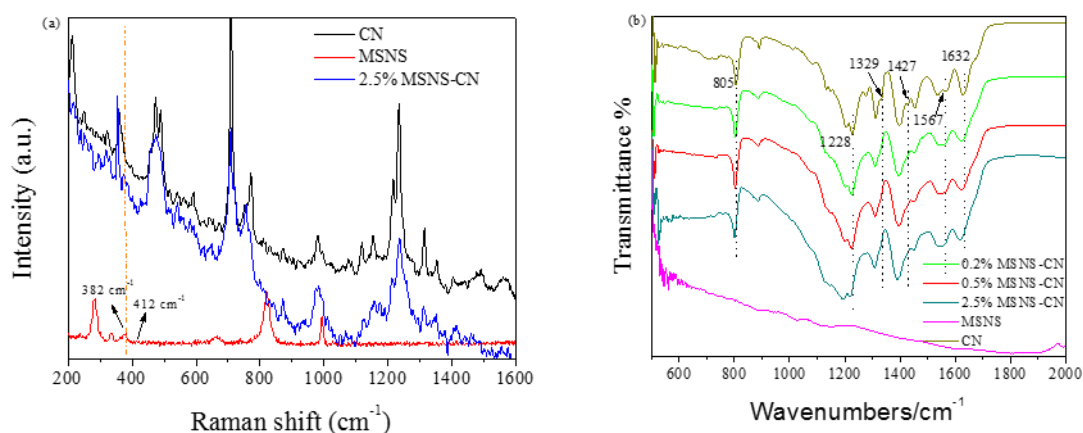


Figure 6.7. (a) Raman spectra of $g\text{-C}_3\text{N}_4$, MoS_2 and 2.5% MSNS-CN; (b) FI-IR spectra of the as-synthesized samples.

6.3.2 Optical Properties

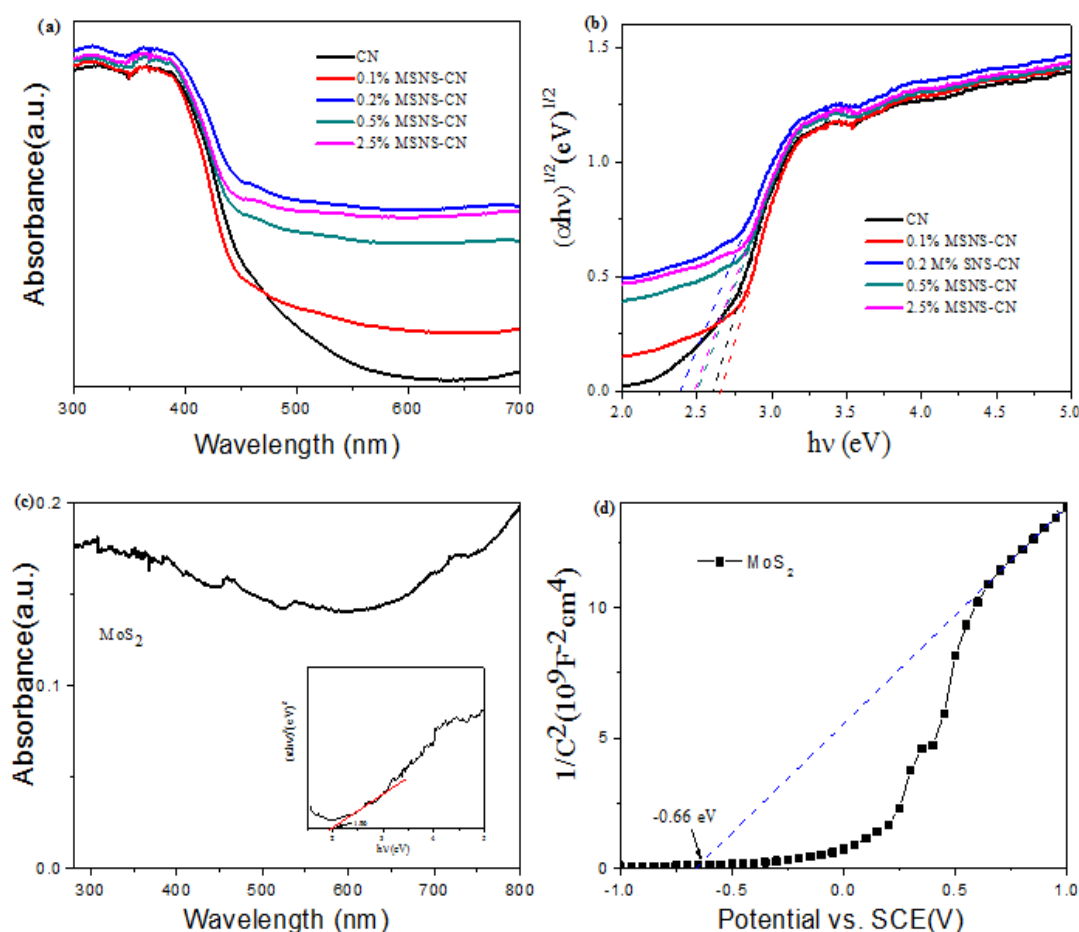


Figure 6.8. (a) UV-vis DRS spectra; (b) the plots of $(\alpha hv)^{1/2}$ versus band-gap energy (hv) of MSNS-CN composite samples; (c) UV-vis absorption spectrum of MoS₂ nanosheets. Right inset: the plots of $(\alpha hv)^2$ versus band-gap energy (hv) and (d) Mott–Schottky plot of pure MoS₂ film electrode.

UV-vis diffuse reflectance spectra (DRS) of g-C₃N₄, MoS₂ and MSNS-CN composites are displayed in Figure 6.8. As it is seen from Figure 6.8a, the absorption edge of pure g-C₃N₄ is estimated to be around 479 nm and most of the composite samples show a slight red-shift to the broader range of visible light. Furthermore, the introduction of MoS₂ has enhanced the light absorption capacity both in UV and visible light range, which might contribute to the enhanced production of electron-hole pairs. Based on Tauc's equation $(\alpha hv)^n = k(hv - E_g)$ (where α , V and E_g represent absorption factor, light frequency and band gap energy, respectively; $n=1/2$ for indirect-gap semiconductors and $n=2$ for direct gap semiconductors) [15, 37], the band-gap energies of all the samples were calculated and listed in Table 6.1. The corresponding band-gap energies are displayed in Figure 6.8b and Figure 6.8c (inset). The shifts of the band-gap energy of the composites also prove that the MoS₂ decoration has changed the properties of g-

C₃N₄ due to the formation of effective heterojunction. The band gap value for pure g-C₃N₄ was estimated to be 2.61 eV, which conforms to the previous reports [17, 55, 56]. MoS₂ exhibits a relatively wide absorption throughout UV-vis light region. Compared to the absorption edge of bulk MoS₂ with a narrow band gap at around 1.23 eV in previous work [57, 58], an obvious blue-shift from MoS₂ thin nanosheets was noticed with a band gap value of 1.96 eV in Figure 6.8c due to strong quantum confinement effects, which makes MoS₂ a possible efficient visible-light co-catalyst.

Table 6.1. Band-gap energy of g-C₃N₄ and MSNS-CN composites.

Sample	Band-gap (eV)
g-C ₃ N ₄	2.61
0.1% MSNS-CN	2.66
0.2% MSNS-CN	2.38
0.5% MSNS-CN	2.50
2.5% MSNS-CN	2.48
MSNS	1.96

6.3.3 Photocatalytic HER Activity and Stability

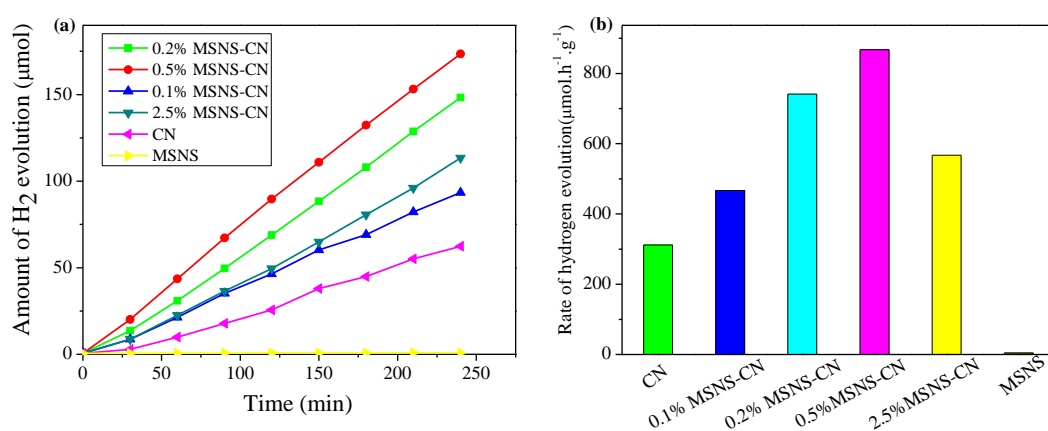


Figure 6.9. Comparison of (a) photocatalytic H₂ evolution amount and (b) photocatalytic H₂ evolution rate over different samples under simulated solar light irradiations. (25 vol% methanol, 2.0 wt% Pt, 0.05 g catalyst in 120 mL aqueous solution)

From our previous work[27], a 0D (MoS₂)/2D (g-C₃N₄) heterojunction has been fabricated with an optimal photocatalytic H₂ evolution rate at 576.6 μmol·h⁻¹·g⁻¹. For comparison, a 2D (MoS₂)/2D (g-C₃N₄) heterojunction was also prepared and presented a relatively lower photocatalytic HER rate at 425.4 μmol·h⁻¹·g⁻¹ under the same reaction conditions. To verify if a novel 3D (MoS₂)/2D (g-C₃N₄) superstructure would facilitate a more superior photocatalytic H₂ evolution performance, the similar study over pure MoS₂ and MSNS-CN with different MoS₂ contents were also conducted (Figure 6.9). It is worth noticing that MoS₂ alone is not active for photocatalytic H₂ evolution from water, although being an excellent co-catalyst for g-C₃N₄. The overall evolved hydrogen over pure g-C₃N₄ after 4 h was only 62.4 μmol. As the MoS₂ content increases, the rate of photocatalytic H₂ evolution increases accordingly and reaches the peak value of 867.6 μmol·h⁻¹·g⁻¹ at 0.5% MSNS-CN, which was approximately 2.8 times higher than pristine g-C₃N₄. As listed in Table 6.2, 0.5% MSNS-CN sample in this study shows the best photocatalytic HER activity compared to previous studies, which is 1.5 times as high as that of 5% MSQD-CN [27] (the optimal one for 0D (MoS₂)/2D (g-C₃N₄) composites) under the same reaction system. However, the hydrogen evolution activity of MSNS-CN decreased with further increasing MoS₂ loading, probably due to the blocking effect for light absorption and the reduced active sites on the surface of g-C₃N₄ [14, 59]. Earlier studies show that thin-layered MoS₂ nanosheets favor accelerated charge transport and separation via a shorter path, thus leading to the enhanced photocatalytic efficiency for hydrogen evolution [23, 60]. As a recognized effective HER catalyst [22, 61, 62], MoS₂ nanosheets with thin layers and a defect-rich structure often boost a superior HER activity by strengthening the exposure of active edge planes except for preferentially exposed stable planes of the (002)[21, 49], contributing to a higher performance of photocatalytic H₂ evolution. For comparison, photocatalytic H₂ evolution testing with 0.5% MSNS-CN without deposition of Pt under the same reaction conditions. As shown in Figure 6.10, only 15.6 μmol of hydrogen was produced after 4 h with an average photocatalytic H₂ evolution rate of 78.0 μmol·h⁻¹·g⁻¹. After deposition of Pt, the H₂ evolution rate was enhanced to 867.6 μmol·h⁻¹·g⁻¹. Indeed, co-catalyst Pt plays an important role in hydrogen generation process with the detailed mechanism further discussed later.

To further study the photocatalytic H₂ evolution activity of 0.5% MSNS-CN under visible light only, photocatalytic HER experiments were conducted with a light cutoff filter ($\lambda > 420$ nm). Figure 6.11 illustrates that 0.5% MSNS-CN exhibits the outstanding H₂ evolution rate at 133.50 μmol·h⁻¹·g⁻¹, which is about 5 times as high as that of pure g-C₃N₄ (26.56 μmol·h⁻¹·g⁻¹

¹). The overall hydrogen evolution amounts over the 0.5% MSNS-CN and g-C₃N₄ reach 533.99 and 106.26 $\mu\text{mol}\cdot\text{g}^{-1}$, respectively, after 4 h visible light irradiations. A full comparison of photocatalytic H₂ evolution performance on 0.5% MSNS-CN sample between simulated sunlight and visible light irradiations is illustrated in Figure 6.12a. Both of the hydrogen production increased continuously with the prolonged irradiation time, while the production amount of H₂ outperformed dramatically under simulated solar light than that under visible light irradiations. Concerning the overall H₂ output, the elevation efficiency of 0.5% MSNS-CN relative to pure g-C₃N₄ was even more prominent under visible light irradiations. After 4 h, the corresponding H₂ evolutions reached 3470.40 $\mu\text{mol}\cdot\text{g}^{-1}$ and 533.99 $\mu\text{mol}\cdot\text{g}^{-1}$, respectively. Thus, 0.5% MSNS-CN was proven to exhibit optimal hydrogen evolution performance and was chosen to further study the intrinsic photocatalytic mechanism. Apart from its excellent photocatalytic H₂ evolution performance, 0.5% MSNS-CN also maintains a high stability with five-cycle runs under simulated sunlight irradiations. In detail, a time-circle photocatalytic H₂ evolution test was performed with evacuation every 4 h (Figure 6.12b). After a 20 h successive reaction, the photocatalytic H₂ evolution amount still achieved 158.20 μmol without a noticeable decrease. After the five runs, the catalysts were stored for 1 year and tested again, showing a similar catalytic performance with only a decay of 18%. This decrease in the photocatalytic performance could be attributed to the various degrees of break down and depletion of 3D flower-like MoS₂ compared to the pristine hybrid material, which could be further convinced by the relevant TEM and EDS tests in Figure 6.13. The XRD analysis from Figure 6.13b also reveals that the crystal structure and core skeleton of 0.5% MSNS-CN did not change after the long-time testing. These results well illustrated that the as-prepared 0.5% MSCN-CN composite has formed a solid heterostructure with a sound stability and durability.

Table 6.2. Photocatalytic HER activities of graphitic carbon nitride modified with different co-catalysts.

Catalyst	Cocatalyst	Electron donor	λ (nm)	Hydrogen Evolution ($\mu\text{mol}\cdot\text{h}^{-1}\cdot\text{g}^{-1}$) ¹	Reference
g-C ₃ N ₄	1.5 wt% polypyrrole+3 wt% Pt	Acetic acid	Xe lamp	154	[63]
g-C ₃ N ₄	3 wt% Pt	Methanol	Xe lamp	300	[64]

g-C ₃ N ₄	0.15 wt% CoTiO ₃ +3 wt% Pt	Ethanol	Xe lamp	858	[65]
g-C ₃ N ₄	5 wt% MSQD+ 2 wt% Pt	Methanol	Xe lamp	576.6	[27]
g-C ₃ N ₄	3 wt% CoP+3 wt% Pt	Methanol	Xe lamp	1125	[66]
g-C ₃ N ₄	0.5%CB-1.0%NiS	TEOA	Xe lamp	366.4	[67]
g-C ₃ N ₄	0.5%MoS ₂ + 2 wt% Pt	Methanol	Xe lamp	867.6	This work

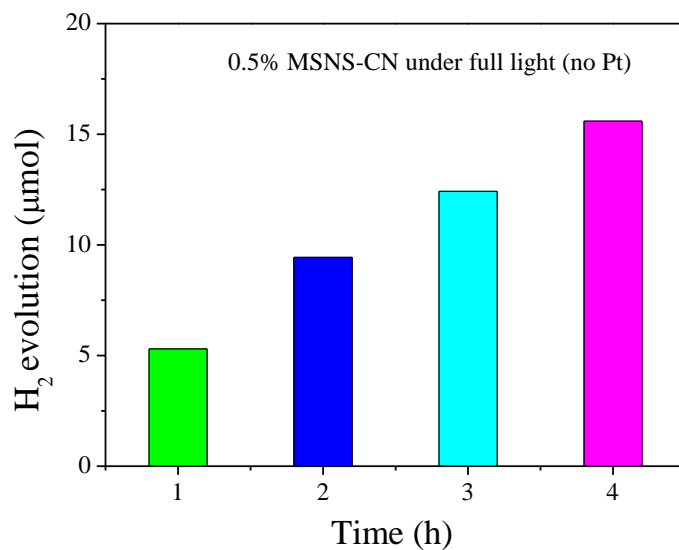


Figure 6.10. Photocatalytic H₂ evolution over 0.5% MSNS-CN under full light irradiations during 4 h without Pt (25 vol% methanol, 0.05 g catalyst in 120 mL aqueous solution).

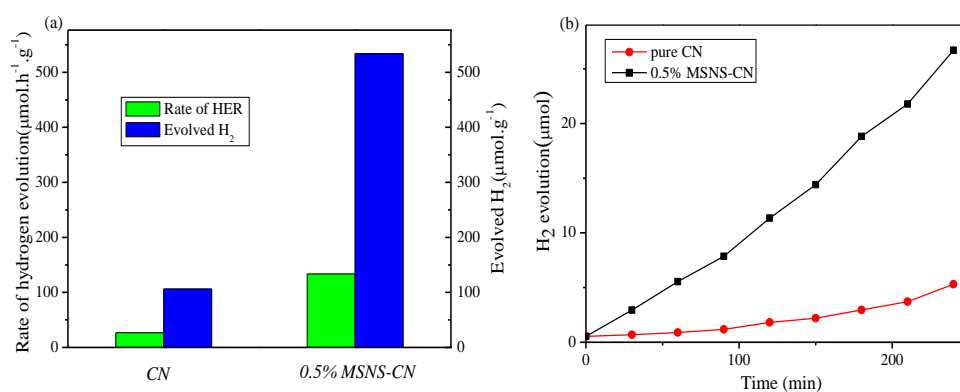


Figure 6.11. (a) Photocatalytic activities for H₂ evolution and (b) time-dependent photocatalytic H₂ evolution process over pure CN and 0.5% MSNS-CN under visible light irradiations during 4 h (25 vol% methanol, 2.0 wt% Pt, 0.05 g catalyst in 120 mL aqueous solution).

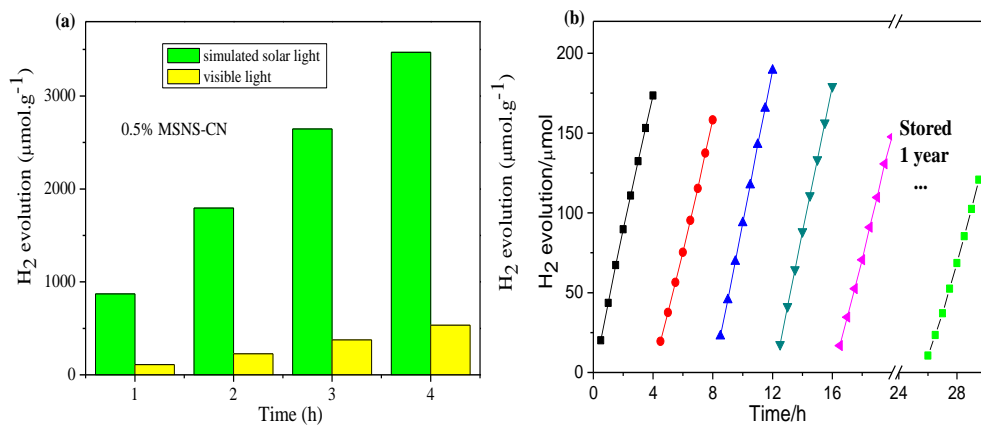


Figure 6.12. (a) Rate of H₂ production over CN and 0.5% MSNS-CN with various light sources and (b) Cyclic runs for the photocatalytic H₂ production on 0.5% MSNS-CN.

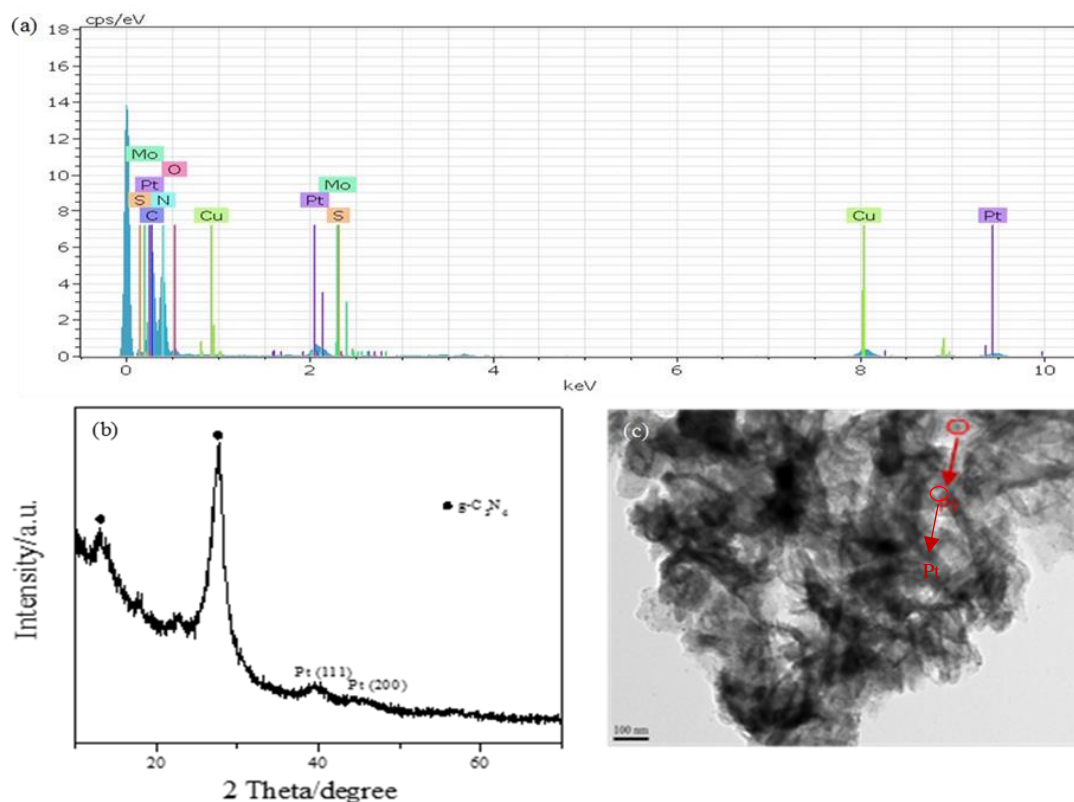


Figure 6.13. (a) EDX spectrum, (b) XRD and (c) TEM image of the recycled 0.5% MSNS-CN sample after long-time testing.

6.3.4 Photocatalytic Mechanism

To gain insight into the enhanced charge transfer and separation efficiency of the interface between g-C₃N₄ and MoS₂ nanojunction, photoluminescence (PL), electrochemical impedance

spectroscopy (EIS), transient photocurrent responses and Mott-Schottky (M-S) measurements were conducted. Figure 6.14a displays the PL spectra of all the MSNS-CN samples at an excitation wavelength of 325 nm. All the samples demonstrate similar emission trends with a main emission peak centered at 460 nm, originating from the recombination of the photoinduced electrons and holes corresponding to the band gap transition[33, 40]. Compared to pure g-C₃N₄, the introduction of MoS₂ leads to a much lower PL intensity, indicating the improved separation efficiency and suppressed recombination rate of the induced charge carriers at the interface. This PL result matches well with the photocatalytic H₂ evolution activities as discussed in Figure 6.9.

Furthermore, the photoelectrochemical properties were studied focusing on the optimal 0.5% MSNS-CN sample to probe into the inherent mechanism for the enhancement of charge carrier separation and transportation. The photocurrent I-t curves for g-C₃N₄ and 0.5% MSNS-CN samples were acquired under intermittent simulated solar light irradiations (Figure 6.14b). It can be seen that the binary photocatalyst exhibits a much higher photocurrent density with a good stability after four cycles than pure g-C₃N₄, indicating that the existence of MoS₂ is able to boost more efficient interfacial charge transfer between the g-C₃N₄ and MoS₂. As a most convincing technique in electrochemical study, EIS was employed to further confirm the interfacial charge transport resistances [68-70]. Figure 6.14c shows that the arc radius for 0.5% MSNS-CN film is much smaller than that of pure g-C₃N₄, suggesting an improved charge migration efficiency across the electrode/electrolyte due to higher conductivity and lower charge transfer resistance of MoS₂. This result is in good agreement with the PL observation, confirming that the heterojunction between g-C₃N₄ and MoS₂ accelerates the electron-hole separation and transport process, and contributes to the enhancement of photocatalytic H₂-production activity.

To better elucidate the intrinsic properties of the electronic band structure of the different films in contact with the electrolyte solution, the flat band potential of g-C₃N₄ and 0.5% MSNS-CN film electrodes were investigated using the Mott-Schottky (M-S) measurements. While plotting $1/C^2$ versus V , the flat band potentials (V_{fb}) can be acquired by extrapolating the linear part of the curves to zero [27, 71, 72]. Both g-C₃N₄ and 0.5% MSNS-CN exhibit the typical n-type semiconductor properties with the minimum potential levels of the conduction band (CB) very close to their flat band potentials. From the intercepts of the tangents on the horizontal axis in Figure 6.14d, the flat band potentials of g-C₃N₄ and 0.5% MSNS-CN were estimated to be -1.09 V vs. SCE (-0.85 V vs. NHE) and -1.18 V vs. SCE (-0.94 V vs. NHE), respectively, displaying a slight negative shift of the conduction band potential. This upward band alignment

might foster the building of an electric field at the interface between g-C₃N₄ and MoS₂, which will drive the faster and more efficient separation of electrons and holes. Considering the band gap energy of 2.61 eV for g-C₃N₄ and 2.50 eV for 0.5% MSNS-CN accordingly, the maximum valence band (VB) energy levels were calculated to be 1.76 and 1.56 eV for g-C₃N₄ and 0.5% MSNS-CN, respectively. Apparently, 0.5% MSNS-CN provides a more negative potential for photocatalytic reduction of water thermodynamically. The M-S plot collected on pure MoS₂ is displayed in Figure 6.8d, in which the MoS₂ also shows a typical n-type feature[73] with a flat band potential at around -0.66 V vs. SCE (-0.42 V vs. NHE).

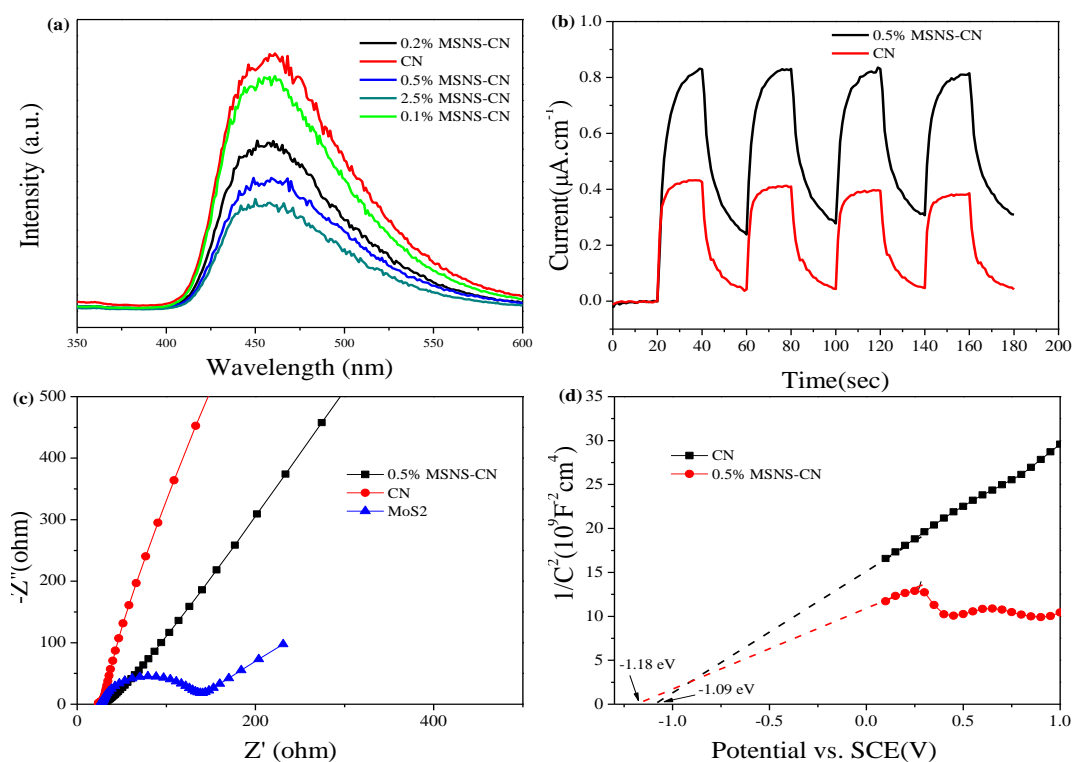


Figure 6.14. (a) PL spectra of pure g-C₃N₄ and different MSNS-CN samples; (b) Transient photocurrent responses of g-C₃N₄ and 0.5% MSNS-CN; (c) Nyquist plots of electrochemical impedance spectroscopy (EIS) with different electrodes in the dark; (d) Mott-Schottky plots collected on g-C₃N₄ and 0.5% MSNS-CN.

To further confirm the separation efficiency of the charge carriers between g-C₃N₄ and MoS₂, time-resolved fluorescence emission decay spectra were recorded (Figure 6.15a). The curves were fitted based on equation $f(t) = A + B1 \times \exp(-t/T1) + B2 \times \exp(-t/T2)$ [74] with the parameters summarized in Table 6.3, where T1/T2 represent lifetimes, B1/B2 represent pre-exponential factors and T_{avg} means the average lifetime of the carriers. The average decay lifetime was increased from 3.569 to 3.881 ns after the introduction of 0.5 wt% MoS₂. The slightly prolonged lifetime of the charge carriers gives rise to the probability of more involvement in photocatalytic reduction reaction instead of recombination, indicating a higher transfer and

separation efficiency. This result well supplements the above PL and photoelectrochemical findings in elucidating the promoted photocatalytic reaction mechanism.

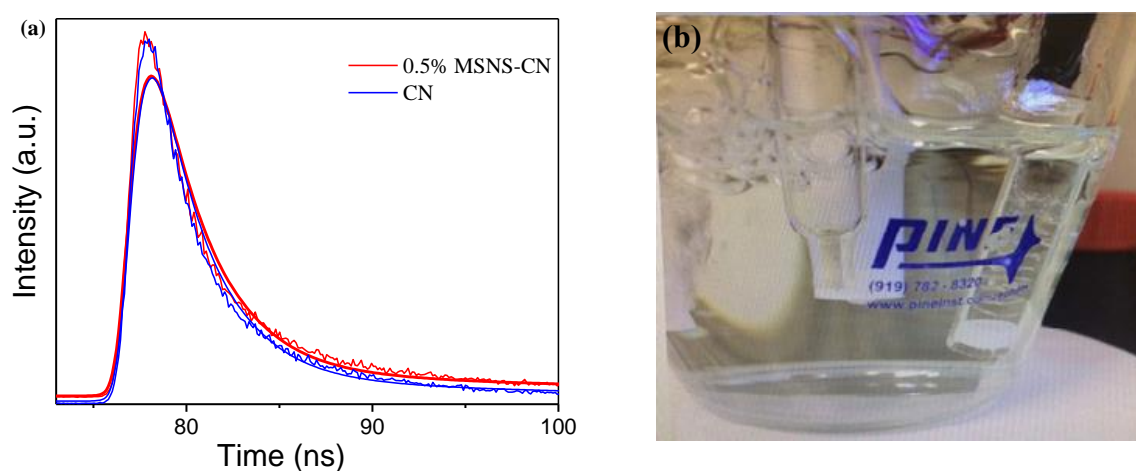


Figure 6.15. (a) Time-resolved fluorescence emission decay curves of g-C₃N₄ and 0.5% MSNS-CN observed at 446 nm with 325 nm laser excitation; (b) Photograph showing the evolution of H₂ gas bubbles during HER process.

Table 6.3. Fitted data summary of time-resolved fluorescence decay of the related samples

Samples	T ₁	B ₁	T ₂	B ₂	T _{avg}
g-C ₃ N ₄	2.605	0.0896	23.284	0.00438	3.569
0.5% MSNS-CN	2.724	0.0837	25.408	0.00450	3.881

The electrochemical HER performance of the optimal 0.5% MSNS-CN sample was then evaluated in comparison with pure g-C₃N₄ and MoS₂ to further identify the roles of MoS₂ as a co-catalyst during the photocatalytic H₂ evolution process. The linear sweep voltammetry (LSV) curves were recorded in N₂-saturated 0.5 M H₂SO₄ solution with a three-electrode system showing their HER activity. As can be seen in Figure 6.16a, all the electrodes display apparent cathodic currents within the range of 0 ~ -0.4 V (versus RHE) with increasing amount of H₂ gas bubbles from the surface of the working electrode (Figure 6.15b). In detail, pure MoS₂ exhibits the highest electrocatalytic activity among the three samples with the lowest onset potential at -0.01 V vs RHE, while the HER catalytic performance of pure g-C₃N₄ was very poor showing a high onset potential of -0.12 V vs RHE and a relatively weak cathodic current. After modification with MoS₂, the HER activity was slightly enhanced with the onset potential shifting to -0.09 V vs RHE, and a significant current of 10 mA·cm⁻² for H₂ evolution

could be obtained at an extremely low overpotential of -0.20 V vs RHE. In addition, Tafel slope is also addressed to reflect the inherent properties of the electrocatalysts, which can be inferred from the linear portions of the Tafel plots based on the Tafel equation ($\eta = b \log j + a$, where η is the overpotential; b is the Tafel slope and j represents the current density)[6, 44, 75]. As it is shown in Figure 6.16b, the Tafel slopes for g-C₃N₄, MoS₂ nanosheet and 0.5% MSNS-CN were estimated to be 194, 98 and 96 mV/dec, respectively. The smaller slope of 0.5% MSNS-CN relative to g-C₃N₄ also signifies a much improved HER performance kinetically. Compared to pure g-C₃N₄, the HER performance of 0.5% MSNS-CN was enhanced with a lower onset potential, a higher current density (at a fixed voltage, for example, -0.3 V), as well as a much smaller Tafel slope, thus the activation barriers were decreased, leading to improved H₂ evolution kinetics and activity. The EIS results in Figure 6.14c may well explain the enhanced HER performance of 0.5% MSNS-CN for its low charge-transfer resistance and high conductivity.

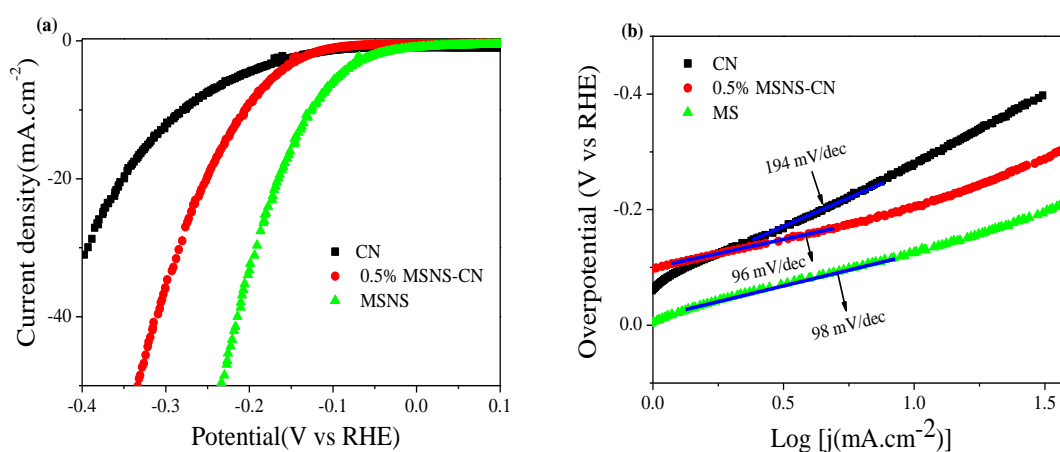


Figure 6.16. (a) Polarization curves; (b) Corresponding Tafel plots of g-C₃N₄, MoS₂ and 0.5% MSNS-CN composite samples.

Given the discussions above, the improved photocatalytic H₂-evolution activity of the MSNS-CN composites can be attributed to the enhanced light absorption ability, decreased electrocatalytic H₂ evolution overpotentials as well as more efficient transfer and separation of photoinduced electron/hole pairs. On one hand, the introduced MoS₂ co-catalyst can serve as an electron acceptor with a higher conductivity and lower charge-transfer resistance. Under light irradiations, the photoinduced electrons from the conduction band of g-C₃N₄ will be transferred to the lower conduction band of MoS₂. The intimate interfacial contact between g-C₃N₄ and MoS₂ is able to foster a shorter charge transport distance and a faster transfer

efficiency of electrons. Without loading of MoS₂ as the co-catalyst, the photo-generated electrons and holes will easily recombine at both bulk and surface of g-C₃N₄. MoS₂ would act as active sites to accelerate the overall photocatalytic and electrochemical H₂ evolution reactions. The unsaturated active S atoms along the exposed edges over the basal planes of MoS₂ layers can bond to H⁺ in the solution, which will then be reduced to H₂ easily by trapping electrons[21]. On the other hand, MoS₂ could serve as an excellent co-catalyst owing to its lower electrocatalytic H₂-evolution overpotential relative to pure g-C₃N₄, which also plays a key role as active sites over g-C₃N₄ nanosheets. The loading ratio of 0.5% with the best photocatalytic H₂-evolution performance may reach an optimal balance between charge carriers transfer at the interface and light absorption on g-C₃N₄ as the light-harvesting semiconductor. Additionally, the loading of MoS₂ also increases the water reduction ability by slightly shifting the conduction band to a more negative potential position. Overall, the energy band structure and proposed mechanism for charge transfer and separation scheme are clearly illustrated in Figure 6.17. It is shown in Figure 6.17a that the conduction band of 0.5% MSNS-CN shifted upward slightly relative to pure g-C₃N₄, providing a more negative potential for photocatalytic water reduction reactions. The bottom energy level of the conduction band (CB) of 0.5% MSNS-CN is at -0.94 V (vs NHE, pH=7), resulting in a stronger thermodynamic force for water reduction. The detailed mechanism for the transport and separation of electron-hole pairs were illustrated in Figure 6.17b.

According to the energy band structure theory, under sunlight irradiations, the electrons excited into the CB of g-C₃N₄ will be transferred to the lower CB of MoS₂ to form an electron center, while most of the holes will remain in the VB of g-C₃N₄ for methanol oxidation to hinder the fast recombination of electron-hole pairs. MoS₂ as a co-catalyst can act as surface active sites owing to its lower overpotential of H₂ evolution reaction and unsaturated bonds to H⁺ [76]. Also because of its high electrical conductivity and low charge-transport resistance, MoS₂ stands out to be a favorable co-catalyst for electrons accepting and storing. Thus, part of the electrons will be further transferred to Pt nanoparticles to drive evolution of H₂. Large amount of H⁺ in the solution will be strongly bonded to the unsaturated active S atoms along the exposed edges over the basal planes of MoS₂, which will then be easily reduced to H₂ by the trapped electrons in the CB of MoS₂[77]. Under visible light irradiations, the modification of MoS₂ has promoted a wider absorption within the visible region with the band edge shifting slightly to the right. The presence of MoS₂ would decrease the reflection of light and also enhance the conductivity over g-C₃N₄, which accelerates the above electron transition process

with strengthened photo-absorption abilities. Overall, the enhanced photocatalytic H₂ evolution performance would be attributed to the introduction of MoS₂ to form an effective interfacial contact with a decreased onset potential, lower charge-transfer resistance and higher reductive potential.

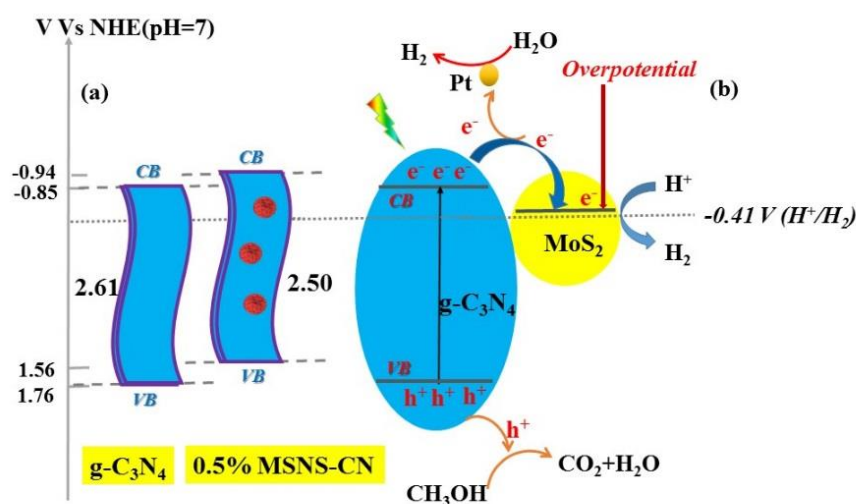


Figure 6.17. (a) Energy band structure diagram of g-C₃N₄ and 0.5% MSNS-CN; (b) Proposed mechanism of photocatalytic H₂ evolution over g-C₃N₄/MoS₂ heterojunction.

6.4 Conclusions

In conclusion, 3D flower-like hexagonal 2H-MoS₂ composed of nanosheets with thin-layers were prepared using a facile hydrothermal approach, and then further employed to modify g-C₃N₄ nanosheets with a similar layered structure to achieve MoS₂/g-C₃N₄ hybrid photocatalysts via a simple ultrasonic process. The as-formed intimate junctions contribute to highly enhanced photocatalytic and electrocatalytic H₂ evolution activities. The highest photocatalytic efficiency was observed on 0.5% MSNS-CN with a hydrogen evolution reaction rate of 867.6 μmol·h⁻¹·g⁻¹ under simulated sunlight irradiations. Compared to pure g-C₃N₄, the photocatalytic H₂ evolution activity was elevated to about 2.8 times higher at sunlight irradiations and about 5 times higher for visible light irradiations, which could be ascribed to the flower-like MoS₂ structural features as well as the synergetic effect between the 3D MoS₂ and 2D g-C₃N₄. This 3D/2D hybrid also presents better photocatalytic performance than its 0D/2D and 2D/2D analogues, which is discussed in Chapter 5. The introduction of MoS₂

nanoflowers leads to a broader absorption range and a strengthened photo-absorption capability compared to pure g-C₃N₄. As an electron acceptor and also the active sites over g-C₃N₄, the unique flower-like nanostructure of MoS₂ boosted a much higher and stable photocatalytic H₂ evolution activity with exposure of more active edge planes and shortened diffusion channels for charge transfer and separation. The proposed mechanism for the enhancement lies in the effective interfacial contact formed at the 3D (MoS₂)/2D (g-C₃N₄) heterojunctions with a decreased onset potential, a lower charge-transfer resistance and a higher reductive potential with a more negative conduction band position. All the combined effects improved the photocatalytic H₂ evolution activity thermodynamically and kinetically. In addition, the lowered overpotential and smaller Tafel slope of 0.5% MSNS-CN also promise the enhanced electrocatalytic H₂ evolution performance with a decreased activation barrier and facilitated kinetics. This study provides insights into synthesizing 3D/2D hybrid photocatalysts with similar layered structures for solar hydrogen production, especially for achieving a sustainable energy solution in the future.

References

- [1] X. Y. Yu, L. Yu, H. B. Wu and X. W. D. Lou, *Angew. Chem. Int. Ed.*, 2015, **127**, 5421-5425.
- [2] J. A. Turner, *Science*, 2004, **305**, 972-974.
- [3] J. Liu, Y. Liu, N. Liu, Y. Han, X. Zhang, H. Huang, Y. Lifshitz, S.-T. Lee, J. Zhong and Z. Kang, *Science*, 2015, **347**, 970-974.
- [4] Y. Li, T. Takata, D. Cha, K. Takanabe, T. Minegishi, J. Kubota and K. Domen, *Adv. Mater.*, 2013, **25**, 125-131.
- [5] A. Kudo and Y. Miseki, *Chem. Soc. Rev.*, 2009, **38**, 253-278.
- [6] Y.J. Tang, Y. Wang, X.L. Wang, S.-L. Li, W. Huang, L.-Z. Dong, C.-H. Liu, Y.-F. Li and Y.-Q. Lan, *Adv. Energy Mater.*, 2016, **6**, 1600116.
- [7] X. Ren, L. Pang, Y. Zhang, X. Ren, H. Fan and S.F. Liu, *J. Mater. Chem. A*, 2015, **3**, 10693-10697.
- [8] A. Fujishima, *Nature*, 1972, **238**, 37-38.
- [9] R. Ye, H. Fang, Y.Z. Zheng, N. Li, Y. Wang and X. Tao, *ACS Appl. Mater. Interfaces*, 2016, **8**, 13879-13889.
- [10] J. Wen, X. Li, H. Li, S. Ma, K. He, Y. Xu, Y. Fang, W. Liu and Q. Gao, *Appl. Surf. Sci.*, 2015, **358**, 204-212.
- [11] G. Zhang, Z.A. Lan, L. Lin, S. Lin and X.Wang, *Chem. Sci.*, 2016, **7**, 3062-3066.
- [12] Y. Zhu, Q. Ling, Y. Liu, H. Wang and Y. Zhu, *Phys. Chem. Chem. Phys.* 2015, **17**, 933-940.
- [13] W.-J. Ong, *Front. Mater.* 2017, **4**, 11.
- [14] Y. Hou, A.B. Laursen, J. Zhang, G. Zhang, Y. Zhu, X. Wang, S. Dahl and I. Chorkendorff, *Angew. Chem., Int. Ed.*, 2013, **52**, 3621-3625.
- [15] H. Sun, G. Zhou, Y. Wang, A. Suvorova and S. Wang, *ACS Appl. Mater. Interfaces*, 2014, **6**, 16745-16754.
- [16] L. Zhou, H.Y. Zhang, H.Q. Sun, S.M. Liu, M.O. Tade, S.B. Wang and W.Q. Jin, *Catal. Sci. Technol.*, 2016, **6**, 7002-7023.
- [17] X. Wang, K. Maeda, A. Thomas, K. Takanabe, G. Xin, J.M. Carlsson, K. Domen and M. Antonietti, *Nat. Mater.*, 2009, **8**, 76-80.
- [18] L. Xu, W.-Q. Huang, L.-L. Wang, Z.-A. Tian, W. Hu, Y. Ma, X. Wang, A. Pan and G.-F. Huang, *Chem. Mater.*, 2015, **27**, 1612-1621.
- [19] J. Li, E. Liu, Y. Ma, X. Hu, J. Wan, L. Sun and J. Fan, *Appl. Surf. Sci.*, 2016, **364**, 694-702.
- [20] K. Maeda, K. Teramura, D. Lu, T. Takata, N. Saito, Y. Inoue, K. Domen, *Nature*, 2006, **440**, 295-295.
- [21] J. Xie, H. Zhang, S. Li, R. Wang, X. Sun, M. Zhou, J. Zhou, X.W. Lou and Y. Xie, *Adv. Mater.*, 2013, **25**, 5807-5813.
- [22] Y. Hou, Z. Wen, S. Cui, X. Guo and J. Chen, *Adv. Mater.*, 2013, **25**, 6291-6297.

- [23] Y. Yang, H. Fei, G. Ruan, C. Xiang and J.M. Tour, *Adv. Mater.*, 2014, **26**, 8163-8168.
- [24] Y. Yan., B. Xia, X. Ge, Z. Liu, J. Y. Wang and X. Wang, *ACS Appl. Mater. Interfaces*, 2013, **5**, 12794-2798.
- [25] D. Zheng, G. Zhang, Y. Hou, X. Wang, *Appl. Catal. A:General.*, **2016**, 521, 2-8.
- [26] W. Fu, H. He, Z. Zhang, C. Wu, X. Wang, H. Wang, Q. Zeng, L. Sun, X. Wang, J. Zhou, Q. Fu, P. Yu, Z. Shen, C. Jin, B.I. Yakobson and Z. Liu, *Nano Energy*, 2016, **27**, 44-50.
- [27] Y. Liu, H. Zhang, J. Ke, J. Zhang, W. Tian, X. Xu, X. Duan, H.Sun, M. O. Tade and S. Wang, *Appl. Catal. B: Environ.*, 2018, **228**, 64-74.
- [28] D. Lu, H. Wang, X. Zhao, K.K. Kondamareddy, J. Ding, C. Li and P. Fang, *ACS Sustain. Chem. Eng.*, 2017, **5**, 1436-1445.
- [29] S. Hu, W. Chen, J. Zhou, F. Yin, E. Uchaker, Q. Zhang and G. Cao, *J. Mater. Chem. A*, 2014, **2**, 7862-7872.
- [30] H. Huang, C. Du, H. Shi, X. Feng, J. Li, Y. Tan and W. Song, *Part. Part. Syst. Character.*, 2015, **32**, 72-79.
- [31] W. Yu, D. Xu and T. Peng, *J. Mater. Chem. A*, 2015, **3**, 19936-19947.
- [32] F. Pan, J. Wang, Z. Yang, L. Gu and Y. Yu, *RSC Adv.*, 2015, **5**, 77518-77526.
- [33] J. Wen, J. Xie, Z. Yang, R. Shen, H. Li, X. Luo, X. Chen and X. Li, *ACS Sustain. Chem. Eng.* 2017, **5**, 2224-2236.
- [34] J.Z. Ou, A.F. Chrimes, Y. Wang, S.-y. Tang, M.S. Strano and K. Kalantar-zadeh, *Nano Lett.*, 2014, **14**, 857-863.
- [35] M. Chhowalla and G. A. Amaratunga, *Nature*, 2000, **407**, 164-167.
- [36] Y. Liu, Y. Zhao, L. Jiao and J. Chen, *J. Mater. Chem. A*, 2014, **2**, 13109-13115.
- [37] H. Zhang, W. Tian, L. Zhou, H. Sun, M. Tade and S. Wang, *Appl. Catal. B: Environ.*, 2017, **223**, 2-9.
- [38] S. M. Lyth, Y. Nabae, S. Moriya, S. Kuroki, M.-a. Kakimoto, J.-i. Ozaki and S. Miyata, *J. Phys. Chem. C*, 2009, **113**, 20148-20151.
- [39] S. Yan, Z. Li and Z. Zou, *Langmuir*, 2009, **25**, 10397-10401.
- [40] X. Jin, X. Fan, J. Tian, R. Cheng, M. Li and L. Zhang, *RSC Adv.*, 2016, **6**, 52611-52619.
- [41] A. Thomas, A. Fischer, F. Goettmann, M. Antonietti, J.-O. Müller, R. Schlögl and J.M. Carlsson, *J. Mater. Chem.*, 2008, **18**, 4893-4908.
- [42] V.N. Khabashesku, J.L. Zimmerman and J.L. Margrave, *Chem. Mater.*, 2000, **12**, 3264-3270.
- [43] L. Ge, F. Zuo, J. Liu, Q. Ma, C. Wang, D. Sun, L. Bartels and P. Feng, *J. Phys. Chem. C*, 2012, **116**, 13708-13714.
- [44] X. Ren, L. Pang, Y. Zhang, X. Ren, H. Fan and S. Liu, *J. Mater. Chem. A*, 2015, **3**, 10693-10697.
- [45] J. Duan, S. Chen, M. Jaroniec and S.Z. Qiao, *ACS nano*, 2015, **9**, 931-940.
- [46] L. Shi, L. Liang, F. Wang, M. Liu, K. Chen, K. Sun, N. Zhang and J. Sun, *ACS Sustain. Chem. Eng.*, 2015, **3**, 3412-3419.

- [47] Q. Xiang, J. Yu and M. Jaroniec, *J. Am. Chem. Soc.*, 2012, **134**, 6575-6578.
- [48] R. Tang, R. Yin, S. Zhou, T. Ge, Z. Yuan, L. Zhang and L. Yin, *J. Mater. Chem. A*, 2017, **5**, 4962-4971.
- [49] X. Shang, W.-H. Hu, X. Li, B. Dong, Y.-R. Liu, G.-Q. Han, Y.-M. Chai and C.-G. Liu, *Electrochim. Acta*, 2017, **224**, 25-31.
- [50] Y.J. Hong and T. Fukui, *ACS nano*, 2011, **5**, 7576-7584.
- [51] A.B. Jorge, D.J. Martin, M.T.S. Dhanoa, A.S. Rahman, N. Makwana, J. Tang, A. Sella, F. Corà, S. Firth, J.A. Darr and P.F. McMillan, *J. Phys. Chem. C*, 2013, **117**, 7178-7185.
- [52] Y. Zhang, J. Liu, G. Wu and W. Chen, *Nanoscale*, 2012, **4**, 5300-5303.
- [53] S. K. Kim, J. J. Wie, Q. Mahmood and H. S. Park, *Nanoscale*, 2014, **6**, 7430-7435.
- [54] X. Zeng, L. Niu, L. Song, X. Wang, X. Shi and J. Yan, *Metals*, 2015, **5**, 1829-1844.
- [55] J. Tong, L. Zhang, F. Li, M. Li and S. Cao, *Phys. Chem. Chem. Phys.*, 2015, **17**, 23532-23537.
- [56] P. Niu, L. Zhang, G. Liu and H.-M. Cheng, *Adv. Funct. Mater.*, 2012, **22**, 4763-4770.
- [57] W. Zhou, Z. Yin, Y. Du, X. Huang, Z. Zeng, Z. Fan, H. Liu, J. Wang and H. Zhang, *Small*, 2013, **9**, 140-147.
- [58] W. Ho, J.C. Yu, J. Lin, J. Yu and P. Li, *Langmuir*, 2004, **20**, 5865-5869.
- [59] H. Zhao, Y. Dong, P. Jiang, H. Miao, G. Wang and J. Zhang, *J. Mater. Chem. A*, 2015, **3**, 7375-7381.
- [60] X. Zong, H. Yan, G. Wu, G. Ma, F. Wen, L. Wang and C. Li, *J. Am. Chem. Soc.*, 2008, **130**, 7176-7177.
- [61] M.A. Lukowski, A.S. Daniel, F. Meng, A. Forticaux, L. Li and S. Jin, *J. Am. Chem. Soc.* 2013, **135**, 10274-10277.
- [62] T. F. Jaramillo, K. P. Jørgensen, J. Bonde, J. H. Nielsen, S. Horch and I. Chorkendorff, *Science*, 2007, **317**, 100-102.
- [63] Y. Sui, J. Liu, Y. Zhang, X. Tian and W. Chen, *Nanoscale*, 2013, **5**, 9150-9155.
- [64] G. Zhang, Z.A. Lan, L. Lin, S. Lin and X. Wang, *Chem. Sci.*, 2016, **7**, 3062-3066.
- [65] R. Ye, H. Fang, Y.Z. Zheng, N. Li, Y. Wang and X. Tao, *ACS Appl. Mater. Interfaces*, 2016, **8**, 13879-13889.
- [66] Z. Pan, Y. Zheng, F. Guo, P. Niu and X. Wang, *ChemSusChem*, 2017, **10**, 87-90.
- [67] J. Wen, J. Xie, Z. Yang, R. Shen, H. Li, X. Luo, X. Chen and X. Li, *ACS Sustain. Chem. Eng.*, 2017, **5**, 2224-2236.
- [68] J.G. Yu, J. Jin, B. Cheng and M. Jaroniec, *J. Mater. Chem. A*, 2014, **2**, 3407-3416.
- [69] X.P. Xiao, J.H. Wei, Y. Yang, R. Xiong, C.X. Pan and J. Shi, *ACS Sustain. Chem. Eng.*, 2016, **4**, 3017-3023.
- [70] D. Jiang, J. Li, C. Xing, Z. Zhang, S. Meng and M. Chen, *ACS Appl. Mater. Interfaces*, 2015, **7**, 19234-19242.
- [71] J. Ke, J. Liu, H. Sun, H. Zhang, X. Duan, P. Liang, X. Li, M.O. Tade, S. Liu and S. Wang, *Appl. Catal., B: Environ.*, 2017, **200**, 47-55.

- [72] Y. Liu, S. Ding, J. Xu, H. Zhang, S. Yang, X. Duan, H. Sun and S. Wang, *Chin. J. Catal.*, 2017, **38**, 1052-1062.
- [73] J. Zhang, Z. Zhu and X. Feng, *Chem. Eur. J.*, 2014, **20**, 10632-10635.
- [74] Y. Guo, J. Li, Z. Gao, X. Zhu, Y. Liu, Z. Wei, W. Zhao and C. Sun, *Appl. Catal. B: Environ.*, 2016, **192**, 57-71.
- [75] X. Xu, Y. Chen, W. Zhou, Z. Zhu, C. Su, M. Liu, Z. Shao, *Adv. Mater.*, 2016, **28**, 6442-6448.
- [76] F. Li, J. Li, Z. Cao, X. Lin, X. Li, Y. Fang, X. An, Y. Fu, J. Jin and R. Li, *J. Mater. Chem. A*, 2015, **3**, 21772-21778.
- [77] H. Zhao, Y. Dong, P. Jiang, H. Miao, G. Wang and J. Zhang, *J. Mater. Chem. A*, 2015, **3**, 7375-7381.

Every reasonable effort has been made to acknowledge the owners of copyright material. I would be pleased to hear from any copyright owner who has been omitted or incorrectly acknowledged.

**Chapter 7. Graphitic Carbon Nitride Decorated with CoP
Nanocrystals for Enhanced Photo, Electro and
Photoelectrochemical H₂ evolution**

Abstract

In this chapter, polydispersed CoP nanoparticles in an orthorhombic phase were synthesized via a gas-solid reaction and then deposited on g-C₃N₄ (CN) to form CoP/g-C₃N₄ heterostructure. Nanorod-like CoP nanoparticles with a length of 10-80 nm were connected to g-C₃N₄ nanosheets via their (011) crystal planes to form an intimate face-to-face contact. This unique heterojunction hybrid exhibits superior photocatalytic and electrocatalytic H₂ evolution performances, photoelectrochemical response as well as excellent overall water splitting activity. Compared with the optimal samples presented in the previous two chapters, 0.5% CoP-CN composite catalyst boasts at its highest photocatalytic H₂ evolution rate of 959.4 $\mu\text{mol}\cdot\text{h}^{-1}\cdot\text{g}^{-1}$ under simulated solar light irradiations, almost 3.1 times as high as that of pure g-C₃N₄. Under visible light irradiations, the photocatalytic H₂ evolution rate was elevated to almost 15.8 times that of pure g-C₃N₄. The onset potential for electrochemical HER process was drastically reduced as compared to pure g-C₃N₄. Also, a larger photocurrent with higher response was detected during the photoelectrochemical hydrogen evolution reactions (PEC HER). The enhancements for photocatalytic, electrocatalytic and PEC HER activity are mainly attributed to the construction of the intimate interfacial contact for reduced overpotentials, lowered charge carrier resistance and stronger photo-reductive potentials, contributing to a much more efficient separation and transfer of charge carriers. This study provides a proof-of-concept design and construction of highly efficient cobalt phosphide-based heterojunctions for hydrogen evolution and water splitting applications.

7.1 Introduction

Recent advancement on developing hydrogen energy via photocatalytic, electrocatalytic and photoelectrochemical (PEC) water splitting has drawn tremendous attention as a promising technology for sustainable energy and clean environment [1-5]. To achieve a high efficiency for solar energy conversion, a rational design of highly efficient semiconductor-based photocatalysts is essential to drive hydrogen evolution from water splitting. Among various systems, non-metal graphitic carbon nitride (g-C₃N₄, CN) has emerged as an ideal candidate for photocatalytic and PEC hydrogen generation with low cost and earth-abundant precursors [6, 7]. Pure g-C₃N₄ with a narrow band gap of ~2.7 eV is responsive to visible light, however

its quantum efficiency is relatively low due to the high recombination rate of photo-generated charge carriers. Moreover, it suffers from low electrical conductivity and also self-decomposition by photo-generated holes during the photocatalytic processes. To address these issues, loading appropriate earth-abundant co-catalysts on g-C₃N₄ to form effective heterostructure can promote efficient spatial charge separation and reduce activation energy of HER process, which is both feasible and economic. Among various noble metal-free cocatalysts for enhanced photocatalytic hydrogen evolution activity, transition metal dichalcogenide (TMD) such as MoS₂ has been mostly studied recently as outstanding cocatalysts to boost H₂ evolution from water reduction [8-12], which could also be found in our previous two chapters.

Metal phosphides, such as CoP, Co₂P and Ni₂P, start to attract wide attention recently as acid-compatible electrocatalysts for HER process as another category of earth-abundant cocatalysts[13-16]. For the first time, Fu's group reported that cobalt phosphide (Co₂P) could be a potential cocatalyst on CdS nanorods for efficient photocatalytic H₂ evolution from water, demonstrating the highest H₂ evolution rate up to 19373 $\mu\text{mol} \cdot \text{h}^{-1} \cdot \text{g}^{-1}$ with the apparent quantum yield reaching 6.8% after 10 h irradiation of LED light ($30 \times 3 \text{ W}$, $\lambda \geq 420 \text{ nm}$) [17]. Apart from the applications in photocatalytic H₂ evolution reaction, cobalt phosphide has also been adopted as a co-catalyst to modify graphitic carbon nitride in overall water splitting without any sacrificial agent [18]. The introduction of CoP could boost the charge separation and reduce the over-potential for oxygen evolution reaction (OER) process as it can also act as a prominent OER electrocatalyst [19]. Due to its dual functional roles in water splitting reactions and scarce research for CoP on photocatalytic or PEC HER process currently, it is worth investigating on cobalt phosphide-based photocatalysts for possible applications on photocatalytic or PEC hydrogen evolution.

Herein, polydispersed CoP nanoparticles in an orthorhombic phase were synthesized via a solid-phase reaction process and were employed to decorate g-C₃N₄ nanosheets by a simple ultrasonic method. The resultant CoP/g-C₃N₄ (CoP-CN) composites exhibit remarkably enhanced photocatalytic, electrocatalytic H₂ evolution performance, photoelectrochemical activity as well as excellent overall water splitting activity, compared to pristine g-C₃N₄. The mechanism and intrinsic properties for charge transfer were comprehensively studied, indicating the formation of an intimate face-to-face contact following a type-II heterojunction system. The introduction of CoP has several benefits such as improving the visible light absorption, reducing the overpotential for hydrogen evolution, lowering charge carrier resistance for higher conductivity and shifting photo-reductive potentials to be more negative.

For the first time, CoP-based photocatalysts as effective photo, electro and photochemical HER catalysts with evident enhancement have been investigated simultaneously.

7.2 Experimental section

7.2.1 Materials

Urea ($\geq 99.5\%$, pellets), cobalt-(II) acetate tetrahydrate, polyvinylpyrrolidone (PVP, K30), sodium hypophosphite monohydrate ($\text{NaH}_2\text{PO}_2 \cdot \text{H}_2\text{O}$), chloroplatinic acid hexahydrate ($\geq 37.5\%$ Pt basis), anhydrous ethanol, and methanol were purchased from Sigma-Aldrich, Australia.

7.2.2 Synthesis of the catalysts

7.2.2.1 Synthesis of g-C₃N₄

Graphitic carbon nitride was prepared by thermal polymerization of urea via heating to 550 °C at a rate of 5 °C/min and annealed at 550 °C for 4 h.

7.2.2.2 Synthesis of Co(OH)₂

Flower-like Co(OH)₂ was synthesized by a modified hydrothermal method [20]. Typically, 0.498 g of Co(CH₃COO)₂·4H₂O, 0.24 g of urea, and 0.5 g of polyvinylpyrrolidone (PVP, K30) were first dissolved in methanol before ultrasonication and mixing. Then, 40 mL of the aqueous solutions were transferred to a 120 mL Teflon-liner with a stainless steel autoclave and subsequently sealed for heating at 200 °C for 6 h in an oven. After centrifugation and washing the possible residual of urea and PVP with water and ethanol several times, the resulting product was obtained as Co(OH)₂.

7.2.2.3 Synthesis of CoP

About 50 mg of the obtained Co(OH)₂ and 250 mg of NaH₂PO₂·H₂O solid were ground in a mortar to form a uniform distribution and put in a quartz boat of the tube furnace. Subsequently the samples were maintained at 300 °C for 1h with a heating rate of 2 °C/min in a flowing 30 mL/min Ar atmosphere. Following cooling to room temperature in continued Ar flow, the obtained black solid was washed subsequently by water and ethanol three times and dried to produce CoP particles.

7.2.2.4 Synthesis of CoP-C₃N₄ composite

CoP-C₃N₄ composite was obtained via an impregnation method. In a typical procedure, 0.1g as-prepared g-C₃N₄ was dispersed in 15 mL methanol, then certain amount of the CoP particles were added to the mixture followed by ultrasonication for 30 min and vigorous stirring at room temperature for 24 h. After evaporation and drying in oven at 80 °C for 24 h to remove the

methanol, the sample was further treated at 150 °C for 2 h in air to strengthen the interaction between CoP nanocrystals and the g-C₃N₄ matrix. It was denoted as 0.5% CoP-CN (0.5 represents weight ratio of CoP to g-C₃N₄).

7.2.2.5 Synthesis of Pt-CoP/C₃N₄ composite

The 3% Pt-0.5% CoP-CN sample was obtained via photodeposition of 0.5% CoP-C₃N₄ in aqueous H₂PtCl₆ solution. Specifically, the mixed aqueous solution was irradiated by a 300 W Xeon lamp for 1 h to reduce H₂PtCl₆ (Pt IV) to metallic Pt under air-free conditions. Finally, the powder was washed well with deionized (DI) water and ethanol, then dried at 70 °C overnight to obtain 3% Pt-0.5% CoP-CN.

7.2.3 Characterization techniques

X-ray diffraction (XRD) spectra were recorded on a Panalytical Empyrean multipurpose research diffractometer utilizing a Cu K α radiation ($\lambda = 1.5418 \text{ \AA}$). Scanning electron microscopic (SEM) images were obtained from a FEI Verios XHR SEM microscope. Transition electron microscopy (TEM) and high-resolution transmission electron microscopy images were collected on a JEOL 2100 TEM microscope. X-ray photoelectron spectroscopy (XPS) testing were performed on a Thermo Escalab 250 with an Al K α X-ray. A Shirley background was first subtracted followed by component fitting using Voigt functions with a 30% Lorentzian component. UV-visible diffuse reflectance spectra (DRS) were collected on an Agilent Cary 100 UV-Visible spectrophotometer equipped with an integrated sphere attachment. Fourier transform infrared (FTIR) spectra were obtained on a PerkinElmer Spectrum 100 spectrometer in the range of 500 - 4000 cm⁻¹.

7.2.4 Evaluation of photocatalytic activity

The photocatalytic hydrogen evolution and water splitting experiments were conducted in a stainless steel vessel sealed with a quartz window with top-irradiation. Details of light source and testing conditions including operating procedures could be found in 5.2.3 of Chapter 5. For overall water splitting to produce H₂ and O₂ simultaneously, 50 mg of 3% Pt-0.5% CoP/g-C₃N₄ sample was dispensed in 100 mL DI water with pH value around 3 (adjusted by hydrochloric acid), followed by fully stirring and evacuation as the same as above. Especially, the reaction vessel was degassed several times to remove air completely before the irradiations. The amount of H₂ and O₂ produced were in situ analyzed by a gas chromatography (Agilent 490 Micro GC) with a thermal conductivity detector.

7.2.5 Photoelectrochemical measurements

Linear sweep voltammetry (LSV), electrochemical impedance spectroscopy (EIS) both in dark and under light, photocurrent-potential (J-V) curves and Mott-Schottky curve measurements were performed on a Zahner Zennium electrochemical workstation in a standard three-electrode framework with a 0.05 M Na₂SO₄ (pH = 6.8) electrolyte solution, adopting a Pt plate (1.5 × 1.5 cm²) as the counter electrode and a Ag/AgCl electrode as the reference electrode. The film of the photoanode was fabricated on a substrate of fluorine-doped tin oxide (FTO) glass, which was ultrasonically cleaned in acetone and ethanol for 20 min in sequence, and then dried at 60 °C. Details of electrode preparation can be found in 5.2.4 of Chapter 5. To be specific, the photocurrent-potential curves were recorded with anodic sweeping (from -1.0 V to +1.0 V) at a scan rate of 10 mV/s with chopped light illumination every 10 s. The PEC responses were also evaluated via current-voltage curves utilizing anodic linear sweep voltammetry (LSV) measurement under irradiation of simulated solar light (300 W Xenon arc lamp, AM 1.5G filter, light intensity: 100 mW·cm⁻²) from 0.2 to 1.0 V (vs. Ag/AgCl).

7.3 Results and discussion

7.3.1 Crystal structure, morphology and composition

XRD patterns of the as-synthesized g-C₃N₄, CoP and 0.5% CoP-CN are shown in Figure 7.1a. Apparently, main peaks of pure CoP could be indexed to the typical orthorhombic phase (JCPDS No. 29-0497) [21]. As for pure g-C₃N₄, two diffraction peaks at 27.3° and 13.0° represent the (002) plane for interplanar stacking of the conjugated bonds and the (100) plane for in-planar ordering of tri-s-triazine units [22], respectively. The XRD pattern of the 0.5% CoP-CN hybrid sample proves the existence of both g-C₃N₄ ((100) and (002)) and CoP ((111), (211), and (020)) phases. The low intensity of characteristic peaks from CoP phases could be ascribed to its extremely low content in the composite.

XPS analysis was performed to study the valence state and surface elemental composition of the 0.5% CoP-CN sample (Figure 7.1b-f). Figure 7.1b presents a XPS survey spectrum, confirming the existence of C, N, and O elements with low contents of Co and P showing poor XPS signals. The presence of O element could originate from the prolonged calcination of g-C₃N₄ in air together with the water molecules adsorbed on its surface [23]. The high-resolution spectra of deconvoluted peaks for C 1s in Figure 7.1c and N 1s in Figure 7.1e conform well with previous reports, indicating the typical species from g-C₃N₄ [24, 25]. Looking into Figure 7.1d and 7.1f, the Co 2p_{3/2} region in Figure 7.1d can be deconvoluted into three peaks at 778.92,

781.28 and 784.57 eV, corresponding to Co 2p_{3/2}, oxidized Co²⁺ (Co-O species) and a satellite peak, respectively [16]. Meanwhile, three typical peaks at 129.49, 131.01 and 134.93 eV were observed from the P 2p region in Figure 7.1f, which can be assigned to P 2p_{3/2}, P 2p_{1/2} and oxidized P-O species, respectively. It was also found that the binding energy of P 2p_{3/2} (129.49 eV) in CoP-CN shifted negatively in comparison to the metallic binding energies of P 2p_{3/2} (130.2 eV), while Co 2p_{3/2} (778.92 eV) shifted positively relative to the metallic binding energies of Co 2p_{3/2} (778.1 eV). That implied that the transfer of electron from Co to P, and that the electron transfer from Co to P to form Co-P bonds with covalent attributes, consistent with previous reports and explaining the mechanism that CoP-based catalysts possess excellent HER activity [16, 26]. Due to the small positive charge of Co, it can act as a catalytic active center, while the small negative charge of P could make it as the proton-acceptor to coordinate the promotion of HER process. The XPS survey spectrum with chemical composition as well as the spectra of Co 2p and P 2p for pure CoP are also illustrated in Figure 7.2. Compared to CoP in Figure 7.2b and 7.2c, both of the Co 2p and P 2p peaks for 0.5% CoP-CN shift slightly to a higher binding energy, implying the change of surrounding chemical environment of Co and P atoms after hybridization with g-C₃N₄ due to the change of bonding.

SEM images of Co(OH)₂, CoP and 0.5% CoP-CN were presented in Figure 7.3. As shown in Figure 7.3a and Figure 7.3b, Co(OH)₂ particles exhibit a well-defined flower-like microstructure composed of thin nanosheets stacked together. The formation of this unique morphology was attributed to the assistance of one of the precursors as PVP, which facilitates the assembling of hydroxides into rods, then further re-arranges them into flakes and stacked together to form this floriform mesoporous microstructure. Figure 7.3c shows that CoP nanoparticles are polydispersed and agglomerated together. After hybridized with g-C₃N₄, CoP nanoparticles have been evenly dispersed and incorporated into matrix of g-C₃N₄ nanosheets exhibiting a more fluffy and porous structure, which can be observed in Figure 7.3d.

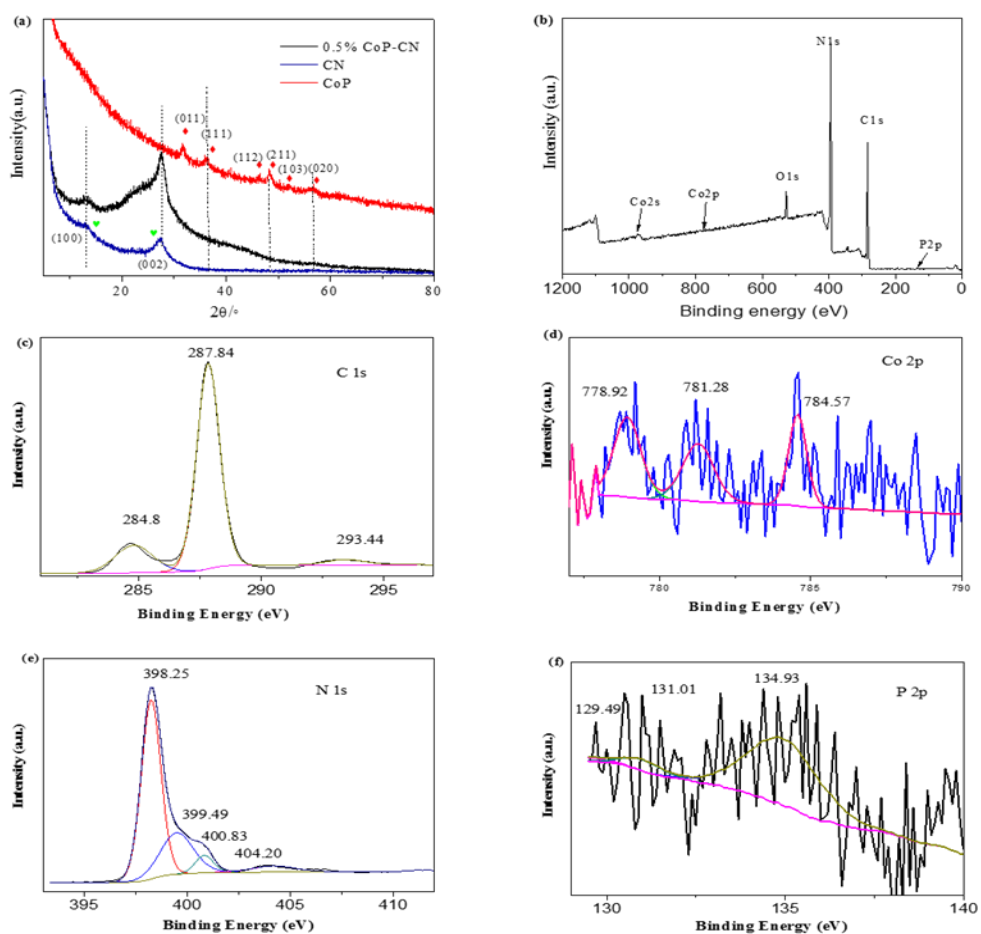


Figure 7.1. (a) XRD patterns of pure CoP, g-C₃N₄ and 0.5% CoP-CN samples; (b) XPS survey of 0.5% CoP-CN; XPS spectra of (c) C 1s (d) Co 2p (e) N 1s and (f) P 2p for 0.5% CoP-CN sample.

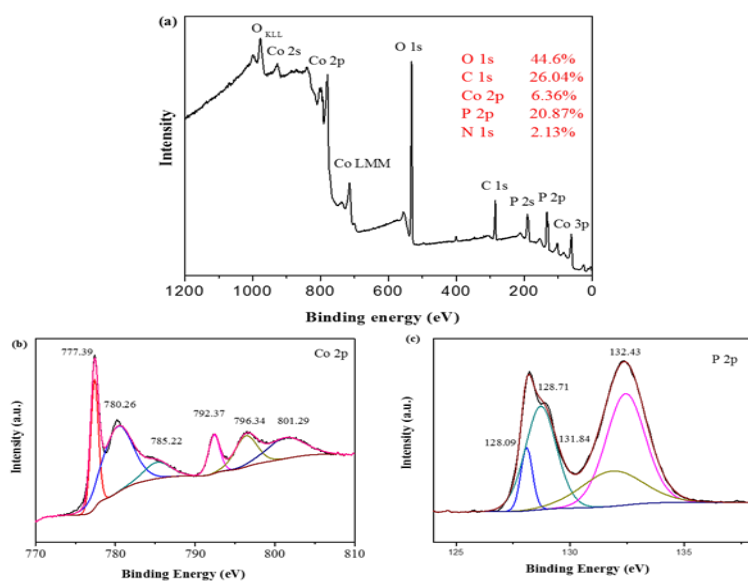


Figure 7.2. (a) XPS survey of pure CoP; XPS spectra of (b) Co 2p and (c) P 2p for CoP sample.

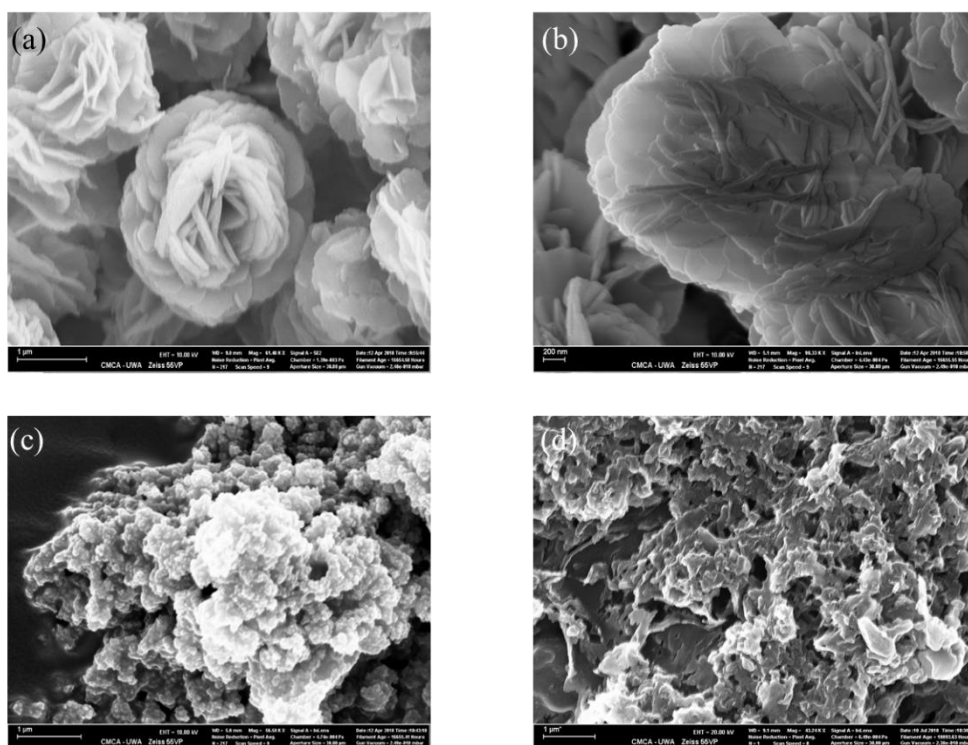


Figure 7.3. SEM images of as-synthesized (a-b) Co(OH)_2 ; (c) CoP and (d) 0.5% CoP-CN.

TEM and HRTEM images of CoP and 0.5% CoP-CN are clearly displayed in Figure 7.4. Figure 7.4a shows the nanorod-like CoP structure with a length of 10-80 nm. The HRTEM image in Figure 7.4b reveals two clear lattice fringe of (011) and (211) crystalline phase, corresponding to the lattice spacing of 0.28 and 0.19 nm, respectively. After being deposited on $\text{g-C}_3\text{N}_4$ support, it also shows a similar nanorod-like structure entrapped in $\text{g-C}_3\text{N}_4$ nanosheet with thin layers. As illustrated in Figure 7.4c and 7.4d, the introduction of $\text{g-C}_3\text{N}_4$ enhanced the dispersity of CoP nanoparticles, forming intimate junctions at the interface. Specifically, the CoP nanostructure with good crystallinity was closely connected to $\text{g-C}_3\text{N}_4$ nanosheets via their (011) crystal planes (lattice spacing of 0.28 nm). This intimate contact between $\text{g-C}_3\text{N}_4$ and CoP would contribute to the more efficient charge transfer and separation via shorter transport paths to the surface, which is beneficial for the enhancement of photocatalytic hydrogen evolution activity. This observation is in accordance with the XRD and SEM results.

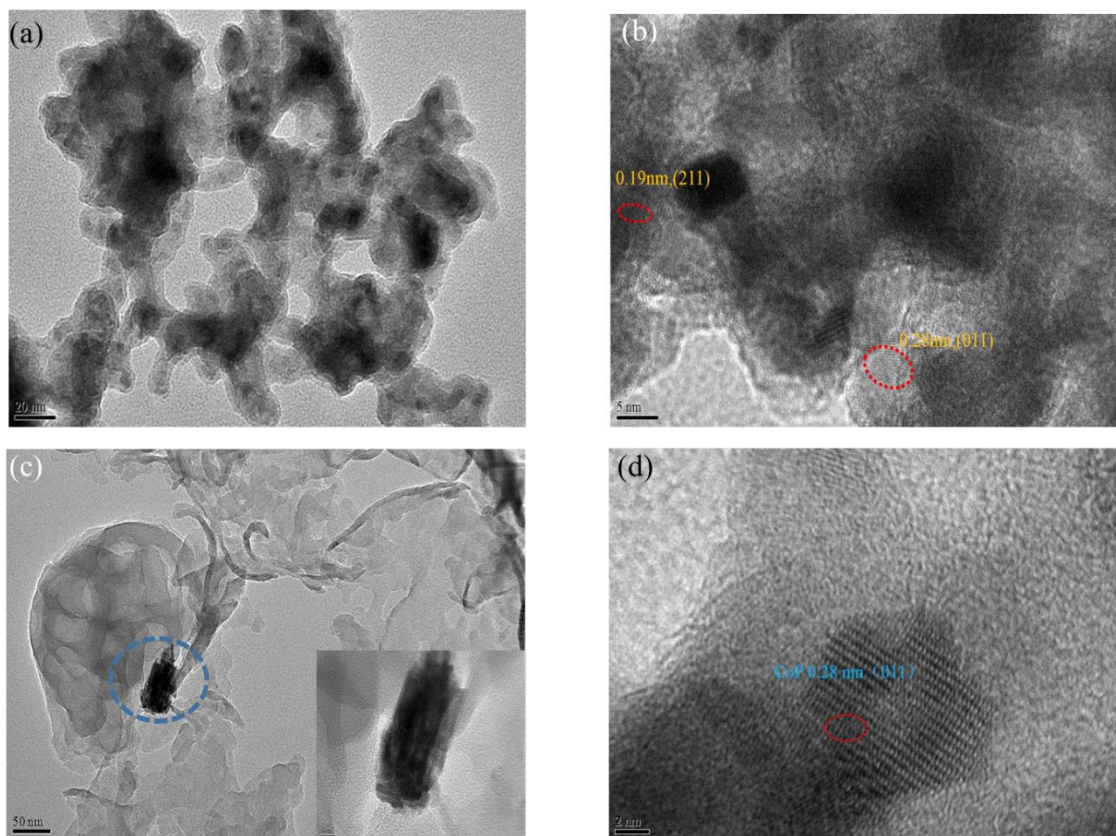


Figure 7.4. (a) TEM and (b) HRTEM images of CoP; (c) TEM image (inset is magnified image) of 0.5% CoP-CN and (d) HRTEM image of 0.5% CoP-CN.

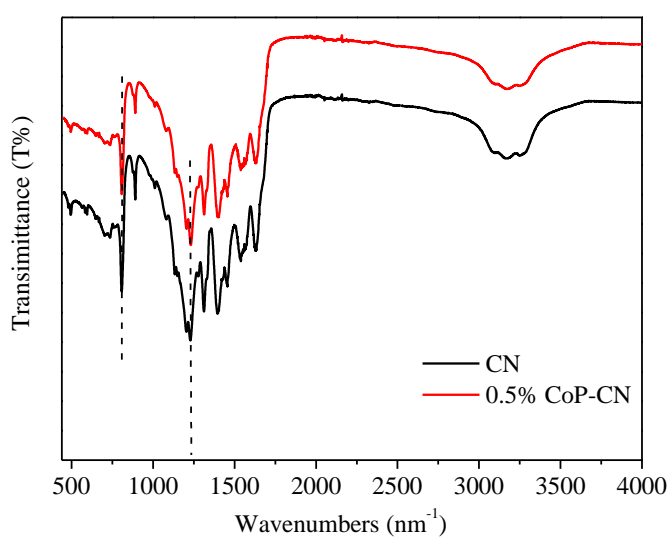


Figure 7.5. FI-IR spectra of the as-synthesized samples.

Figure 7.5 shows FT-IR spectra of pure g-C₃N₄ and 0.5% CoP-CN composite sample. The deposition of CoP did not affect the core chemical skeleton of g-C₃N₄ with no noteworthy changes observed. Most of the absorption bands within the range of 1100-1700 cm⁻¹ are attributed to the characteristic stretching modes of heterocyclic compounds of g-C₃N₄ [27]. In addition, the sharp absorption band at 806 cm⁻¹ corresponds to the vibration mode of the tri-s-triazine (C₆N₇) rings as basic tectonic units of g-C₃N₄.

7.3.2 Optical properties

Figure 7.6 demonstrates the ultraviolet-visible diffuse reflectance spectra (DRS) of g-C₃N₄, CoP and 0.5% CoP-CN composite samples. As it is seen from Figure 7.6a, no significant change of absorption edges could be observed for 0.5% CoP-CN, relative to pure g-C₃N₄. The loading of CoP is found to contribute to a slightly increased light absorption within the visible light range, which makes it possible to be an efficient visible-light photocatalyst. For pure CoP, it manifests good light absorption over the whole range of UV-visible wavelength. Their Tauc plots based on equation $(\alpha h\nu)^n = k(h\nu - E_g)$ [6, 28] are displayed in Figure 7.4b and 7.4c accordingly with transform details discussed in Chapter 5 and Chapter 6 (For g-C₃N₄ and 0.5% CoP-CN, transition type of n is 1/2 as indirect transition semiconductors, while for CoP, n is 2 as a direct gap semiconductor). All the band-gap energies are summarized in Table 7.1. The slight band-gap shift of the composite proves that CoP was successfully deposited onto the surface of g-C₃N₄ to form effective heterojunctions.

Table 7.1. Band-gap energies of g-C₃N₄ and MSNS-CN composites.

Sample	Band-gap (eV)
g-C ₃ N ₄	2.79
0.5% CoP-CN	2.82
CoP	2.15

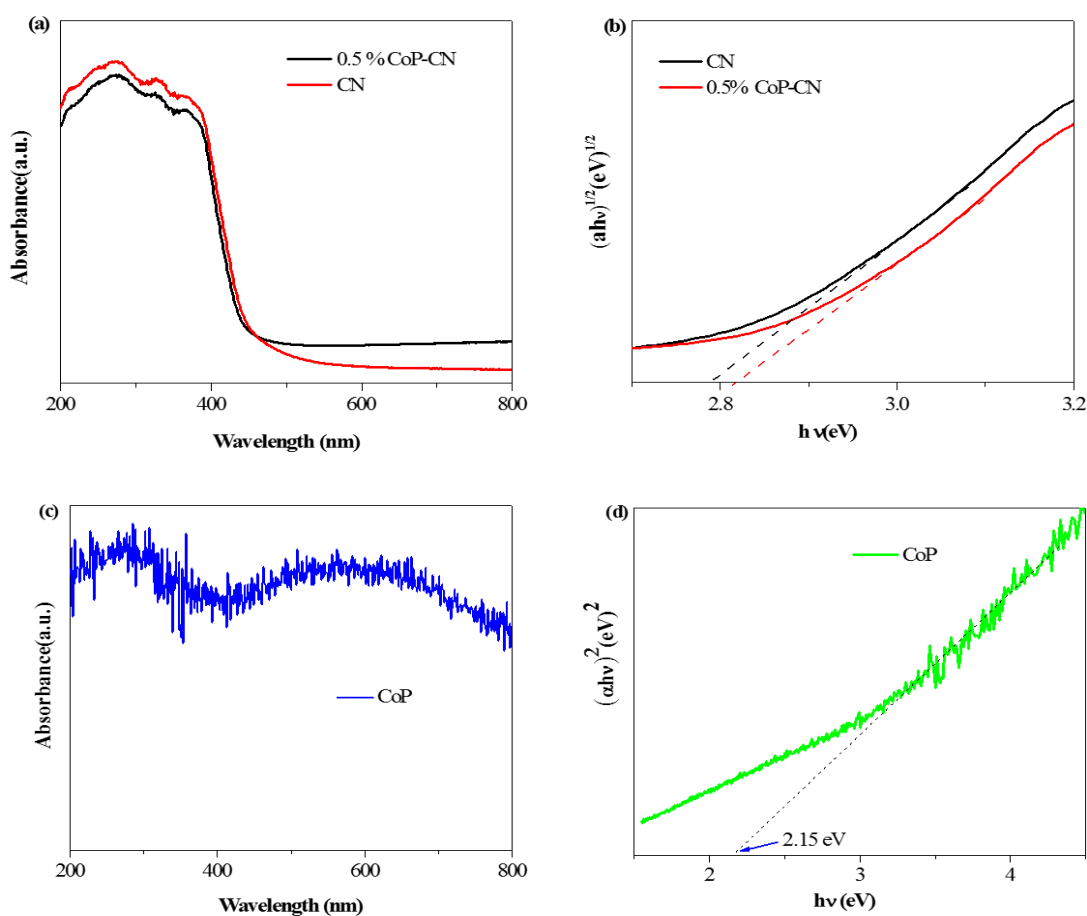


Figure 7.6. (a) UV-vis DRS spectra; (b) the plots of $(\alpha h\nu)^{1/2}$ versus photon energy ($h\nu$) for 0.5% CoP-CN and CN; (c) UV-vis DRS spectrum and (d) the plots of $(\alpha h\nu)^2$ versus photon energy ($h\nu$) for CoP.

7.3.3 Photocatalytic HER and water splitting activity

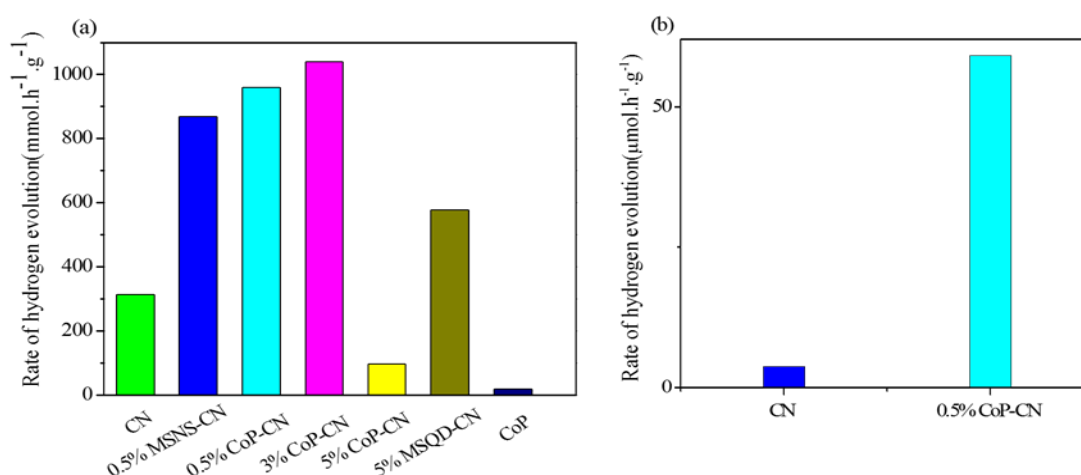


Figure 7.7. (a) Photocatalytic H₂ evolution of g-C₃N₄ loaded with different co-catalysts under simulated solar light irradiations (25 vol% methanol, 2.0 wt% Pt, 0.05 g catalyst in 120 mL aqueous solution, pH=6.8) and (b) Comparison of photocatalytic H₂ evolution over g-C₃N₄ and 0.5% CoP-CN under visible light irradiations (25 vol% methanol, 3.0 wt% Pt, 0.05 g catalyst in 120 mL aqueous solution, pH=3)

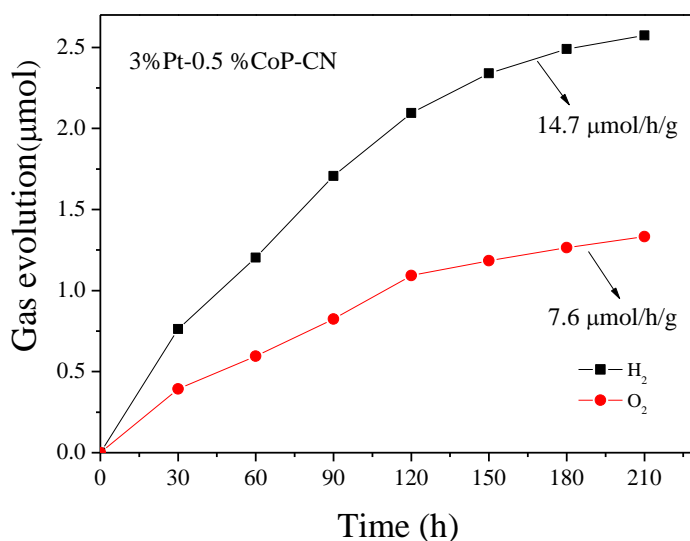


Figure 7.8. Photocatalytic overall water splitting over 3% Pt-0.5% CoP/g-C₃N₄ under simulated solar light irradiations for 4 h (0.05 g catalyst in 100 mL aqueous solution, pH=3).

The photocatalytic H₂ evolution performance of 0.5% CoP-CN and other various catalysts under simulated solar light were evaluated (Figure 7.7a). The as-synthesized 0.5% CoP-CN has outperformed all the optimal photocatalysts from our previous chapters [24]. Although CoP alone is not showing any photocatalytic activity for hydrogen evolution, it has been proven to be an excellent co-catalyst for g-C₃N₄. The hydrogen evolution rate of 0.5% CoP-CN reached 959.4 μmol·h⁻¹·g⁻¹ during 4 h of irradiation, which is approximately 3.1 times as high as that of pristine g-C₃N₄. Improving the content of CoP to 3% would lead to an even higher hydrogen output rate at 1038.1 μmol·h⁻¹·g⁻¹, however, a further loading content of CoP will encounter a drastic decrease in photocatalytic hydrogen performance.

To verify if 0.5% CoP-CN displays an excellent photocatalytic activity for hydrogen evolution under visible light excitation, a light cut-off filter ($\lambda > 420$ nm) was adopted to further study its performance under the similar condition. The comparative results in Figure 7.7b show that the introduction of CoP nanoparticles led to a drastic enhancement of photocatalytic H₂ evolution rate of g-C₃N₄ from 3.75 to 59.1 μmol·h⁻¹·g⁻¹, indicating the significantly enhanced photocatalytic activity due to higher absorption capacity of visible light and more efficient charge separation as well as faster transfer to the surface.

Therefore, 0.5% CoP-CN was proven to possess a superior photocatalytic hydrogen evolution performance and was employed further to investigate its overall water splitting activity without addition of a sacrificial agent. After further deposited with Pt nanoparticles, this 3%Pt-0.5% CoP-CN photocatalyst with dual co-catalysts exhibited distinct activity for

overall water splitting into O₂ and H₂ simultaneously, as shown in Figure 7.8. The evolution rates of H₂ and O₂ were estimated to be 14.7 and 7.6 μmol·h⁻¹·g⁻¹, which is in a molar ratio of 1.93:1, much close to the theoretical value of H₂/O₂ evolution for water splitting stoichiometrically. After 4 h of full-arc irradiation as simulated solar light, the produced amount for H₂ and O₂ achieved 2.57 and 1.33 μmol, respectively. We also tested with pure g-C₃N₄ and 0.5% CoP-CN, but both of them showed extremely poor photoactivity for this overall water splitting process without noticeable yields observed for H₂ and O₂. Thus, the dual co-catalyst system is beneficial and determining in the enhancement of photocatalytic activity for overall water splitting due to the cooperative and synergistic effect between the two co-catalysts, which serve as active sites to promote H₂ and O₂ evolutions simultaneously. To be more specific, Pt could serve as electron collectors as reduction sites to reduce overpotentials for H₂ evolution, while the deposition of CoP could serve as active sites by reducing overpotentials for O₂ evolution and promote the reaction rate as well as charge separation [18, 29].

7.3.4 Photocatalytic mechanism

To further probe if the introduction of CoP nanoparticles can reduce the overpotential for hydrogen production as well as improve the charge transfer and separation efficiency across the interface, electrochemical impedance spectroscopy (EIS) testing under both dark and irradiation conditions, polarization curves, photoelectrochemical response and Mott-Schottky (M-S) analysis were conducted.

For the band structure of the different catalysts, Mott-Schottky (M-S) plots and valence band (VB) XPS spectra were measured to obtain the flat band potentials and the maximum valence band potentials, respectively. The M-S plots of film electrodes made by various samples can be found in Figure 7.9 (a-c), which display the flat band potentials of g-C₃N₄, CoP and 0.5% CoP-CN at approximately -0.2 V, 0.35 V and -0.28 V vs. Ag/AgCl in the dark, respectively, obtained from the x intercepts by extrapolating the linear regions to the horizontal axis[24, 30, 31]. All of them present typical n-type semiconductor attributes with a positive slope, indicating that their minimum conduction band potentials should be very close to their flat band potentials. Looking into Figure 7.9a and 7.9c, the conduction band potential of 0.5% CoP-CN shifted upward to be more negative and reductive, which might facilitate the establishment of certain electric field to foster more efficient transfer and separation of charge carriers at the

interface. Apparently, 0.5% CoP-CN boasts at a more negative potential for stronger water reduction capability thermodynamically.

The Fermi levels (E_f) can be inferred from the flat band potentials considering the difference from the water reduction potentials[32-34]. From VB XPS spectra (Figure 7.10), the maximum valence band energies were estimated to be 2.08 and 1.72 eV relative to the Fermi level. Combining above analysis from VB XPS and M-S plots with the results from DRS for band energy values as listed in Table 7.1, it is possible to calculate the approximate band energy levels for each semiconductor. In detail, the maximum VB energy levels of CN and CoP were estimated to be 1.68 and 1.75 eV, respectively. Accordingly, the minimum CB energy levels were calculated to be -1.11 and -0.40 eV. Based on above discussions, the detailed electronic band positions of various catalysts are illustrated in Figure 7.11d.

A series of photoelectrochemical measurements were performed to investigate the inherent properties for photoelectrochemical response as well as transfer mechanism of charge carriers. As one of the most convincing techniques, EIS analysis was conducted on the photoanodes both in the dark and under the full light irradiation conditions. In comparison with their arc radius in the dark, all the three samples exhibit distinctly diminished semicircles under light irradiations, especially for g-C₃N₄ and 0.5% CoP-CN. This observation indicates that the charge transfer resistance was largely reduced due to significant enhancement of charge carrier flow excited by photons. Focusing on the three catalysts, it is no doubt that g-C₃N₄ exhibits the largest interfacial charge transfer resistance owing to its low electrical conductivity. The introduction of CoP nanoparticles with a higher conductivity has been proved to boost a much more efficient charge transport across the interface of electrode and electrolyte, producing a much smaller arc radius than that of pure g-C₃N₄ and CoP. The rational construction of the CoP/CN heterostructure has effectively facilitated the conductivity with reduced charge carrier resistance.

The electrochemical HER performance of the samples was also evaluated utilizing polarization curves. As displayed in Figure 7.11a, both of the electrodes made from g-C₃N₄ and 0.5% CoP-CN present distinct cathodic currents covering the range of -0.2 ~ -1.0 V (versus Ag/AgCl) with continuous hydrogen bubbles released around the working electrode. Obviously, pure g-C₃N₄ shows a relatively poor electrocatalytic performance towards HER, with an onset potential as high as -0.61 V vs. Ag/AgCl plus a relatively weak cathodic current, while 0.5% CoP-CN composite catalyst manifests a drastically enhanced HER activity with much lower onset potential at -0.31 V vs. Ag/AgCl and also a higher current density. At an applied potential of -0.4 V vs. Ag/AgCl, apparent current of 0.06 mA·cm⁻² with respect to H₂ evolution was

detected. Thus, the deposition of CoP can lower the activation barriers for hydrogen evolution, reducing the overpotentials and accelerating the H₂ evolution kinetics.

The photocurrent-potential response curves under chopped light illumination were acquired (Figure 7.11b). As expected, the binary photocatalyst of 0.5% CoP-CN exhibits a much higher photocurrent response than pure g-C₃N₄ throughout the polarization potential range of -1.0 - 0 V vs. Ag/AgCl. With the increasing positive polarization potential from 0-1.0 V vs. Ag/AgCl, the photocurrent response of g-C₃N₄ sample becomes larger and gets close to that of 0.5% CoP-CN. Apart from the photocurrent response, it is worth noting that the onset current potential for g-C₃N₄ electrode has been shifted more negatively from 0 V vs. Ag/AgCl to -0.2 vs. Ag/AgCl after coupling with CoP, which is consistent with previous observations and results. The modification of g-C₃N₄ film with CoP could boost the photooxidation or photoreduction ability of the catalyst, leading to much higher photocatalytic or photoelectrochemical activity. The enhanced photocurrent indicates that the introduction of CoP might contribute to higher efficiency for generation and migration of interfacial charge carriers[12]. Additionally, the current-potential curves of various samples before and after light irradiations were obtained and are shown in Figure 7.11c. Significant anodic currents could be observed for both g-C₃N₄ and 3% CoP-CN after light was switched on at the applied bias of +0.2 V vs. Ag/AgCl, implying that the photo-excited electrons were injected from the working electrode film to the FTO glass, and then further transferred to the counter electrode for hydrogen evolution via the external circuit. The prompt increase of the anodic current indicates the quick release of hydrogen from the Pt electrode, thus the photogenerated electrons will be quickly separated from the holes to avoid recombination. In the photoelectrochemical (PEC) test, usually a n-type semiconductor material will be adopted as the photoanode to form a positive anodic photocurrent[35], which further confirms the M-S results from Figure 7.9 to prove that 0.5% CoP-CN is a n-type semiconductor. As for pure g-C₃N₄, no detectable increase for the photocurrent density could be observed after the light is on. Based on Figure 7.11c, the maximum η_{ABPE} (applied bias photon-to-current efficiency) could be calculated according to the following equation [36]:

$$ABPE = \frac{J_{ph} * (1.23 - |V|)}{P} * 100\% \quad (7.1)$$

Where P is the incident light intensity ($\text{mW}\cdot\text{cm}^{-2}$), J_{ph} is the measured photocurrent density ($\mu\text{A}\cdot\text{cm}^{-2}$) at the applied bias potential V (vs. Ag/AgCl), while 1.23 V is the minimum potential required for water splitting thermodynamically. Hence, the maximum η_{ABPE} of $\text{g-C}_3\text{N}_4$ and 3% CoP-CN were estimated to be 0.039% and 0.051%, respectively. The enhanced ABPE and photoelectrochemical response denote a promoted separation and transfer efficiency of photo-induced electrons and holes, owing to the construction of CoP-CN heterostructure. This result was further confirmed by transient photocurrent-time response and photocurrent-voltage characteristics as depicted in Figure 7.12. Under intermittent light illumination of 20 s in Figure 7.12a, 3% CoP-CN film achieves stable photocurrent of $150 \mu\text{A}\cdot\text{cm}^{-2}$, much higher than that of pure $\text{g-C}_3\text{N}_4$. As observed in Figure 7.12b, under the same bias potential at + 0.55 V (vs. Ag/AgCl), the film of 3% CoP-CN also presents a much higher anodic photocurrent density of $120 \mu\text{A}\cdot\text{cm}^{-2}$ relative to $\text{g-C}_3\text{N}_4$, which only reaches $1.48 \mu\text{A}\cdot\text{cm}^{-2}$ with more stable photocurrent response. Similar trends can be found in Figure 7.12b for the negative shift of onset photocurrent potential with 3% CoP-CN.

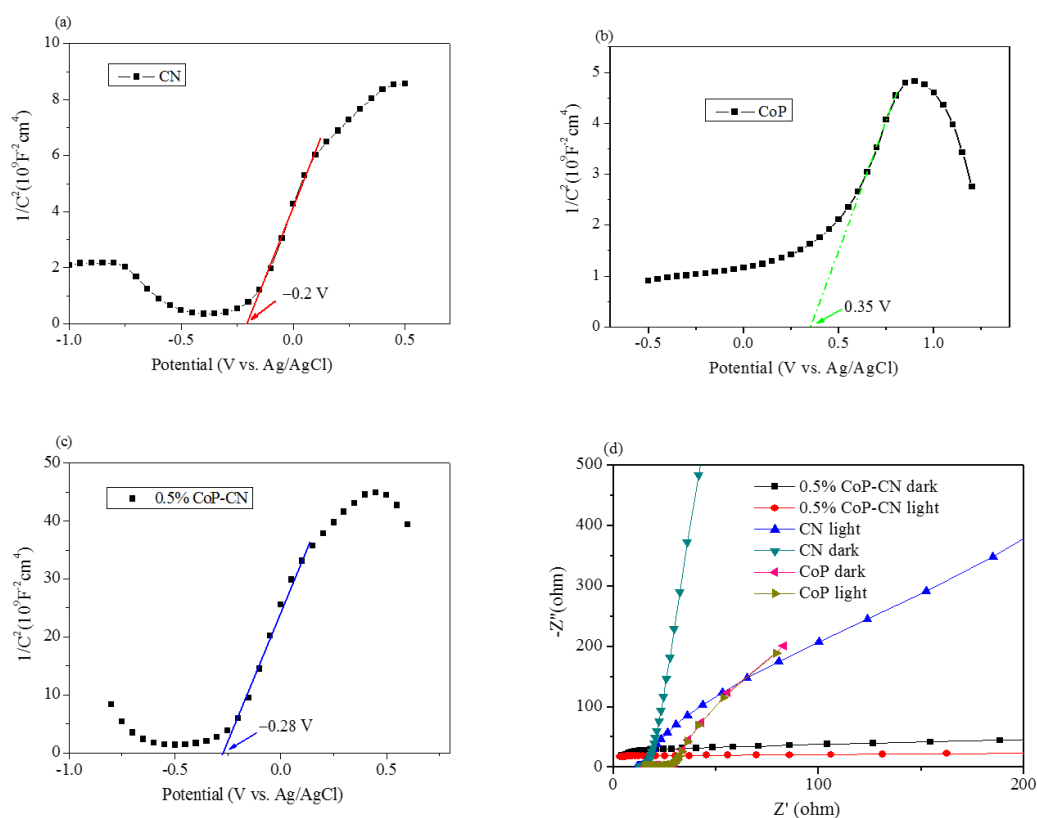


Figure 7.9. Mott–Schottky plots collected on (a) $\text{g-C}_3\text{N}_4$; (b) CoP; (c) 0.5% CoP-CN; (d) Electrochemical impedance spectroscopy (EIS) Nyquist plots of different electrodes both in the dark and under light irradiations.

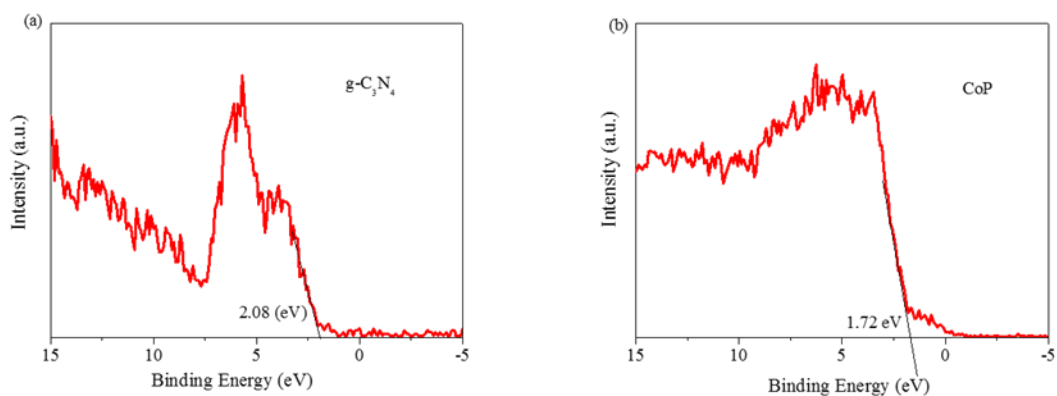


Figure 7.10. VB XPS spectra of (a) $g\text{-C}_3\text{N}_4$ and (b) CoP.

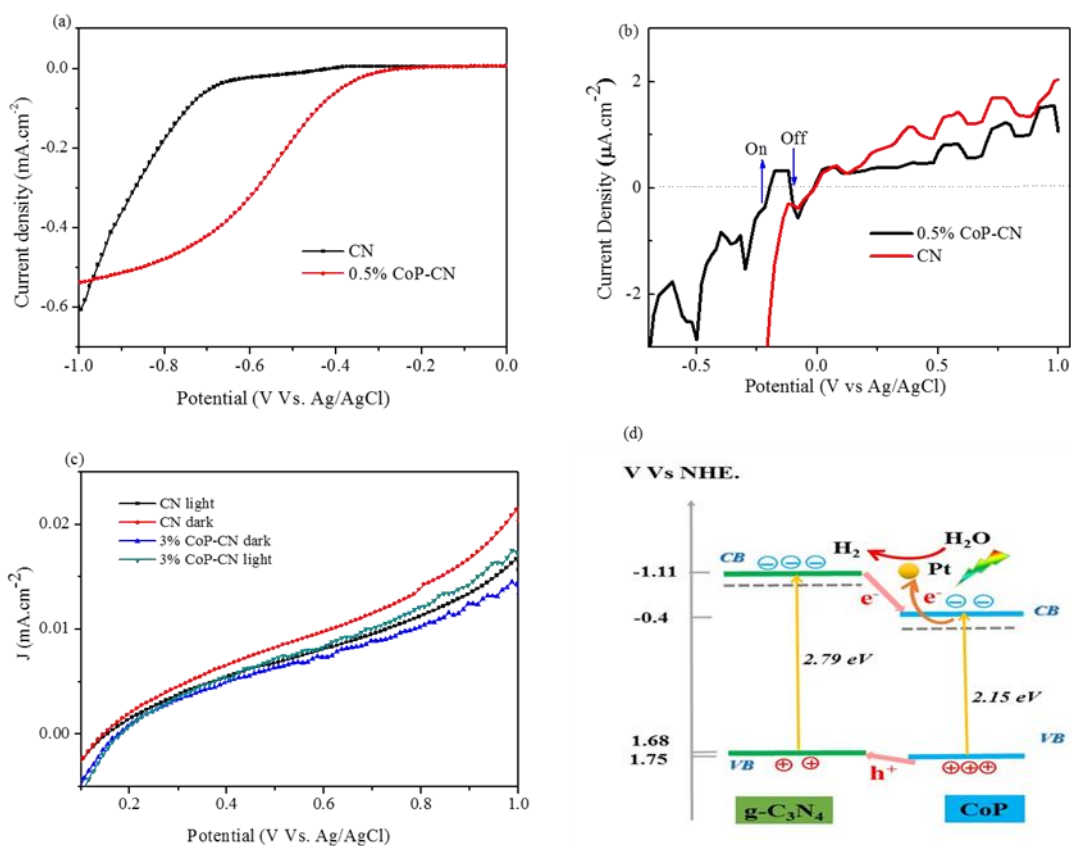


Figure 7.11. (a) Polarization curves of $g\text{-C}_3\text{N}_4$ and 0.5% CoP-CN; (b) The chopped illuminated photocurrent-potential (I-V) curves of $g\text{-C}_3\text{N}_4$ and 0.5% CoP-CN; (c) Current-voltage curves of $g\text{-C}_3\text{N}_4$ and 3% CoP-CN both in dark and under light; (d) Band structure diagram of 0.5% CoP-CN.

Given the explorations above, the superior performance of 0.5% CoP-CN in photocatalytic H₂-evolution as well as overall water splitting can be attributed to the reduced overpotentials for H₂ evolution and accelerated separation and transfer of charge carriers. The introduction of CoP serves as an electron collector and also active sites to reduce overpotentials for hydrogen evolution. Additionally, it will also affect the light absorption ability and photoreduction potentials of the g-C₃N₄ film. Based on above discussions, the energy band positions and proposed charge transfer scheme are illustrated in Figure 7.11d, which is in agreement with the type-II heterojunction system [37]. Under sunlight irradiations, the electrons excited into the CB of g-C₃N₄ will be injected to the lower CB of CoP to produce an electron center, while most of the holes will move in the opposite direction from VB of CoP to that of g-C₃N₄ to form a hole center. As the electron collector, CoP will further transfer some of the electrons to Pt nanoparticles on the surface for quick hydrogen release. The collected holes on VB of g-C₃N₄ will be responsible for the oxidation of methanol, by which the photo-generated electrons and holes will get separated and hindered for possible recombination. Under visible light irradiations, the CoP with a narrower band gap could also get photo-excited and make utilization of the long-wavelength region. Overall, the deposition of CoP nanoparticles on surface of g-C₃N₄ can contribute to the significantly enhanced photocatalytic hydrogen evolution activity by constructing an intimate interfacial contact for reduced overpotentials, lowered charge carrier resistance and stronger photo-reductive capability.

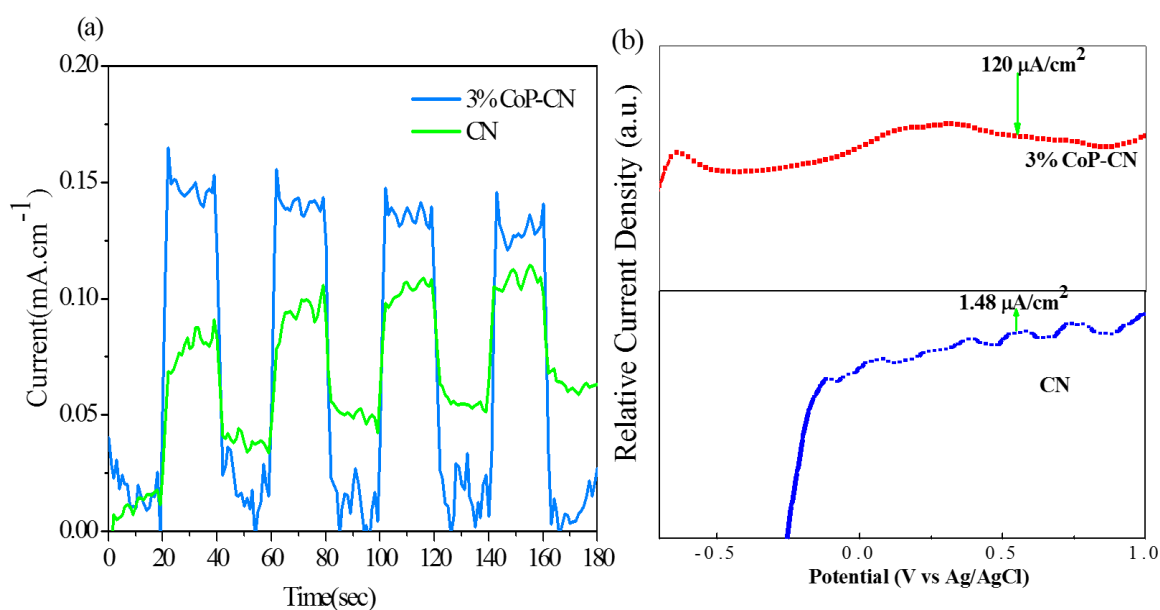


Figure 7.12. (a) Transient photocurrent-time curves of g-C₃N₄ and 3% CoP-CN; (b) The chopped illuminated photocurrent-potential (I-V) curves of g-C₃N₄ and 3% CoP-CN.

Regarding the mechanism for distinct overall water splitting activity, we assume that Pt can act as H₂ evolution sites while CoP may act as O₂ evolution sites with reduced overpotentials for hydrogen and oxygen evolutions simultaneously. This verification of dual co-catalysts function still needs further evidences except for the current discussion. For example, electrochemical OER as well as photocatalytic OER measurements for CoP-CN should also be conducted in future study.

7.4 Conclusions

To summarize, polydispersed orthorhombic phase CoP particles were prepared via a gas-solid reaction and further employed to be deposited on the surface of g-C₃N₄ nanosheets to form CoP/g-C₃N₄ heterostructure. The as-prepared intimate junctions of 0.5% CoP-CN boosted a drastically enhanced photocatalytic, electrocatalytic and photoelectrochemical HER performance. The photocatalytic hydrogen evolution rate reached 959.4 $\mu\text{mol}\cdot\text{h}^{-1}\cdot\text{g}^{-1}$ under simulated sunlight irradiations, almost 3.1 times as high as that of pristine g-C₃N₄. The photocatalytic H₂ evolution activity under visible light was elevated to almost 15.8 times that of pure g-C₃N₄. The onset potential for electrochemical HER process was lowered from -0.61 V vs. Ag/AgCl for pristine g-C₃N₄ to -0.31 V vs. Ag/AgCl. A larger photocurrent density with higher response was reflected with 0.5% CoP-CN for the photoelectrochemical (PEC) HER testing. Finally, it also showed excellent overall water splitting activity without any sacrificial agent. The simultaneous evolution rates of H₂ and O₂ were estimated to be 14.7 and 7.6 $\mu\text{mol}\cdot\text{h}^{-1}\cdot\text{g}^{-1}$. The enhancements for photocatalytic, electrocatalytic and PEC HER activities can be ascribed to the deposition of CoP nanoparticles by constructing an intimate interfacial contact for reduced overpotentials, lowered charge carrier resistance and stronger photo-reductive capability, promoting much more efficient separation and transfer of charge carriers. This finding provides novel perspective for designing and constructing highly efficient cobalt phosphide-based heterojunctions as photocatalytic, electrocatalytic and PEC HER catalysts.

References

- [1] J. Bai, R. Wang, Y. Li, Y. Tang, Q. Zeng, L. Xia, X. Li, J. Li, C. Li and B. Zhou, *J Hazard Mater*, 2016, **311**, 51-62.
- [2] O. Monfort, L.-C. Pop, S. Sfaelou, T. Plecenik, T. Roch, V. Dracopoulos, E. Stathatos, G. Plesch and P. Lianos, *Chem. Eng. J.*, 2016, **286**, 91-97.
- [3] Y.-J. Tang, Y. Wang, X.-L. Wang, S.-L. Li, W. Huang, L.-Z. Dong, C.-H. Liu, Y.-F. Li and Y.-Q. Lan, *Adv. Energy Mater.*, 2016, **6**, 1600116.
- [4] Y. Zhu, Q. Ling, Y. Liu, H. Wang and Y. Zhu, *Phys Chem Chem Phys*, 2015, **17**, 933-940.
- [5] D. Zheng, X.N. Cao and X. Wang, *Angew. Chem., Int. Ed.*, 2016, **55**, 11512-11516.
- [6] H. Sun, G. Zhou, Y. Wang, A. Suvorova and S. Wang, *ACS Appl. Mater. Interfaces.*, 2014, **6**, 16745-16754.
- [7] L. Zhou, H.Y. Zhang, H.Q. Sun, S.M. Liu, M.O. Tade, S.B. Wang and W.Q. Jin, *CATAL SCI TECHNOL*, 2016, **6**, 7002-7023.
- [8] L. Shi, W. Ding, S. Yang, Z. He and S. Liu, *J Hazard Mater*, 2018, **347**, 431-441.
- [9] D. Zheng, G. Zhang, Y. Hou and X. Wang, *Appl. Catal., A: General.*, 2016, **521**, 2-8.
- [10] Y. Hou, A.B. Laursen, J. Zhang, G. Zhang, Y. Zhu, X. Wang, S. Dahl and I. Chorkendorff, *Angew. Chem., Int. Ed.*, 2013, **52**, 3621-3625.
- [11] J. Xie, H. Zhang, S. Li, R. Wang, X. Sun, M. Zhou, J. Zhou, X.W. Lou and Y. Xie, *Adv. Mater.*, 2013, **25**, 5807-5813.
- [12] L. Ye, D. Wang and S. Chen, *ACS Appl. Mater. Interfaces.*, 2016, **8**, 5280-5289.
- [13] D. Zeng, W.-J. Ong, Y. Chen, S.Y. Tee, C.S. Chua, D.-L. Peng and M.-Y. Han, *PART PART SYST CHAR*, 2018, **35**, 1700251.
- [14] C. Wu, Y. Yang, D. Dong, Y. Zhang and J. Li, *Small*, 2017, **13**, 1602873.
- [15] P. Ye, X. Liu, J. Iocozzia, Y. Yuan, L. Gu, G. Xu and Z. Lin, *J. Mater. Chem. A*, 2017, **5**, 8493-8498.
- [16] Y. Pan, Y. Lin, Y. Chen, Y. Liu and C. Liu, *J. Mater. Chem. A*, 2016, **4**, 4745-4754.
- [17] S. Cao, Y. Chen, C.-C. Hou, X.-J. Lv and W.-F. Fu, *J. Mater. Chem. A*, 2015, **3**, 6096-6101.
- [18] Z. Pan, Y. Zheng, F. Guo, P. Niu and X. Wang, *ChemSusChem*, 2017, **10**, 87-90.
- [19] J. Ryu, N. Jung, J.H. Jang, H.-J. Kim and S.J. Yoo, *ACS Catal.*, 2015, **5**, 4066-4074.
- [20] H. Zhang, W. Tian, X. Guo, L. Zhou, H. Sun, M.O. Tade and S. Wang, *ACS Appl. Mater. Interfaces.*, 2016, **8**, 35203-35212.
- [21] S.-S. Yi, J.-M. Yan, B.-R. Wulan, S.-J. Li, K.-H. Liu and Q. Jiang, *Appl. Catal., B: Environ.*, 2017, **200**, 477-483.
- [22] J. Wen, J. Xie, Z. Yang, R. Shen, H. Li, X. Luo, X. Chen and X. Li, *ACS Sustain. Chem. Eng.*, 2017, **5**, 2224-2236.
- [23] S.M. Lyth, Y. Nabae, S. Moriya, S. Kuroki, M.-a. Kakimoto, J.-i. Ozaki and S. Miyata, *J. Phys. Chem. C*, 2009, **113**, 20148-20151.

- [24] Y. Liu, H. Zhang, J. Ke, J. Zhang, W. Tian, X. Xu, X. Duan, H. Sun, M. O Tade and S. Wang, *Appl. Catal., B: Environ.*, 2018, **228**, 64-74.
- [25] Y. Liu, X. Xu, J. Zhang, H. Zhang, W. Tian, X. Li, M.O. Tade, H. Sun and S. Wang, *Appl. Catal., B: Environ.*, 2018, **239**, 334-344.
- [26] Q. Liu, J. Tian, W. Cui, P. Jiang, N. Cheng, A.M. Asiri and X. Sun, *Angew. Chem., Int. Ed.*, 2014, **126**, 6828-6832.
- [27] Y. Zhang, J. Liu, G. Wu and W. Chen, *Nanoscale*, 2012, **4**, 5300-5303.
- [28] H. Zhang, W. Tian, L. Zhou, H. Sun, M. Tade and S. Wang, *Appl. Catal., B: Environ.* 2017, **223**, 2-9.
- [29] G. Zhang, Z.-A. Lan, L. Lin, S. Lin and X. Wang, *Chem. Sci.*, 2016, **7**, 3062-3066.
- [30] J. Ke, J. Liu, H. Sun, H. Zhang, X. Duan, P. Liang, X. Li, M.O. Tade, S. Liu and S. Wang, *Appl. Catal., B: Environ.*, 2017, **200**, 47-55.
- [31] Y. Liu, S. Ding, J. Xu, H. Zhang, S. Yang, X. Duan, H. Sun and S. Wang, *Chin. J. Catal.*, 2017, **38**, 1052-1062.
- [32] L. Liao, Q. Zhang, Z. Su, Z. Zhao, Y. Wang, Y. Li, X. Lu, D. Wei, G. Feng, Q. Yu, X. Cai, J. Zhao, Z. Ren, H. Fang, F. Robles-Hernandez, S. Baldelli and J. Bao, *Nat Nanotechnol*, 2014, **9**, 69-73.
- [33] J. Liu, J. Ke, D. Li, H. Sun, P. Liang, X. Duan, W. Tian, M.O. Tade, S. Liu and S. Wang, *ACS Appl. Mater. Interfaces.*, 2017, **9**, 11678-11688.
- [34] X. Chen, L. Liu, P.Y. Yu and S.S. Mao, *Science*, 2011, **331**, 746-750.
- [35] Y. Liu, Y.-X. Yu and W.-D. Zhang, *J. Phys. Chem. C*, 2013, **117**, 12949-12957.
- [36] U. Shaislamov, K. Krishnamoorthy, S.J. Kim, W. Chun and H.-J. Lee, *RSC Adv.*, 2016, **6**, 103049-103056.
- [37] H. Li, W. Tu, Y. Zhou and Z. Zou, *Adv Sci (Weinh)*, 2016, **3**, 1500389.

Every reasonable effort has been made to acknowledge the owners of copyright material. I would be pleased to hear from any copyright owner who has been omitted or incorrectly acknowledged.

Chapter 8. Conclusions and Perspectives

8.1 Conclusions

Two typical types of visible-light-responsive photocatalysts, bismuth-based and g-C₃N₄-based heterojunction composites, were chosen for systematic studies towards the applications in both artificial photosynthesis and environmental remediation. Heterogeneous coupling has been proven to be a promising and practical way to improve the photocatalytic activity by inhibiting the recombination rate of photo-generated charge carriers as well as lowering the over-potential for photoreduction or photooxidation reactions. A rational design of novel p-n heterojunction nanomaterials with a core-shell structure provides a new perspective in practical application related to photocatalysis and solar energy conversion. Bismuth-based hybrids such as BiOI/BiOCl have shown superb photocatalytic activity for the degradation of various industrial dyes under natural sunlight irradiations, demonstrating a high significance in the remediation of industrial wastewater. Metal sulfides (phosphides)/g-C₃N₄ composite heterostructures with metal sulfides (phosphides) as co-catalysts have demonstrated enhanced photocatalytic and electrocatalytic hydrogen evolution performances. MoS₂ or CoP can serve as an electron acceptor and also the active sites over g-C₃N₄, leading to the formation of an intimate contact interface with a decreased onset potential, a lower charge-transfer resistance and a higher reductive potential with a more negative conduction band position. Several fabrication techniques and modification strategies have been elaborated to study the morphology and facets control as well as the construction of heterojunction composites. Charge transfer mechanism for most of the constructed heterostructure composites follows a type- II or Z-scheme heterojunction principle for a drastically facilitated separation and migration of electron-hole pairs to enhance the photocatalytic efficiency. These research findings provide novel perspectives for designing and constructing highly efficient metal sulfides (phosphides)/g-C₃N₄ composite heterojunctions as photocatalytic, electrocatalytic and photoelectrochemical HER catalysts with broad application in energy conversion and environmental purification.

8.1.1 Preparation of p-n Heterojunction of BiFeO₃@TiO₂ with a Core-Shell Structure for Visible Light Photocatalytic Degradation

- ❖ A citrate self-combustion approach combined with a hydrolysis precipitation

processing was developed to synthesize nanocomposite photocatalyst $\text{BiFeO}_3@\text{TiO}_2$ with a core-shell structure.

- ❖ The $\text{BiFeO}_3@\text{TiO}_2$ heterojunction (at a mass ratio of 1:1) with a shell thickness of 50-100 nm exhibited much higher photocatalytic oxidation of different dyes (MV, MO and CO) under visible light irradiations than pure BiFeO_3 , TiO_2 and $\text{BiFeO}_3@\text{TiO}_2$ composites with other ratios, attributing to the efficient inhibition of charge recombination, strong light absorption as well as its core-shell structure geometry.
- ❖ The photoelectrochemical results confirm the formation of p-n heterojunction interface between p- BiFeO_3 and n- TiO_2 , which enhances the charge carrier transportation and donor density, leading to the enhancement of the quantum efficiency.
- ❖ MV degradation is mainly attributed to hydroxyl radicals and photo-generated electrons based on energy band theory and the building of an internal electrostatic field. In addition, its unique core-shell structure also favors the charge transfer at the $\text{BiFeO}_3/\text{TiO}_2$ interface via increasing the contact area between BiFeO_3 and TiO_2 .

8.1.2 Three-Dimensional BiOI/BiOX ($X = \text{Cl}$ or Br) Nanohybrids for Enhanced Visible-Light Photocatalytic Activity

- ❖ Flower-like 3D BiOI/BiOX ($X = \text{Br}$ or Cl) hybrids were successfully fabricated via a facile one-pot solvothermal approach. The BiOI/BiOCl hybrids present a morphology of fluffy and porous 3D microspheres with large specific surface areas and high light absorption abilities.
- ❖ Under visible light irradiations, both the composites exhibited significant enhancements of the photocatalytic oxidation performance compared to pure BiOI . The apparent reaction rate for MO degradation on BiOI/BiOCl is 2.1 times higher, and 1.6 times higher than that of pure BiOI , respectively. Moreover, BiOI/BiOCl demonstrated a slight promotion under UV light irradiations, which is 1.3 times higher than pure BiOI . Moreover, BiOI/BiOCl composite also displayed an excellent water oxidation ability with enhanced O_2 evolution from the water, which was 1.5 times higher than that of BiOI .

- ❖ The enhancement of photocatalytic activity can be attributed to the formation of a heterojunction between BiOI and BiOCl, which facilitates the separation and transportation of charge carriers more efficiently with a rationally-engineered energy band structure. In addition, the nanoporous structure, larger specific surface area, and the stronger light absorption capacity both in the visible and UV region also contributed to the excellent photocatalytic activity of the BiOI/BiOCl composites.
- ❖ The photodegradation was evidenced to be ascribed to the superoxide radicals, oxidative holes, and a minor amount of hydroxyl radicals. This study deepens the understanding of BiOI/BiOCl composites for enhanced photodegradation and water oxidation.

8.1.3 0D (MoS₂)/2D (g-C₃N₄) Heterojunctions in Z-Scheme for Enhanced Photocatalytic and Electrochemical Hydrogen Evolution

- ❖ Uniform water-soluble and highly dispersed MoS₂ quantum dots with sizes of 2-5 nm were prepared via a facile one-pot hydrothermal process and were employed to modify g-C₃N₄ nanosheets for MoS₂ QDs/g-C₃N₄ (MSQD-CN) photocatalysts with high photocatalytic and electrochemical H₂ evolution activities.
- ❖ The hydrogen-evolution rate over 0.2 wt% MSQD-CN increased by 1.3 and 8.1 times as high as that of 0.2 wt% Pt-CN and g-C₃N₄, respectively. With deposition of 2 wt% Pt as a cocatalyst, 5 wt% MSQD-CN exhibited the highest photocatalytic efficiency with an average hydrogen evolution reaction (HER) rate of 577 $\mu\text{mol}\cdot\text{h}^{-1}\cdot\text{g}^{-1}$, which is also superior to the as-synthesized 5 wt% MSNS-CN analogue.
- ❖ The introduction of MoS₂ QDs results in a red shift and stronger light absorption capability in comparison with pure g-C₃N₄. Owing to quantum confinement effect, MoS₂ QDs facilitate a faster electron transfer and efficiently prevent the charge recombination via lowering over-potential barriers and charge-transfer resistance.
- ❖ The well-matched band potentials of the MSQD-CN hybrid with an intimate contact interface of p-n heterojunction also inhibited the recombination of photo-generated carriers, leading to the enhanced photocatalytic HER performance. A direct Z-scheme charge transfer mechanism of the MSQD-CN hybrid was proposed to further elaborate the synergic effect between MSQDs, Pt and g-C₃N₄.

8.1.4 Flower-Like MoS₂ on Graphitic Carbon Nitride for Enhanced Photocatalytic and Electrochemical Hydrogen Evolutions

- ❖ 3D flower-like hexagonal 2H-MoS₂ composed of nanosheets with thin-layers were prepared using a facile hydrothermal approach, and then further employed to modify g-C₃N₄ nanosheets with a similar layered structure to achieve MoS₂/g-C₃N₄ hybrid photocatalysts via a simple ultrasonic process.
- ❖ The as-formed intimate junctions contribute to highly enhanced photocatalytic and electrocatalytic H₂ evolution activities. The highest photocatalytic efficiency was observed on 0.5% MSNS-CN with a hydrogen evolution reaction rate of 867.6 μmol·h⁻¹·g⁻¹ under simulated sunlight irradiations. Compared to pure g-C₃N₄, the photocatalytic H₂ evolution activity was elevated to about 2.8 times higher at sunlight irradiations and about 5 times higher for visible light irradiations.
- ❖ This 3D/2D hybrid also presents better photocatalytic performance than its 0D/2D and 2D/2D analogues, which is discussed in Chapter 2. The introduction of MoS₂ nanoflowers leads to a broader absorption range and a strengthened photo-absorption capability compared to pure g-C₃N₄. As an electron acceptor and also the active sites over g-C₃N₄, the unique flower-like nanostructure of MoS₂ boosted a much higher and stable photocatalytic H₂ evolution activity with exposure of more active edge planes and shortened diffusion channels for charge transfer and separation.
- ❖ The proposed mechanism for the activity enhancement lies in the effective interfacial contact formed in the 3D (MoS₂)/2D (g-C₃N₄) heterojunctions with a decreased onset potential, a lower charge-transfer resistance and a higher reductive potential with a more negative conduction band position.
- ❖ In addition, the lowered overpotential and smaller Tafel slope of 0.5% MSNS-CN also promise the enhanced electrocatalytic H₂ evolution performance with a decreased activation barrier and facilitated kinetics.

8.1.5 Graphitic Carbon Nitride Decorated with CoP Nanocrystals for Enhanced Photo, Electro and Photoelectrochemical H₂ Evolution

- ❖ Polydispersed CoP nanoparticles in an orthorhombic phase were synthesized via a gas-solid reaction and further deposited on g-C₃N₄ to form CoP/g-C₃N₄ heterostructure.

Nanorod-like CoP nanoparticles with a length of 10-80 nm were connected to g-C₃N₄ nanosheets via their (011) crystal planes to form an intimate face-to-face contact.

- ❖ This unique heterojunction exhibits superior photocatalytic, electrocatalytic H₂ evolution performance, photoelectrochemical response as well as excellent overall water splitting activity.
- ❖ The photocatalytic hydrogen evolution rate of 0.5% CoP-CN reached 959.4 μmol·h⁻¹·g⁻¹ under simulated sunlight irradiations, almost 3.1 times as high as that of pristine g-C₃N₄. Its photocatalytic H₂ evolution activity under visible light was elevated to almost 15.8 times that of pure g-C₃N₄. The onset potential for electrochemical HER process was lowered from -0.61 V vs. Ag/AgCl for pristine g-C₃N₄ to -0.31 V vs. Ag/AgCl. The 0.5% CoP-CN presented a larger photocurrent density with higher response and more negative onset photocurrent potential in the photoelectrochemical (PEC) testing. It also showed excellent overall water splitting activity without any sacrificial agent. The simultaneous evolution rates of H₂ and O₂ were estimated to be 14.7 and 7.6 μmol·h⁻¹·g⁻¹.
- ❖ The enhancement for photocatalytic, electrocatalytic and PEC HER activity can be ascribed to the deposition of CoP nanoparticles by constructing an intimate interfacial contact for reduced overpotentials, lowered charge carrier resistance and stronger photo-reductive capability, promoting much more efficient separation and transfer of charge carriers.
- ❖ For the first time, CoP-based photocatalysts as effective photo, electro and photochemical HER catalysts with evident enhancement have been investigated comprehensively.

8.2 Perspectives and suggestions for future research

As shown above, substantial research outcomes have been achieved during this study. However, there is a long way to go to attain practical application of these experimental findings to solve critical issues concerning environmental remediation and energy crisis. Due to time limitations and equipment deficiency, further exploring on mechanism concerning overall water splitting and PEC-H₂ evolution need to be conducted later on. Looking into the future, more efforts should be devoted to the following aspects:

- ✧ Employing scalable exfoliation techniques for single or few-layered g-C₃N₄ for potential industrial applications;
- ✧ Developing green and simple synthesis techniques without any secondary hazards.
- ✧ Combining theoretical calculation with innovative approach for the design of site-selective loading of cocatalysts and crystal facet tailoring of photocatalysts;
- ✧ Reinforcing the heterostructure between cocatalyst and the photocatalyst to achieve a high stability, especially for metal sulfides;
- ✧ Developing new strategies for exploiting efficient visible light absorption to longer wavelength (above 500 nm) to mimic the natural photosynthesis process;
- ✧ The evaluation system for photocatalytic pollutants degradation should include various types of pollutants other than dyes in aqueous phases;
- ✧ Advanced in-situ characterization techniques such as infrared spectroscopy and GC-MS using H₂¹⁸O as reagent should be taken into consideration;
- ✧ The mechanism for overall water splitting activity over 3% Pt-0.5% CoP-CN as well as the verification of this dual co-catalysts function should be studied systematically.

In summary, g-C₃N₄-based and bismuth-based photocatalysts will definitely keep booming as a research hotspot with challenges and opportunities in the following years, with a few challenges and difficulties to be conquered on the way to scalable applications.

Appendix

Copyright Permissions

Copyright licenses from the copyright owners have been granted to reproduce copyright materials in Chapter 2 of this thesis with details shown below:



RightsLink®

Home

Account
Info

Help



Title: Dye-Sensitized Solar Cells
Author: Anders Hagfeldt, Gerrit Boschloo, Licheng Sun, et al
Publication: Chemical Reviews
Publisher: American Chemical Society
Date: Nov 1, 2010
Copyright © 2010, American Chemical Society

Logged in as:
Yazi Liu
Curtin University
Account #:
3001378881

LOGOUT

PERMISSION/LICENSE IS GRANTED FOR YOUR ORDER AT NO CHARGE

This type of permission/license, instead of the standard Terms & Conditions, is sent to you because no fee is being charged for your order. Please note the following:

- Permission is granted for your request in both print and electronic formats, and translations.
- If figures and/or tables were requested, they may be adapted or used in part.
- Please print this page for your records and send a copy of it to your publisher/graduate school.
- Appropriate credit for the requested material should be given as follows: "Reprinted (adapted) with permission from (COMPLETE REFERENCE CITATION). Copyright (YEAR) American Chemical Society." Insert appropriate information in place of the capitalized words.
- One-time permission is granted only for the use specified in your request. No additional uses are granted (such as derivative works or other editions). For any other uses, please submit a new request.

If credit is given to another source for the material you requested, permission must be obtained from that source.

BACK

CLOSE WINDOW

Copyright © 2018 [Copyright Clearance Center, Inc.](#) All Rights Reserved. [Privacy statement.](#) [Terms and Conditions.](#)

Comments? We would like to hear from you. E-mail us at customer@copyright.com

Title: Graphitic Carbon Nitride (g-C₃N₄)-Based Photocatalysts for Artificial Photosynthesis and Environmental Remediation: Are We a Step Closer To Achieving Sustainability?

Author: Wee-Jun Ong, Lling-Lling Tan, Yun Hau Ng, et al

Publication: Chemical Reviews

Publisher: American Chemical Society

Date: Jun 1, 2016

Copyright © 2016, American Chemical Society

LOGIN

If you're a [copyright.com](#) user, you can login to RightsLink using your [copyright.com](#) credentials.

Already a [RightsLink](#) user or want to [learn more?](#)

PERMISSION/LICENSE IS GRANTED FOR YOUR ORDER AT NO CHARGE

This type of permission/license, instead of the standard Terms & Conditions, is sent to you because no fee is being charged for your order. Please note the following:

- Permission is granted for your request in both print and electronic formats, and translations.
- If figures and/or tables were requested, they may be adapted or used in part.
- Please print this page for your records and send a copy of it to your publisher/graduate school.
- Appropriate credit for the requested material should be given as follows: "Reprinted (adapted) with permission from (COMPLETE REFERENCE CITATION). Copyright (YEAR) American Chemical Society." Insert appropriate information in place of the capitalized words.
- One-time permission is granted only for the use specified in your request. No additional uses are granted (such as derivative works or other editions). For any other uses, please submit a new request.

If credit is given to another source for the material you requested, permission must be obtained from that source.

BACK

CLOSE WINDOW

Copyright © 2018 [Copyright Clearance Center, Inc.](#) All Rights Reserved. [Privacy statement.](#) [Terms and Conditions.](#)

Comments? We would like to hear from you. E-mail us at customer@copyright.com



Title: A New Metal-Free Carbon Hybrid for Enhanced Photocatalysis
Author: Hongqi Sun, Guanliang Zhou, Yuxian Wang, et al
Publication: Applied Materials
Publisher: American Chemical Society
Date: Oct 1, 2014
Copyright © 2014, American Chemical Society

Logged in as:
Yazi Liu
Curtin University
Account #:
3001378881

LOGOUT

PERMISSION/LICENSE IS GRANTED FOR YOUR ORDER AT NO CHARGE

This type of permission/license, instead of the standard Terms & Conditions, is sent to you because no fee is being charged for your order. Please note the following:

- Permission is granted for your request in both print and electronic formats, and translations.
- If figures and/or tables were requested, they may be adapted or used in part.
- Please print this page for your records and send a copy of it to your publisher/graduate school.
- Appropriate credit for the requested material should be given as follows: "Reprinted (adapted) with permission from (COMPLETE REFERENCE CITATION). Copyright (YEAR) American Chemical Society." Insert appropriate information in place of the capitalized words.
- One-time permission is granted only for the use specified in your request. No additional uses are granted (such as derivative works or other editions). For any other uses, please submit a new request.

If credit is given to another source for the material you requested, permission must be obtained from that source.

BACK

CLOSE WINDOW

Copyright © 2018 [Copyright Clearance Center, Inc.](#) All Rights Reserved. [Privacy statement](#). [Terms and Conditions](#).

Comments? We would like to hear from you. E-mail us at customer@copyright.com



Title: A Realizable Renewable Energy Future
Author: John A. Turner
Publication: Science
Publisher: The American Association for the Advancement of Science
Date: Jul 30, 1999
 Copyright © 1999, The American Association for the Advancement of Science

Logged in as:
 Yazi Liu
 Curtin University
 Account #:
 3001378881

[LOGOUT](#)

Permissions Request

AAAS may not control the rights to the image you wish to use. Please submit your request directly to the publisher by following the guidelines at <http://www.sciencemaq.org/about/permissions.dtl>. Please allow 10 to 15 days to receive a response.

[BACK](#)

[CLOSE WINDOW](#)

Copyright © 2018 [Copyright Clearance Center, Inc.](#) All Rights Reserved. [Privacy statement](#). [Terms and Conditions](#).

Comments? We would like to hear from you. E-mail us at customercare@copyright.com



Title: Enhancement of Photocatalytic H₂ Evolution on CdS by Loading MoS₂ as Cocatalyst under Visible Light Irradiation
Author: Xu Zong, Hongjian Yan, Guopeng Wu, et al
Publication: Journal of the American Chemical Society
Publisher: American Chemical Society
Date: Jun 1, 2008
 Copyright © 2008, American Chemical Society

Logged in as:
 Yazi Liu
 Curtin University
 Account #:
 3001378881

[LOGOUT](#)

PERMISSION/LICENSE IS GRANTED FOR YOUR ORDER AT NO CHARGE

This type of permission/license, instead of the standard Terms & Conditions, is sent to you because no fee is being charged for your order. Please note the following:

- Permission is granted for your request in both print and electronic formats, and translations.
- If figures and/or tables were requested, they may be adapted or used in part.
- Please print this page for your records and send a copy of it to your publisher/graduate school.
- Appropriate credit for the requested material should be given as follows: "Reprinted (adapted) with permission from (COMPLETE REFERENCE CITATION). Copyright (YEAR) American Chemical Society." Insert appropriate information in place of the capitalized words.
- One-time permission is granted only for the use specified in your request. No additional uses are granted (such as derivative works or other editions). For any other uses, please submit a new request.

If credit is given to another source for the material you requested, permission must be obtained from that source.

[BACK](#)

[CLOSE WINDOW](#)

Copyright © 2018 [Copyright Clearance Center, Inc.](#) All Rights Reserved. [Privacy statement](#). [Terms and Conditions](#).

Comments? We would like to hear from you. E-mail us at customercare@copyright.com



Title: Graphitic Carbon Nitride (g-C₃N₄)-Based Photocatalysts for Artificial Photosynthesis and Environmental Remediation: Are We a Step Closer To Achieving Sustainability?

Author: Wee-Jun Ong, Lling-Lling Tan, Yun Hau Ng, et al

Publication: Chemical Reviews

Publisher: American Chemical Society

Date: Jun 1, 2016

Copyright © 2016, American Chemical Society

Logged in as:

Yazi Liu
Curtin University

Account #:
3001378881

LOGOUT

PERMISSION/LICENSE IS GRANTED FOR YOUR ORDER AT NO CHARGE

This type of permission/license, instead of the standard Terms & Conditions, is sent to you because no fee is being charged for your order. Please note the following:

- Permission is granted for your request in both print and electronic formats, and translations.
- If figures and/or tables were requested, they may be adapted or used in part.
- Please print this page for your records and send a copy of it to your publisher/graduate school.
- Appropriate credit for the requested material should be given as follows: "Reprinted (adapted) with permission from (COMPLETE REFERENCE CITATION). Copyright (YEAR) American Chemical Society." Insert appropriate information in place of the capitalized words.
- One-time permission is granted only for the use specified in your request. No additional uses are granted (such as derivative works or other editions). For any other uses, please submit a new request.

If credit is given to another source for the material you requested, permission must be obtained from that source.

BACK

CLOSE WINDOW

Copyright © 2018 Copyright Clearance Center, Inc. All Rights Reserved. [Privacy statement](#). [Terms and Conditions](#).

Comments? We would like to hear from you. E-mail us at customercare@copyright.com



Title: In Situ Microwave-Assisted Synthesis of Porous N-TiO₂/g-C₃N₄ Heterojunctions with Enhanced Visible-Light Photocatalytic Properties

Author: Xiao-jing Wang, Wen-yan Yang, Fa-tang Li, et al

Publication: Industrial & Engineering Chemistry Research

Publisher: American Chemical Society

Date: Dec 1, 2013

Copyright © 2013, American Chemical Society

Logged in as:

Yazi Liu
Curtin UniversityAccount #:
3001378881

LOGOUT

PERMISSION/LICENSE IS GRANTED FOR YOUR ORDER AT NO CHARGE

This type of permission/license, instead of the standard Terms & Conditions, is sent to you because no fee is being charged for your order. Please note the following:

- Permission is granted for your request in both print and electronic formats, and translations.
- If figures and/or tables were requested, they may be adapted or used in part.
- Please print this page for your records and send a copy of it to your publisher/graduate school.
- Appropriate credit for the requested material should be given as follows: "Reprinted (adapted) with permission from (COMPLETE REFERENCE CITATION). Copyright (YEAR) American Chemical Society." Insert appropriate information in place of the capitalized words.
- One-time permission is granted only for the use specified in your request. No additional uses are granted (such as derivative works or other editions). For any other uses, please submit a new request.

If credit is given to another source for the material you requested, permission must be obtained from that source.

BACK

CLOSE WINDOW

Copyright © 2018 [Copyright Clearance Center, Inc.](#) All Rights Reserved. [Privacy statement.](#) [Terms and Conditions.](#)

Comments? We would like to hear from you. E-mail us at customercare@copyright.com



Title: Synthesis and Efficient Visible Light Photocatalytic Hydrogen Evolution of Polymeric g-C₃N₄ Coupled with CdS Quantum Dots

Author: Lei Ge, Fan Zuo, Jikai Liu, et al

Publication: The Journal of Physical Chemistry C

Publisher: American Chemical Society

Date: Jun 1, 2012

Copyright © 2012, American Chemical Society

Logged in as:
Yazi Liu
Curtin University
Account #:
3001378881

LOGOUT

PERMISSION/LICENSE IS GRANTED FOR YOUR ORDER AT NO CHARGE

This type of permission/license, instead of the standard Terms & Conditions, is sent to you because no fee is being charged for your order. Please note the following:

- Permission is granted for your request in both print and electronic formats, and translations.
- If figures and/or tables were requested, they may be adapted or used in part.
- Please print this page for your records and send a copy of it to your publisher/graduate school.
- Appropriate credit for the requested material should be given as follows: "Reprinted (adapted) with permission from (COMPLETE REFERENCE CITATION). Copyright (YEAR) American Chemical Society." Insert appropriate information in place of the capitalized words.
- One-time permission is granted only for the use specified in your request. No additional uses are granted (such as derivative works or other editions). For any other uses, please submit a new request.

If credit is given to another source for the material you requested, permission must be obtained from that source.

BACK

CLOSE WINDOW

Copyright © 2018 [Copyright Clearance Center, Inc.](#) All Rights Reserved. [Privacy statement.](#) [Terms and Conditions.](#)

Comments? We would like to hear from you. E-mail us at customercare@copyright.com

Order Date	Article Title	Publication	Type of Use	Order Status	Licence Number
11-Dec-2018	Fabrication of flower-like Bi ₂ WO ₆ superstructures as high performance visible-light driven photocatalysts	Journal of materials chemistry	Thesis/Dissertation	completed	4485920768552
11-Dec-2018	Advanced chemical compositions and nanoarchitectures of bismuth based complex oxides for solar photocatalytic application	RSC advances	Thesis/Dissertation	completed	4485920275111
11-Dec-2018	Enhanced visible-light activities of porous BiFeO ₃ by coupling with nanocrystalline TiO ₂ and mechanism	Applied Catalysis B: Environmental	reuse in a thesis/dissertation	completed	4485911277553
11-Dec-2018	Self-assembled growth of BiFeO ₃ meso-octahedral particles synthesized by a facile surfactant-free hydrothermal method	Journal of Crystal Growth	reuse in a thesis/dissertation	completed	4485911104425
11-Dec-2018	A review on the visible light active BiFeO ₃ nanostructures as suitable photocatalyst in the degradation of different textile dyes	Environmental Nanotechnology, Monitoring & Management	reuse in a thesis/dissertation	completed	4485910952105
11-Dec-2018	Increasing visible-light absorption for photocatalysis with black BiOCl	Physical chemistry chemical physics	Thesis/Dissertation	completed	4485910837998
11-Dec-2018	Preparation and first-principles study for electronic structures of BiOI/BiOCl composites	Journal of Molecular Catalysis A:	reuse in a thesis/dissertation	completed	4485910257296

	with highly improved photocatalytic and adsorption performances	Chemical			
11-Dec-2018	Recent advances in BiOX (X = Cl, Br and I) photocatalysts: synthesis, modification, facet effects and mechanisms	Environmental Science: Nano	Thesis/Dissertation	completed	4485910046943
11-Dec-2018	Decorating CoP and Pt Nanoparticles on Graphitic Carbon Nitride Nanosheets to Promote Overall Water Splitting by Conjugated Polymers	ChemSusChem	Dissertation/Thesis	completed	4485901261575
11-Dec-2018	Noble-metal-free cobalt phosphide modified carbon nitride: An efficient photocatalyst for hydrogen generation	Applied Catalysis B: Environmental	reuse in a thesis/dissertation	completed	4485901121815
11-Dec-2018	Synthesis of MoS ₂ /g-C ₃ N ₄ nanosheets as 2D heterojunction photocatalysts with enhanced visible light activity	Applied Surface Science	reuse in a thesis/dissertation	completed	4485900413321
11-Dec-2018	Layered Nanojunctions for Hydrogen-Evolution Catalysis	Angewandte Chemie	Dissertation/Thesis	completed	4485900290520
11-Dec-2018	Monodisperse Co ₃ O ₄ quantum dots on porous carbon nitride nanosheets for enhanced visible-light-driven water oxidation	Applied Catalysis B: Environmental	reuse in a thesis/dissertation	completed	4485900118672

11-Dec-2018	Novel visible light induced Co_3O_4 -g- C_3N_4 heterojunction photocatalysts for efficient degradation of methyl orange	Applied Catalysis B: Environmental	1	reuse in a thesis/dissertation	completed	4485891217098
11-Dec-2018	Enhanced photocatalytic performance of direct Z-scheme g- C_3N_4 - TiO_2 photocatalysts for the decomposition of formaldehyde in air	Physical chemistry chemical physics		Thesis/Dissertation	completed	4485890957191
11-Dec-2018	Porous graphitic carbon nitride synthesized via direct polymerization of urea for efficient sunlight-driven photocatalytic hydrogen production	Nanoscale		Thesis/Dissertation	completed	4485890476283
11-Dec-2018	Effect of graphitic carbon nitride microstructures on the activity and selectivity of photocatalytic CO_2 reduction under visible light	Catalysis Science		Thesis/Dissertation	completed	4485890045713
11-Dec-2018	Natural dyes as TiO_2 sensitizers with membranes for photoelectrochemical water splitting: An overview	Renewable and Sustainable Energy Reviews		reuse in a thesis/dissertation	completed	4485861433087
11-Dec-2018	Noble metal-free hydrogen evolution catalysts for water splitting	Chemical Society reviews		Thesis/Dissertation	completed	4485850998276
11-Dec-2018	Synthesis and Photocatalytic Application of Novel Heterojunction	Chemical Society reviews		Thesis/Dissertation	completed	4485750069448

	Nanocomposites as Photocatalysts				
11-Dec -2018	Effect of graphitic carbon nitride microstructures on the activity and selectivity of photocatalytic CO ₂ reduction under visible light	Catalysis Science	Thesis/Disser tation	completed	4485731416 720
